Surface-enhanced Raman Spectroscopy and Fluorescence Spectroscopy towards detection of Pterins

Ciarán Smyth

September 2013

A thesis submitted for a degree of
Doctor of Philosophy
to the University of Dublin
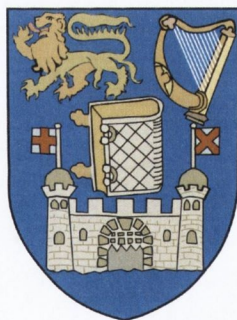
School of Physics
Trinity College
University of Dublin
Ireland
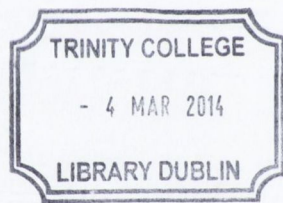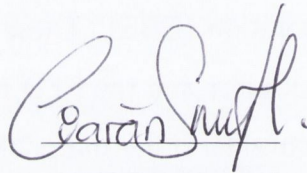
Abstract

In this thesis, a preliminary study is conducted into surface-enhanced Raman spectroscopy (SERS) and fluorescence spectroscopy towards the detection and analysis of pterins. Firstly, investigation of some optical properties of various pterin species is considered, using absorption and fluorescence spectroscopy. Silver colloids for SERS anlaysis are then investigated, particularly concerning substrate reproducibility and analysis optimisation. Complementary to the study of using silver colloids is the investigation of SERS using two nanoparticulate substrates, prepared using pulsed laser deposition (PLD) and electron beam evaporation (EBE). These materials are also characterised according to their SERS reproducibility and the PLD films are compared to a commercial substrate. The appendices consider other materials and techniques used during the project, and an outlook for future work is also presented.

DECLARATION

I declare that this thesis has not been submitted as an exercise for a degree at this or any other university and it is entirely my own work.

I agree to deposit this thesis in the University's open access institutional repository or allow the library to do so on my behalf, subject to Irish Copyright Legislation and Trinity College Library conditions of use and acknowledgement.

Ciarán Smyth

Publications

Peer Reviewed

1. **C. Smyth**, I. Mirza, J.G. Lunney and E.M. McCabe, *Surface-Enhanced Raman Spectroscopy (SERS) using Ag nanoparticle films produced by Pulsed Laser deposition (PLD)*. Submitted to Journal of Surface Science, 2012.

2. **C. Smyth**, S. Mehigan, Y. P. Rakovich, S.E. J Bell and E.M. McCabe, *Pterin detection using surface-enhanced Raman spectroscopy incorporating a straight-forward silver colloidbased synthesis technique.* J. Biomed. Opt. (2011) **16** 077007; also selected for the July 15, 2011 issue of Virtual Journal of Biological Physics Research.

3. **C. Smyth**, R. Reilly, Y. Rakovich and E. McCabe, *Synthesis and formation of one-dimensional Au nanoparticle chains.* J.Surf.Sci.Nanotech. (2009) **7** 327-329

4. R. Reilly, **C. Smyth**, Y. Rakovich and E. McCabe, *Photoluminescent lifetime of polyelectrolytes in thin films formed via layer by layer self assembly.* Nanotechnology (2009) **20** 095707

Conference Contributions

1. S. Mehigan **C. Smyth** and Eithne McCabe, *SERS using Silver Nanoparticles*, Poster presented at Institute of Physics Rosse Medal Research Round-up Ireland Conference, Dublin, 2012

2. **C. Smyth**, I. Mirza, J.G. Lunney and E.M. McCabe, *Surface-Enhanced Raman Spectroscopy of Pterins.* Proc.SPIE 8234, 82341G1-G7, doi:10.1117/12/, 2012.

3. **C. Smyth**, I. Mirza, S.E.J. Bell, Y.P. Rakovich, J.G. Lunney and E.M. McCabe, *Surface-enhanced Raman spectroscopy of pterins using silver nanoparticles.* Photonics Ireland, Malahide, Dublin, 2011

4. **C. Smyth**, S.E.J. Bell, Y.P. Rakovich and E.M.McCabe, *Surface-Enhanced Raman Spectroscopy (SERS) of pterins.* Nanotechnology Conference 2011, Carton House, Co. Kildare, Ireland

5. **C. Smyth**, S. Mehigan, Y. P. Rakovich, S. E. J. Bell and E. M. McCabe, *Biological sensing with Surface-Enhanced Raman Spectroscopy (SERS) using a facile and rapid silver colloid-based synthesis technique.* Proc. SPIE 7911, 79111H (2011); doi:10.1117/12.876123, 2011.

6. **C. Smyth**, J.J. Wang, S.E.J.Bell, Y.P. Rakovich and E.M. McCabe, *Surface enhanced Raman spectroscopy using metal nanostructure substrates towards the study of pterins.* Biosensors 2010, 20th Anniversary World Congress on Biosensors, Glasgow, UK, 26-28 May, 2010

7. **C. Smyth**, Y.P. Rakovich and E.M. McCabe, *Alignment and FLIM imaging of Ag nanowires with CdTe quantum dots.* 11th International Conference on Transparent Optical Networks Ponta Delgada University, Azores, Portugal, 2009

8. **C. Smyth**, Y.P. Rakovich and E.M. McCabe, *Investigation and characterisation of 1-dimensional plasmonic structures.* Photonics Ireland, Kinsale, Co. Cork , 2009

9. **C. Smyth**, Y.P. Rakovich and E.M. McCabe, *Synthesis and characterisation of one-dimensional silver nanostructures.* 37th Spring Weekend Meeting of the Institute of Physics, Wexford, 2009

10. **C. Smyth**, R. Reilly, Y.P. Rakovich and E.M. McCabe, *Synthesis and formation of one-dimensional Au nanoparticle chains.* 14th International Conference on Solid Films and Surfaces, 25, 228, 2008

11. **C. Smyth**, R. Reilly, Y.P. Rakovich and E.M. McCabe, *Synthesis and forma-*

tion of one-dimensional Au nanoparticle chains. 2nd International Conference on Advanced Nano Materials, Aveiro, Portugal, 29, 159, 2008

12. **C. Smyth**, R. Reilly, Y.P. Rakovich and E.M. McCabe, *Characterisation of gold nanoparticles towards nanowire production and imaging.* 36th Spring Weekend Meeting of the Institute of Physics, Monaghan, 2008

Acknowledgements

First and foremost, I would like to thank my supervisor Prof. Eithne McCabe. Over the course of my work she has been very supportive, and our weekly meetings have always been enjoyable and productive. Over the course of my project I would also like to thank Dr. Yury Rakovich, Roseanne Reilly and Sam Mehigan, all of whom have been involved in our research group during my time. Also within Trinity College, Dr. Jing Jing Wang has helped with various Raman measurements in CRANN and Prof. James Lunney and Inam Mirza were both involved in the study of the SERS substrates. I would particularly like to thank Inam for preparing the PLD films for SERS measurements, helping me with AFM measurements and for the various discussions in what has been a very useful collaboration. I would also like to thank Dr. Niall McEvoy, who has helped over a wide range of Raman issues and investigations, and who was also responsible for annealing the various SERS substrates. Externally I would like to thank Prof. Steven Bell in Queen's University Belfast for his many helpful suggestions and continued collaboration. I would also like to thank the Trinity College Postgraduate Research Scholarship, the School of Physics and Science Foundation Ireland for providing the funding towards this work.

I would further like to thank the entire Photonics group in Trinity College; there are a wide range of projects within the group, and I have thoroughly enjoyed my time working with everyone. I am particularly grateful to those with whom I have shared my office over the years, as it has been a very enjoyable environment in which to work. Also to all those in the university with whom I have played football or scuba dived or indulged in other sporting ventures or otherwise, I offer my appreciation, as it has all contributed to a very enjoyable time.

I would like to thank Íde for all her patience and support; it has been a long and some-times stressful process, and she has been understanding and encouraging throughout. I would also like to add my particular thanks to Diarmuid and Maria, with whom I lived

Contents

1

Introduction and Theory

An understanding of light has been developed over the centuries to include Isaac Newton's work on prism refractions and their consequent colour distribution[1] and James Clerk Maxwell's demonstrations of its electromagnetic wave nature.[2] Coupled with the wave nature of light, further thinking by Max Planck[3] and Albert Einstein[4] led to the development of the theories of the particle and quantum nature of light. The particle view considered light to behave as if it was composed of a stream of particles, with an associated and quantised energy per particle that was related to its frequency. These particles have become known as photons, and the energy contained in a photon can interact with charged particles, such as the electrons within a molecule. The study of such interactions has led to the fields of photophysics and photochemistry, with many spectroscopic techniques being developed. In this thesis the detection and quantification of a class of biological compounds known as pterins has been considered, using fluorescence spectroscopy and surface-enhanced Raman spectroscopy (SERS). Comparisons have been made with standard fluorescence and SERS probes, and SERS in particular is investigated with respect to its viability in pterin detection.

1.1 Pterins

1.1.1 History and Description

Research into pterins began with Frederich Gowland Hopkins in 1889 when he isolated the yellow pigment from the wings of the Brimstone butterfly (*Gonepteryx rhamni*),[5] a feat that he repeated with the white pigment from the Cabbage White butterfly (*Pieris rapae*).[6] These pigments were named xanthopterin and leucopterin respectively by H. Wieland and C. Shopf, after the Greek words for yellow and white (*xanthos* and *leukos*) and for wing (*pteron*).[7] Details of their molecular structure proved difficult and it was 1940 by the time that the compounds were synthesised by Purrmann and the structures were validated.[7] Purrmann also established the structure for isoxanthopterin and soon afterwards a system was devised to nominate a basic pterin unit, composed of a pyrazine ring and a pyrimidine ring combined together, from which derivatives could be described based on attached substituents. The basic pterin structure is shown below in Figure 1.1.
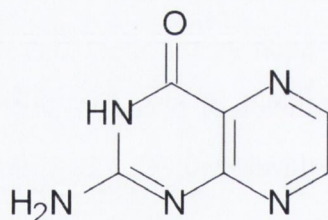
Figure 1.1: Pterin, composed of a pyrazine and a pyrimidine ring.

1.1.2 Photochemical & Photophysical Properties

One important factor concerning pterins is that many species exhibit poor solubility in water and most organic solvents.[8–10] This solubility varies from species to species with solubilities for xanthopterin and isoxanthopterin in water at 20°C found to be one part in $40,000$ (2.5×10^{-5} M), one part in $200,000$ (5.0×10^{-6} M)[11] and biopterin and 7,8-dihydrobiopterin one part in $10,000$ (1.0×10^{-4} M) and one part in 500 (2.0×10^{-3} M)

respectively. The solubility of compounds is, however, affected by the pH of the solution, and in the datasheet from Schircks Laboratories, a prominent provider of pterins, it is stated that a concentrated solution of biopterin may be prepared in 0.05 M NaOH.[12]

The involvement of pterins in various photobiological processes is a topic that has been investigated in recent times.[13–15] They are particularly prone to UV absorption,[16] although similar species can show quite pronounced differences in their UV properties - isoxanthopterin has an almost twice as large extinction coefficient as xanthopterin under 254 nm excitation[17] - 12400 to 6500. Under UV exposure pterins can become fluorescent and can photo-oxidate into separate photoproducts, and they are also capable of photoinducing the oxidation of DNA and its derivatives.[18–20] Particular fluorescence and photooxidation properties of the pterins have been suggested as being relevant in certain biological systems. Pterins behave as weak acids in aqueous solution, and have been seen to form an acid-base equilibrium, displaying an amine group and a phenolate group respectively, at pH values greater than 5.[21] The acid dissociation constant (pK_a) is a measure of the strength of an acid in solution; with values of 9.42 for xanthopterin,[22] 10.8 for isoxanthopterin,[23] 8.1 for biopterin[21] and greater than 10 for 7,8-dihydrobiopterin.[15]

Their changing fluorescent properties with pH have also resulted in pterins being used in pH sensing.[24] Shown in Figure 1.2 are the structures and literature UV/Vis spectra of the pterins investigated in this thesis.
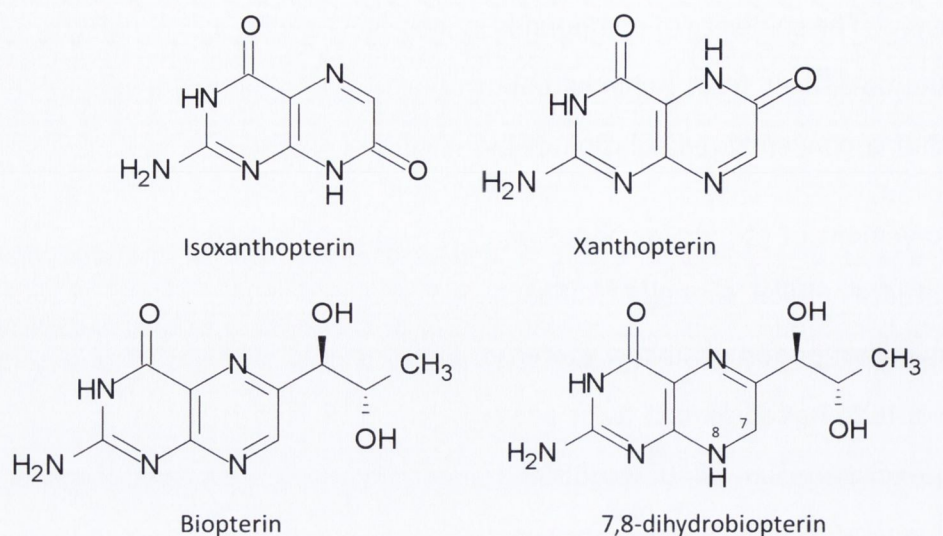
(a)
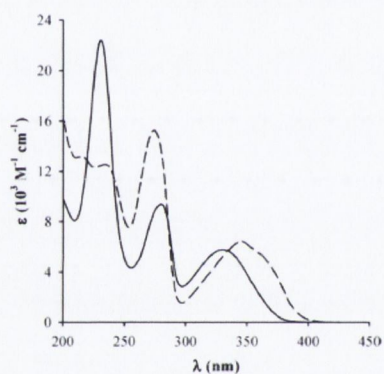
(b)
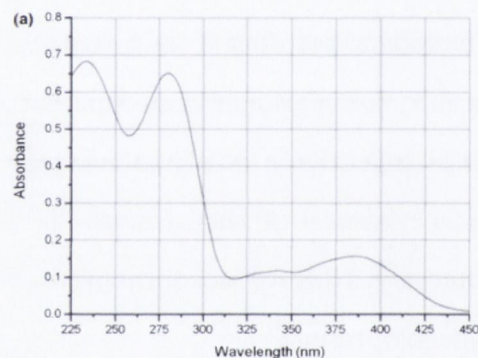
(c)
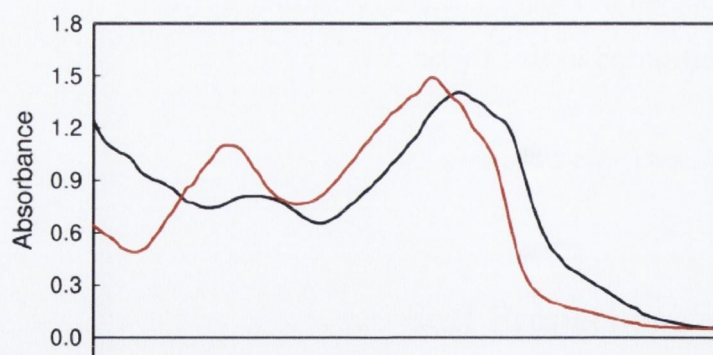
(d)

Figure 1.2: (a) The structures of isoxanthopterin, xanthopterin, biopterin and 7,8-dihydrobiopterin. (b) shows the UV/Vis spectra of biopterin (Dashed line) and 7,8-dihydrobiopterin (Solid line), reproduced from Vignoni et. al.[14] (c) shows the spectrum for xanthopterin taken from Plotkin et. al.[25] and (d) shows the spectrum for isoxanthopterin (Black spectrum), taken from Hall et. al.[26]

1.1.3 Pterins in Biological Systems

Pterins have been widely studied in biological systems, in all manner of living organisms. Much of the work has been concerned with colour pigmentation, and indeed much has been directed towards members of the Lepidoptera, the insect order that contains butterflies and moths. In the Oriental Hornet (*Vespa orientalis*) xanthopterin is found in the thorax of the adults, seemingly to absorb harmful UV radiation.[25] Pterins have also been studied as blue-light receptors[27] and can be found in photoreceptive organs in plants,[28] in the pigments of insect eyes,[29] and in the skin of amphibians,[30] the scales of fish[31] and the feathers of birds.[32]

Other organisms found to exhibit pterins include the tunicate *Ascidiella aspersa*, which shows pterin and isoxanthopterin to be excreted from the organism, though whether the compounds are synthesised by the organism or acquired through diet is not known.[33] The Great Crested Newt, *Triturus cristatus*, has been found to possess increased levels of tetrahydrobiopterin during tail regeneration, which is later replaced by isoxanthopterin, and these changes affect protein synthesis.[7] Studies in rats have shown that the concentration of biopterins varies in different areas of the anatomy, with the tetrahydro form being the most plentiful, with high concentrations found in the pineal gland, bone marrow and in the spleen.[34] Rat brains, while showing a relatively low concentration overall, did show a distribution of the biopterin with one of the highest concentrations found in the area known for high levels of serotonin. Other studies on rats have shown increased concentrations of the tetrahydrobiopterin during liver regeneration,[35] with rapid excretion of the reduced dihydrobiopterin form.[36]

In humans, biopterin is also found in body fluids, along with similar concentrations of neopterin.[7] Blood and serum levels of biopterin in humans have been linked as indicators of various diseases, including tumour-growth, gout, liver disease and neurological diseases. Changes in pterin concentrations in human urine have also been associated with various diseases; neopterin and biopterin both exist in high concentrations in normal human urine, and other species such as isoxanthopterin and xanthopterin area also found.[37] Pterins have also been linked to roles in the early stages of postpartum de-

pression.[38]

Xanthoptein, and its structural isomer isoxanthopterin, have come under further study regarding research into the diagnosis of various diseases, and in particular various cancers. While both xanthopterin and isoxanthopterin are both excreted by cells, leading to potential in diagnoses, they have also been applied to studies on the reaction of cells to pterin addition. One interesting study involving both xanthopterin and isoxanthopterin was conducted with respect to their potential cytotoxicity towards MCF-7 cells.[39] MCF-7 is a breast cancer cell line, and in the course of the research these cells were exposed to varying pterin concentrations, and mixtures of the two pterin compounds. The aim of the study was to examine the IC_{50} values for each pterin and for a range of mixtures of the two, and in doing so examine the potential of the pterins in treatment of breast cancer. IC_{50} is the half maximal inhibitory concentration of a substance, and relates to the concentration of the substance that will cause an inhibition of a biological process to the factor of a half. Results showed that incubating the cell line with increasing concentrations of both xanthopterin and isoxanthopterin produced a decreasing trend in the percentage of surviving cells. Mixtures of the two pterins in varying concentrations showed a rise in the percentage survival of cells at a certain concentration ratio, with the authors speculating that it could potentially be due to concentration-dependant reactions within the cell. Another study into the anti-tumour properties of pterins was performed with regards to Dalton's Lymphoma, where mice induced with the condition showed a greater survival rate following treatment with 2-amino-4-hydroxypteridine.[40]

In metabolic pathways the reactions that take place can be classified either as anabolic pathways or catabolic pathways. Anabolism is the set of pathways that are concerned with construction, the building of useful compounds from smaller components, and is a process that requires energy input. Catabolism is the opposite of this where dietary compounds are broken down into smaller units, a process that releases energy. The released energy is stored by the synthesis of adenosine triphosphate (ATP) or by the reduction of the coenzyme nicotinamide adenine dinucleotide phosphate ($NADP^+$ to NADPH). These become energy-rich fuel sources, which can then be used in the anabolic pathways.

Amino acids are one type of compound that are broken down in these catabolic processes. The product of these degradation steps are usually compounds that can be metabolized to CO_2 and H_2O or else can be used in gluconeogenesis. This latter term refers to a process whereby glucose is synthesized in the body from non-carbohydrate sources, and represents a significant fraction of the glucose produced in the human body, occurring within only a few hours of eating.

Pterins are important molecules in these metabolic pathways as they act as coenzymes that facilitate enzyme reactions.[41] Phenylketonuria is a condition that can result in mental health problems within a few months of birth if not detected and treated immediately. The reason for this condition is an inhibition to the metabolic pathway that converts the amino acid phenylalanine to tyrosine. Tyrosine then plays a further important role in biological functions, as it is further converted into neurotransmitters such as dopamine.[42]

The pathway for the conversion of phenylalanine is shown in Figure 1.3, where it can be seen that the reaction is catalysed by the enzyme phenylalanine hydroxylase. This reaction, however, cannot occur without the pterin species 7,8-dihydrobiopterin, which is converted to 5,6,7,8-tetrahydrobiopterin by the enzyme dihydrofolate reductase and the energy-rich NADPH. The pterin is then oxidized in the same step that facilitates the oxidation of phenylalanine, before being reduced back to the starter molecule again by dihydropterin reductase and NADH.

Analysis of the relative concentrations of coenzyme 7,8-dihydrobiopterin would therefore be of some significance within biological analysis, and likewise with many other species of pterins.

1.1.4 Pterin Detection

Other pterin species, such as xanthopterin and isoxanthopterin, are found to be present in heightened concentrations in the urine samples of cancer patients.[43] Much of the diagnosis work undertaken on pterins has been done through the means of separation
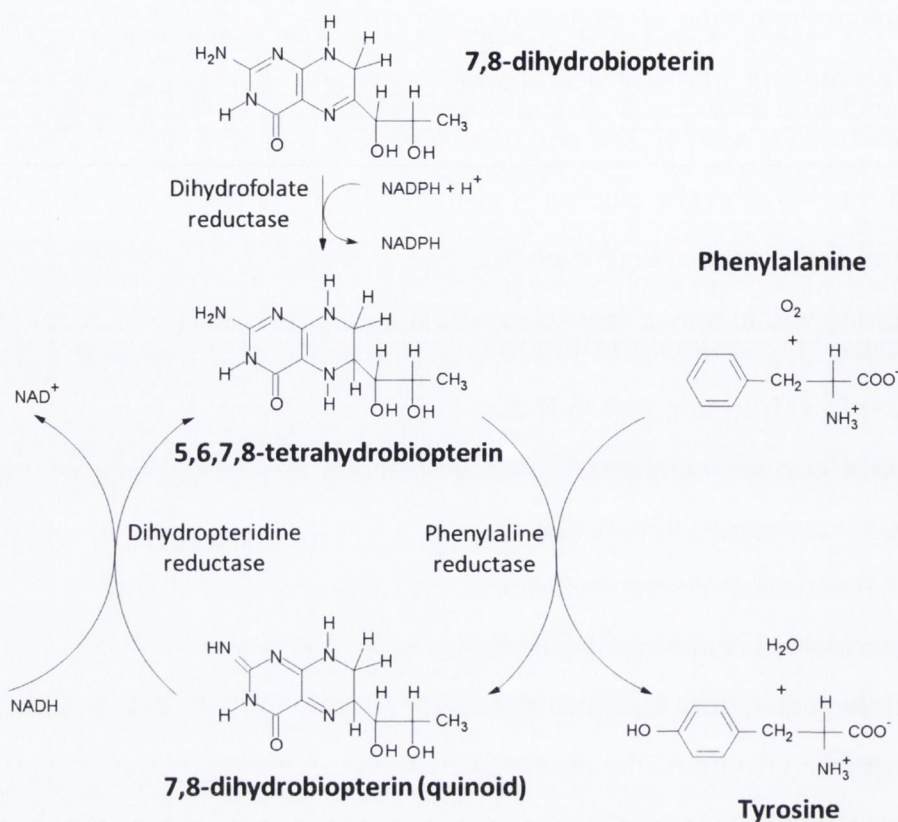
Figure 1.3: The metabolic pathway for converting phenylalanine to tyrosine, with 7,8-dihydrobiopterin playing a role as coenzyme.

techniques coupled with established detection systems. Popular separation methods such as liquid chromatography,[44] high-performance liquid chromatography (HPLC)[45–50] and capillary electrophoresis (HPCE)[43,51,52] have all been used for pterin studies, most frequently employing fluorescence detection, though other techniques such as mass spectrometry have also been used.[53] Although these methods have become very sensitive over the years (Limits of detection of about 1×10^{-10} M) they still offer only a limited amount of information about the structure of the molecules. Nuclear magnetic resonance (NMR) spectroscopy is one method that has been applied to obtain structural information.[54–56] Raman spectroscopy can also be used for structural analysis of pterins,[57] and because of the potential of surface-enhanced Raman spectroscopy (SERS) in the detection of lower concentration levels there have been some studies on this,[58–60] with Feng et. al. obtaining a detection limit for xanthopterin of 5×10^{-9} M.[58]

1.2 Light Interactions with Matter

Photons of a particular energy can be absorbed by a molecule, so long as the energy spacing between the levels within the system allow this, and the molecule will be promoted into an excited state. This concept is shown in Figure 1.4.

$$E_2 \qquad \Delta E = E_2 - E_1 \qquad E_1$$
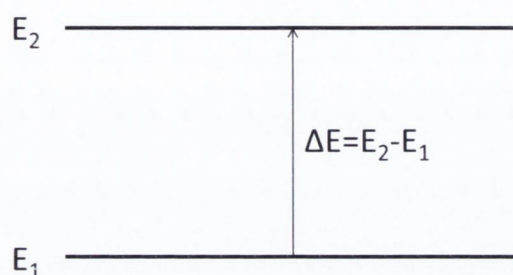
Figure 1.4: The absorption of electromagnetic radiation.

Light interactions with matter can result in many different processes, three of which discussed here will be absorption, fluorescence and scattering.

1.2.1 Optical Absorption

When light is incident on a material, the interaction between it and the molecules within the material can be described though the use of molecular energy distribution diagrams. Changes in the energy levels in a molecule can originate from changes in the electron orbitals as they are promoted to different states, or indeed through the movement of atoms within the molecule, be it molecular rotations or vibrations about the atom positions.

One of the most widespread ways in which the motion of electrons within a molecule is described is by use of Jabłoński diagrams, which were devised by the Polish physicist Aleksander Jabłoński.[61] Figure 1.5 shows a simple representation of one of these diagrams.

In Figure 1.5 the electronic states of the system are described by a series of levels, and in this case the ground state (S_0) and the first excited singlet state (S_1) are shown.

9
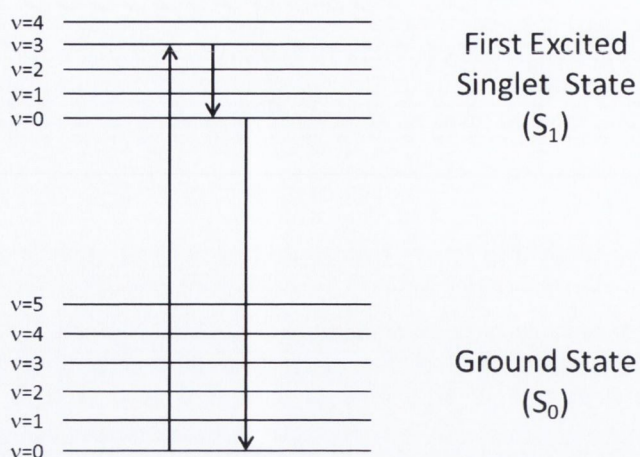
Figure 1.5: Jabloński diagram showing the absorption and subsequent relaxation processes involved when a photon of light promotes an electron from the ground state (S_0) to the first excited singlet state (S_1).

Within these states are shown the vibrational states of the species, which are much closer in energy than the electronic states, and these are described as $v = 0$ for the lowest vibration state within an electronic state through to $v = n$. The upward arrow on the diagram relates to absorption; in this case energy is absorbed to promote an electron in the lowest vibrational state within S_0 into the $v = 4$ vibrational state in S_1. Relaxation processes occur within the S_1 state, followed by relaxation back down to the S_0 state, which is often associated with an optical emission event.

Electrons from a molecule in the ground state occupy the lowest available energy state, with electrons usually paired and occupying different spin states.[62] Once promoted to an excited state, an electron from this pair can be of the same spin, as it is in a different electronic state.

The motional states of a molecule refer to the rotations and vibrations, which can produce small variations in the electronic distributions. The energies involved in transitions between vibrational states are usually much lower than those between the electronic states, while those relating to rotations are usually lower again. The rotational and vibrational states are typically coupled to the electronic states, a state which is termed as a vibronic state.[63]

Transitions between different electronic or vibrational states of a molecule can be either

radiative or non-radiative.[61] Radiative transitions concern the absorption or emission of a photon, facilitating a change in the energy state of the molecule. Radiative transitions between singlet and triplet states are forbidden, but can occur if a spin-relaxation mechanism is present. Non-radiative transitions in a molecule can occur because of external interactions, such as with the solvent or with other molecules, or because of internal interactions such as internal conversion. Thermal interactions can also cause transitions, and non-radiative transitions can also occur between singlet and triplet states. A transitions between a singlet and triplet state is usually referred to as inter-system crossing, which involves a transition between states of different multiplicities, and is usually not very likely, though it is involved in processes such as phosphorescence.

Absorption occurs when a photon of energy E is absorbed by a molecular species, promoting the molecule from the electronic energy level E_1 to the level E_2; in the simplest form this refers to excitation from S_0 to S_1. This occurs due to the energy between the two energy levels corresponding to the absorbed energy of the photon, and is the principle of UV/Vis spectroscopy. Infra-red absorption concerns excitation to a higher vibrational state within the molecule, and occurs due to the absorption of photons of much smaller energy. Infra-red spectroscopy is used to investigate the vibrational structure of molecules.[64]

1.2.2 Fluorescence

Fluorescence has been observed for many centuries, and in fact its presence is mentioned in a medical report by Nicólas Monardes in 1565 of artefacts acquired from expeditions to the West Indies. This observation was concerned with the bluish opalescence of the water infusion of the wood of a small Mexican tree.[65] Translations of Monardes's work into both Latin and English resulted in the phenomenon becoming more widely studied, and the Jesuit priest Athanasius Kircher noted in a publication in 1646 that light passing through an aqueous infusion of the wood appeared yellow, while the light reflected from it appeared blue.[66] The effect was noticed in further materials, such as quinine sulphate in 1845 by John Herschel, the discovery of which was published

in the Philosophical Translations.[67] George Gabriel Stokes investigated this further in 1852,[68] using a prism to disperse the spectrum, and discovered that there was no effect on a solution of quinine until it was placed in the UV region of the spectrum. From this he was able to deduce that the emitted radiation was of a longer wavelength to that of the incident radiation, an effect that is now termed the Stokes shift. Further research led to the discovery and development of a variety of fluorescent materials and dyes, and eventually fluorescence microscopes were developed from UV microscopes by Otto Heimstaedt and Heinrich Lehmann between 1911 and 1913. From then onwards fluorescence spectroscopy grew rapidly, and has been widely used as a research and detection technique in the century since.

Fluorescence occurs in certain molecules through the absorption of a certain wavelength of light and, after a brief period of time, the subsequent re-emission of the absorbed energy at a longer wavelength. This absorption represents a change in the molecule from a ground electronic state to an excited electronic state, an event that typically takes place at very small time values, on the order of 10^{-15} seconds.[69] The absorption is characterised by the energy spacing available between the ground state and excited electronic, vibrational and rotation values. A relaxation process then occurs whereby the molecule reverts to the lowest vibrational energy level of the excited singlet state, denoted as the $v = 0$ value in the S_1 state in Figure 1.6. This relaxation process is known as internal conversion, which is a thermal process characterised by collisions of the excited state molecule with solvent molecules, a process usually occurring on the order of 10^{-11} seconds. The molecule now exists in the lowest vibrational energy level of the excited singlet state (S_1) for a time on the order of nanoseconds before relaxing back to the ground state (S_0). A second process can also occur within the molecule, known as inter-system crossing, also shown in Figure 1.6, whereby the molecule relaxes to a long-lived triplet state (T_1), which is the basis for the phenomenon of phosphorescence.[61]

The quantum yield of a fluorophore is a ratio of the photons emitted as fluorescence to the photons absorbed from the radiation source, and as such is a measure of the emission efficiency. The fluorescence lifetime, usually denoted as τ, is the time the molecule remains in its excited state before returning to the ground state. Excitation
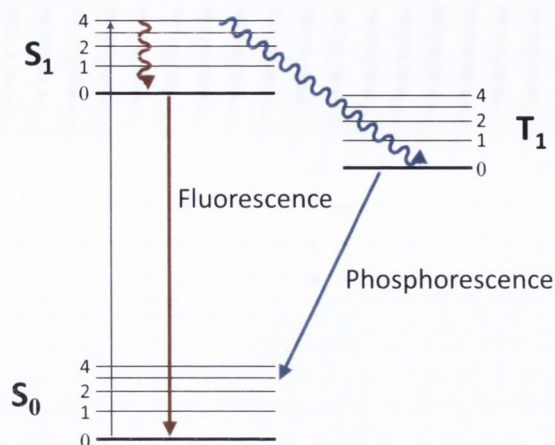
Figure 1.6: Jabłoński diagram showing the absorption, relaxation and emission processes involved in both fluorescence and phosphorescence.

using a brief pulse of light from, for example, a laser light source, will result in a fluorescence decay described by the equation

$$I(t) = I_0 e^{(-\frac{t}{\tau})} \tag{1.1}$$

where $I(t)$ is the intensity after a time t and I_0 is the initial light intensity.[61] Thus the fluorescence lifetime is defined as the time taken for the fluorescence intensity to decay to $1/e$ of the initial intensity.

1.2.3 Scattering Processes

Another important interaction between incident photons and a molecular species is that of scattering, which is a process involving the absorption of one photon and the emission of another one. The type of scattering is described according to the energy of the scattered photon. If the energy of the incident and scattered photon is the same, the process is known as elastic scattering, or as Rayleigh scattering. After such an interaction the energy of the molecule is in the same state as before the interaction with the light, and not much information is provided about the internal structure of the molecule. In the case of the scattered photon possessing a different energy to that of the incident photon, the process is called inelastic scattering, with the energy difference relating to a transition within the molecule. Raman scattering is a form

of inelastic scattering concerning the transitions between vibrational and/or rotational energy levels.[63]

Raman scattering and fluorescence processes are in a way similar, with both involving the emission of a photon of different energy following interaction with the incident photon. The important difference between the two is the timeframe upon which both are based. Fluorescence occurs after a delay of about 10^{-9} seconds following absorption while Raman scattering is a much faster process. Scattering processes are, however, weak when compared with other processes such as fluorescence or absorption.

1.2.4 The Width & Intensity of Spectral Lines

It might be expected that the energy transitions within molecules or atoms would result in very precise, sharp and defined spectral peaks. One reason why this does not occur, and why peaks of a certain width are seen instead, is because of the resolution of the spectrometer grating itself. There will be an inherent range of frequencies, however small this range might be, passed through the sample, which will in turn lend a certain lack of definition to the peaks in the shape of broadening. But despite progress towards instrumentation of higher resolution there is still a natural line width associated with any spectrum, which cannot be avoided through advanced instrumentation. Two factors that in particular contribute to this natural line width are collision broadening and Doppler broadening.[64]

Collision broadening, as the name suggests, is based on collisions that occur between free-moving atoms or molecules in gaseous or liquid media. Collisions result in slight deformations of the molecules, particularly in liquids where there is a greater concentration of molecules, and this manifests itself particularly regarding the outer electrons of molecular species. This particularly affects transitions examined in UV/Vis spectroscopy, as the outer electrons contribute predominantly in this process. Doppler broadening is again evident in both gaseous and liquid samples, due to the Doppler shift of frequencies based on the movement of bodies emitting the radiation. This effect broadens the spectral lines on either side of the peak because of the random motion

of the particles; the frequencies are shifted to both higher and lower frequencies. The Heisenberg uncertainty principle, in this case, states that a system existing in an energy state for a certain time will have an intrinsic uncertainty in its energy.

The intensity of any given spectral line can also be attributed to a combination of factors, in particular the transition probability, the population of states and the concentration of the sample. The transition probability relates to the selection rules that govern the transition in question, and are defined for different spectroscopic techniques. The population of states is described by Boltzmann distribution statistics, and the ratio of the relative populations of the upper and lower energy states can be determined through the formula:

$$\frac{N_{Upper}}{N_{Lower}} = e^{-\frac{\Delta E}{kT}} \tag{1.2}$$

where ΔE is the energy gap between the upper and lower energy levels, T is the temperature in Kelvin and k is the Boltzmann constant.[64]

Regarding the concentration, the Beer-Lambert Law can be implemented, which in terms of the absorbance can be represented as thus:

$$A = \log\left(\frac{I}{I_0}\right) = \epsilon c l \tag{1.3}$$

where ϵ is what is known as the molar absorption coefficient, and is specific to the material in question. c refers to the concentration of the sample and l is the path length, i.e. the distance through which the incident light passes.

1.3 The Raman Effect

Raman spectroscopy was discovered by the Indian physicist C.V. Raman in 1928,[70] for which he won the 1930 Nobel Prize in Physics. The effect is based on the scattering of light, at higher and lower frequencies to that of the incident light. When a monochromatic light beam is passed through a transparent sample, there will be some scattering of the light. The majority of the light undergoes elastic scattering, i.e. it is scattered at

the same frequency as the incident radiation, in a process known as Rayleigh scattering. But some of the light will also undergo inelastic scattering, both of higher and lower energies. The signal received due to lower energy scattering is referred to as having undergone a Stokes shift, while that of higher energy is said to have undergone an anti-Stokes shift. It is these shifts that are considered in Raman spectroscopy.

Both Stokes and anti-Stokes shifted spectral lines are very weak, and the intensity of the lines is dependent on the sample temperature and thus the relative populations of the vibrational energy levels. At room temperature Stokes shifted signals are the more strongly observed, and so are usually the ones studied in conventional Raman spectroscopy. Laser light is now implemented in obtaining Raman signals, as it is both highly monochromatic and extremely powerful, so as to obtain resolved and strong material spectra. One issue with using the laser source for Raman measurements is that the heat caused by intense beam absorption can cause decomposition of the sample,[71] especially if the sample has an absorption peak at the same frequency as the incident laser. One method for dealing with this problem is by changing the incident wavelength. Fluorescence can also be an issue, as it is a much stronger signal and as such can completely swamp a Raman sample measurement.[72] One way to combat this is to use time-resolved detectors that can differentiate between the Raman signals and the significantly slower fluorescence lifetimes.[73]

The Raman effect can be described both classically and by the use of quantum theory. Following will be a brief account of both.

1.3.1 Classical Interpretation of the Raman Effect

The classical interpretation of Raman scattering concerns the molecular polarisability of a molecule. In an electric field the electrons and nuclei experience a force and as such respond, causing a certain distortion of the molecular species. This causes what is known as an induced dipole moment and the molecule becomes polarised. This induced dipole moment is termed μ and can be related to the magnitude of the applied electric field, E, and to what is known as the polarisability of the molecule, α, which is the ease

with which a molecule can become polarised.[64]

$$\mu = \alpha E \tag{1.4}$$

The induced dipole moment varies with molecular orientation in a static electric field; for a H_2 molecule the value is found to be about twice as large for a field applied along the bond axis compared to one applied perpendicular to the axis.[64]

One of the ways of representing this relationship is by using a polarisation ellipsoid, which is essentially a surface surrounding the molecule. The distance from the electrical centre of the molecule to this surface is proportional to $1/\sqrt{a_i}$, with a_i being the polarisability joining the electrical centre to a point i on the surface. Because this is an inverse relationship, the points at which the polarisability is greatest will correspond to points on the surface that are closest to the electrical centre.[64] A schematic is shown in Figure 1.7, which represents a cross-section taken of this ellipsoid in the case of the H_2 example.
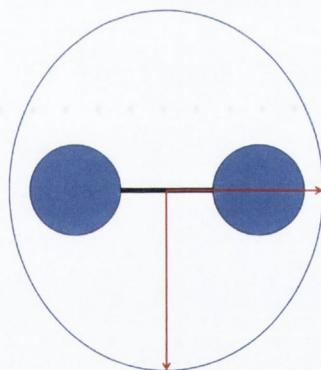
Figure 1.7: Schematic showing the cross-section of a polarisability ellipsoid for H_2. The red arrows show the distance from the electrical centre of the molecule to points on the ellipsoid, with the greatest polarisability to be found along the bond axis.

The electric field experienced by a molecule when a sample is irradiated by a beam of radiation is described by the formula:

$$E = E_0 \sin 2\pi \upsilon t \tag{1.5}$$

and coupling this with Equation 1.4 gives us:

$$\mu = \alpha E = \alpha E_0 \sin 2\pi \upsilon t \tag{1.6}$$

which means that the induced dipole also undergoes oscillations of frequency υ. This oscillating dipole emits radiation, which is of course that which is associated with Rayleigh scattering. If vibration or rotation of the molecule occurs, altering the polarisability periodically, then there will also be an oscillation according to the motion in question. This can be represented by an equation in the form

$$\alpha = \alpha_0 + \beta \sin 2\pi \upsilon_{vib} t \tag{1.7}$$

where α_0 is the polarisability at equilibrium and β is the rate of change of the polarisability and υ_{vib} is the vibrational frequency. Substituting this into Equation 1.6 leaves us with:

$$\mu = \alpha E = (\alpha_0 + \beta \sin 2\pi \upsilon_{vib} t) E_0 \sin 2\pi \upsilon t \tag{1.8}$$

and multiplying this out gives us

$$\mu = \alpha E = \alpha_0 E_0 \sin 2\pi \upsilon t + \beta E_0 \sin 2\pi \upsilon_{vib} t \sin 2\pi \upsilon t \tag{1.9}$$

which can be modified using the trigonometric relation:

$$\sin A \sin B = \frac{1}{2}\{\cos (A - B) - cos(A + B)\} \tag{1.10}$$

to give:

$$\mu = \alpha_0 E_0 \sin 2\pi \upsilon t + \frac{1}{2}\beta E_0\{\cos 2\pi(\upsilon - \upsilon_{vib})t - \cos 2\pi(\upsilon + \upsilon_{vib})t\} \tag{1.11}$$

From all this it can be seen that the dipole has oscillations of $\upsilon \pm \upsilon_{vib}$ in addition to that of the incident frequency.[64] From this the general selection rule for Raman scattering can also be established; for a molecular vibration or rotation to be Raman active, there must be an associated change in the molecular polarisability. This is a useful requirement, as it differs from that of infra-red spectroscopy, which also studies vibrational bands but has the requirement that the motion alters the molecule's electric dipole. For this reason Raman spectroscopy can be a complementary technique to infra-red spectroscopy, as the two techniques can provide different information on a molecule's vibrational structure.[64,74]

1.3.2 Quantum Interpretation

Considering an incident photon of energy $h\upsilon$ on a molecule, the majority of the scattered radiation will be Rayleigh scattered, and the radiation reaching the detector will be of the same energy as the incident light. Instances where the scattered light is not of the same frequency as the incident light, where the light is inelastically scattered, can either occur where the scattered light will be of more or of less energy than the incident light. In the case where the scattered light has less energy, then this will correspond to $h\upsilon - \Delta E$ and the scattered radiation will have a frequency equal to $\upsilon - \Delta E/h$. This incidence, where the frequency of the scattered light is less than that of the incident light, is known as Stokes shifted radiation. The converse case, where the energy of the light is $h\upsilon + \Delta E$, is known as anti-Stokes radiation, although it is generally observed at much lower intensities than Stokes radiation. Both are very small though regardless, with Stokes scattered radiation usually accounting for only 1 in 10^6 photons of incident light. The process is described in Figure 1.8, which also shows the presence of what are known as "virtual states".[63]
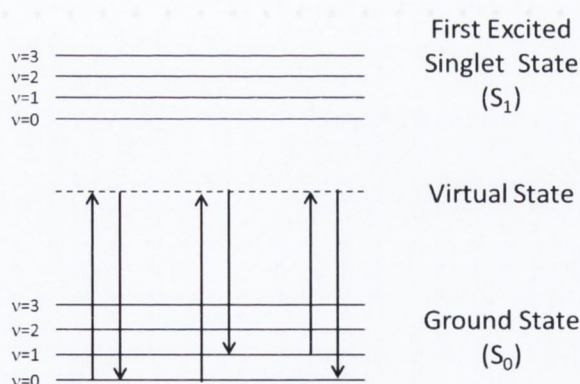

Figure 1.8: Raleigh, Stokes and anti-Stokes scattering processes.

In this representation, virtual states are used to describe each of the three scattering events. While there is no physical meaning to this virtual state concept, it stems from a quantum mechanical understanding of Raman scattering, and helps to visualise scattering occurring at any incident laser wavelength.[63]

1.4 Plasmons

Plasmons are involved in the surface-enhancing properties of metals on Raman signals, and they are generally described as quantised waves, arising from the collective excitation of conduction electrons in metallic materials.[75] Many metals can be treated as free electron systems, which means that it is the conduction electrons within the material that define the overall electronic and optical properties of the material. Because the free electron model contains an equal number of electrons and fixed positive ions, the material can be related to as a plasma, and under an external electric field these electrons can oscillate coherently at a specific frequency.

1.4.1 Plasmons and the Free Electron Model

Plasmons that occur within an infinite bulk material will have the frequency of oscillation described by the formula

$$\omega_p = \sqrt{\frac{Ne^2}{\epsilon_0 m_e}} \tag{1.12}$$

where N is the number density of mobile electrons, ϵ_0 is the dielectric constant of a vacuum, e is the electron charge and m_e is the electron mass.[75] The electrons oscillate according to the applied electromagnetic field, although they do experience collisions, which are described by the damping constant, or the collision frequency γ. This frequency is also represented in an inverse form, $\gamma = 1/\tau$ where τ is the relaxation time of the free electron gas, which is typically about 10^{-14} s at room temperature.[76] The plasmon frequency and the damping constant are both involved in the definition of the dielectric function of the free electron gas:

$$\epsilon(\omega) = 1 - \frac{\omega_p^2}{\omega^2 + i\gamma\omega} \tag{1.13}$$

The real and imaginary parts of this equation, whereby $\epsilon(\omega) = \epsilon_1(\omega) + i\epsilon_2(\omega)$, are given by[76]

$$\epsilon_1(\omega) = 1 - \frac{\omega_p^2 \tau^2}{1 + \omega^2 \tau^2} \tag{1.14}$$

$$\epsilon_2(\omega) = \frac{\omega_p^2 \tau}{\omega(1 + \omega^2 \tau^2)} \tag{1.15}$$

The region where $\omega < \omega_p$, is an important region for plasmonics. For frequencies close to ω_p there is negligible damping, and $\epsilon(\omega)$ is predominantly real. The low frequency regime sees greater influence from the imaginary part of the function, in which region metals are mainly absorbing. The region of $\omega > \omega_p$ sees a greater background contribution from the positive ion cores, and because of this a further dielectric constant ϵ_∞ is brought into the equation.[63]

$$\epsilon(\omega) = \epsilon_\infty \left(1 - \frac{\omega_p^2}{\omega^2 + i\gamma_0\omega}\right) \tag{1.16}$$

The dielectric function of this model, the Drude model, describes the optical response of metals only for energies below the threshold before interband transitions occur. For noble metals this can begin to occur from energies of about 1 eV,[76] which corresponds to a wavelength of about 1200 nm, so the transitions occur by the time the energy approaches the visible region of the spectrum. Plots of the real and imaginary data for gold and silver have previously been plotted against fits of the Drude model, showing the breakdown of this model in the visible region.[76] At frequencies above this threshold, due to the presence of the interband transitions, there is an increased damping of the surface plasmon excitation, resulting in increased competition at visible frequencies.[76] Because of this a further term can be added to Equation 1.16 to account for the inter-band transitions.

$$\epsilon(\omega) = \epsilon_b - \epsilon_\infty \frac{\omega_p^2}{\omega^2 + i\gamma\omega} \tag{1.17}$$

From studies into the plasmonic properties of various metals, gold and copper are found to behave favourably at wavelengths greater than about 600 nm. Below this silver is the most prominent material, and indeed it and gold are the most widespread of the plasmonic materials.[63]

An infinite bulk material is of course an ideal concept. Electromagnetic waves, incident on the surface of a metal, will only penetrate a certain depth into the material. This is related to the wavelength and is less than 50 nm for noble metals such as gold or

silver in the visible region.[75] This means that the electric field required for the coherent excitation of the conduction electrons is limited to electrons within this region. The concept of infinite dimensions cannot be applied here, as the surface of the metal and the surrounding materials of varying dielectric constants must also be considered. For a metal-vacuum interface the plasmon frequency will be lower than in a bulk material,[75] and is described as $\omega_p/\sqrt{2}$. These collective oscillations at a metal surface are known as surface plasmon polaritons (SPPs). On a surface these can be represented as periodic alternations of surface charge density, propagating along the surface in the form of a longitudinal wave. This concept is shown in Figure 1.9.

In very small particles or spherical colloids the surface plasmons are confined further, to a finite volume. The oscillations within the particles mean that the charge density will result in a separation of charge across the particle, but as there is nowhere for the wave to travel the plasmon is confined to the particle. These types of surface plasmons are known as localised surface plasmons (LSPs) and are generated when the conduction electrons oscillate coherently with an incident electromagnetic wave. In a vacuum the resonant frequency will become $\omega_p/\sqrt{3}$ as the plasmons are confined in three dimensions.
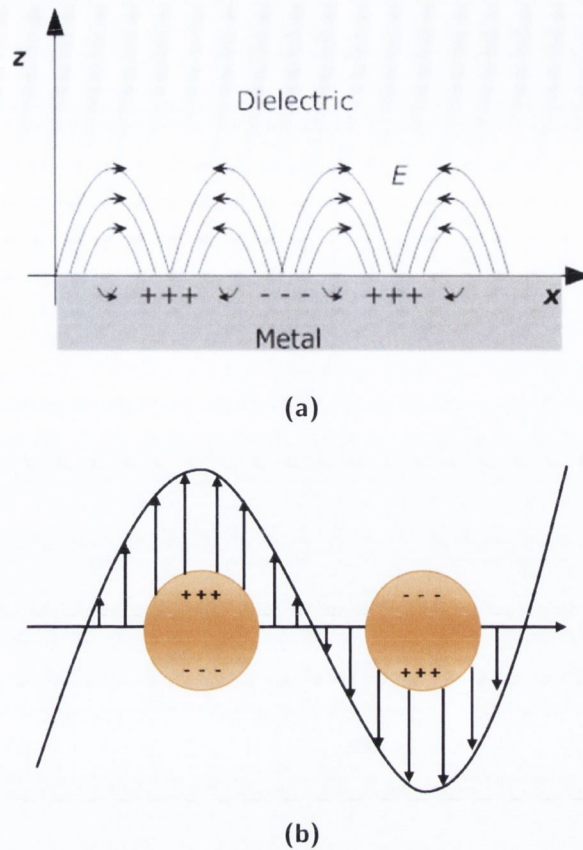
(a)

(b)

Figure 1.9: (a) Schematic showing the collective oscillations of free electrons leading to the propagation of longitudinal surface charge density waves. (b) Schematic of the oscillations in a spherical gold particle. Because of the confinement there are only dipole plasmon resonance effects.

The shape of the particle is also of some importance. Gustav Mie developed an expression to describe the extinction coefficient $E(\lambda)$ of spherical particles in the long-wavelength limit.[77]

$$E(\lambda) = \frac{24\pi N_A a^3 \epsilon_m^{3/2}}{\ln(10)} \left(\frac{\epsilon_i}{(\epsilon_r + 2\epsilon_m)^2 + \epsilon_i^2} \right) \tag{1.18}$$

In this formula, N_A is the areal density of the nanoparticles, a is the particle radius, ϵ_m is the dielectric constant of the surrounding medium and ϵ_r and ϵ_i are the real and imaginary parts of the metal dielectric function. When $\epsilon_r = -2\epsilon_m$ a resonant peak is observed, and for gold and silver this appears in the visible part of the spectrum. The $\epsilon_r + 2\epsilon_m$ term in Equation 1.18 describes a spherical particle, but for other shapes this is replaced by $\epsilon_r + \chi\epsilon_m$, where χ is what is known as the shape factor. Thus there is clearly quite a strong dependence on the particle shape, and the resonant peak can be tuned according to this relationship.

1.5   Surface-enhanced Raman Scattering (SERS)

Surface-Enhanced Raman Spectroscopy (SERS) is a technique that was initially developed in the late 1970's. It was discovered through observations of an enhanced Raman scattering from pyridine adsorbed to electrochemically-roughened silver surfaces. Two independent research groups discovered this phenomenon separately,[78,79] but the technique initially failed to build on early promise, in a large part due to the difficulty of being able to reproducibly replicate substrate surfaces.

In recent times there has been a renewal of interest in the area due to nanofabrication techniques now being able to combat this issue, producing more reproducible substrate features capable of achieving signal enhancement. The use of the word "features" is important when applied to the substrate fabrication, as the shapes and dimensions of these features play a critical part in reproducibly obtaining high enhancement fields. The discovery of single molecule SERS (SMSERS) in 1997 was a major breakthrough for the technique,[80,81] and since then SERS has been applied to a number of analytical and theoretical studies,[82,83] and the increased exposure has led to the development of more sophisticated instrumentation.

A thorough understanding of the principals behind SERS has been challenging. The initial enhancement factor (EF) of 10^6-fold was seen as originating from two factors an electromagnetic enhancement and a chemical enhancement. This happens because the intensity of the Raman scattering is directly proportional to the square of the induced dipole moment, which is itself the product of the Raman polarisability and the magnitude of the incident electric field.[64] The SERS concept is shown in Figure 1.10.
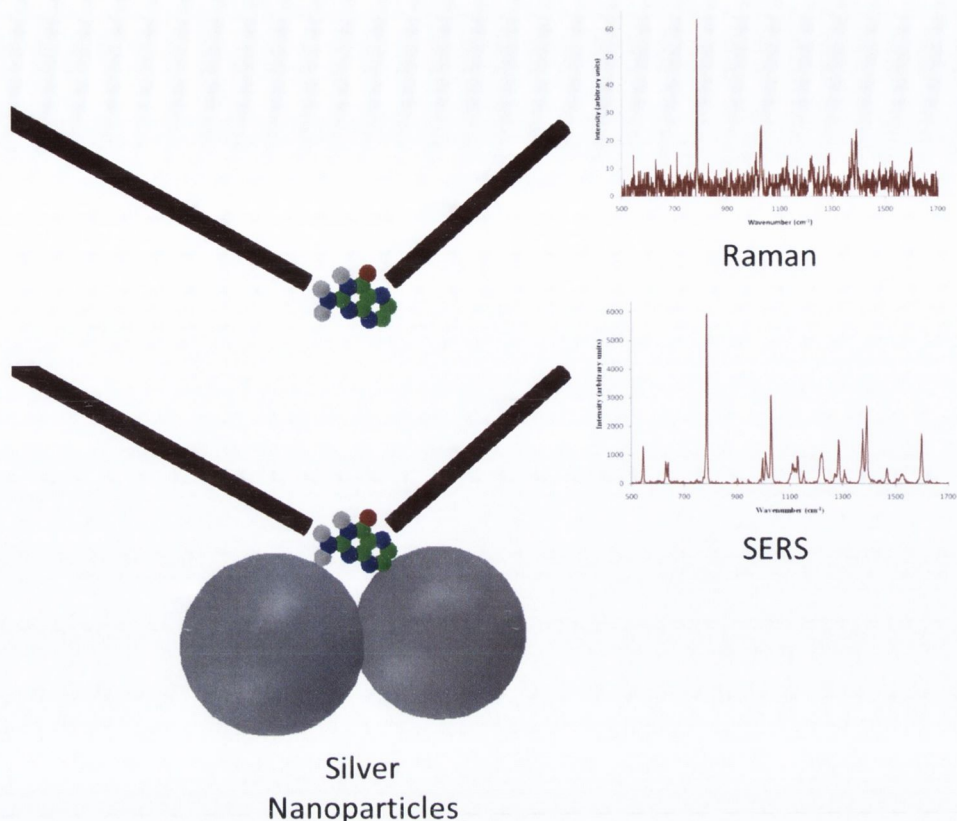
Figure 1.10: Representation of surface-enhanced Raman scattering, showing enhancement of the Raman signal due to adsorption of a compound to silver colloids.

1.5.1 Plasmons & SERS Enhancements

The Raman cross-section from a given vibrational mode can usually be translated to a SERS cross-section through an enhancement factor.[63] SERS enhancements are generally believed to stem from two sources; an electromagnetic enhancement or a chemical enhancement. The electromagnetic enhancement is thought to contribute the most towards the SERS effect; it is essentially the coupling of the incident field and the Raman scattering field with the SERS substrate.[63] The Raman field enhancement is dependent on the excitation of localised surface plasmons on the SERS substrate. The chemical enhancement is still poorly understood, though it is believed to originate from some kind of alteration to the polarisation of the molecule when it becomes adsorbed onto the SERS substrate,[84] after which resonant effects can come into being, even at non-resonance wavelengths.

1.5.2 Surface Enhanced Resonance Raman Spectroscopy (SERRS)

The Raman scattering intensity observed can vary by many orders of magnitude depending on the probe used and on the incident laser wavelength.[63] Regular Raman scattering is found to be higher for molecules that have an electronic energy close to that of the incident laser, for example dyes. This effect is termed resonance Raman scattering and can be up to about 10^6 times greater than that for off-resonance molecules. This resonance effect also translates to SERS; if the incident laser is in resonance with the electronic transition of a molecule that is close to an enhancing substrate then the cross-section of the molecule can become much more enhanced, which leads to the observation of surface-enhanced resonance Raman spectroscopy (SERRS).[85] Any fluorescence due to excitation of the SERS probe is quenched by the enhancing substrate.

SERS enhancements on the order of 10^6 are regularly described but the multiplicative resonance effects from SERRS can result in 10^4 to 10^8 enhancements.[86,87] The added sensitivity offered by SERRS has led to the possibility of single-molecule detection,[80,88] though this sensitivity is dependent on the excitation wavelength.[89] SERRS has also recently been used for the immunochemical localization of ovalbumin in paintings,[90] for the investigation of metmyoglobin[91] and for the investigation of enzyme-like properties of silver nanoparticles towards the detection of hydrogen peroxide.[92] The processes of Raman, SERS and SERRS are shown in Figure 1.11.
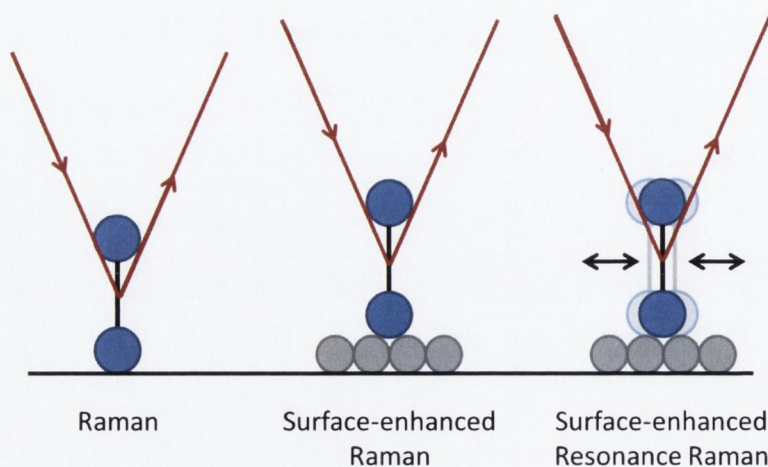

Raman

Surface-enhanced
Raman

Surface-enhanced
Resonance Raman

Figure 1.11: Comparison of Raman, SERS and SERRS.

2

Optical Properties of Pterins

The response of pterins to light has been investigated for several decades,[93,94] and their presence has been well documented in many photobiological roles in the animal kingdom. Many pterin species have also been found to be fluorescent, with these properties found to vary with pH.[95] In this chapter the optical response of pterins has been examined using UV/Vis spectrometry and fluorescence spectroscopy.

2.1 UV/Vis & Fluorescence Spectra

Four pterin species were examined using a Shimadzu UV-2401PC UV/Vis spectrometer; xanthopterin, isoxathopterin, biopterin and 7,8-dihydobiopterin. The spectrometer was operated at a fast scan rate using a 1 nm slit width, using disposable PMMA cuvettes (manufactured by Plastibrand®) with a 1 cm path-length and 18 Ω Millipore water was used as the solvent throughout. Xanthopterin and isoxanthopterin were obtained from Sigma-Aldrich at 97% purity and biopterin and 7,8-dihydrobiopterin were obtained from the School of Biochemistry, originally sourced from Shircks Laboratories at 98% purity. These purities were not verified prior to use. The structures of each species are shown in Figure 2.1. The solubility of xanthopterin was tested, with a sonicated 1×10^{-3} M solution vacuum filtered through a Buchner Flask and the remaining solute weighed. This was repeated four times and the results found the solubility limit to be 7.6×10^{-4} M, which is in the region of stock solutions that were prepared during the thesis. This

insolubility means that there will be an error associated with the absolute concentrations quoted in the thesis, meaning that measurements are purely comparative.
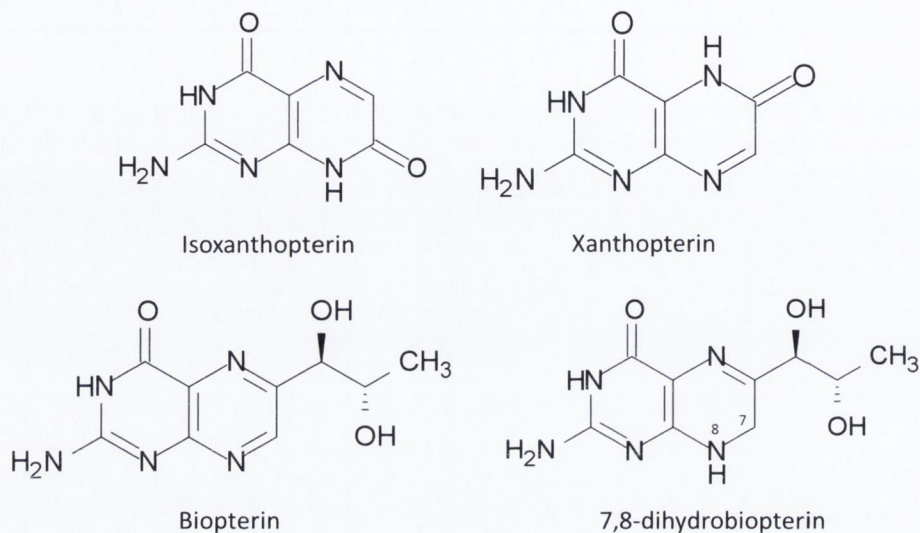

Figure 2.1: The chemical structures of isoxanthopterin, xanthopterin, biopterin and 7,8-dihydrobiopterin. The 7 and 8 labels on the final species show the position of the extra two H atoms, that differentiate it from biopterin.

The absorption spectra of pterins usually consist of two main absorption bands between 230-500 nm.[21,96] These two absorption bands relate to transitions between singlet states of the pterins. The high energy band, at 290 nm, corresponds to a transition from the singlet ground state to the second excited singlet state ($S_0 \rightarrow S_2$), while the lower energy band relates to a transition to the first excited singlet state ($S_0 \rightarrow S_1$).[21] Moving to higher concentrations can affect the absorption profiles of many materials, due to re-absorption effects.[97] Other factors such as the type of solvent used, the pH of the solutions and the temperature can also affect the absorption profiles.

Biopterin and 7,8-dihydrobiopterin are very similar compounds, and the latter is known to be involved in the metabolism of amino acids.[98] Both of these species, and other derivatives, are also known to accumulate in sufferers of the chronic depigmentation disorder vitiligo.[99] Fluorescence spectra were measured on a Varian Cary Elipse fluorescence spectrometer using 5 nm excitation and emission slit widths and a 10 nm/s scan rate. 1 mL cuvettes with a 1 cm path length were used for measurement and water was employed as the solvent for each investigation. For some measurements the integrated

fluorescence is used for data analysis; this refers to the area under the curve in each incidence. Fluorescence excitation spectra taken at an emission wavelength of 450 nm, and the respective UV/Vis spectra are shown in Figure 2.2.
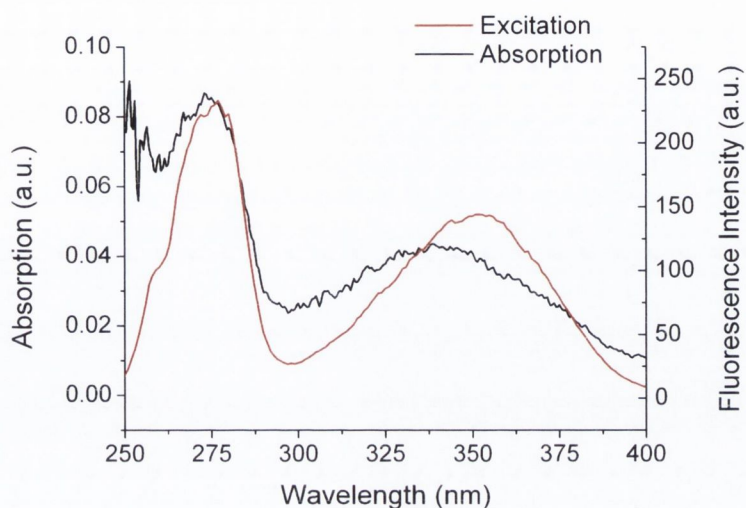
(a)
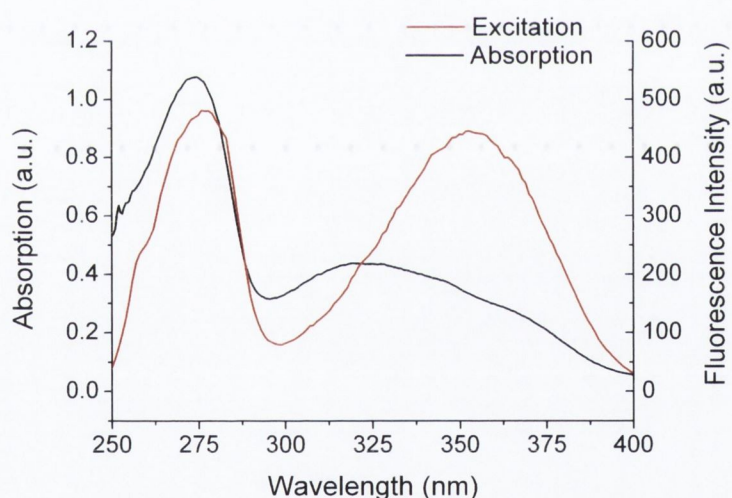
(b)

Figure 2.2: The absorption and excitation spectra of 5×10^{-6} M aqueous solutions of (a) biopterin and (b) 7,8-dihydrobiopterin. The absorption spectra were taken using 1 nm slit widths and a scan rate of 10 nm/s and the excitation spectra using 5 nm excitation and emission slit widths and a 10 nm/s scan rate. Both excitation spectra were measured at an emission wavelength of 450 nm.

The two compounds show similar high-energy absorption bands, with a peak located at about 275 nm, though the lower energy peak differs slightly, with that of biopterin

slight red-shifted from that of 7,8-dihyrdobiopterin, which is consistent with literature observations.[14] The high energy band in both cases displays a greater absorption compared to the lower energy band, while in the excitation spectra the lower energy bands become more prominent. Because the emission spectra remain unchanged regardless of the excitation wavelength, this suggests that only the S_1 band is emissive.[21] A similar investigation was carried out with isoxanthopterin and xanhopterin, shown in Figure 2.3.
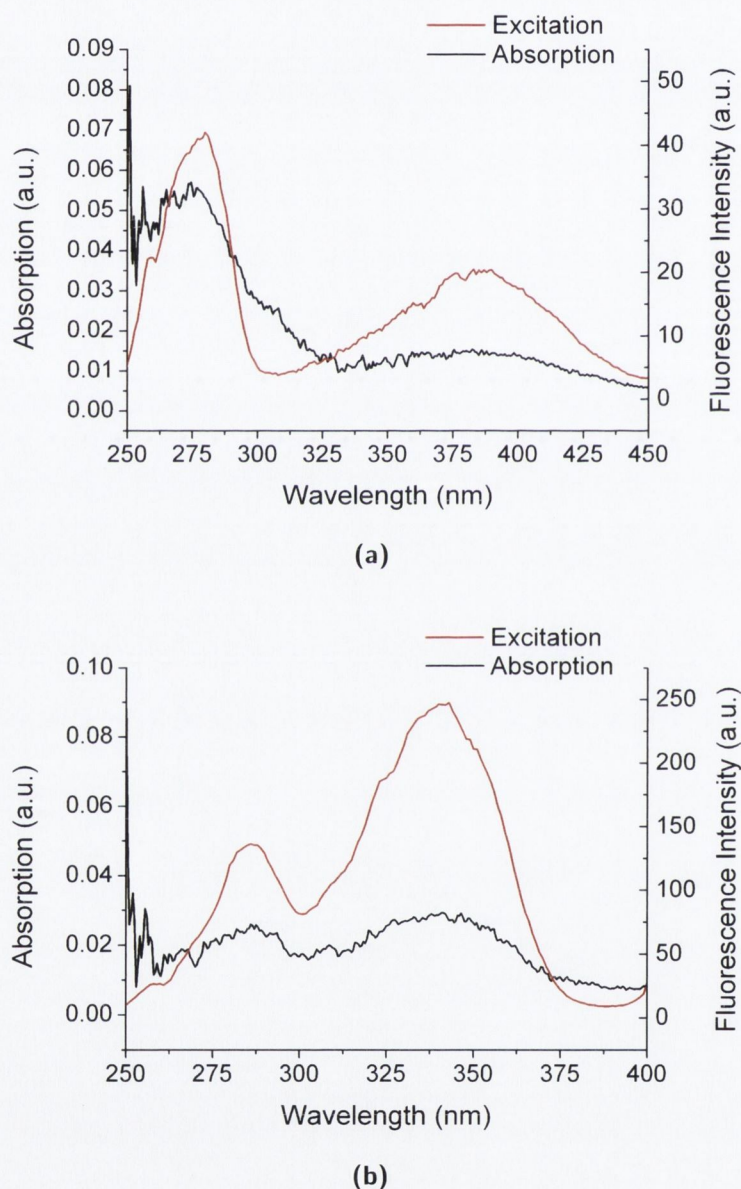

(a)

(b)

Figure 2.3: The absorption and excitation spectra of 1×10^{-5} M aqueous solutions of (a) xanthopterin and (b) isoxanthopterin. The absorption spectra were taken using 1 nm slit widths and a scan rate of 10 nm/s and the excitation spectra using 5 nm excitation and emission slit widths and a 10 nm/s scan rate. The excitation spectrum of the former species was measured at an emission wavelength of 490 nm and the latter was measured at 410 nm.

The absorption spectra in both cases were quite weak, though xanthopterin was observed to show a greater absorption regarding its higher-energy band, the opposite of which was true for isoxanthopterin. The excitation spectra, taken at a 490 nm emission wavelength for xanthopterin and a 410 nm wavelength for isoxanthopterin, showed a better response, with the lower-energy band becoming more prominent in both cases.

The emission spectra of each of the four pterin species were also measured, and are shown in Figure 2.4. Fluorescence quantum yield calculations by Thomas et. al. suggested that only a fraction of the energy excited to higher-energy excited states (S_2 etc.) is translated to the lowest excited singlet state.[95]
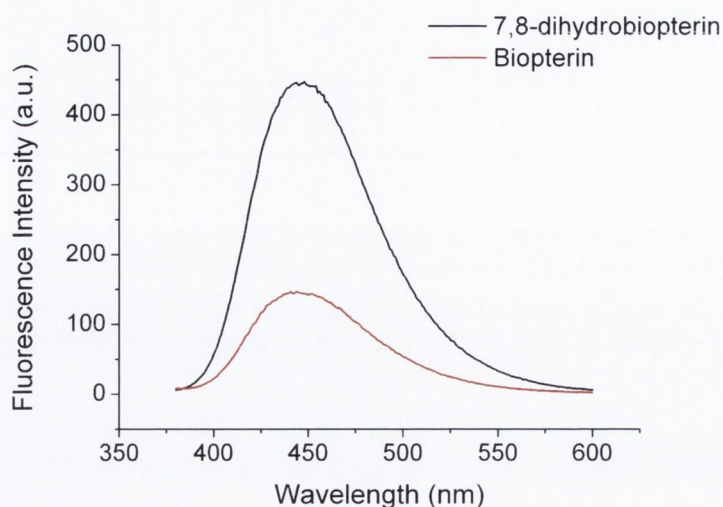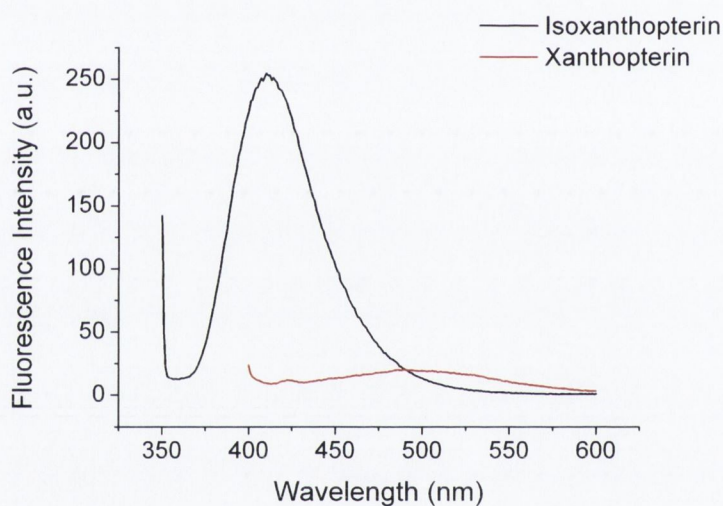
Figure 2.4: The emission spectra of aqueous solutions of (a) 1×10^{-4} M biopterin and 1×10^{-4} M 7,8-dhydrobiopterin ($\lambda_{max} = 450nm$) and (b) 1×10^{-5} M isoxanthopterin $\lambda_{max} = 410nm$ and 1×10^{-5} M xanthopterin $\lambda_{max} = 490nm$. The spectra were taken using 5 nm excitation and emission slit widths and a 10 nm/s scan rate. The excitation wavelength in (a) was set to 352 nm for both species and in (b) it was set to 342 nm and 390 nm for isoxanthopterin and xanthopterin respectively.

The emission spectra for the two biopterin species shows the position of the fluorescence band to be at 450 nm for each, although the 7,8-dihydrobiopterin shows a greater fluorescence intensity despite a similar concentration being used. The two species are very structurally similar, differing only in the presence of extra hydrogen atoms at posi-

tion 7 and 8 on the pyrimidine group, as shown in Figure 2.1. The similar fluorescence peak value would make the species difficult to resolve through conventional fluorescence spectroscopy. The emission spectra for isoxanthopterin, in Figure 2.4(b), shows a much stronger fluorescence to xanthopterin, again despite similar concentrations being used.

2.2 The Inner Filter Effect

The intensity of fluorescence can be dependent on the optical density or turbidity of the sample, which can lead to an inner-filtering effect.[97,100] This effect, which can decrease the observed fluorescence through re-absorption processes, means that fluorescence intensities are only proportional to concentration over a limited range. The effect can be reduced by using shorter path lengths or can be corrected for by using the equation:

$$F_{Corr} = F_{Obs} 10^{\left(\frac{OD_{ex} + OD_{em}}{2}\right)} \qquad (2.1)$$

where OD_{ex} and OD_{em} are the optical densities at the excitation and emission wavelengths respectively. High optical densities can also display other distortions to emission spectra, such as in a shift in the emission spectrum of Rhodamine 6G to longer wavelengths at higher concentrations.[101] This occurs due to a re-absorption of the shorter wavelength region of the emission profile. Another problem with using samples that are too concentrated is that all of the light can be absorbed at the surface facing the incident light.

Xanthopterin solutions were prepared in the concentration range from 1×10^{-4} M to 2×10^{-5} M, and the fluorescence response was measured over this range. Shown in Figure 2.5(a) and (b) are the emission spectra for the xanthopterin before and after inner-filter correction respectively. Figure 2.5(c) shows the spectra integrated from 260 nm to 400 nm and plotted against concentration.
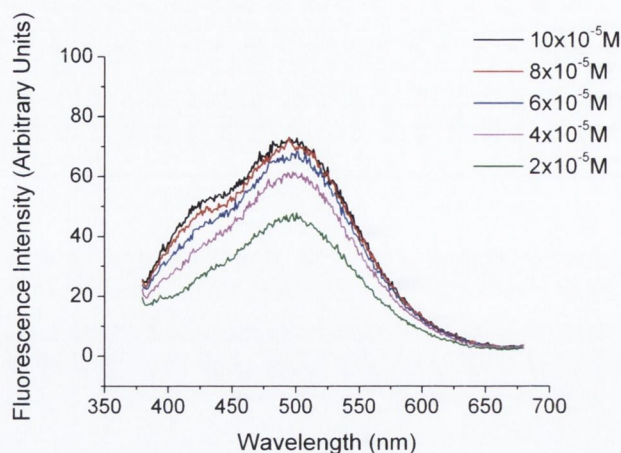
(a)
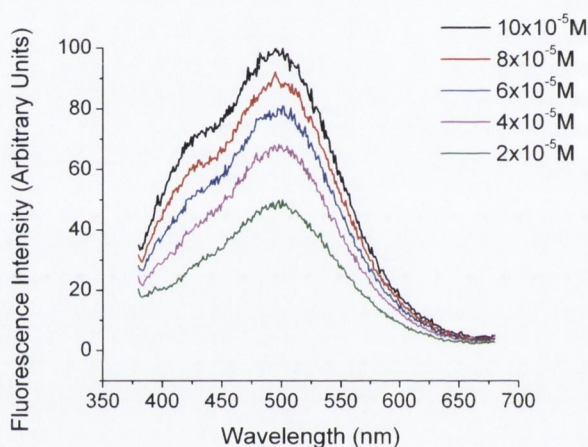
(b)
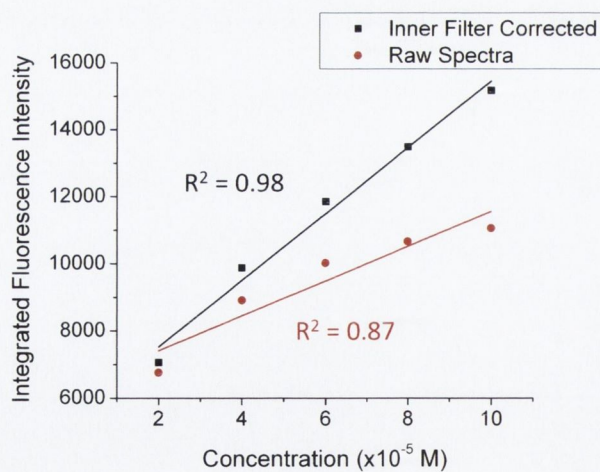
(c)

Figure 2.5: The excitation spectra of xanthopterin in aqueous solution from 1×10^{-4} M to 2×10^{-5} M (a) before and (b) after inner-filter correction according to Eq. 2.1. The spectra were taken using 5 nm excitation and emission slit widths and a 10 nm/s scan rate, with the emission wavelength set at 410 nm. (c) shows the spectra integrated between 260 and 400 nm plotted against concentration.

Evident from these spectra is that the response loses linearity at higher concentrations, due to re-absorption effects. Applying the correction for inner-filter effects yields a better response.

2.3 pH

The pH of the solvent can have a large effect on the properties of pterins; the acidic and basic forms are different molecules, meaning that the electronic energy levels will be different in energy, symmetry and/or conformation and this can result in different absorption and fluorescence spectra. In general, pterins behave as weak acids in aqueous solutions and in solutions of pH greater than 5 possess an equilibrium involving an acid form (or amide form) and a basic form (or phenolate form).[21,95] This acid-base equilibrium is shown in Figure 2.6.
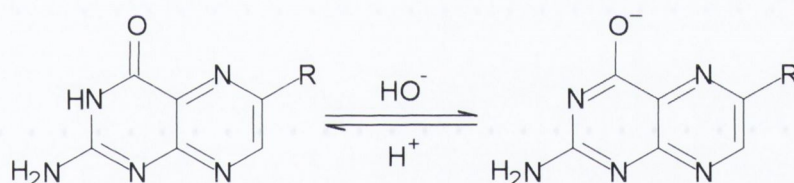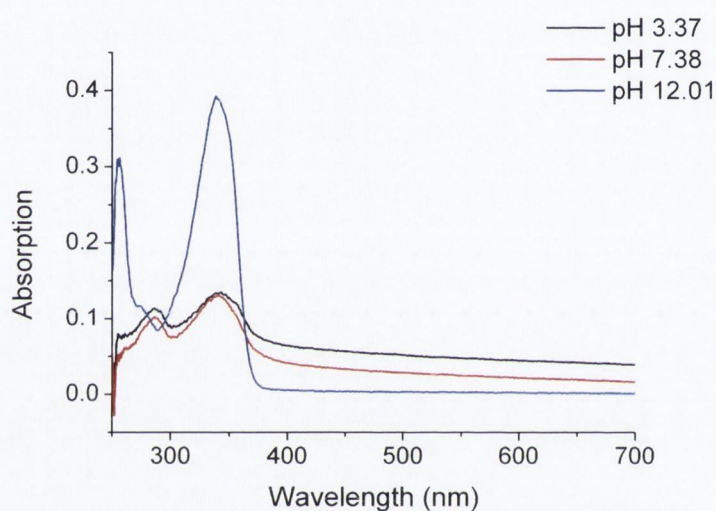

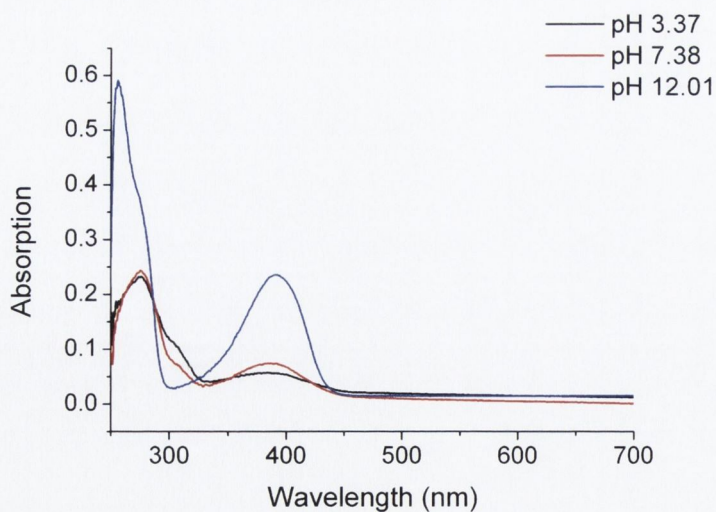**Figure 2.6:** The acidic and basic forms of pterins.

For many pterin species this equilibrium exists in the pH range from 4-12.[102] The acid dissociation constant (pK_a), which is a measure of the strength of an acid, has been measured at about 8 for many pterins, though some functional groups that are attached to certain types have stronger values of about 2. Differences in the photophysical behaviour of pterins due to the pH environment is an important consideration concerning fluorometric analyses,[103–105] and understanding these variations could aid in understanding their roles in biological systems.

2.3.1 UV/Vis Spectra

The absorption spectra of pterins are known to be highly sensitive to pH.[104,106,107] Solutions of 2.54×10^{-4}M isoxanthopterin and xanthopterin at pH 3 and 12 were prepared, with the pH varied using an Orion 420a pH meter and dilute HCl and NaOH to prepare the acidic and basic solutions respectively.[95] The meter was calibrated using pH 4 and pH 7 standard solutions. Neutral solutions of about pH 7 were also prepared using Millipore water. The UV/Vis spectra are shown of these solutions in Figure 2.7.
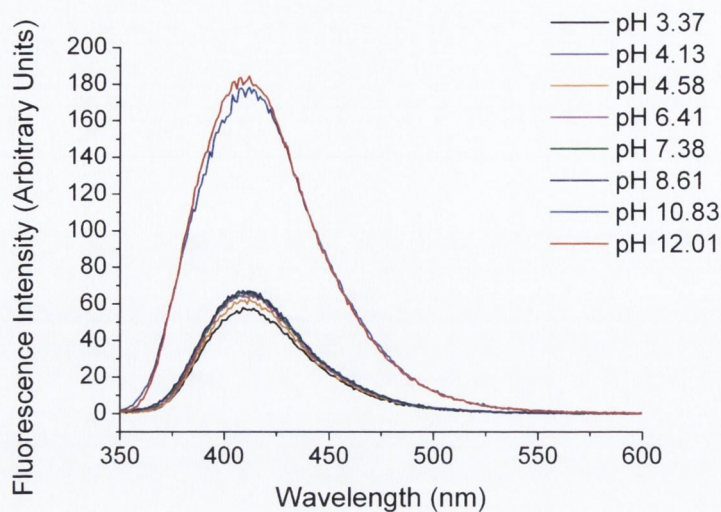

(a)

(b)

Figure 2.7: The UV/Vis spectra of acidic, neutral and basic pH solutions of 2.54×10^{-5}M of (a) isoxanthopterin and (b) xanthopterin.

The basic forms of each compound in Figure 2.7 show a quite dramatic increase in absorption, which corresponds to the phenolate form from Figure 2.6. The acidic form does not appear to show much change in the absorption properties from the neutral pH measurement, suggesting that the equilibrium at this pH favours that of the acidic form. This would be consistent with pH studies carried out on other pterin species, where pterins were found to behave as weak acids in aqueous solution.[95] The large increase in the absorption value between the acid form and the basic form is not, however, something that appears to be noted in relation to other pterin species.

The high energy band in both basic forms is blue-shifted from the acidic and neutral forms, which is consistent with investigations by Lorente on other species.[21] For the higher energy bands Lorente found the basic form to be red-shifted from that of the basic form, while in our measurements we found little variation in this peak position across all pH values investigated.

2.3.2 Fluorescence Spectra

The fluorescence properties of isoxanthopterin and xanthopterin in different pH solutions were also analysed, using a greater range of pH values. A similar trend was observed as with that of the UV/Vis measurements, with the basic pH values producing the fluorescence. This relationship can be seen in the emission spectra for each of isoxanthopterin and xanthopterin (measured at excitation wavelengths of 342 nm and 390 nm respectively) at a concentration of 2.54×10^{-5} M, shown in Figure 2.8.
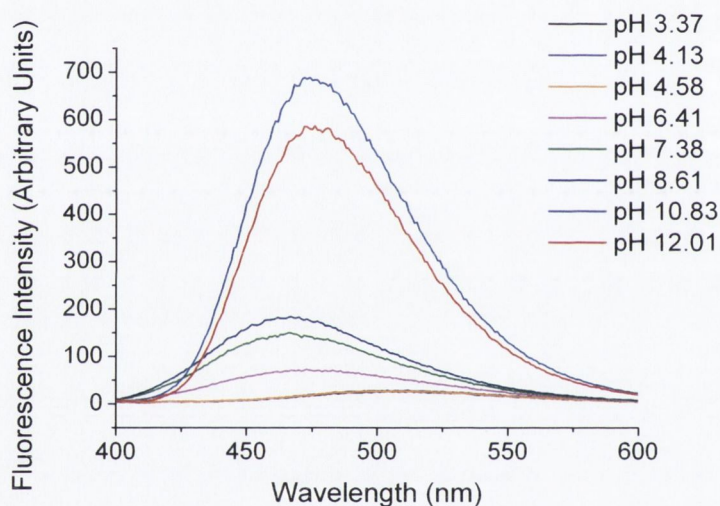
Figure 2.8: The fluorescence spectra of acidic, neutral and basic pH solutions of 2.54×10^{-5} M of (a) isoxanthopterin and (b) xanthopterin, taken at excitation wavelengths of 342 nm and 390 nm respectively.

The change in signal between the acidic and basic media is the most striking for xanthopterin, in Figure 2.8(b). The intensity for the 390 nm excitation peak at pH 3 is only about 5% of the intensity at pH 12. There is also more of a shift in the position of the emission peak for xanthopterin, with the peak in the basic solution being red-shifted from that of the neutral solution, and the acidic form being red-shifted even further, though the fluorescence decreases with acidity. This contrasts with the investigations of Thomas et. al. who found the acidic forms of four pterin species to produce a

red-shifted fluorescence relative to the basic form.[95] Xanthopterin and isoxanthopterin were not involved in this study however, and it is possible that these species behave differently to those investigated by Thomas.
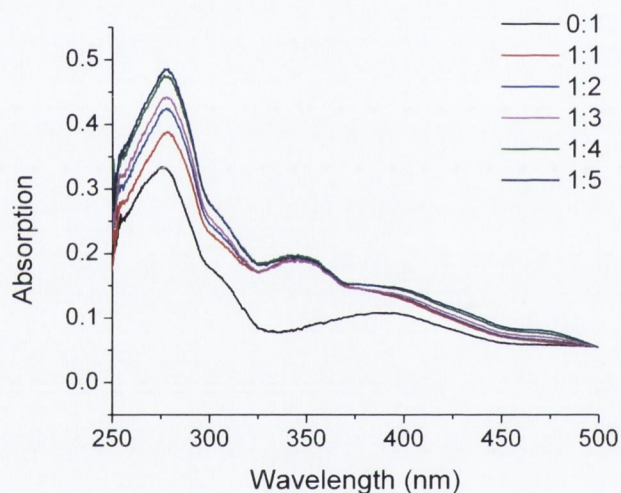
2.4 Pterin Mixtures

Isoxanthopterin and xanthopterin are found in abnormal levels in the urine samples of cancer patients,[43,51] and the relative concentration of pterin species is also a useful measurement, as incremental variations in these ratios have also been reported in cancer research.[108,109] Relative pterin concentrations can be investigated using synchronous fluorescence spectroscopy,[110] but here we wanted to explore the use of isoxanthopterin as an internal standard for the determination of xanthopterin using conventional fluorescence spectroscopy.

2.4.1 UV/Vis Properties of Pterin Mixtures

The two pterins were mixed together in varying ratios, beginning with a 0:1 isoxanthopterin-to-xanthopterin ratio, with the one ratio unit corresponding to 1×10^{-4}M concentration. Ratios were then made up keeping the isoxanthopterin concentration constant and changing that of the xanthopterin, from 1:1 up to 1:5.
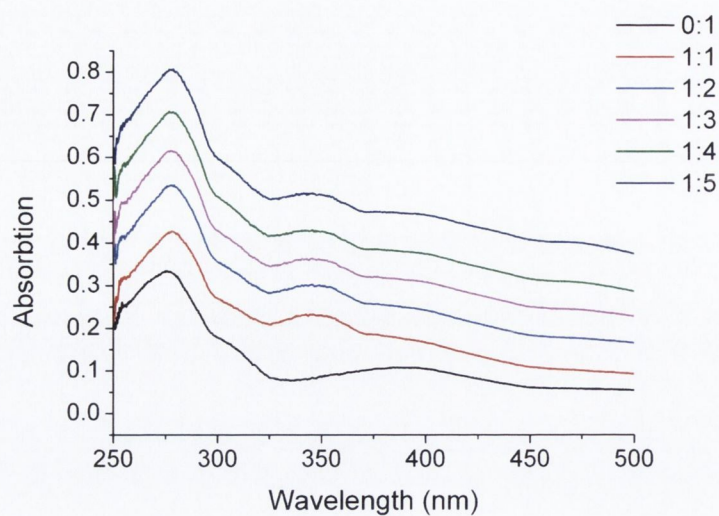
(a)

(b)

Figure 2.9: (a) The original absorption spectra of the aqueous isoxanthopterin:xanthopterin mixtures and (b) the spectra overlaid.

In the plots shown above in Figure 2.9, the xanthopterin absorption spectrum on its own can be seen as the 0:1 line. As the isoxanthopterin is added in for the 1:1 solution the properties change slightly, with a representative peak appearing at about 350 nm. Henceforth the baseline of the plots continues to increase periodically, and from Figure 2.9(b) it can be seen that the peak at about 280 nm also increases slightly with the added xanthopterin concentration.

2.4.2 Excitation and Emission Properties

The samples were also analysed both using the isoxanthopterin and the xanthopterin excitation and emission maxima, as the mixed solutions had elements of both. This required excitation spectra to be taken at both a 410 nm and 490 nm fixed emission for isoxanthopterin and xanthopterin respectively, and emission spectra to be taken at both 342 nm and 390 nm. The resulting excitation spectra at the two emission wavelengths are shown in Figure 2.10.
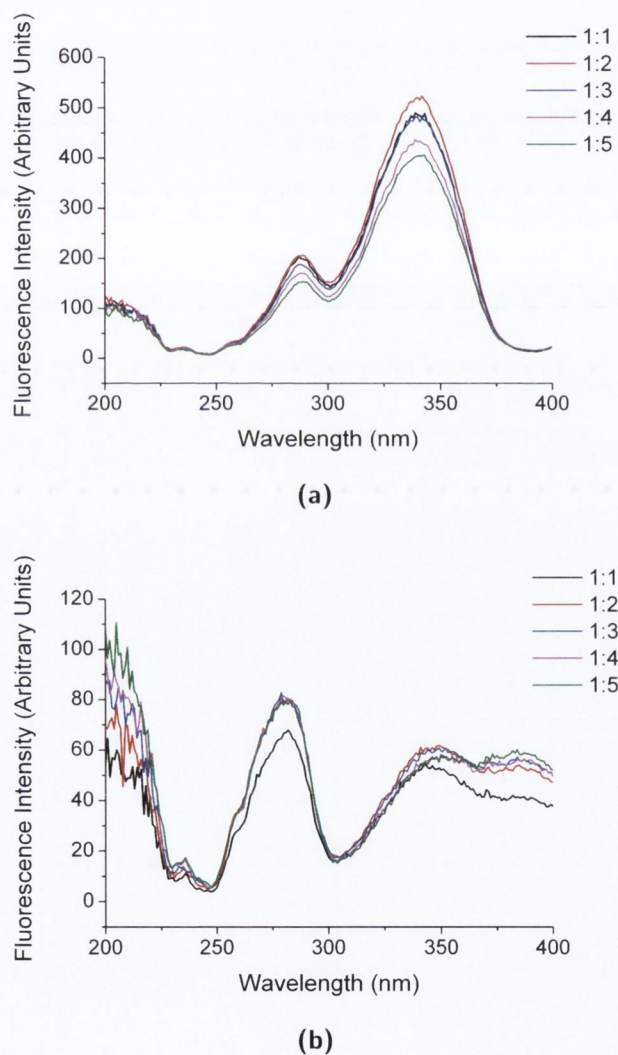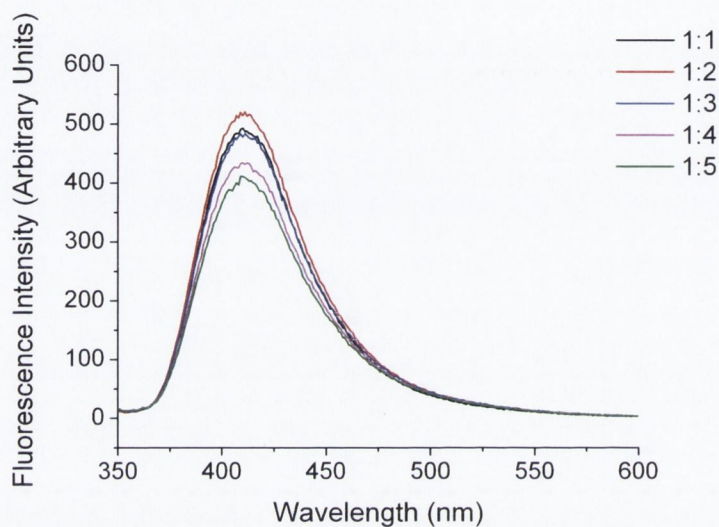

(a)

(b)

Figure 2.10: The excitation spectra of the aqueous mixed pterin solutions at different isoxanthopterin:xanthopterin ratios for emission wavelengths of (a) 410 nm and (b) 490 nm.

The spectrum shown in Figure 2.10(a) shows the excitation of isoxanthopterin. For the xanthopterin spectra in Figure 2.10(b) there is not as much of a change as might be

41

expected for the increasing xanthopterin concentration.

The same approach was taken to look at the emission spectra, this time using the chosen excitation maxima for both pterin species. The results of this are shown in Figure 2.11.


(a)
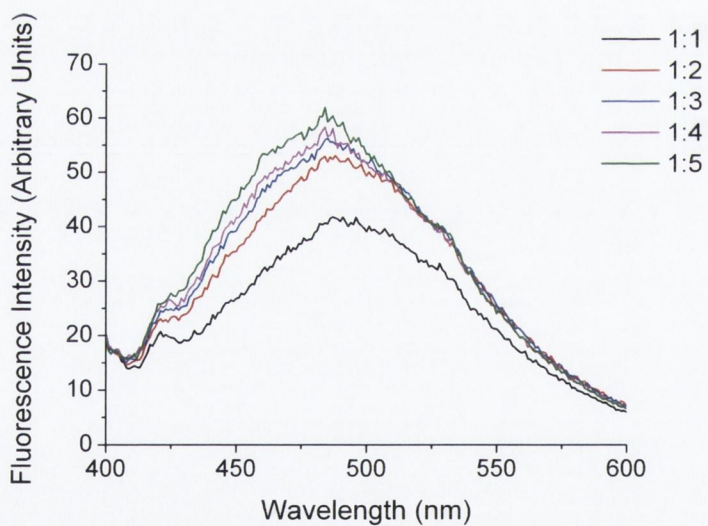
(b)

Figure 2.11: The emission spectra of the aqueous mixed pterin solutions at different isoxanthopterin:xanthopterin ratios for excitation wavelengths of (a) 342 nm and (b) 390 nm.

The spectra shown in Figure 2.11(a) show the emission spectra according to excitation at 342 nm, which is the excitation wavelength of isoxanthopterin. There are variations in the observed signals despite a similar concentration being used, probably due to re-

absorption by the xanthopterin, which absorbs close to the isoxanthopterin emission. The emission spectra excited at 390 nm in Figure 2.11(b) show the emission of xanthopterin to increase gradually, but not linearly, according to the increasing xanthopterin concentration in the mixture.

Plotting the integrated xanthopterin emission peaks, between 410 and 600 nm, against the concentration results in the graph shown in Figure 2.12(a). Normalising these points with the integrated peak values of the isoxanthopterin data shows a linear response, as can be seen in Figure 2.12(b).
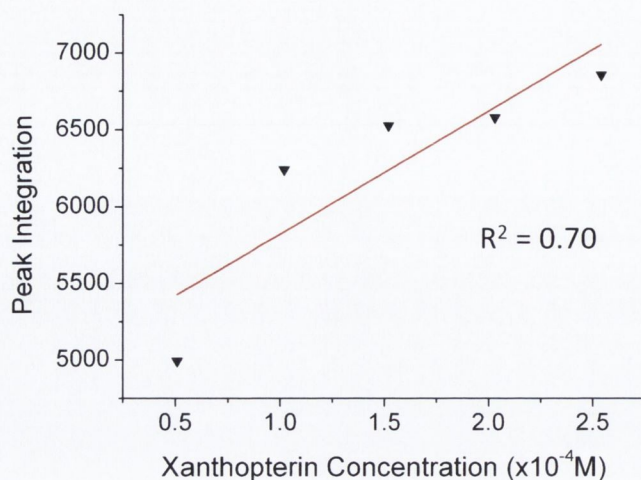
(a)
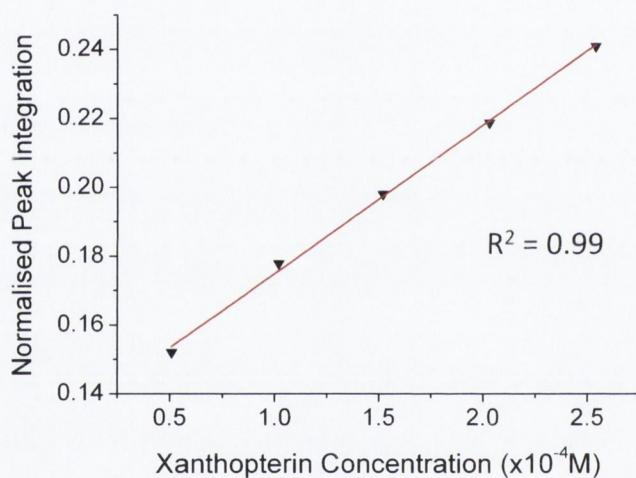
(b)

Figure 2.12: (a) The integrated emission spectra, between 410 and 600 nm, at 390 nm excitation for the mixed pterin solutions plotted against xanthopterin concentration and (b) these integrated values normalised by the integrated values obtained from the emission spectra at 342 nm excitation.

The normalisation of the pterin mixture by using isoxanthopterin as an internal standard does seem to work in this instance. Powerful methods such as HPLC and CE are capable of separating out pterin compounds based on their different migration times through an active medium, which would likely give more accurate and quantifiable data. Synchronous fluorescence pterin measurements in solution in this way could however be useful as an indicator towards relative pterin concentrations.

2.5 Oxygen Quenching

One factor that can affect the fluorescence and absorption behaviour of pterin species is the presence of oxygen in solution. In a study by Cabrerizo et. al.[111] solutions purged of oxygen and irradiated for 2 hours showed no changes in their absorption or fluorescence spectra, but a decrease in the pterin concentration over time was observed in aerobic conditions. This was attributed to photoactivated reactions, which produced non-fluorescent photoproducts. This is an important factor in quantitative pterin analysis as it is a dynamic process, occurring as the compound is being investigated. A 5×10^{-5} M aqueous solution of isoxanthopterin was tested in air-equilibrated conditions and also after bubbling under nitrogen for five minutes, with the emission spectra shown in Figure 2.13
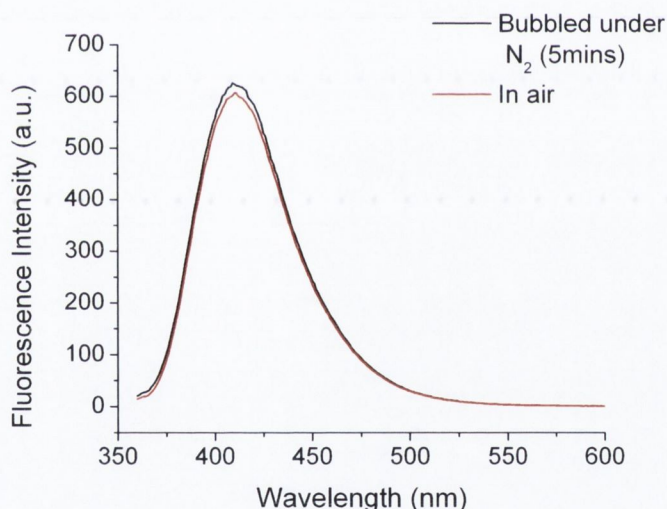

Figure 2.13: The fluorescence emission spectra of a 5×10^{-5} M aqueous solution of isoxanthopterin in air-equilibrated and N_2-treated conditions. The spectra were averaged from three measurements and an excitation slit of 10 nm and an emission slit of 2.5 nm were used at a scan rate of 10 nm/s.

From the information shown in Figure 2.13 it can be seen that there is a small decrease in the fluorescence of the isoxanthopterin in the air-equilibrated solution, which could be attributed to the presence of molecular oxygen reacting under UV exposure to form photoproducts and thus decreasing the concentration of isoxanthopterin. This prospect

was investigated further by looking at the UV/Vis absorption spectra of air-equilibrated 7,8-dihydrobiopterin and xanthopterin solutions over time. A 1×10^{-6} M solution of 7,8-dihydrobiopterin and a 2.5×10^{-4} M solution of xanthopterin were prepared, with twenty consecutive scans taken from 250-400 nm, equating to a 36.6 minute exposure time to UV light. The resulting spectra are shown in Figure 2.14.
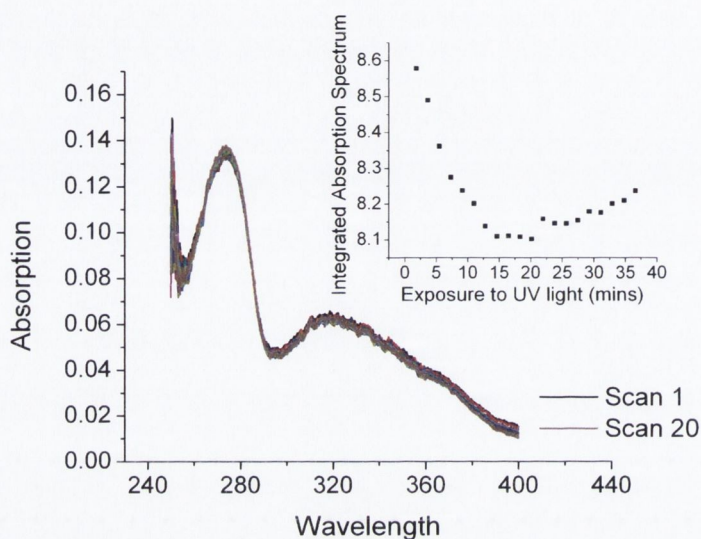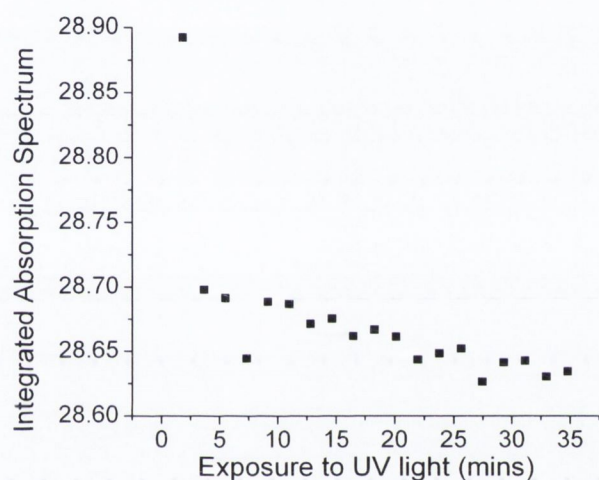

(a)
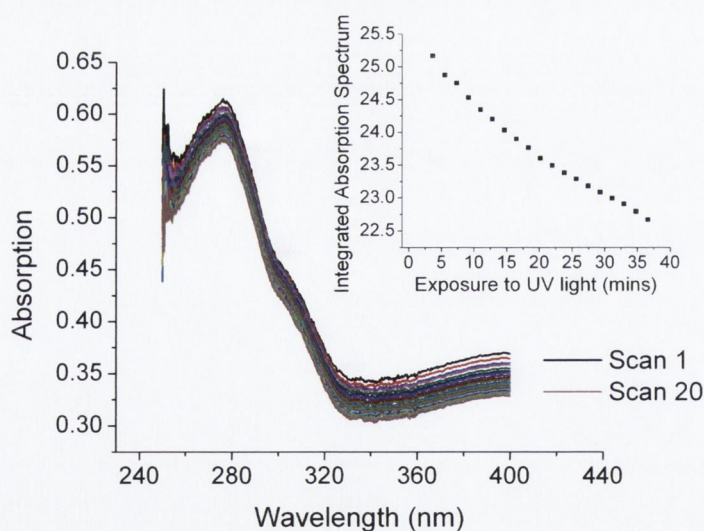
(b)

Figure 2.14: The UV/Vis spectra of air-equilibrated solutions of (a) 1×10^{-6} M 7,8-dihydrobiopterin and (b) 2.5×10^{-4} M xanthopterin. The insets show the spectra integrated between 260 and 400 nm plotted against time.

The U-shaped plot obtained from the 7,8-dihydrobiopterin spectra can potentially be ex-

plained according to Vignoni et. al. who describe the consumption of 7,8-dihydrobiopterin with UV irradiation time and a concomitant increase in the concentration of biopterin.[14] Because the two species have a similar absorption profile, this could explain the shape of the curve in Figure 2.14. In contrast the absorption of xanthopterin decreases linearly with irradiation time.

The UV response of the pterins were also investigated after bubbling under nitrogen for 10 minutes, with the responses plotted versus time in Figure 2.15.

(a)
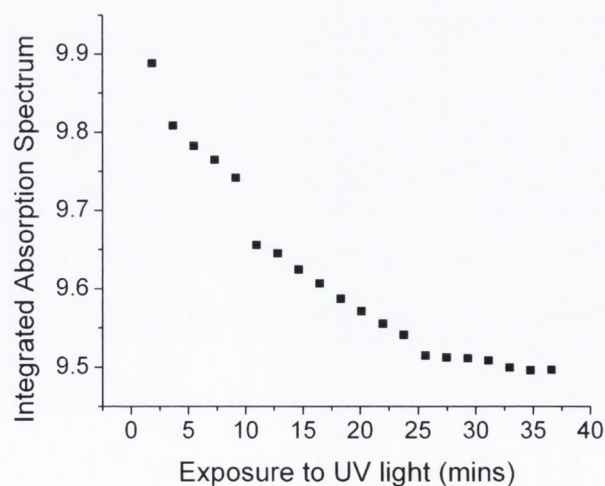
(b)

Figure 2.15: The UV/Vis spectra of N_2-equilibrated solutions of (a) 1×10^{-6} M 7,8-dihydrobiopterin and (b) 2.5×10^{-4} M xanthopterin integrated from 260 - 400 nm and plotted against time.

From the responses shown in Figure 2.15 it can be observed that there is still a decrease in signal following a 10-minute period of N_2 bubbling. For xanthopterin the decrease is still generally linear (although the first point could be an outlier), but the decrease is 1% following the N_2 treatment whereas it was 10% beforehand. For the 7,8-dihydrobiopterin a decline of 4% as opposed to 6% is observed following the N_2 treatment, and there is no increase of the signal again after about 20 minutes. This could be due to a lower oxygen content not allowing or slowing down the photoconversion to another form of biopterin, assuming from the continuing decrease in signal that 10 minutes N_2 treatment is insufficient to eliminate all of the oxygen.

The photophysical properties of pterins investigated in this chapter were all undertaken using air-equilibrated solutions, so it is likely that photodegradation of the compounds is occurring. This in turn will detract from quantitative analysis, and any future work to consider using UV/Vis and fluorescence spectroscopy for quantitative means would need to consider the impact of molecular oxygen and the photoreactivity of each of the pterin species.

2.6 Conclusions

Many pterin compounds show a strong interaction with UV radiation,[16] which can induce fluorescence or photo-oxidative effects. These effects have been studied in detail in the papers of A.H. Thomas,[14,21,95] though not in the cases of isoxanthopterin and xanthopterin. Both of these latter species do appear in the literature, in many cases regarding their presence in the urine samples of cancer patients.[43,51,110] Much of the detection work involves separation of the pterins from solution, using designated separating techniques, followed by detection, usually fluorometric.

Initial fluorescence spectroscopy with respect to concentration led to the observation of saturation at higher pterin concentrations, and to how this could be somewhat compensated for by using inner-filter correction. Measurements of the pterins in different pH environments showed both absorption and fluorescence to be more pronounced in

basic environments. This is something that occurs in some fluorescent proteins.[112] Fluorescence spectroscopy of mixed pterin solutions showed a linear response upon normalisation of increasing xanthopterin concentrations with a fixed isoxanthopterin concentration, though fluorescence detection of multiple species in solution would be difficult without the use of some form of separation technique.

Analysis of solutions of isoxanthopterin, one air-equilibrated and the other bubbled under nitrogen to remove some of the oxygen content, found the fluorescence intensity of the air-equilibrated solution to be slightly lower than that of the nitrogen-bubbled analogue. Subsequent UV/Vis analysis of 7,8-dihydrobiopterin and xanthopterin over a period of 36.6 minutes UV exposure in the UV/Vis spectrometer showed changes in the UV/Vis spectra, due to conversion to alternative photoproducts.[14]

<div style="text-align: right; font-size: 3em;">3</div>

Silver Colloids in Surface-enhanced Raman Spectroscopy

Silver colloids prepared according to Leopold and Lendl[113] were used to investigate the SERS response towards the reproducible detection of various chemical compounds. SERS probes used for the characterisation and optimisation were benzotriazole and the Rhodamine dyes B and 6G, the latter of which is particularly prevalent in the literature when characterising SERS responses.[114–116] Finally, xanthopterin and isoxanhopterin were considered with the focus on the applicability of SERS towards their detection and quantification.

3.1 Colloids

Surface-enhanced Raman Spectroscopy (SERS) has long been considered a technique of some potential, but this is tempered by the fact that it is a difficult technique to control. Irreproducibility in measurements is the major drawback,[114,117,118] which can occur for a number of reasons. Variations in the size or separation of the enhancing colloids[119,120] or in the type of aggregating agent used[121] are two such reasons, and indeed variations can even occur between colloid batches prepared according to the same procedure. Many synthesis procedures for a variety of different nanoparticle shapes are available,[122] and controlling monodispersity is also possible.[123] Degradation of the

sample due to interaction with the incident laser is also an issue,[124,125] and can often be identified by the appearance of bands due to graphitic or amorphous carbon.[126] As a consequence of these factors it is important to consider the effect of signal variations in SERS and to take measures in order to reduce their effects as much as possible.

Silver colloid suspensions have proved popular in SERS research, in particular those prepared by the Lee-Meisel method,[127] though there are other competitive synthesis techniques, such as that developed by Leopold and Lendl.[113] Work has also been published on the use of other synthesised metal nanostructures, such as triangular nanoplates and nanorods, in the investigation of the SERS effect. Sancı and Volkan report the growth of silver nanorods directly onto a sol-gel covered glass surface as an alternative to synthesis of the nanostructures in solution before their deposition onto the substrate. This study was carried out as an analysis for its potential with respect to various dyes, with results showing intense spectra and indicating that the procedure could offer potential in SERS detection probes.[128] Another interesting material employed towards SERS are triangular nanoplates, as it is possible to tune the light absorption maximum by varying the aspect ratios of the triangles during synthesis.[129]

One of the important things to note with regard to using these features as substrates for SERS is the significance of the LSP bands. These bands shift with respect to the aspect ratios and degree of aggregation of the nanomaterials, and the maximum SERS enhancement is expected when the λ_{max} of the LSPR is slightly longer than that of the laser excitation source. Because of its sensitivity and selectivity there is the inevitable link of SERS to chemical and biological sensing. A further advantage is that there is little impact on the data from water.[130] However, one other point of consideration regards that of the interaction between the analyte molecules and the metal surface of the substrate. Bare gold and silver surfaces as direct adsorption sites for biological molecules can cause a denaturing of the molecules of interest, as was first investigated by Cotton et. al. with regards to myoglobin and cytochrome c.[131] Another issue with colloidal-based substrates regards certain characteristics of the solution, for example pH, ionic strength or the concentration of the target biological molecule, which cause aggregation of the colloids and greatly affect the enhancement profile.[132]

Bare metal surfaces have a further issue of being unable to isolate the biological compound of interest from other unwanted species. Due to the distance-dependence of SERS, signals are still obtainable up to a few nanometres from the surface of the enhancing metal, so it possible to functionalise the surface using a self-assembled monolayer of certain molecules, such as thiols.[133] Atomic layer deposition is another technique applied to this purpose,[134,135] though label-free, reproducible SERS detection is still actively sought.[136]

In this chapter a Horiba LabRAM HR Raman spectrometer was used for the SERS experiments using 532 nm and 633 nm excitation. A $10\times$ objective lens and a grating of 600 lines/mm were also used.

3.2 Synthesis of Silver Colloids

The silver nanoparticles were synthesised according to a method developed by Leopold and Lendl.[113] Briefly, $AgNO_3$ was reduced using an alkaline hydroxylamine hydrochloride solution, the alkalinity of which was obtained through addition of sodium hydroxide. A final pH of 7 is obtained from the resultant nanoparticle solution. Two approaches can be taken in the synthesis. The first (NP1) involved adding 10 mL of a 10^{-2} M solution of silver nitrate dropwise to 90 mL of a 1.67×10^{-3} M hydroxylamine hydrochloride solution, containing 3.33×10^{-3} M sodium hydroxide. The second (NP2) used 10 mL of a more concentrated solution of the reducing agent (1.5×10^{-2} M), mixed with 3×10^{-2} M sodium hydroxide and then adding this dropwise to 90 mL of a 1.11×10^{-3} M solution of $AgNO_3$. The solutions were stored in plastic containers. Using an approximation of a silver atomic radius of 165 pm and an fcc unit cell structure[137] a colloid concentration of 0.38 nM was calculated (See Appendix A). Other nanomaterials were also considered for SERS, but showed poorer performances, albeit with less investigation than the Leopold/Lendl colloids (See Appendices A-C for details of their synthesis and application).

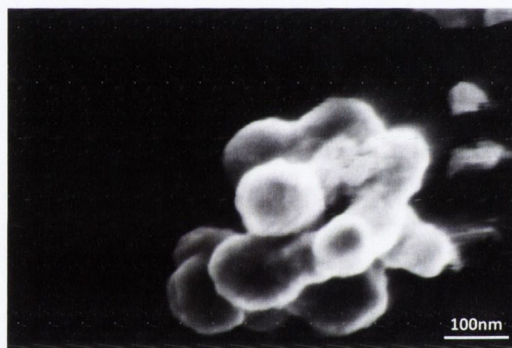UV/Vis and SEM images were taken of both methods of colloid preparation for the

Leopold and Lendl technique, as shown in Figure 3.1.
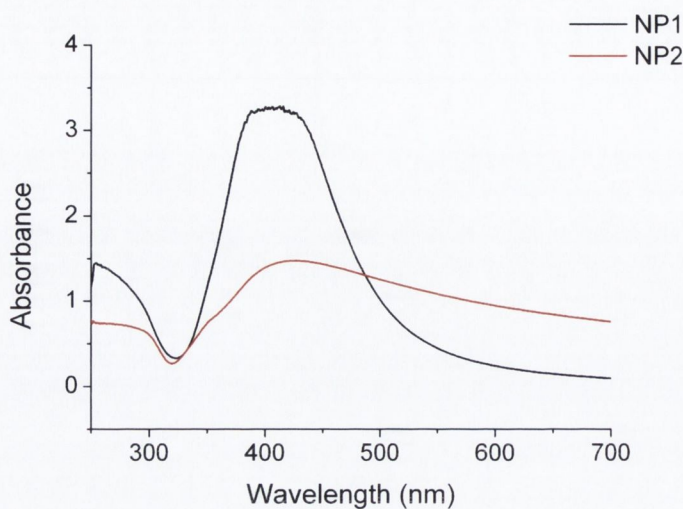
(a)
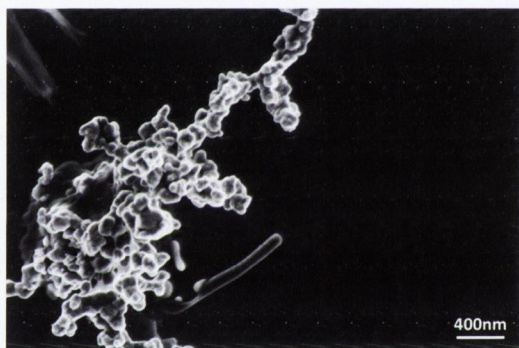
(b)   (c)

Figure 3.1: (a) UV/Vis absorption spectra of both sets of colloid. (b) & (c) show SEM images taken of the NP1 and NP2 colloids respectively.

For the NP1 solution in Figure 3.1(b) it can be seen that the colloids seem to have aggregated quite closely. The individual particle sizes are difficult to make out, but appear to be in the 50 nm−100 nm range, which is a little larger than expected. The NP2 solution shows quite large particles, of about 100 nm.

3.3 Reproducibility Measurements in Colloid Batches

Five batches of the silver colloids were prepared together, in order to assess their performance from batch to batch. A 9.1×10^{-6} M concentration of Rhodamine 6G was

used to investigate the SERS response of each batch, and 3 droplets were used for each batch to observe variations within batches.

For these experiments the relative percentage deviation (%RSD) was used as a figure-of-merit, according to the following formula[138]

$$\%RSD = 100 \times \left(\frac{\sigma}{\mu}\right) \tag{3.1}$$

where σ and μ are the standard deviation and mean of the peak heights or integrated spectra values of the data. Ten spectra were nominally taken of each droplet.

3.3.1   Colloid Preparation and UV/Vis Spectra

The colloids were prepared according to the more monodispersed Leopold & Lendl suspension,[113] as described in section 3.2.   This procedure corresponds to 17.0 mg of the silver nitrate being measured out into 10 mL of water and 10.4 mg of the hydroxylamine hydrochloride being measured out into 90 mL of water. 18 Ω Millipore water was used in all of the solutions.

A UV/Vis spectrum was taken of each resulting colloid batch, with the suspension diluted one-in-four in water to avoid saturation of the signal on the spectrometer. The resultant spectra are shown in Figure 3.2
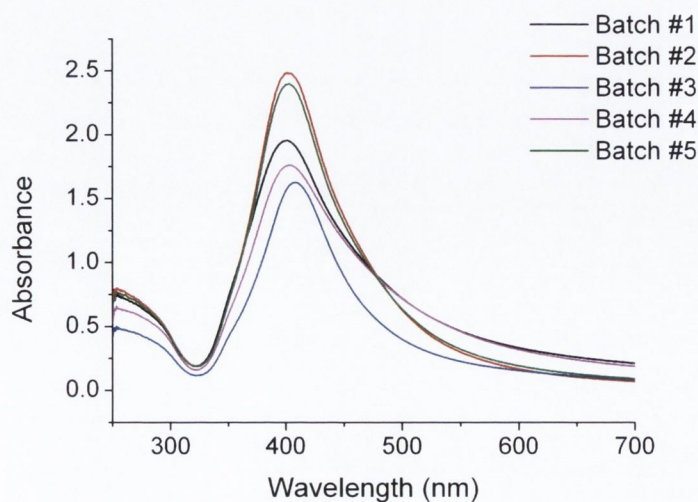

Figure 3.2: UV/Vis spectra for each of the five batches of silver colloids prepared.

From the UV/Vis spectra a clear variation over the five batches can be seen. Batches 1 and 4 show a broader tail-off of the 410 nm absorption peak, while the three other batches show a narrower peak width, albeit with varying absorption intensity. These variations could have arisen from small variations in the amount of reagent measured for the the syntheses.

3.3.2 SERS Measurements

SERS measurements on the colloid batches were all conducted using a 9.1×10^{-6} M concentration of Rhodamine 6G. A solution of twice this concentration was mixed half-and-half with the respective colloid batch in order to obtain this concentration value. All measurements were conducted on a 6 μL droplet deposited onto a glass slide and ten spectra were taken from each of three separate droplets for each colloid batch, at an exposure time of 0.5 s using a $10\times$ objective lens. Shown in Figure 3.3 are the ten spectra for each of the three drops used in the analysis of the Batch 1 solution, as well as a table of some %RSD figures.

(a)
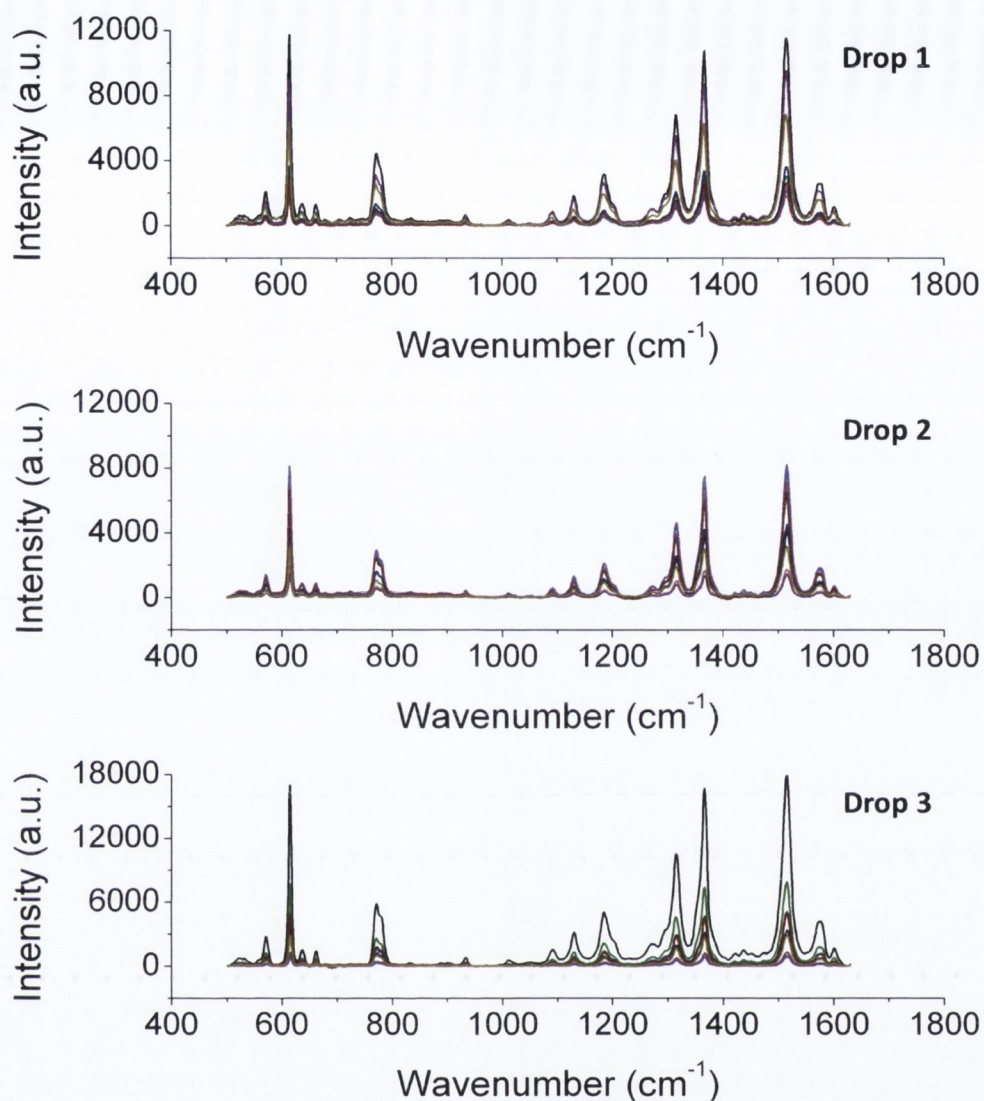
		Batch 1 - %RSD Values			
		Drop 1	Drop 2	Drop 3	All Drops
All Spectra	616cm⁻¹	74.6	47.9	98.1	7.3
	771cm⁻¹	75.2	47.7	94.3	6.4
	1315cm⁻¹	76.0	46.8	100.7	4.9
	1367cm⁻¹	75.4	47.6	100.0	6.1
	1514cm⁻¹	76.5	48.1	99.8	6.4
	Int. Peaks	75.3	46.6	101.8	4.2

(b)

Figure 3.3: (a) shows the spectra taken of a 9.1×10^{-6} M Rhodamine 6G solution for each of the three drops measured, using a 633 nm excitation wavelength and a 0.5 s exposure time. (b) shows the %RSD values for the maximum peak heights for the five principle peaks for each drop, as well as that for the integrated area under the spectral curves (Int. Peaks). The final column represents the %RSD in the peak heights and integrated spectra across the three drops.

What can be observed from both the spectra in Figure 3.3(a) is that there is much variation between spectra from within a single droplet. The table in Figure 3.3(b) shows the %RSD in the maximum peak height for the five principle Rhodamine 6G peaks and the %RSD in the integrated spectra for each of the three droplets. Also shown is the %RSD in the average signal from across the three droplets, shown in the 'All Drops' column, which corresponds to the variation between droplets, again for the five principle peaks and the integrated spectra values. The %RSD values of $\sim 50 - 100\%$ are very high and not of promise quantitatively. The variation across the droplets is better, but given the high uncertainty within each drop this is somewhat insignificant.

One method to improve these figures can be achieved through the removal of the highest and lowest spectra from the data set; applying this approach resulted in the data shown in Figure 3.4.

(a)
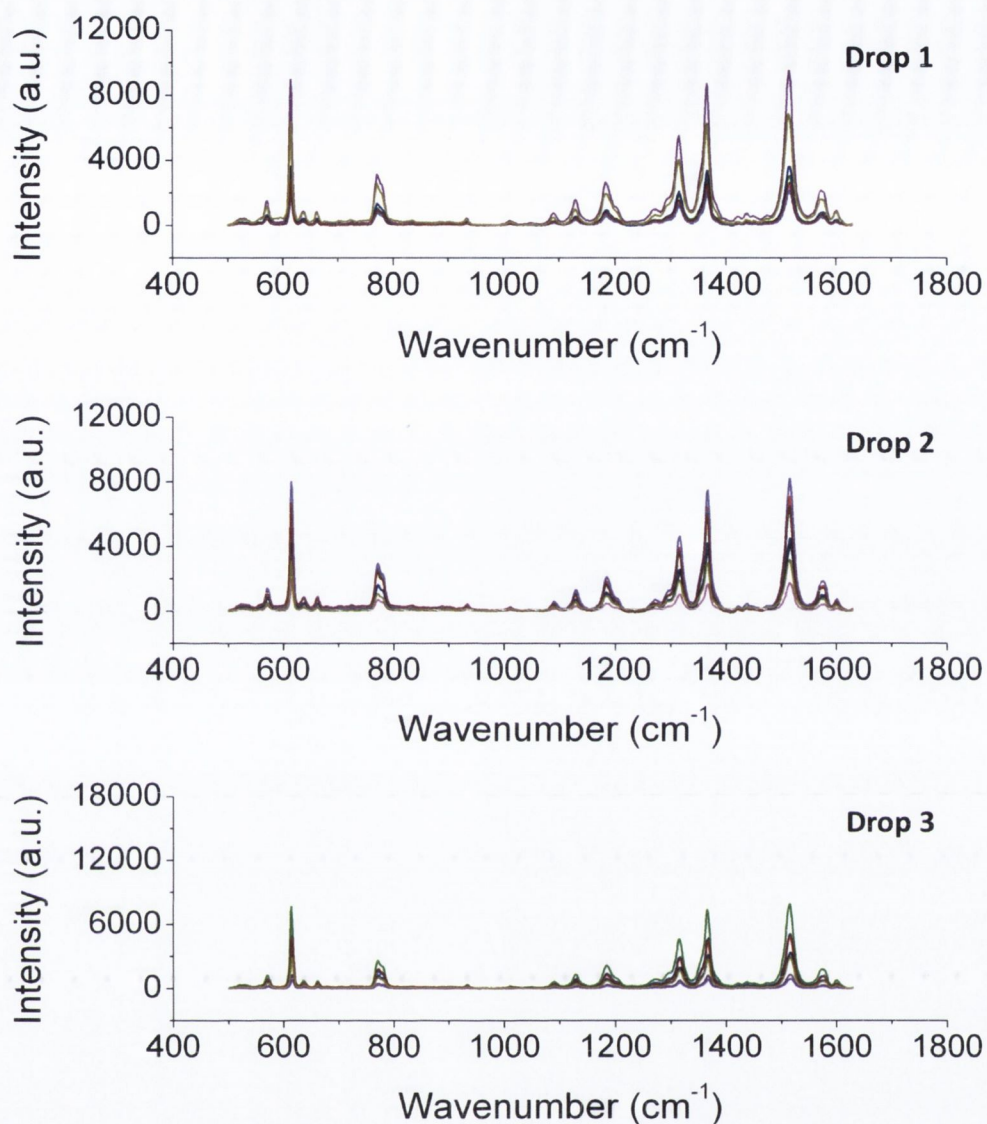
		Batch 1 - %RSD Values			
		Drop 1	Drop 2	Drop 3	%RSD
Highest & Lowest Spectra Removed	616cm⁻¹	62.0	41.0	57.4	19.4
	771cm⁻¹	61.2	41.8	55.2	19.0
	1315cm⁻¹	66.2	40.1	58.0	15.0
	1367cm⁻¹	65.3	40.8	58.0	16.2
	1514cm⁻¹	67.1	41.8	57.9	16.3
	Int. Peaks	65.28	39.66	58.16	13.7

(b)

Figure 3.4: (a) shows the spectra taken of a 9.1×10^{-6} M Rhodamine 6G solution using a 633 nm excitation wavelength and a 0.5 s exposure time, but with the highest and lowest spectra removed. (b) again shows the %RSD values for the maximum peak heights and integrated spectra.

59

The 'Best 8' spectra in each of the droplets in Figure 3.4(a) still show large variations, as is reflected in the %RSD values of $\sim 40 - 60\%$, which although better is is still too high. The variation across the droplets increased in this case, though again this is somewhat irrelevant given the variation within the droplets themselves. This high level of variation was not observed in all of the batches, as can be observed in Figure 3.5, which shows the averaged spectra integration for each droplet for each batch, with error bars showing the standard deviation within each droplet. Figure 3.5(a) shows the data averaged over all ten acquired spectra and Figure 3.5(b) shows the data for the 'Best 8' data.
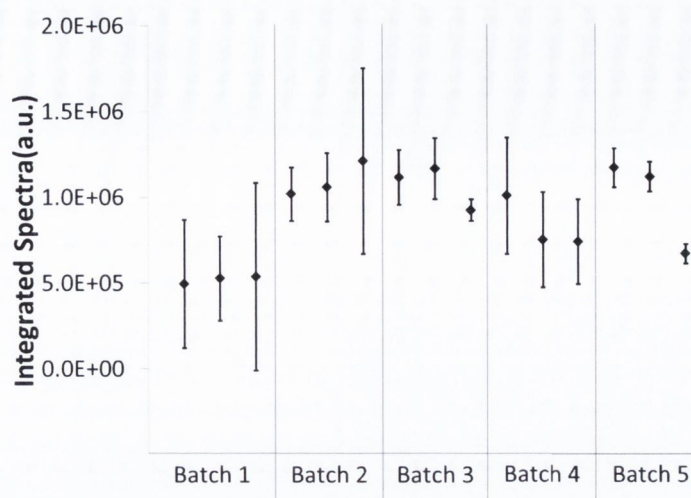
(a)
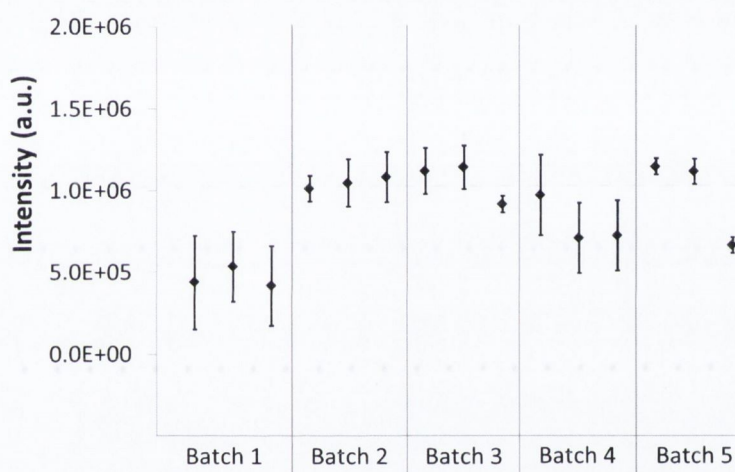
(b)

Figure 3.5: (a) shows the average integrated spectra values (between 500 and 1630 cm^{-1}) taken for each of the droplets over each of the five colloid batches. The error bars show the standard deviation over the range of spectra taken. (b) shows the same relationship but with the highest and lower spectra removed from each data set.

From this data the impact of using the 'Best 8' approach can clearly be seen, with a significant decrease in the extent of the error bars. Also evident is that Batch 1 is the poorest of the batches, showing both the lowest spectral intensities and the highest irreproducibility between spectra. Batch 4 also shows a poor %RSD count, and comparing back to the UV/Vis spectra in Figure 3.2 these two batches correspond to the two that showed the slightly broader absorption peaks. It is thus possible that

a poor colloid batch can be identified through the UV/Vis profile, although further investigation would be required to validate this observation.

The three other batches, batches 2, 3 and 5, show better reproducibility within each of the droplets, although batch 5 shows a drop-off in the average intensity of the third droplet, possibly due to contamination. The table shown in Figure 3.6 shows the %RSD values across the three droplets for each of the droplets measured, for data involving all ten spectra and that involving the 'Best 8' data.

%RSD Across Droplets		
	All 10	Best 8
Batch 1	4.2	13.7
Batch 2	9.3	3.4
Batch 3	11.9	11.7
Batch 4	18.2	18.4
Batch 5	27.8	27.6

Figure 3.6: UV/Vis spectra for each of the five batches of silver colloids prepared.

From this it can be concluded that batch 2 shows the greatest potential towards quantifiable SERS analysis, due to low variations within each of the droplets and a low %RSD of 3.4% across the three droplets measured, in the 'Best 8' scenario. The data for each of the droplets for batch 2 is shown in Figure 3.7.
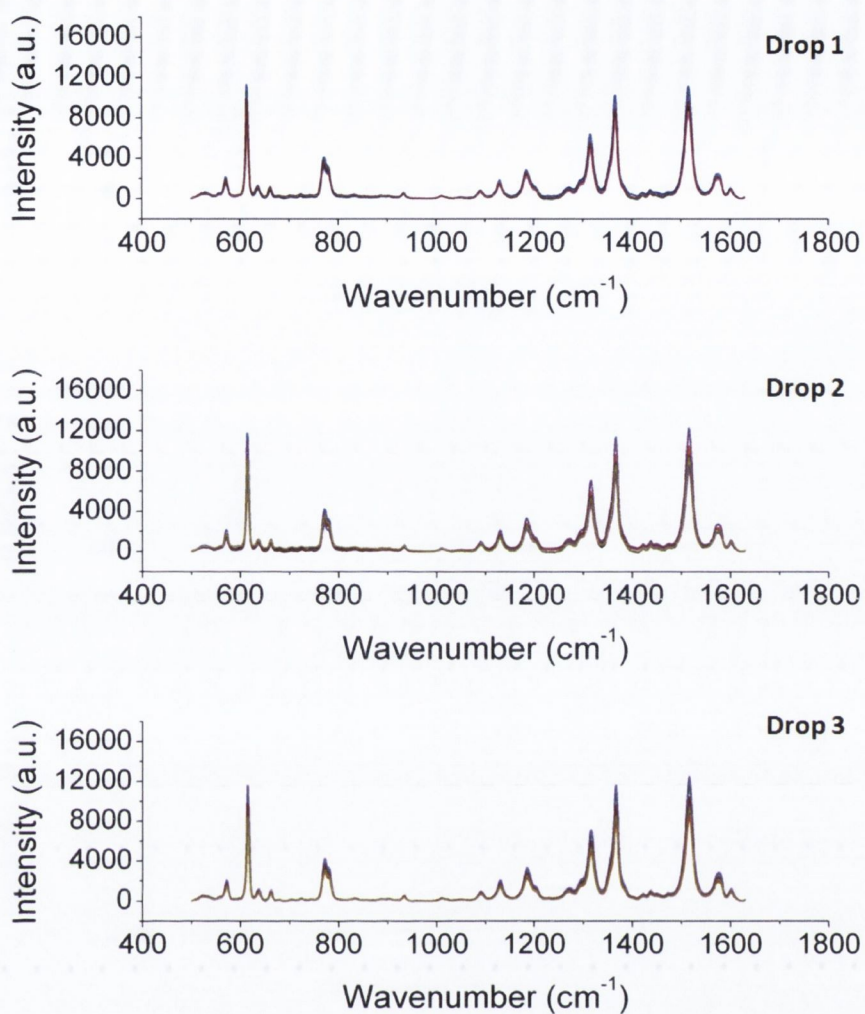
(a)

		Batch 2 - %RSD Values			
		Drop 1	Drop 2	Drop 3	%RSD
Highest & Lowest Spectra Removed	616cm⁻¹	9.1	14.5	14.2	0.8
	771cm⁻¹	8.8	15.0	13.5	1.5
	1315cm⁻¹	8.2	14.8	14.1	3.1
	1367cm⁻¹	8.1	15.0	14.7	2.7
	1514cm⁻¹	7.6	14.6	13.7	2.6
	Int. Peaks	7.9	13.9	14.1	3.4

(b)

Figure 3.7: (a) shows the same 'Best 8' spectra as in Figure 3.4 but for Batch 2 instead of Batch 1. (b) again shows the %RSD values for the maximum peak heights and integrated spectra.

While batch 2 showed the greatest signal response for the combination of signal and reproducibility using Rhodamine 6G as the SERS probe a different relationship was

observed when examining xanthopterin. Only one droplet of each was examined in this case, with the resulting spectra all shown in Figure 3.8.
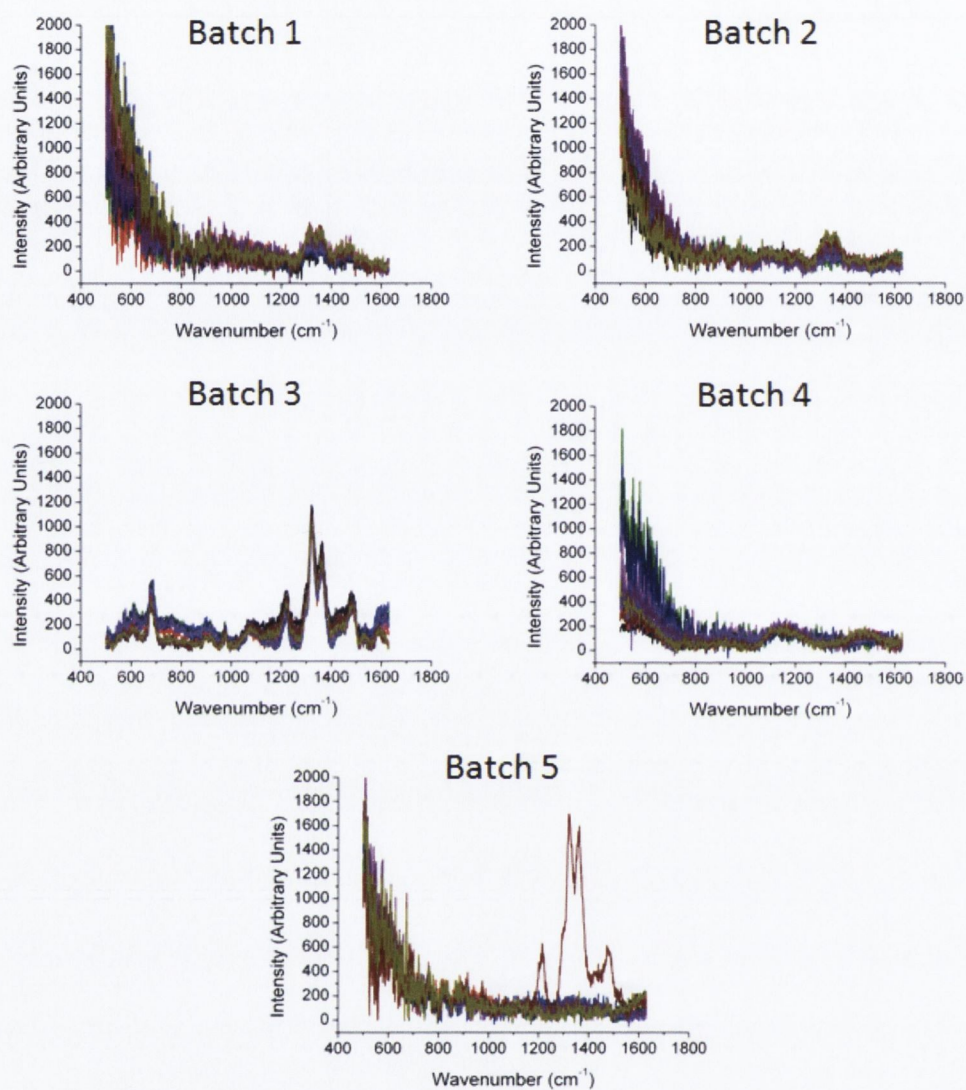
Figure 3.8: SERS spectra for 2.54×10^{-4} M xanthopterin mixed with each of the different silver colloid batches. A 633 nm excitation wavelength was used with a 10 s exposure time.

All the xanthopterin spectra were taken at 10 s exposure times, with batch 3 being the only set of colloids to show an appreciable SERS response with xanthopterin. The consistency of the measurements is good with a %RSD value of 9% across the 10 spectra taken. Batch 5 did show one large xanthopterin response, probably due to excitation at a 'hot-spot' region. A possible explanation for this is the need to add an aggregation agent, which will be discussed in the next section.

3.3.3 Colloid Contamination

Another issue with the implementation of silver colloids in SERS experiments is that it is not uncommon to see spectral features due to the presence of an impurity or contaminant. This can arise from a number of sources, be it from the synthesis glassware used, from the pipette tips being handled by a contaminated glove or indeed from the ink of the marker used to mark the solution vials. Careful preparation procedures are required to prevent these contamination issues from arising and colloids should be checked for such artefacts prior to further SERS analysis. Background signals for the batch 3 colloid solution are shown in Figure 3.9, with no obvious contaminants being present in this case.
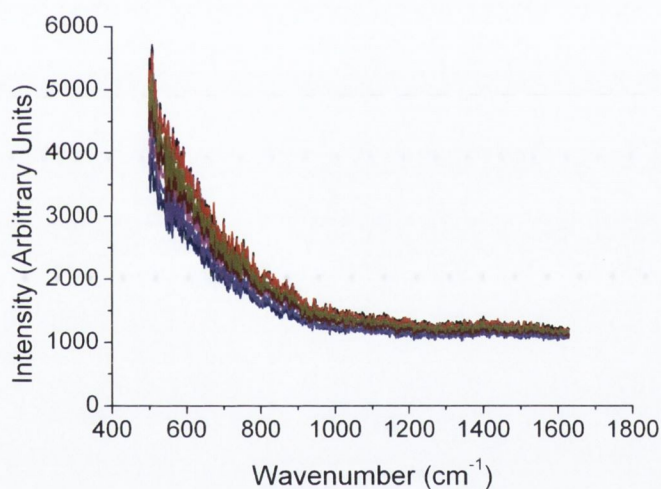
Figure 3.9: Raman spectra of the batch 3 colloid set.

The spectra for the four other batches can be found in Appendix E from Figure E.1 to Figure E.20.

3.3.4 Laser Power Fluctuations

Another issue with taking reproducible SERS measurements concerns the incident power of the laser on the sample.[63] This was investigated over an initial hour-long period following the initial switching on of the system. The power was measured at 10-minute intervals and the power was observed to stabilise after about 20 minutes.

3.3.5 Objective Lenses

The Raman system consisted of two lasers, a 633 nm red laser and a 532 nm green one. The system also contained two objective lenses, one a 100× magnification with a 0.75 numerical aperture, the other a 10× with a 0.25 numerical aperture. The theoretical diffraction limited spatial resolution can be predicted according to the following formula[139]

$$\text{Laser Spot Size} = \frac{0.61\lambda}{NA} \qquad (3.2)$$

where λ is the wavelength of the laser and NA is the numerical aperture of the objective lens. Thus the minimum resolution for the 10× and 100× objective lenses can be calculated to be 1.5 μm and 0.5 μm respectively for the 633 nm laser and 1.3 μm and 0.24 μm respectively for the 532nm laser.

Regarding the SERS data obtained, using a 100× objective tended to produce large variations within the same sample droplet. One reason for this is due to the very small volume being probed, as large local variations due to "hot spots" on the colloid aggregates would produce large variation from scan to scan. Measurements carried out with a 10× objective lens, which probes a larger sample area and thus can to some extent average out local variations in the enhancements, were found to improve the signal strength and the reproducibility as can be observed in Figure 3.10, though this was not quantified.
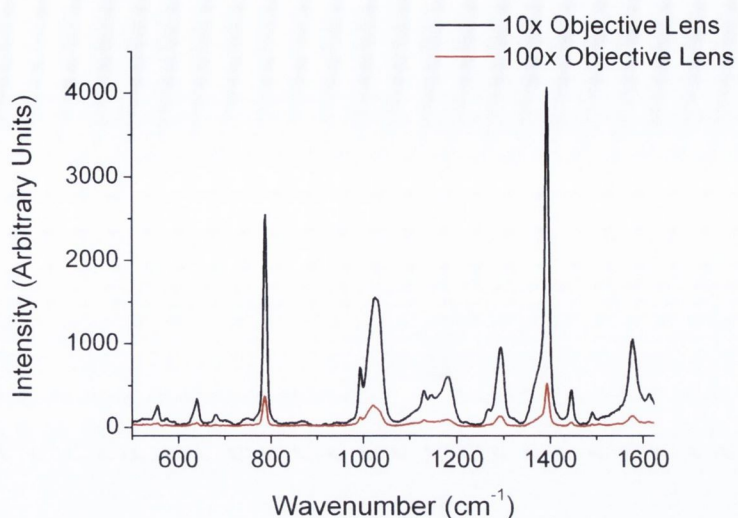
Figure 3.10: SERS spectra for a 4.2×10^{-4} M benzotriazole solution, taken using $10\times$ and $100\times$ objective lenses.

3.3.6 Glass Microslide Background

Droplets deposited onto glass microslides were investigated as the media for SERS analysis due to the ease with which this was applicable to the Raman system. One of the issues with using glass as a Raman substrate is that of the potential presence of bands due to silica bonds in the glass. The slides also received no prior cleaning before use, which could provide a source of contamination. In our experiments we found that the influence of the glass substrates on the Raman signals obtained to be minimal, and comparing the background signal with that of an alternative substrate such as aluminium foil appeared to offer little advantage. The background spectra for a glass microslide are shown in Figure 3.11.
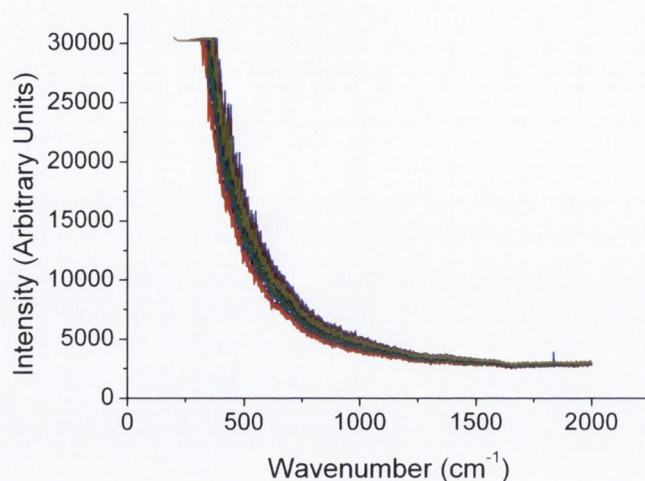
Figure 3.11: The background Raman signals obtained from ten scans of a glass microslide using a 633 nm laser and 10 s exposure time.

3.3.7 Droplet Evaporation

Because the droplets used were of a small 6 μL volume, much of the surface of the liquid was exposed to the surrounding environment, and as such to the effects of evaporation, which would result in the sample becoming more concentrated as the water content evaporated off. To examine these effects an analysis was set up using a 6 μL droplet of a 9.1×10^{-6} M concentration of Rhodamine 6G with silver colloids from the most reproducible batch 3 set. A spectrum was taken every 15 seconds over a 30-minute period, with the integrated spectra of this analysis plotted against time in Figure 3.12.

In Figure 3.12(a) there is a very evident impact on the SERS spectra due to evaporation, with the obtained signal increasing by quite an amount by the 30-minute stage. Taking the first five minutes of the data however shows a less obvious increase in signal over time, as shown in Figure 3.12(b), and indeed the %RSD of this data works out at 5.4%, which is less than the figures obtained during the batch analysis. While evaporation will occur immediately after droplet deposition, the SERS measurements are also taken as soon after deposition as possible, and given the low %RSD over a five-minute period SERS data can be taken that lies within the error range inherent in the colloid batch.
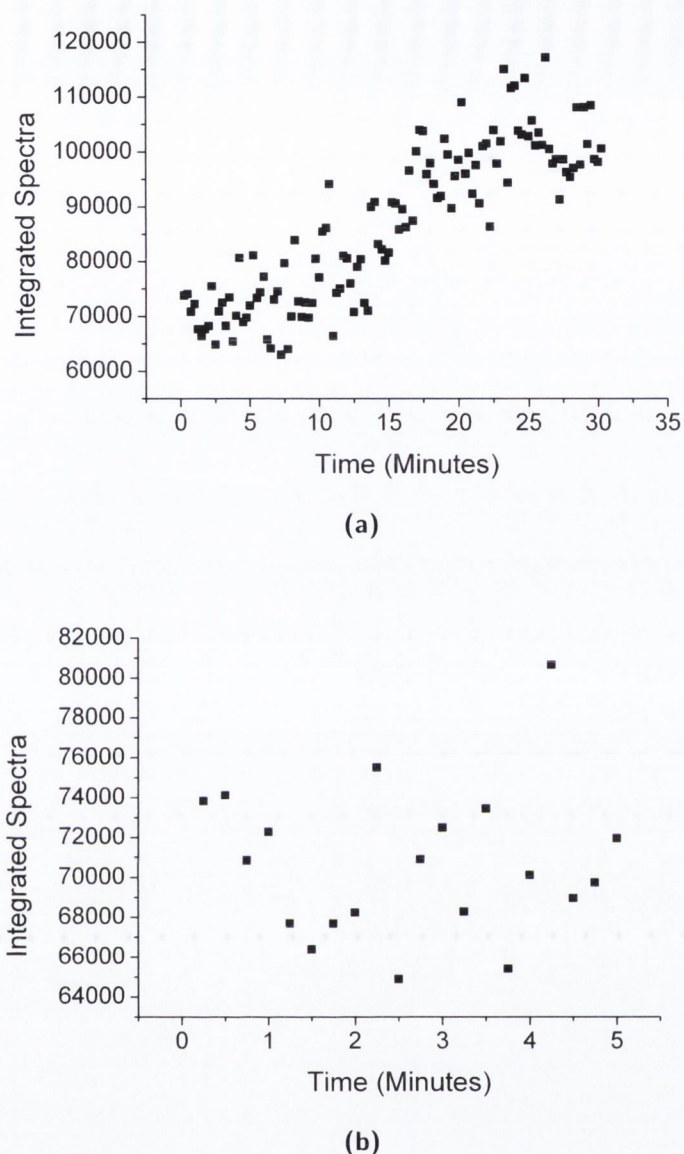
(a)

(b)

Figure 3.12: (a) shows the increase in the integrated spectrum values as the SERS spectrum of a droplet of Rhodamine 6G and silver colloids is measured at 15 second intervals over a half hour period. (b) shows the first five minutes of this data, over which the %RSD is 5.4%.

3.4 Quantitative SERS & SERS of pterins

SERS has previously been applied to the study of pterins, but there does not seem to be an extensive amount of work on this in the literature. Concentration-related studies involving the detection of folic acid using silver nanoparticles have been accomplished, leading on to the technique being applied to human serum samples.[59] Pterin analysis

has also been conducted using silver nanoparticles in the work of Stevenson et. al. where studies were carried out on synthesised samples of 6-acetyl-7,7-dimethyl-7,8-dihydropterin and 5,6,7,8-tetrahydropterin, which shows detection down to nanomolar concentrations.[60] Also, Feng et. al. have shown similar nanomolar detection with enhancements of 10^5 for xanthopterin using silver nanoparticles as the SERS substrates.[58] The spectrum of xanthopterin obtained from this latter source is shown in Figure 3.13.
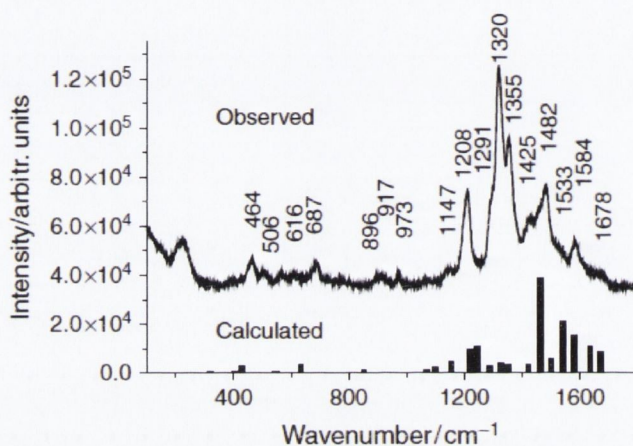
Figure 3.13: The SERS spectrum of xanthopterin (Obtained from Feng et. al.[58])

Raman spectroscopy can experience variation in the signal levels based on only small changes in experimental procedure, for example sample positioning.[124] SERS has the added complication of reproducibility in the enhancing substrates; for example molecules can adsorb at different orientations, which may result in the appearance of different Raman bands in the spectra, or of band broadening.

Another factor in SERS reproducibility in colloids is in the aggregation of the colloids.[63,140] SERS enhancements from aggregated colloids are larger than for those of individual colloids, though control is important for the aggregation steps so as to avoid time-dependent results or precipitation from solution. A stable solution of small colloidal aggregates is considered an ideal system.[63] The most widespread method for obtaining colloid aggregation is through the addition of a salt as an aggregating agent. For Lee & Meisel colloids, the addition of 10 mM KCl to the solution has been found to result in a stable solution with good SERS activity.[141] The use of halide ions such as Cl$^-$ as aggregation agents are also thought to provide anion-enhancement effects as well as

providing colloid aggregation.[63,142,143]

Signals generated by Raman measurements are proportional to concentration, meaning that direct calibration plots should be obtainable. Irreproducibility due to factors such as were mentioned above can be a serious issue for SERS, and is a major issue for quantitative measurements using this technique.

3.5 Internal standardisation using Rhodamine dyes

One method to address the reproducibility issues is to use an internal standard of constant concentration, and use this to normalise that of the compound being investigated.[124] Rhodamine 6G and Rhodamine B were used to investigate this; the structure and SERS spectra of both dyes are shown in Figure 3.14.

(a)

Rhodamine B

(b)

Rhodamine 6G

(c)
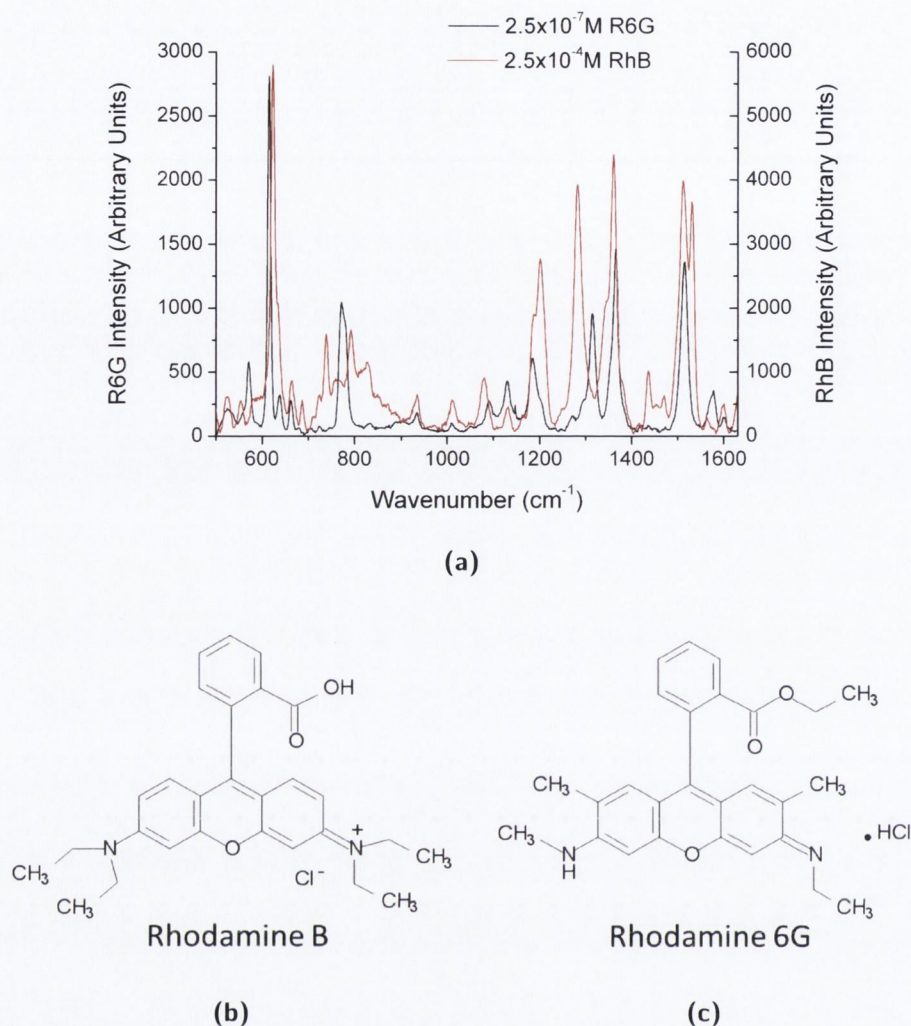
Figure 3.14: (a)Comparison between the SERS spectra of Rhodamine 6G (R6G) and Rhodamine B (RhB). (b) & (c) show the chemical structure of both dyes.

The SERS response of Rhodamine B was found to be much less than for Rhodamine 6G; similar concentrations of the two compounds were found to show a several-fold difference in signal intensity. This is due to steric hindrance on the Rhodamine B molecule, due to the positions of the nitrogen atoms, giving it a lower binding affinity to the silver surface. A range of concentrations of Rhodamine B were prepared from $0.5 - 2.5^{-4}$ M, with 10 SERS scans being taken of each and the spectral peaks at 1281 cm^{-1} being integrated to give the peak areas. These values were then plotted against the respective concentrations, and two separate analyses were conducted, using the same sets of solutions.
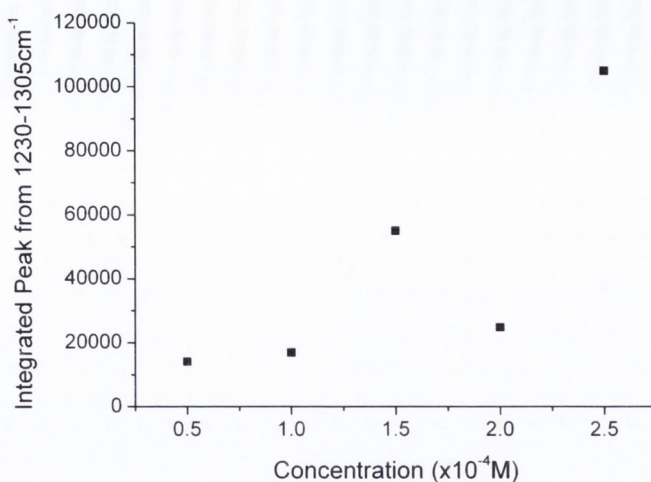
(a)
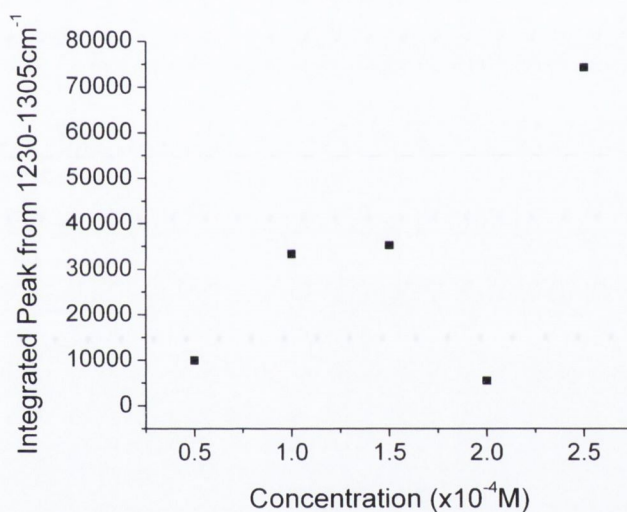
(b)

Figure 3.15: The integrated 1281 cm^{-1} peaks plotted against a range of Rhodamine B concentrations from $0.5 - 2.5^{-4}$ M. Two sets of data (a) and (b) were taken. The %RSD for each data point was less than 20%.

The concentration curves in Figure 3.15(a) and (b) do not show a linear trend, with the 2×10^{-4} M data point particularly offset. Similar concentrations of Rhodamine B were again prepared, including 2.5×10^{-7} M Rhodamine 6G as an internal standard. While the two compounds are quite similar in terms of their molecular structure, there are a few differences in their vibrational Raman modes. The most prominent are the strong bands at 770 and 1313 cm^{-1} for Rhodamine 6G, which are absent in Rhodamine B, and

the 1281 cm^{-1} band for Rhodamine B, which is absent in Rhodamine 6G. There is also a double peak at about 1500 cm^{-1} for Rhodamine B, while there is only a single peak here for the Rhodamine 6G. These differences in the spectra offer the opportunity to normalise one set of data with respect to the other. In terms of internal standardisation this means keeping one of the compound's concentrations constant whilst varying the other, before using the data obtained from the standard to normalise that of the variable. The benefit of this sort of setup is that any variance in data due to external factors (i.e. not concentration) can be somewhat compensated for, if the standard responds in the same way to these variances.[144] Using two similar compounds is useful because they should respond similarly to external conditions.

When adding a concentration of 2.5×10^{-7} M Rhodamine 6G to the same concentration range as studied before for the Rhodamine B, it was found that the peaks for the former species could be seen amongst the more prominent Rhodamine B peaks. The following three graphs show the full spectra and also magnifications of certain wavenumber ranges.
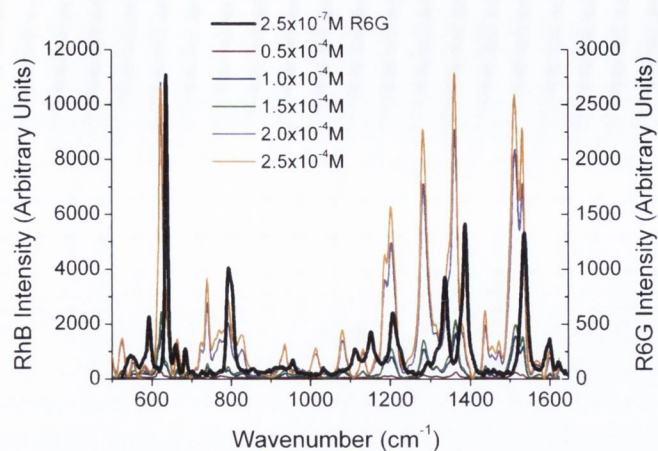
(a)
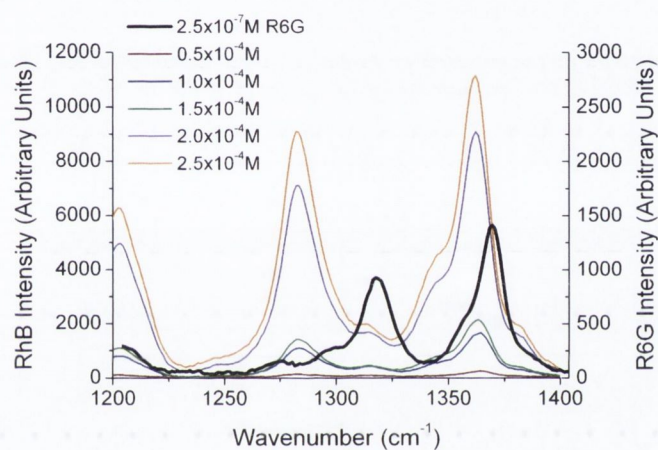
(b)
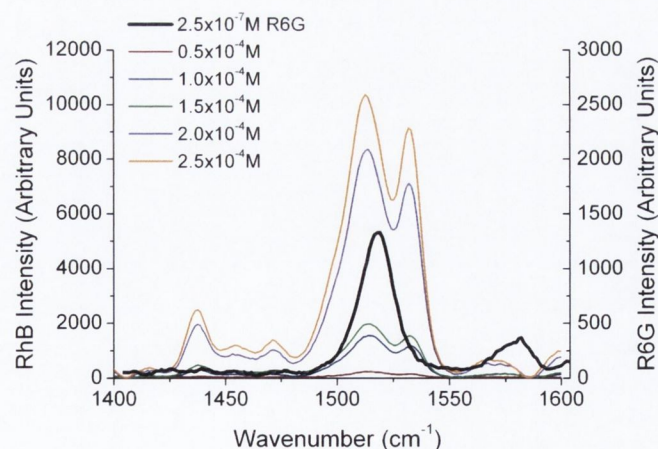
(c)

Figure 3.16: (a) Spectra from 500 to 1625 cm^{-1} showing 2.5×10^{-7} M Rhodamine 6G against spectra of mixed Rhodamine samples where the Rhodamine B concentration was varied from $0.5 - 2.5^{-4}$ M with Rhodamine 6G kept constant at 2.5×10^{-7} M. (b) shows a magnification of the spectra from 1200 to 1400 cm^{-1} and (c) shows the spectra from 1400 to 1600 cm^{-1}.

Observing these differences in the spectra it was decided to use the 1281 cm^{-1} Rhodamine B peak and the 1321 cm^{-1} Rhodamine 6G peak for one set of normalisation data. A second set was taken from the ratio of the Rhodamine B double peak intensities at 1512 cm^{-1} and 1532 cm^{-1}; with the Rhodamine 6G only displaying the lower wavenumber peak of this double it was expected that the ratio would change with decreasing Rhodamine B concentration. The results of the normalisation data are shown in Figure 3.17.
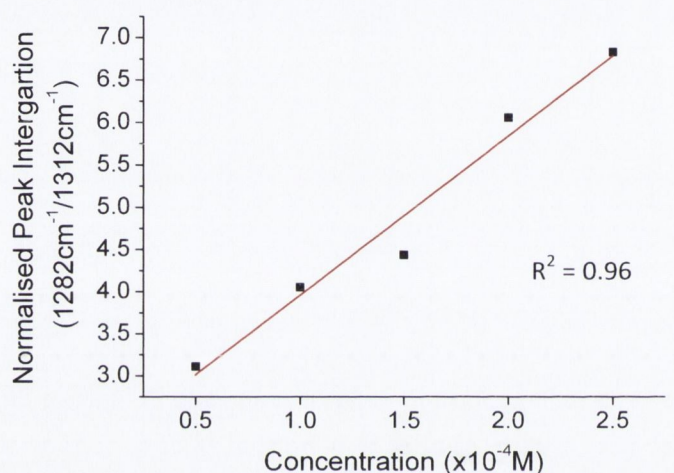
(a)
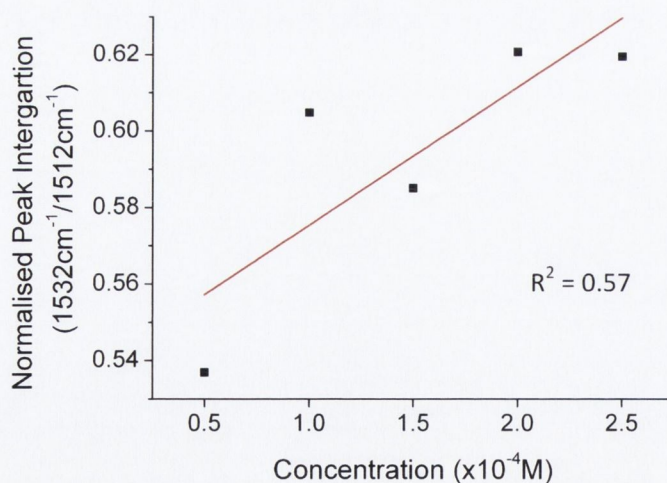
(b)

Figure 3.17: Normalised peaks comparing the integrated Rhodamine B and Rhodamine 6G peaks in the mixed solution. (a) shows the 1282cm^{-1} Rhodamine B peak divided by the 1312cm^{-1} Rhodamine 6G peak while (b) shows the 1532cm^{-1} Rhodamine B peak divided by the 1512cm^{-1} one.

The data plotted in Figure 3.17 shows the normalising process involving the 1282 cm^{-1} and the 1312 cm^{-1} peaks to be the more successful, with a reasonably linear relationship, and displaying an R^2 value of 0.96. In comparison the R^2 value for the normalisation involving the 1532 cm^{-1} and 1512 cm^{-1} peak is 0.57.

It is interesting to note the good linearity shown using the first normalisation data set, particularly as the original data included a very low value in the case of the 2.0×10^{-4} M concentration of Rhodamine B. The process was repeated using the same solutions, with the R^2 values working out at 0.9 and 0.88 for the same normalisation protocols.
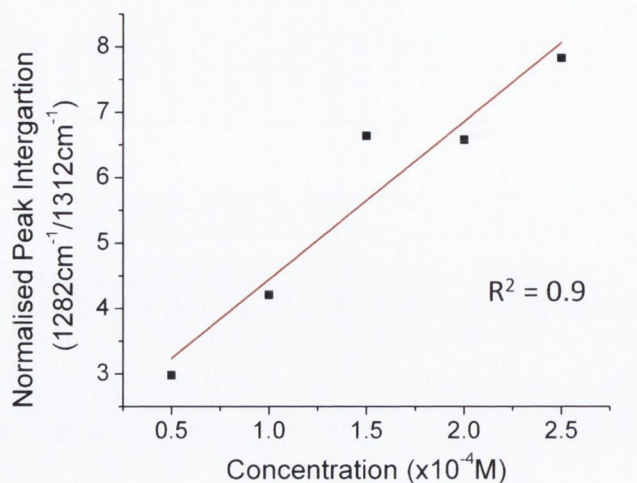
(a)
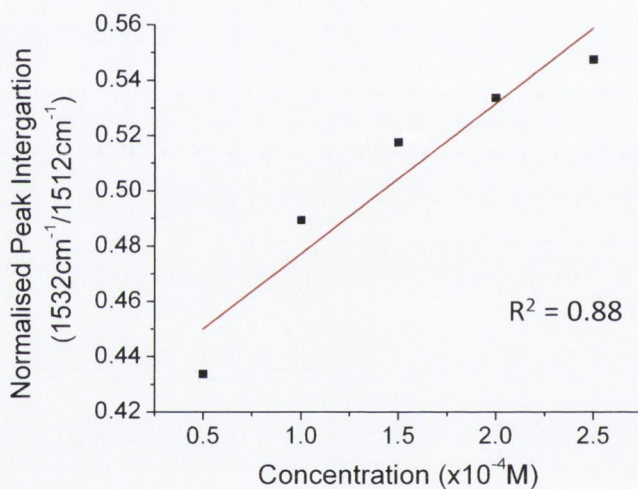
(b)

Figure 3.18: Normalised peaks comparing the integrated Rhodamine B and Rhodamine 6G peaks in the mixed solution. (a) shows the $1282 cm^{-1}$ Rhodamine B peak divided by the $1312 cm^{-1}$ Rhodamine 6G peak while (b) shows the $1532 cm^{-1}$ Rhodamine B peak divided by the $1512 cm^{-1}$ one.

3.6 Investigation of quantitative pterin SERS

Quantitative analysis of two pterin species was carried out using a series of mixed concentrations in varying ratios, with the aim of using internal standardisation for quantita-

tion. This analysis was initially carried out using a solution of aggregated silver colloids and 532 excitation. Solutions were prepared of xanthopterin and isoxanthopterin in a 1 : 1 ratio with the aggregates before a droplet of 6μL was deposited onto a glass microslide, with a suitable aggregate being located using the CCD viewfinder on the instrument. The 532 nm laser was used in the case of these experiments as it performed better than the 633 nm laser, due to both the inherent relationship between wavelength (λ) and scattering intensity (I_{scat}) where $I_{scat} = 1/\lambda^4$ and to resonance Raman contributions obtained by using an excitation wavelength closer to the pterin absorption transitions.[145]

One of the great advantages of Raman spectroscopy is its ability to offer information on the molecular structure of a compound. The fine-structure of the spectral data can differentiate between molecules with highly similar structures. Xanthopterin and isoxanthopterin are structural isomers, differing only by the orientation of their pyramidine unit, but despite this structural similarity they do exhibit quite different properties, particularly in their fluorescence characteristics, and SERS is also capable of differentiating between the two compounds.

3.6.1 Variation in pterin SERS signals

The SERS intensity of isoxanthopterin was investigated with respect to concentration, working from 2.5×10^{-4} M through to 2.5×10^{-7} M. In the spectra shown in Figure 3.19 it can be seen that the intensity of the isoxanthopterin peaks generally decrease with concentration, but the relationship is not linear.
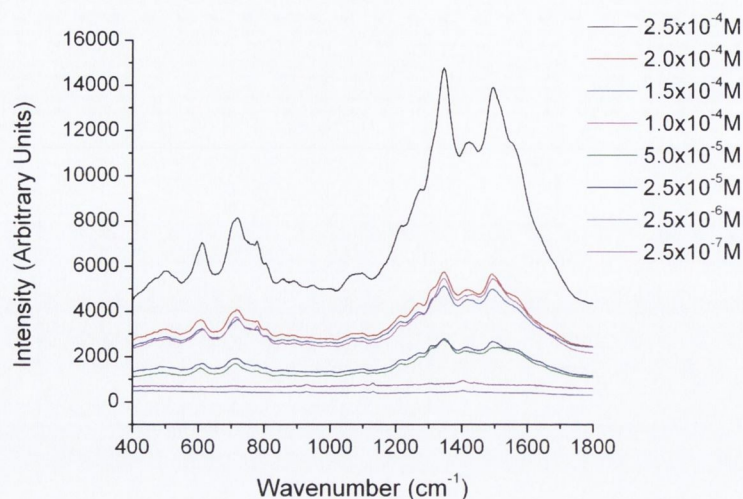
Figure 3.19: SERS spectra of 2.5×10^{-4} M - 2.5×10^{-7} M isoxanthopterin at 532 nm excitation and 5 s exposure time with 5 accumulations.

The spectra in Figure 3.19 were obtained using a five-second exposure with five accumulations in order to reduce noise in the spectra. The colloids were aggregated using 10 mM NaCl and spectra were taken for three different aggregates within the solutions before averaging. Xanthopterin SERS spectra were also taken and are presented in Figure 3.20(a) from 2.5×10^{-4} M down to 2.5×10^{-8} M.
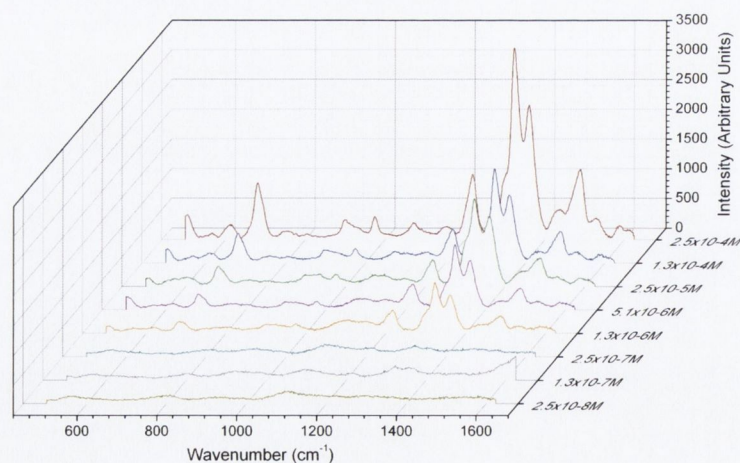
Figure 3.20: SERS spectra of 2.5×10^{-4} M - 2.5×10^{-8} M xanthopterin at 532 nm excitation and 5 s exposure time.

The SERS intensity for xanthopterin decreases with concentration in Figure 3.20, with

each spectrum in this case the average of ten spectra taken from a 6 μL droplet.

A normalisation process was investigated for the two pterins mixed together in solution, based on the ratios in which the two are mixed.[146] Because of their similar chemical structure the two pterins should respond similarly to any variations in experimental conditions, and should represent similar adsorption characteristics.[144]

In order to investigate the potential of simultaneous xanthopterin and isoxanthopterin detection, mixtures of different ratios of the two substances were examined. In Figure 3.21 spectra are shown for the isoxanthopterin and the xanthopterin separately, as well as for the 1 : 1 ratio mix of the two compounds (Each was present at a concentration of 5×10^{-5} M).
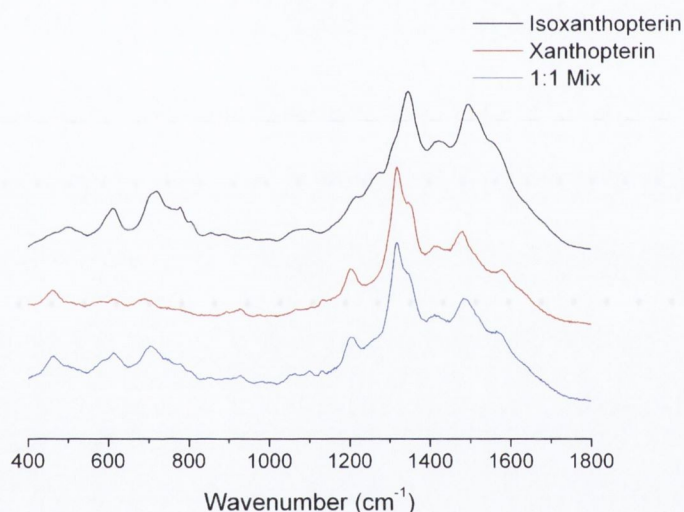
Figure 3.21: SERS spectra of 5×10^{-5} M isoxanthopterin, xanthopterin and a mixture of the two at a 1 : 1 ratio. All spectra were taken at 532 nm and a 5 s exposure time.

In this figure the data has been manipulated for presentation purposes, with each of the spectra normalised to make them the same height, and each separated out from each other. Raw data is presented in Appendix E.5. For this reason the y-axis for SERS intensity has been omitted as the figure is solely for comparison of the spectra.

There are a number of differences between the two pterin spectra. Working from left to right, the group of peaks between 400 and 800 cm^{-1}, attributed to skeletal vibrations,[58] are in differing ratios for each of the molecules. The main group of peaks between 1000

and 1600 cm^{-1} are quite different, with the isoxanthopterin showing fewer observable features, and moreover, the xanthopterin spectrum has a greater range of peaks from which to deduce information. For example, the peak at 1200 cm^{-1} is absent from the isoxanthopterin spectrum.

For the spectrum of the mixed solutions features of both pterins can be observed, which is further elaborated in Figure 3.22, where the data is composed of a set of ratios ranging from 5:1 in favour of xanthopterin to 5:1 in favour of isoxanthopterin. In each case one ratio unit corresponds to a concentration of 5×10^{-5} M. One way of looking at this is to consider that either the xanthopterin or the isoxanthopterin is being used as an internal standard to the other one, and while many of the band energies lie in similar regions, there are sufficient difference in the spectra for potential normalisation information.
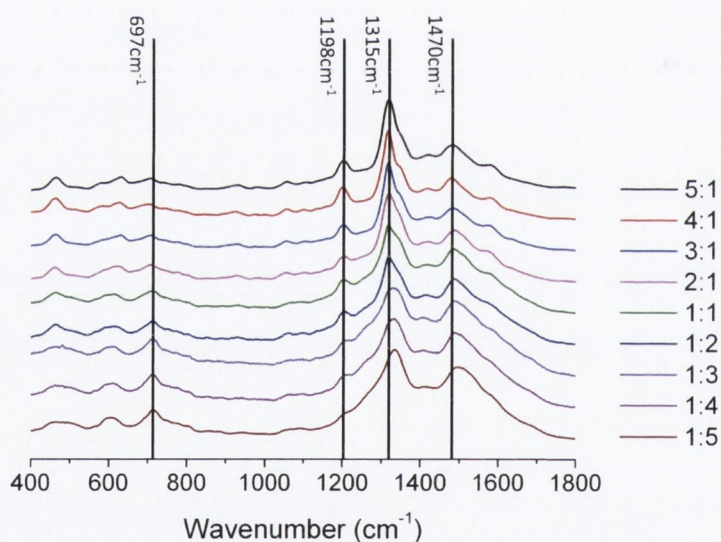
Figure 3.22: SERS spectra for a range of pterin mixtures, at differing ratios of xanthopterin : isoxanthopterin.

The data represented in Figure 3.22 was again modified for presentation purposes; in reality the absolute intensities from one sample to the next varied, but from the representation shown there are some useful changes that can be of use, such as the decreases in the peaks at 1315 cm^{-1} and 1198 cm^{-1} with increasing isoxanthopterin presence, and an increase in the peak at 697 cm^{-1}.

Four SERS spectra were taken of each of the pterin mixture concentration ratios, and using the raw data of the spectra, the peak areas for the 697, 1198, 1315 and 1470 cm^{-1} peaks were all calculated through integration. The ratio of the 1315 cm^{-1} peak area when compared to the 1470 cm^{-1} peak generally decreases with increased isoxanthopterin presence, as does that of the peak area of the 1198 cm^{-1} peak relative to the 697 cm^{-1} peak. Both of these relationships are plotted in Figure 3.23(a) and (b) respectively, while combining these two plots, by multiplying the two sets of data, results in the plot in Figure 3.23(c), which shows an increased linearity as shown by the R^2 value of almost 0.9.
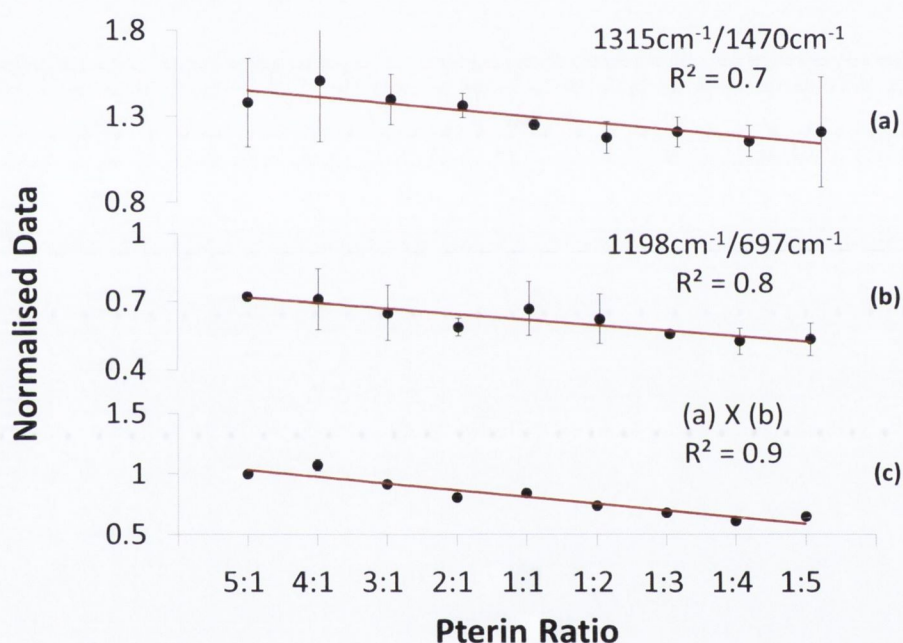
Figure 3.23: (a) shows the ratio of the peak area of the 1315 cm^{-1} peak relative to the 1470 cm^{-1} peak. (b) shows the ratio of the 1198 cm^{-1} peak to the 697 cm^{-1} peak. Both of these plots decrease in a linear fashion, and when the data from each is combined (multiplied) the linearity increases, as is displayed in graph (c). n=4 for the original data sets.

While this analysis shows the differences between the two species, more quantitative analysis could be provided by greater control of the aggregation procedure and analysis could be performed by more sophisticated techniques such as multivariate analysis.

3.7   SERS of xanthopterin using stainless steel wells.

Stainless steel wells were prepared, according to Ryder et. al,[147] as this platform should help to reduce surface evaporation and contamination. The material, stainless steel 316L grade was obtained from Impact Ireland Metals before holes were drilled according to the schematic in Figure 3.24. A photo of the finished wells is also shown. The wells were cleaned using isopropanol and rinsed thoroughly with Millipore water before use.
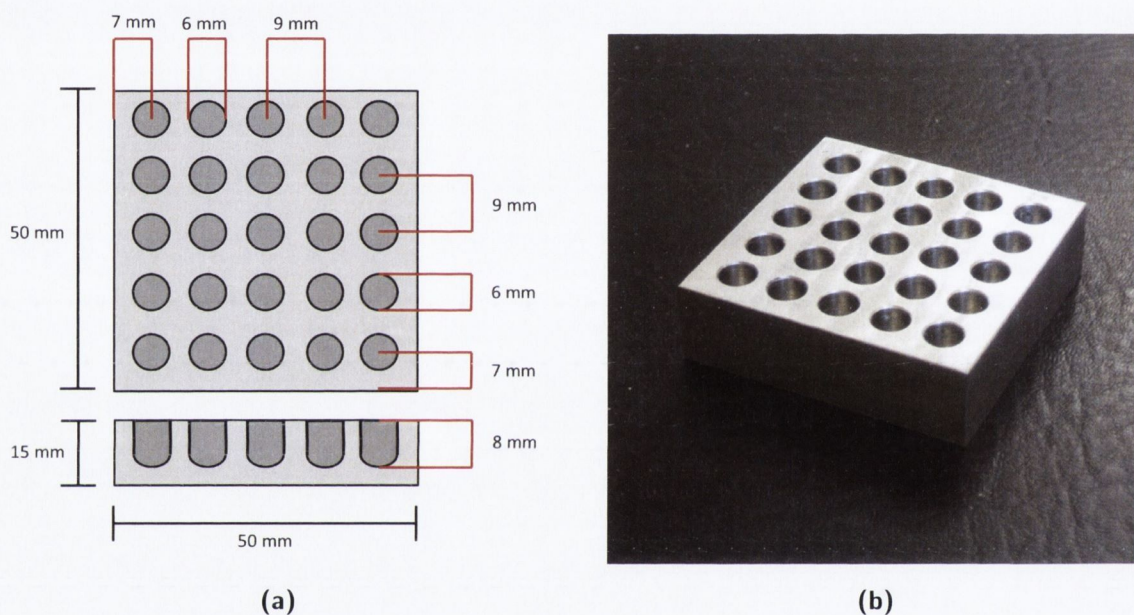

Figure 3.24: (a) A schematic of the stainless steel wells and (b) a photograph of the finished device.

Xanthopterin solutions of concentrations from 2 - 10 $\times 10^{-5}$ M were prepared for analysis using both the stainless steel wells and the glass microslides. The effects of aggregation were also investigated by preparing separate samples aggregated using 10 mM NaCl. A 633 nm laser was used in all instances.

Four sample sets for xanthopterin were thus prepared; 1) using aggregated colloids measured in the wells, 2) using unaggregated colloids in the wells, 3) using aggregated colloids measured on the slides and 4) using unaggregated colloids on the slides. The first of the these is considered in the first figure below in Figure 3.25. 100 μL of the sample was deposited into the well and ten spectra were taken, with the highest and lowest being removed, and the remaining eight being used for analysis. Only the

average spectra are shown in the following figures but all of the spectra can be found in Appendix E.
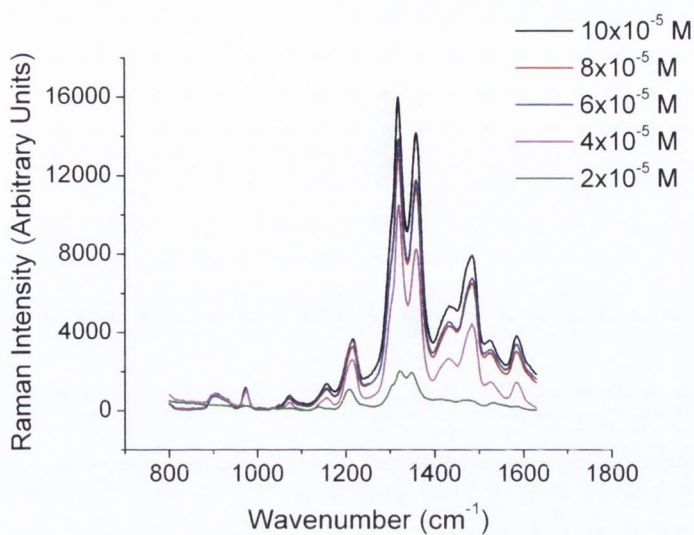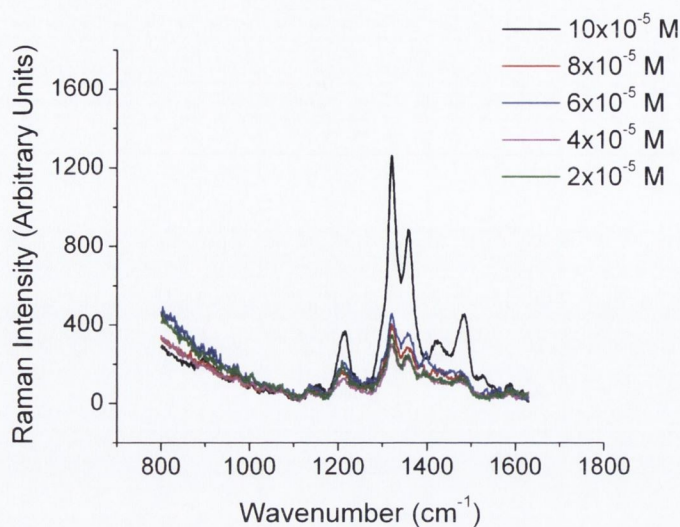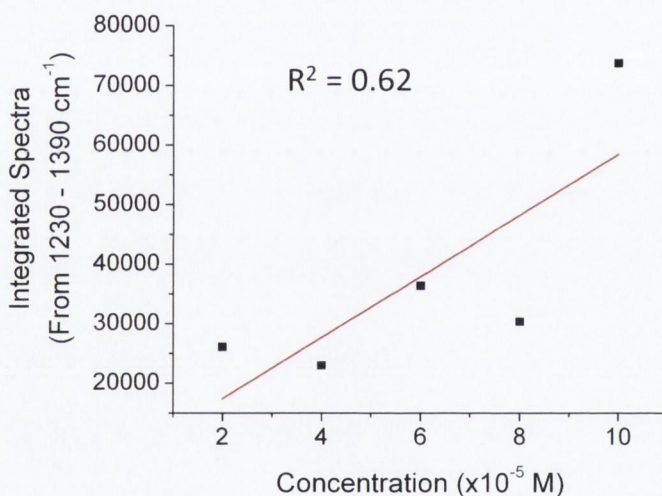

(a)
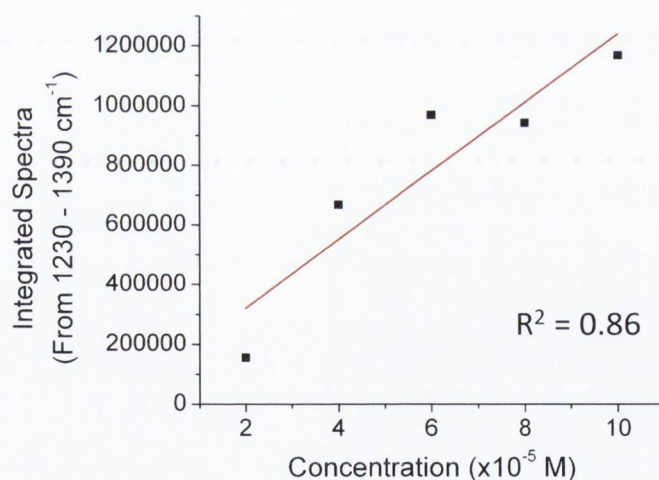
(b)

Figure 3.25: (a) Xanthopterin from 2 - 10 $\times 10^{-5}$ M measured in stainless steel wells with 10 mM NaCl aggregating agent, using a 633 nm laser and 20 s exposure time. (b) shows the integrated spectra between 1230 and 1390 cm^{-1} plotted against concentration.

The xanthopterin response using the wells was good, and the average spectra across the different concentrations showed a general linear response, with an R^2 of 0.86. The response according to the lack of aggregating agent was also investigated in the wells, with these spectra shown in Figure 3.26.

(a)

(b)

Figure 3.26: (a) Xanthopterin from 2 - 10 $\times 10^{-5}$ M measured in stainless steel wells with no aggregating agent, using a 633 nm laser and 20 s exposure time. (b) shows the integrated spectra between 1230 and 1390 cm^{-1} plotted against concentration.

From the spectra shown in Figure 3.26 it can be observed that the response is much lower than that of the aggregated solutions. The linearity of the response is also much worse, with an R^2 value of only 0.62. The %RSD values were measured across the spectra taken for each xanthopterin concentration, with the results shown in the table in Figure 3.29. From this it can be seen that the reproducibility of the responses was far superior for the aggregated samples. These observations show much improved

sensitivity and reproducibility for aggregated colloids over non-aggregated colloids.

	%RSD				
Conc. (x10^{-5}M)	10	8	6	4	2
Wells - With NaCl	3.7	8.3	4.7	4.3	8.6
Wells - Without NaCl	7.5	16.8	19.2	14.4	13.1

Figure 3.27: Comparison of the %RSD values for each of the xanthopterin concentrations, with and without the additional aggregating agent. The spectra for the aggregated samples are shown in Figures E.6 to E.10 and those for the unaggregated samples are shown in Figures E.11 to E.15.

Droplets deposited onto the glass microslides were also investigated for comparison with the wells. The average spectra obtained for the aggregated colloids are shown in Figure 3.28.
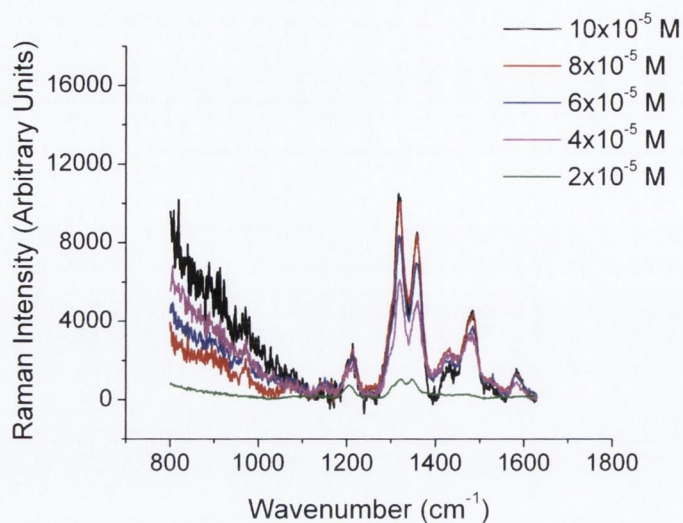
(a)
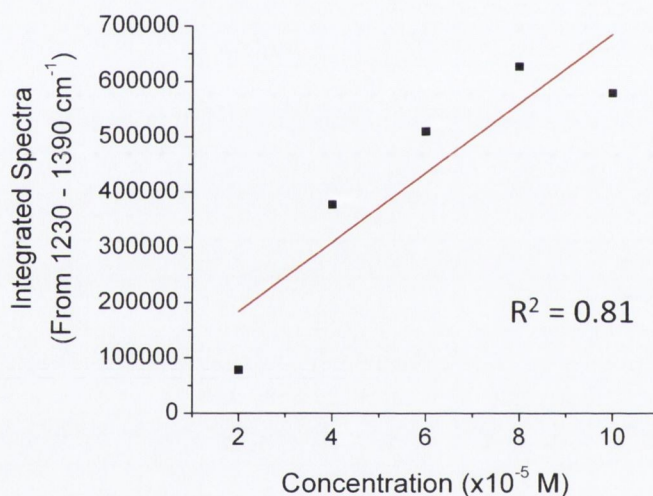
(b)

Figure 3.28: (a) Xanthopterin from 2 - 10 $\times 10^{-5}$ M measured on glass microslides with 10 mM NaCl aggregating agent, using a 633 nm laser and 20 s exposure time. (b) shows the integrated spectra between 1230 and 1390 cm^{-1} plotted against concentration.

From these spectra it can be observed that the responses and linearity with concentration are lower than those obtained when using the wells. The %RSD for the slides was also much worse than for the wells, as can be seen in the table in Figure 3.25.

	%RSD				
Conc. (x10⁻⁵M)	10	8	6	4	2
Wells - With NaCl	3.7	8.3	4.7	4.3	8.6
Slides - With NaCl	5.9	25.7	24.8	22.6	22.4

Figure 3.29: Comparison of %RSD values for each of the xanthopterin concentrations, using both the stainless steel wells and the glass microslide. The spectra for the wells are shown in Figures E.6 to E.10 and those for the microslide are shown in Figures E.16 to E.20.

The non-aggregated samples were also investigated using the glass microslides but no appreciable signal was obtained for using this method of analysis. From this it can be concluded that using the stainless steel wells is the superior method of analysis, in terms of signal response and in terms of reproducibility. Unfortunately the study could not be repeated due to subsequent issues with the Raman laser.

3.8 Conclusions

Colloid reproducibility was investigated through the preparation and analysis of five colloid batches, with distinct variability observed in the response across these batches. This was not investigated using aggregated colloids though. Analysis of droplet evaporation found the SERS signal to increase markedly over the course of half an hour as the droplet volume decreased and the analyte concentration increased. However, over the first five minutes of this measurement the SERS variations were observed to be consistent with the %RSD for the given colloid batch.

In order to obtain concentration dependent molecular detection normalisation techniques were investigated using Rhodamine dyes and pterins. Rhodamine 6G was used as an internal standard for Rhodamine B, with the results showing increased linearity with spectral normalisation. Relative concentrations of xanthopterin and isoxanthopterin were investigated in mixed pterin solutions, with the resulting SERS spectra being used to create normalised data that yielded a somewhat linear relationship over a large relative range.

The effects of aggregation and of the use of stainless steel wells over glass microslides

were finally considered. The response using the wells was found to be superior to that of the slides, both in signal obtained and in reproducibility. Similarly, aggregation was found to dramatically increase the quality of the obtained signals, showing that the use of aggregated colloids and a well-plate setup to be advantageous for effective SERS analysis.

4

Nanostructured Substrates for SERS

In this chapter silver nanoparticle films prepared using electron beam evaporation (EBE) and pulsed laser deposition (PLD) will be discussed with respect to their SERS responses. EBE was carried out on a Temescal FC-2000 system in a clean room environment in the CRANN institute, with deposition at a rate of 0.1 Å/sec. Two varieties of PLD film were prepared, using two different laser systems; a 248 nm KrF laser with a pulse width of 25 ns and an 800 nm solid state Ti-Sapphire laser with a pulse width of 130 fs. This preparation was carried out by Inam Mirza in James Lunney's photonics group.[148] The morphological and SERS-dependent effects of annealing were also investigated on the films.[149]

4.1 SERS using metal nanoparticle films

Nanoparticle films with feature sizes in the range of $1 - 100$ nm is an area that has received attention due to their novel magnetic, catalytic and optical properties.[150] Moreover, the ability to selectively control the optical properties of such nanoparticle films is an area of particular relevance regarding SERS.[151] Techniques such as nanosphere lithography (NSL) have shown the ability to carefully control the size, height and shape of nanoparticles films,[152] and with this is provided the opportunity to prepare more ordered and reproducible SERS-active films.[153,154] Using this technique has also resulted in the development of metal film over nanoparticle (MFON) substrates,[155,156]

91

that demonstrate good stability over time.[157] Many reviews exist of metal films for SERS applications[125,158,159] and several other fabrication techniques that have been investigated regarding their plasmonic and SERS properties include films prepared by e-beam lithography,[160,161] Langmuir-Blodgett,[162,163] electrochemical deposition,[164,165] micro-contact printing[166] and self assembly.[167] A wide range of shapes and structures have been developed and examined for their SERS activity, including nanowires,[168] nanopillar arrays,[169] nanostars[170] and even nanotrees.[171]

The adsorption properties of the investigated materials are also a consideration in substrate preparation; investigations into SERS for protein analysis have found changes in signal due to conformational or orientation changes on the metal surface.[172] Issues such as protein multiadsorption and irreproducible nanoparticle aggregation on bare metal substrates have also led to the development of media such as silica-silver core-shell substrates, which show good SERS activity.[173]

Pulsed laser deposition (PLD) is a relatively simple and effective fabrication technique for nanoparticle films. In PLD, a high power pulsed laser is focused on the target surface. For a sufficiently high laser fluence (for metals about 1 J/cm^2), each laser pulse vaporises, or ablates, a small amount of material which expands rapidly from the target surface in vacuum. This ablated material provides the deposition flux for thin film growth, and the morphology and size of nanoparticles can be controlled by the number of laser pulses. Nanostructured Ag substrates prepared using PLD in a background gas have proved to be a promising candidate for SERS,[174–177] and have previously performed well in comparison with commercial substrates.[178]

Both nanosecond (ns) and femtosecond (fs) pulsed lasers can be used for the ablation of a metal target and fabrication of a nanoparticle film but the physical mechanism is different in both cases. In the nanosecond case there is much evidence that the nanoparticle growth takes place on the substrate by surface diffusion of the deposited material,[179,180] while in the femtosecond case it has been observed by studying the dynamics of the laser ablation plume using fast photography and optical emission spectroscopy that the nanoparticles are present in the ablation plume,[181] which can later be collected on the solid substrate.

Film evaporation is another relatively straightforward technique, which has also been investigated regarding its SERS properties.[182,183] Subsequent annealing at temperatures ranging up to 350°C was found to improve the SERS performance of some films,[184,185] and increased stability of the SERS response over time was also discovered,[186] while in other cases it was found to reduce performance.[187]

4.2 Comparison of PLD films

PLD films were prepared on glass microslides to varying thicknesses and then subsequently investigated regarding their SERS responses. Both nanosecond PLD (nsPLD) and femtosecond PLD (fsPLD) films were prepared at up to 10 nm thickness. They were generally used for SERS analysis as soon after preparation as possible, but any overnight storage was carried out in an argon-filled vacuum environment.

4.2.1 UV/Vis properties of PLD films with respect to film thickness

The UV/Vis spectra for the fsPLD films from $1 - 10$ nm thickness were taken, while those from $5 - 10$ nm for the nsPLD films were obtained. SERS activity below 5 nm thickness was found to be low so focus was generally applied to films of 5 nm plus. The UV/Vis data for these films is shown in Figure 4.1.
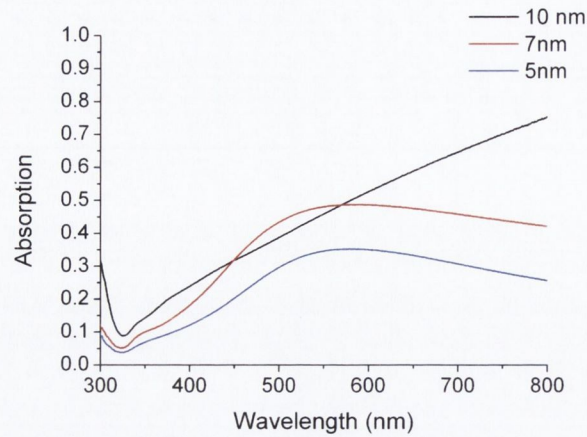
(a)
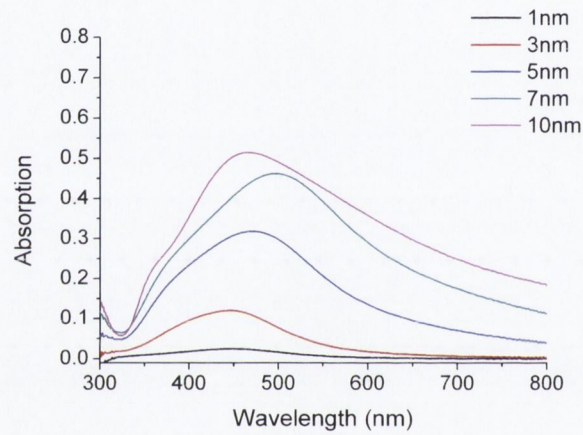
(b)

Figure 4.1: (a) shows the UV/Vis spectra for 5 − 10 nm nsPLD films and (b) shows the 1 − 10 nm fsPLD films.

From these spectra it is clear that there is an increase in the light absorption (and also an increase in the contibution from reflection) as the thickness of silver increases, as expected. For the fsPLD films the spectra are all relatively broad and there is also a shift in the peak maximum towards the IR region, except for the 10 nm film, which shifts back towards about 450 nm again. In the nsPLD films there is also a change in the 10 nm film, with a dramatic broadening of the UV absorption profile.

4.2.2 Scanning transition electron microscopy of nsPLD films

The $5 - 10$ nm nsPLD films were also imaged using scanning transmission electron microscopy (STEM), shown in Figure 4.2.

(a)

(b)

(c)
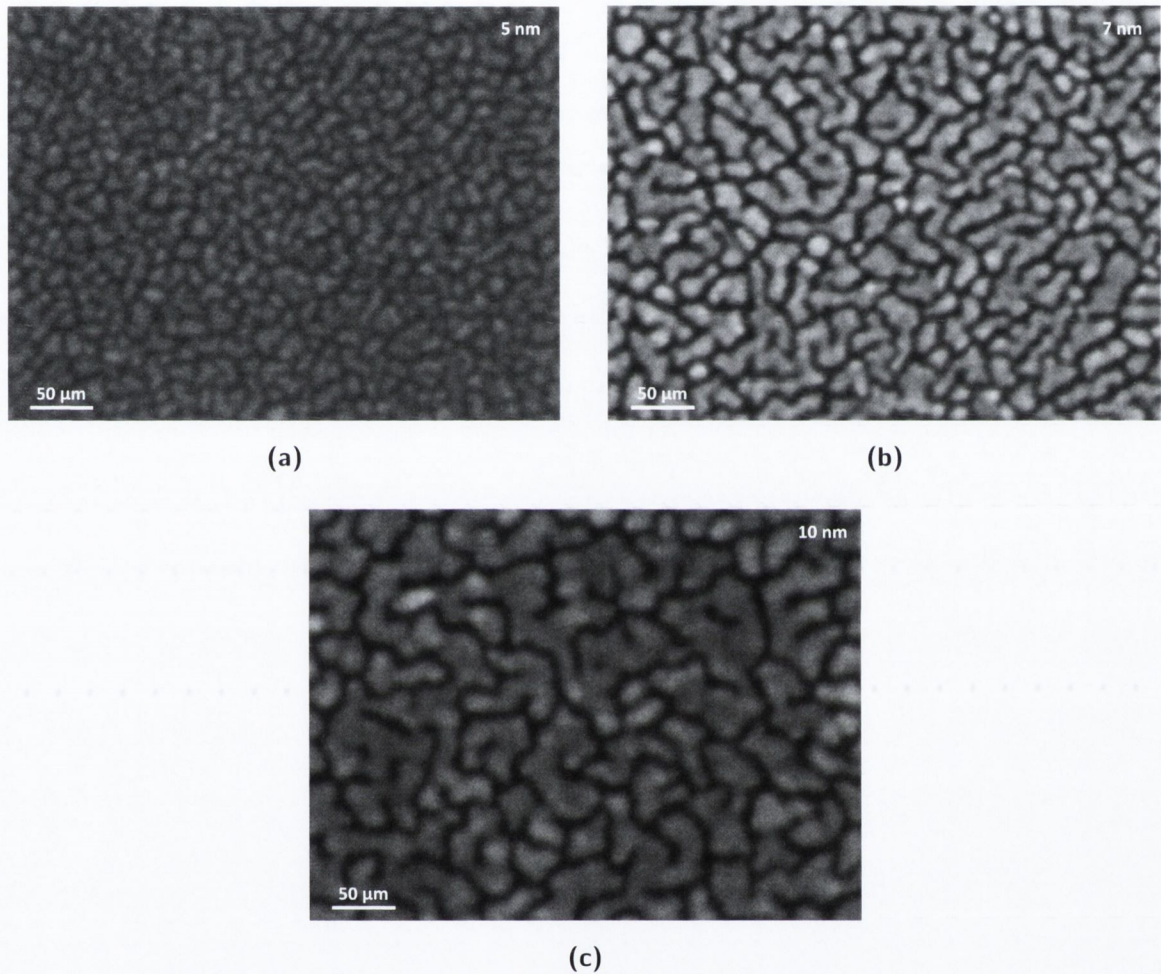
Figure 4.2: STEM images of (a) a 5 nm, (b) a 7 nm and (c) a 10 nm nsPLD film.

From the STEM images the general observation is that there is an increase in the size of the nanoparticulate structures from 5 nm through to 10 nm. As the film thickness is increased the nanoparticle features appear to become more fused, leaving these larger structures, and smaller gaps in between the structures.

4.2.3 SERS response of PLD films of varying thickness

As previous mentioned, the SERS response of the lower thicknesses yielded a small to negligible signal; appreciable SERS responses were only observed from 5 nm thickness upwards for both the nsPLD and the fsPLD films. 6 μL droplets were deposited onto the films and spectra were taken from the interface between the liquid and the film. The hydrophobicity of the liquid on the films was also observed to increase with the film thickness, which is shown in Appendix G. In terms of the SERS response regarding thicknesses, a gradual increase in signal was observed from 5 nm through to 10 nm for both of the preparation methods. The spectra taken for a 4.2×10^{-4} M solution of benzotriazole on each of the 3 films are shown in Figure 4.3.

From these spectra a couple of things can be observed. Firstly, the average signal strength does increase gradually with increasing film thickness and secondly, the relative error also increases with thickness.
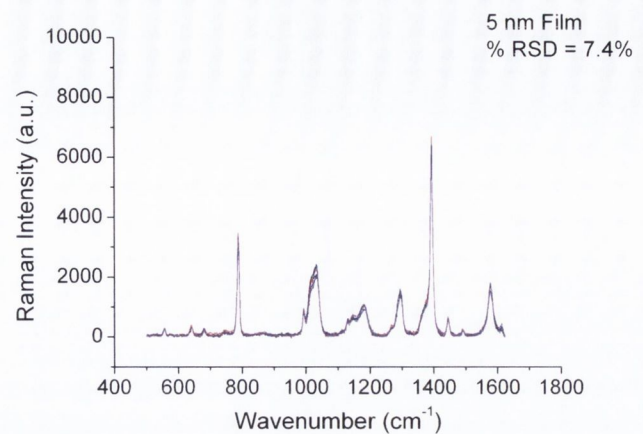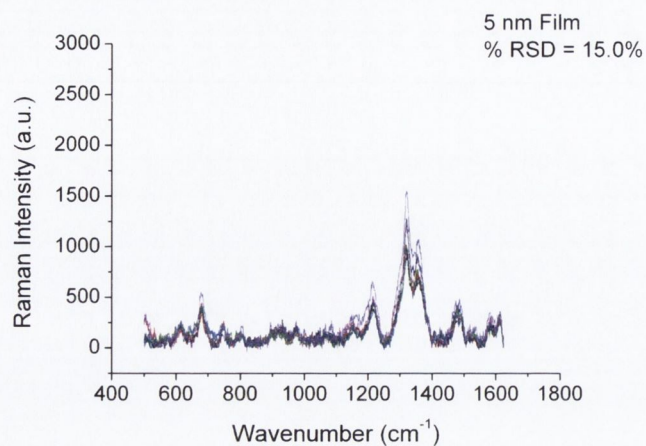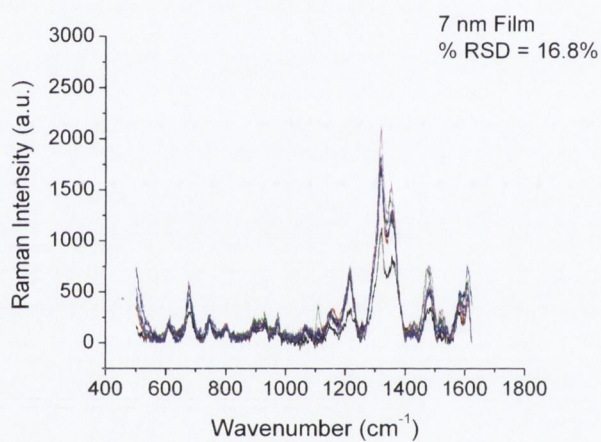
(a)
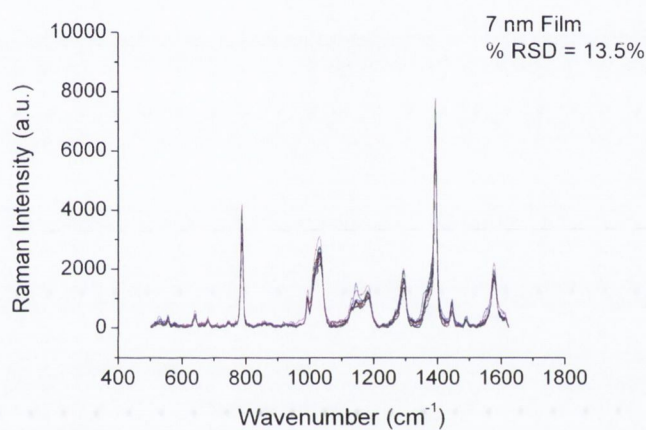
(b)
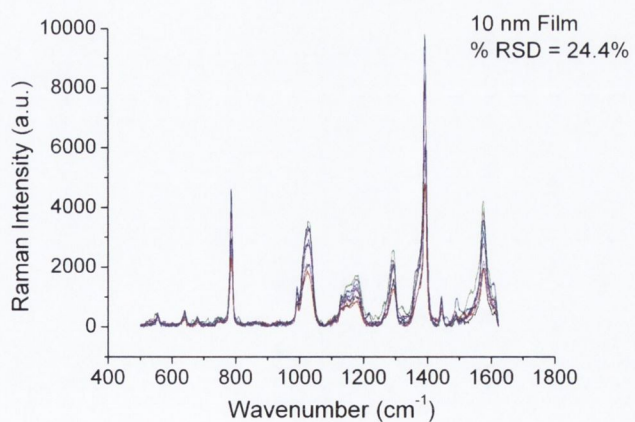
(c)

Figure 4.3: A set of eight spectra of a 4.2×10^{-4} M benzotriazole solution on a (a) 5 nm, (b) 7 nm and (c) 10 nm nsPLD film. All spectra were taken at 633 nm with a 5 s exposure time.

This initial exploratory work was also carried out for each of the films using a 2.4×10^{-4}
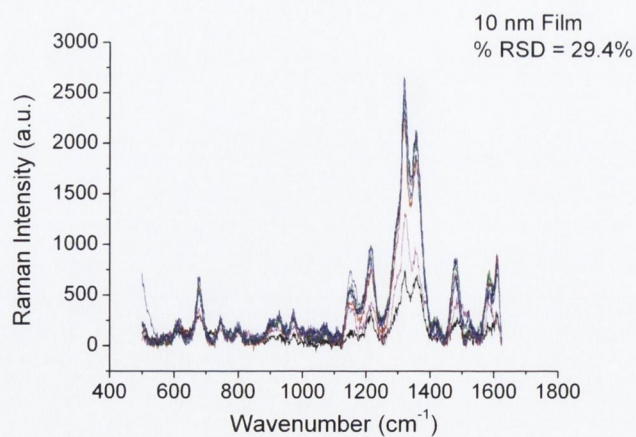
M solution of xanthopterin, the spectra of which can be seen in Figure 4.4.

(a)

(b)

(c)

Figure 4.4: A set of eight spectra of a 2.4×10^{-4} M xanthopterin solution on a (a) 5 nm, (b) 7 nm and (c) 10 nm nsPLD film. All spectra were taken at 633 nm with a 10 s exposure time.

A similar trend is observed in Figure 4.4, with an increase in both the obtained SERS response and of the relative error as the film thickness increases.

4.2.4 Comparison of ns and fsPLD films

Using 10 nm films prepared both by the nanosecond system and by the femtosecond system, SERS measurements were made to compare the two. Structural differences can be observed from STEM images, as shown in Figure 4.5.

(a)
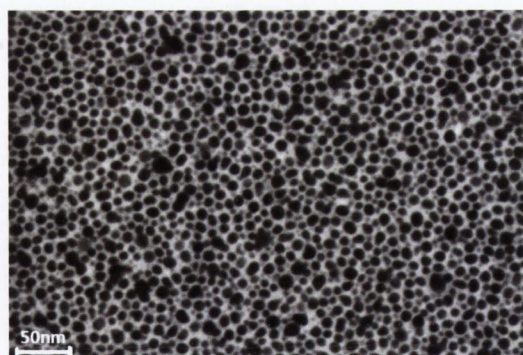
(b)

Figure 4.5: STEM images of (a) a 10 nm nsPLD film and (b) a 10 nm fsPLD film.

In both cases the films are nanostructured, with the nsPLD film showing a percolated structure due to nucleation and coalescence between small nanoparticles into single units, while the fsPLD film shows more spherically-shaped nanoparticles with diameters in the range of about $5 - 15$ nm. Comparison of the SERS response of the two films was performed using a 4.2×10^{-4} M solution of benzotriazole, with the resultant spectra shown in Figure 4.6.
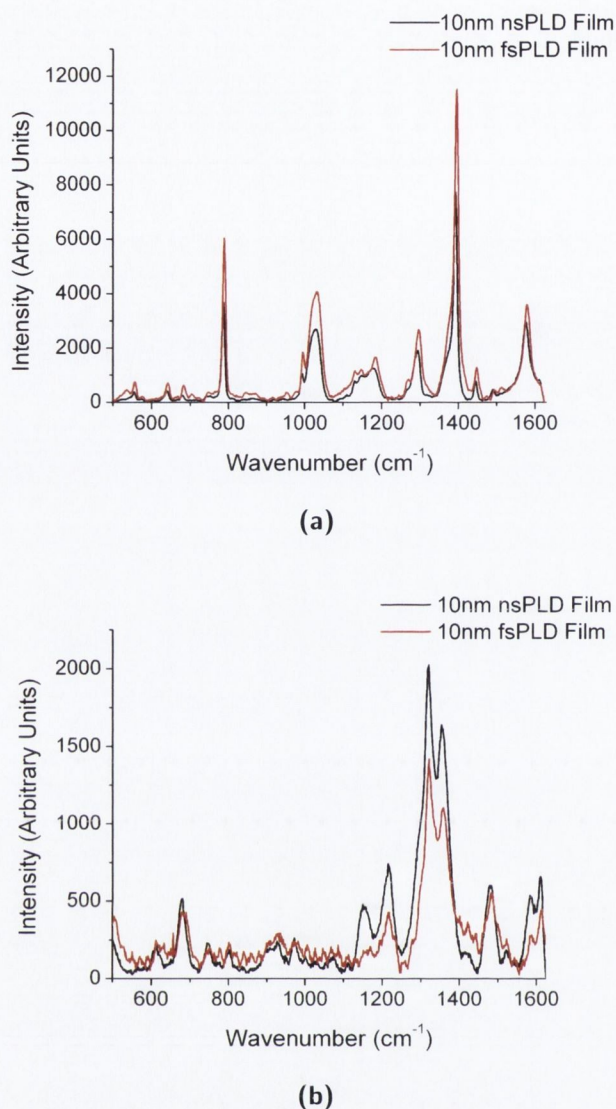
(a)

(b)

Figure 4.6: The average SERS spectra on the 10 nm nsPLD and fsPLD films, taken at 633 nm and compiled from eight spectra, of (a) 4.2×10^{-4} M benzotriazole at 5 s exposure time and (b) 2.4×10^{-4} M xanthopterin, taken at 10 s exposure.

Benzotriazole has a better SERS response than xanthopterin due to its triazole group, which has a strong affinity to bind to gold or silver substrates.[63] In this analysis the film prepared using the femtosecond laser was observed to perform better for the benzotriazole but worse for the xanthopterin. The %RSD values for the benzotriazole were measured at 18.6% and 24.5% for the femtosecond and nanosecond films respectively and 21.3% and 33.0% for the xanthopterin. These figures show the femtosecond film to perform slightly better in both cases. Due to issues with the femtosecond laser equipment this exploratory study could not be investigated further, though it would be

an interesting study for future work.

## 4.3 Analysis of annealed and non-annealed EBE and PLD films

The electron beam evaporated (EBE) silver films were prepared on glass microslides to a thickness of 10 nm, using a deposition rate of 0.1 Å/sec. 10 nm fsPLD films were also prepared and annealing was carried out at 400°C under forming gas (Ar:H$_2$) at 1 Torr. Characterisation was carried out by UV/Vis spectroscopy and atomic force microscopy (AFM).

4.3.1 UV/Vis spectra of the EBE films

Three EBE films were investigated as-prepared and a further three were annealed subsequent to investigation. The UV/Vis properties of each film are shown in Figure 4.7.
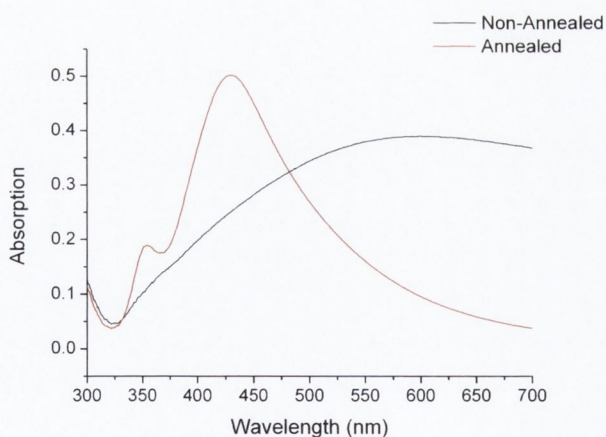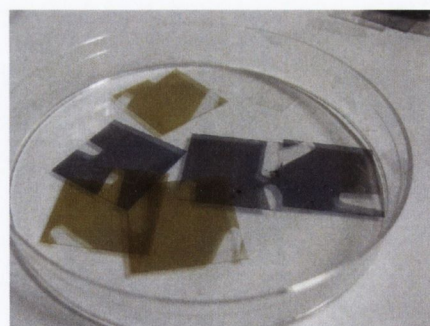
Figure 4.7: (a) shows the UV/Vis spectra for an as-prepared and an annealed 10 nm EBE films, while (b) shows a photograph of both films. (Grey = as-prepared and yellow = annealed)

The two films differed visually subsequent to annealing, with the as-prepared films showing a grey-purple colour and the annealed ones a yellow one. This alteration is

clearly reflected in the absorption properties of the EBE films with the as-prepared films showing a broad absorption band stretching towards the IR region of the spectrum and the annealed films showing a much narrower distribution, with a peak centred at about 420 nm.

4.3.2 Atomic Force Microscopy of the EBE films

AFM, measured using an MFP-3D Stand-Alone AFM from Asylum Research, was used to investigate the surface features of the EBE films, and in particular to any morphological or surface-roughness changes that occur due to the annealing process.

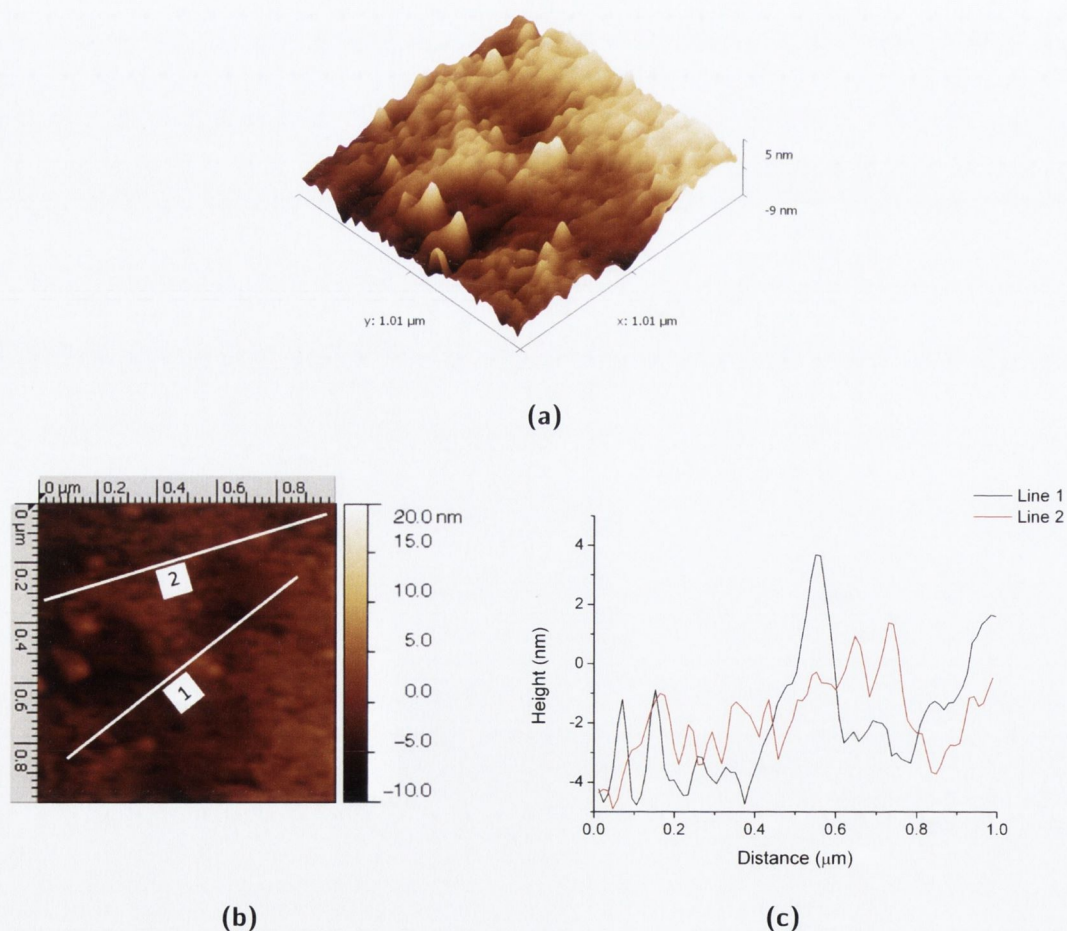The AFM data from a 1 μm^2 region of an as-prepared EBE film is shown in Figure 4.8.

Figure 4.8: A 1 μm^2 area of the as-prepared EBE film, showing (a) a 3D AFM map, (b) a 2D image with two lines that are subsequently plotted as the profiles in (c). Line 1 represents the black plot in (c) and Line 2 the red plot.

The 3D map in Figure 4.8(a) shows the surface profile of the region examined, with a number of small features, confined to sub-10 nm in height dimensions. The image in Figure 4.8(b) shows a 2D representation of this area, with two lines drawn onto it to examine the lateral profiles of the surface features. Line 1 was drawn to encompass the large, double-peaked feature in the centre of the examined area, which was found to measure about 200 nm laterally, though only about 5 nm vertically. Line 2 was drawn to encompass an area that held no larger features, and this showed narrower lateral features of between $50 - 100$ nm. Root mean squared (RMS) data is often used to represent the surface roughness of a material, and in the case of the area measured above this was found to be 2.30 nm.

AFM mapping of an annealed EBE film was also carried out, with data from a 1 μm^2 region shown in Figure 4.9

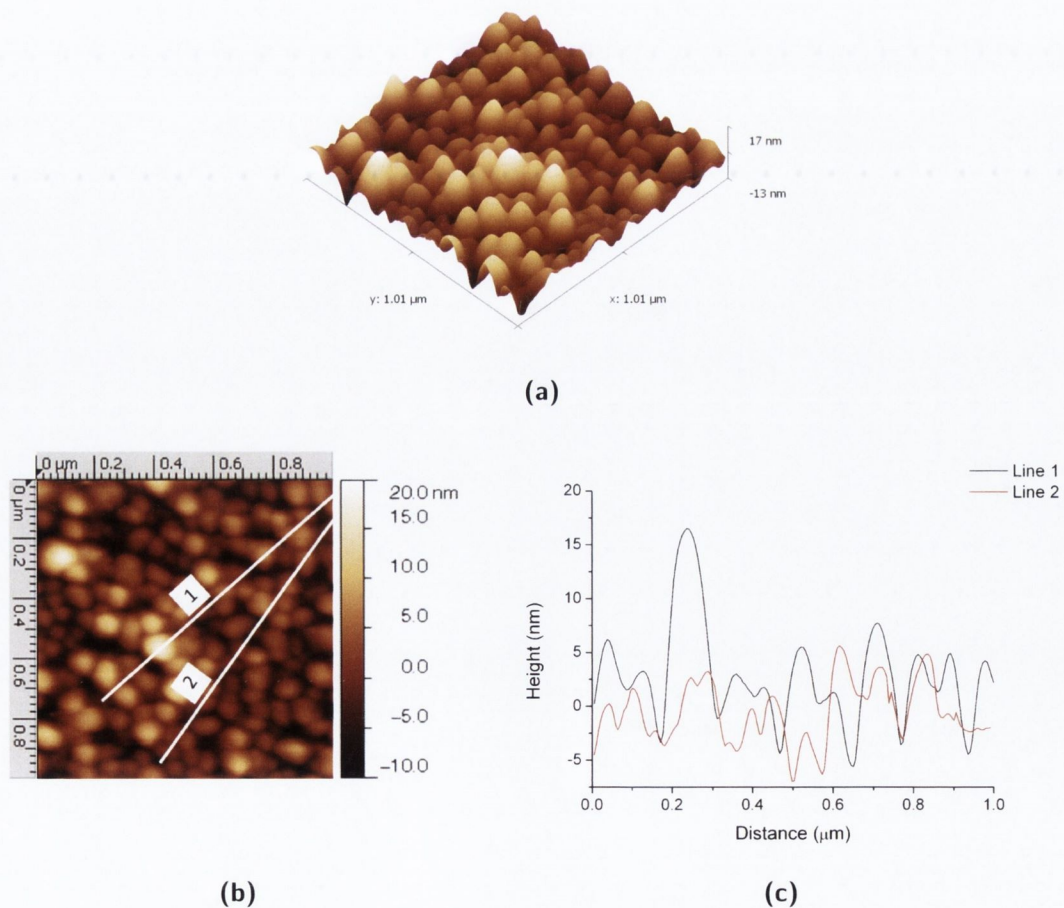**(a)**

(b)

(c)

Figure 4.9: A 1 μm^2 area of the annealed EBE film, showing (a) a 3D AFM map, (b) a 2D image with two lines that are subsequently plotted as the profiles in (c).

From the 3D map in Figure 4.9(a) the film surface is observed to show a greater array of nanoparticulate features than for the non-annealed film. The map shows quite an even distribution of features, while the Line 1 profile shown in Figure 4.9(c) shows the features to protrude from about $10 - 20$ nm from the film surface, with lateral dimensions of about 150 nm. The profile drawn by Line 2 shows the smaller features to protrude only a few nanometres, with smaller lateral dimensions of about $20 - 30$ nm. The RMS value for this surface was found to be 4.36 nm, and this rougher surface could be expected to provide a greater SERS enhancement.

4.3.3 UV/Vis spectra of the fsPLD films

The annealing process also affected the appearance and UV/Vis profiles of the PLD films, as can be seen in the photograph and spectra of the 7 nm fsPLD films shown in Figure 4.10.
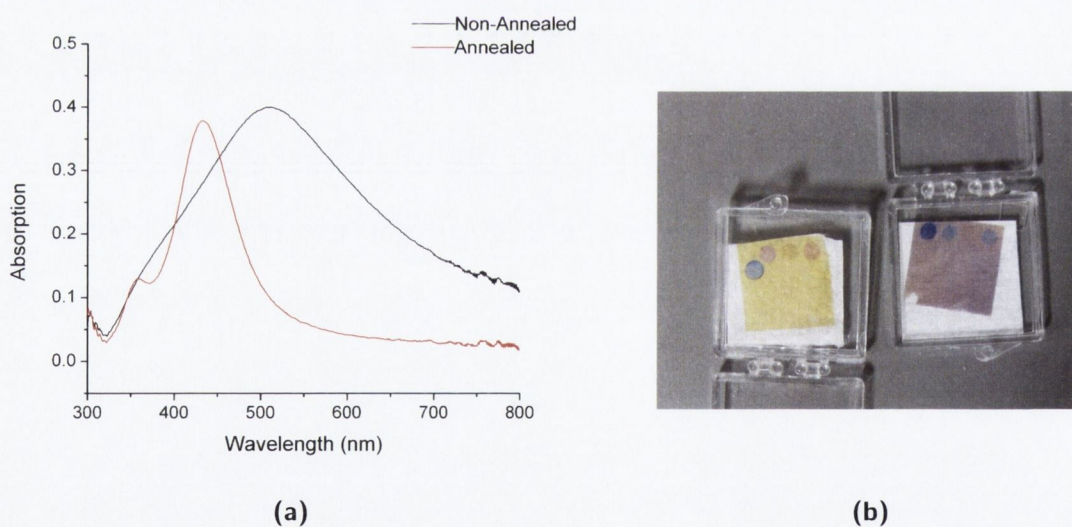

(a)   (b)

Figure 4.10: (a) The UV/Vis spectra of the as-prepared and annealed fsPLD films and (b) a photograph showing the two films. (Grey = as-prepared and yellow = annealed)

From Figure 4.10 a narrow absorption maximum is found to occur around the region of $410 - 420$ nm for the annealed film, which is similar to that observed for silver colloids and which may indicate that the feature sizes are equivalent. The as-prepared substrate was again found to possess a much broader absorption profile for both the nsPLD and the fsPLD films, although there is still an absorption maximum feature at around 525

nm. The films were also quite different in colouration, with the annealed films appearing yellow and the non-annealed films grey-purple.

4.3.4 AFM of as-prepared and annealed fsPLD Films

As-prepared and annealed 7 nm fsPLD films were also examined using AFM, taking a surface area of about 5 μm^2 and then magnifying to a 1 μm^2 region for a more resolved image of the surface profile. The images and data obtained from this are featured in Figure 4.11.
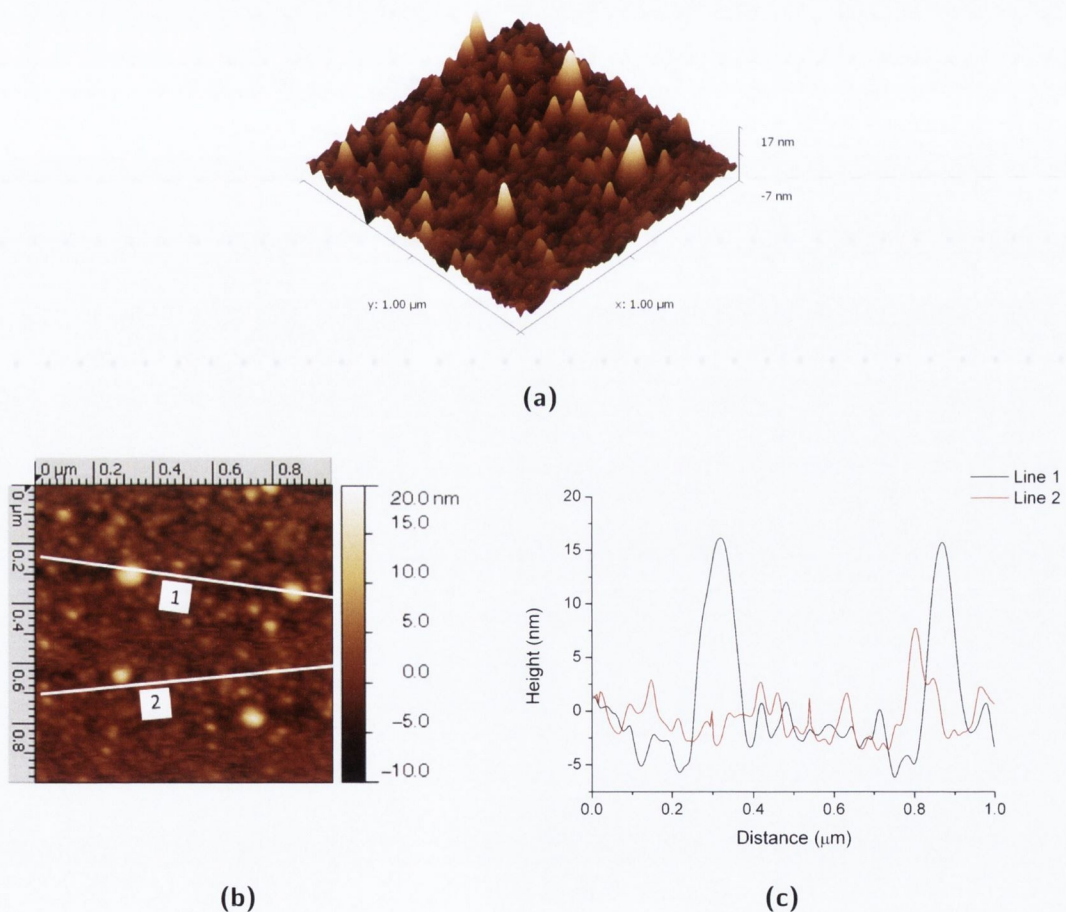

(a)

(b)

(c)

Figure 4.11: A 1 μm^2 area of the as-prepared fsPLD film, showing (a) a 3D AFM map, (b) a 2D image with two lines that are subsequently plotted as the profiles in (c).

In the case of the 3D representation shown in Figure 4.11(a), the surface appears to possess more nanoparticulate features than that found on the as-prepared EBE film in

Figure 4.8(a). The profile lines in Figure 4.11(c) show larger features on the order of about 15 − 20 nm vertically, and about 150 nm laterally, but the RMS value of 2.38 nm is similar to that observed for the as-prepared EBE film. The AFM data for the annealed substrate is shown in Figure 4.12.
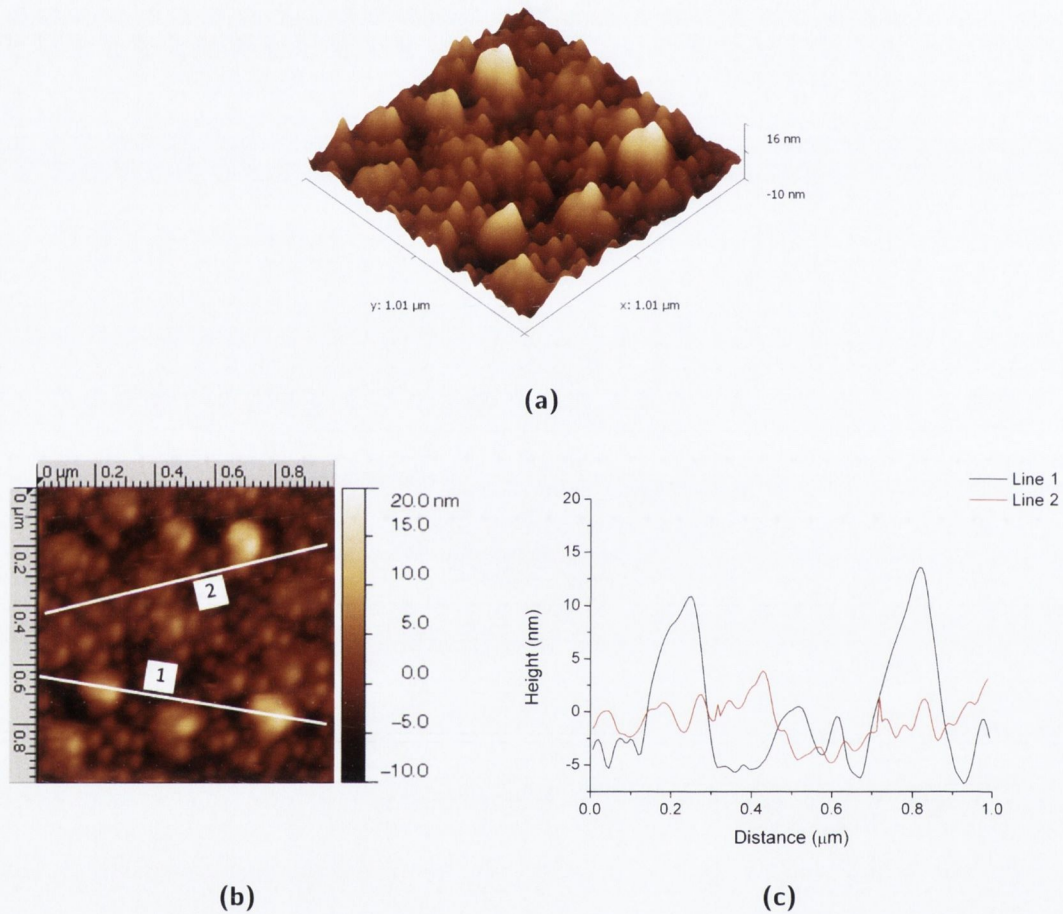

(a)

(b)

(c)

Figure 4.12: A 1 μm^2 area of the annealed fsPLD film, showing (a) a 3D AFM map, (b) a 2D image with two lines that are subsequently plotted as the profiles in (c).

Figure 4.12(a) shows a surface that possesses features that appear a little more rounded. The profiles displayed in Figure 4.12(c) show the larger features to consist of mainly the same height as those seen for the as-prepared substrate, though the lateral dimensions are a little wider at about 200 nm. The RMS value recorded for the annealed fsPLD film was 3.31 nm, a greater value than for the as-prepared film, but not as great as for the annealed EBE film. Line 2 shows the features in between the larger protrusions, and these appear broader than the equivalent measurement in Figure 4.11(c).

## 4.4 Investigation of the reproducibility of EBE and PLD films

In this section the SERS response of the various nanoparticle films will be considered, particularly regarding reproducible performance. 10 nm films prepared by EBE and nsPLD were used for this study; the fsPLD films were not investigated due to the femtosecond laser being out of operation at the time.

4.4.1 SERS response of EBE films

In this investigation six 10nm EBE films were prepared, with three of them being subsequently annealed. The UV/Vis profile of all of the films are shown in Figure 4.13
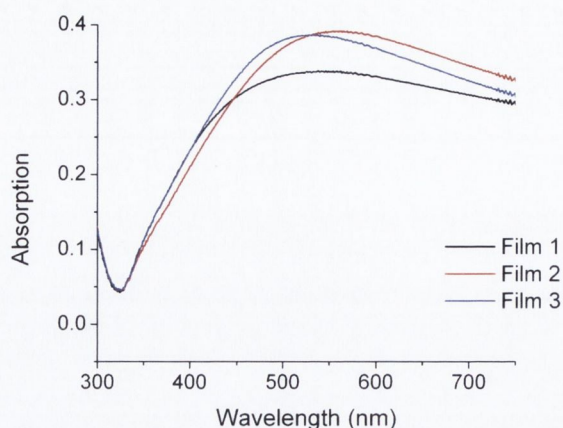
(a)
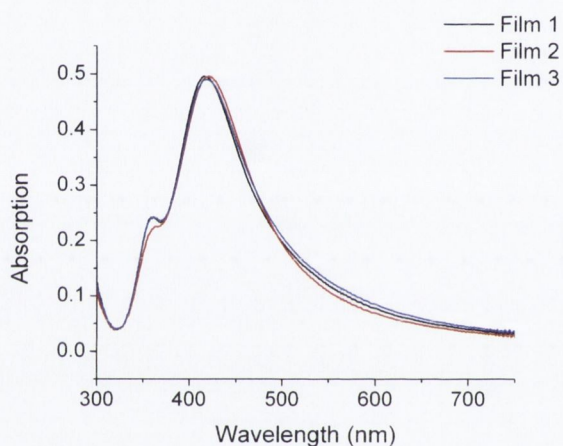
(b)

Figure 4.13: The UV/Vis spectra of (a) the three as-prepared EBE films and (b) the three annealed films.
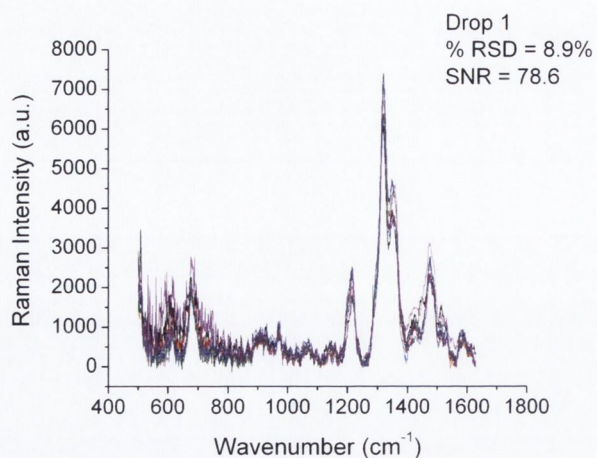
The three spectra in each case show the same general profile, with the annealed films displaying the expected narrowing to form a peak at about 420 nm. There are slight variations in the absorption profiles in each case, which are possibly due to size effects.

A solution of 2.5×10^{-4} M xanthopterin was used as the SERS probe, and three droplets were deposited on each film for measurement. Within each droplet 10 spectra were taken at an exposure time of 20 s, with the most intense and least intense spectra being removed from the data set to leave a 'best 8' set. These remaining spectra were integrated between 1270 and 1395 cm^{-1} for direct comparison of the %RSD values for each droplet. A value for the signal-to-noise ratio (SNR) was also calculated, which
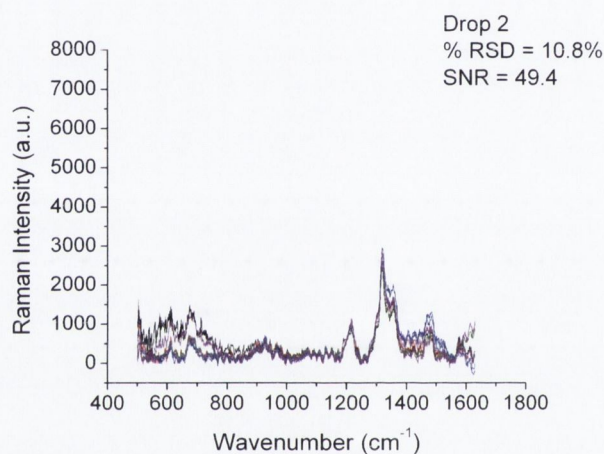
can be thought of as a figure-of-merit for the quality of a signal. This figure is a ratio of the true signal amplitude to the standard deviation of the noise, and for random fluctuations a general rule is that the standard deviation is approximately one-fifth of the peak-to-peak variations of the fluctuations.[188] For the xanthopterin SERS spectra the noise fluctuations were obtained by calculating the peak-to-peak variation for three baseline regions of the spectra where no signals were observed; the regions from 812-875 cm^{-1}, from 998-1031 cm^{-1} and from 1085-1118 cm^{-1}. The three values were then averaged to obtain a single peak-to-peak value to describe the noise fluctuations in a single spectrum. The standard deviation of the noise was then calculated by dividing this peak-to-peak value by five, as described above, and the SNR was then approximated by taking the ratio of the amplitude of the signal, i.e. the height of a specific peak, to this standard deviation value. The 1320 cm^{-1} peak of xanthopterin was used for the calculation of the SNR figures.

The eight spectra investigated for each of the three droplets on the first of the EBE films are shown in Figure 4.14(a) - (c).
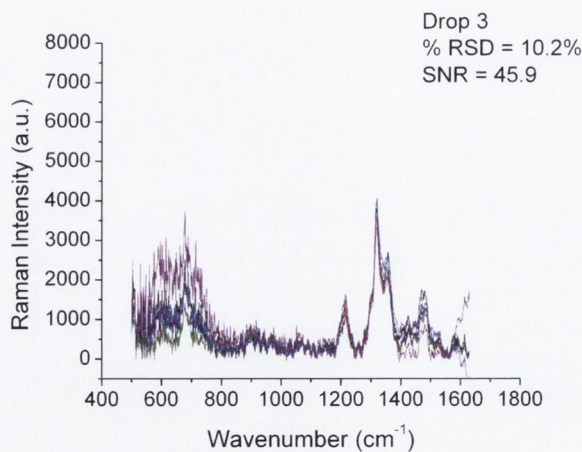
Figure 4.14: Three separate drops of a 1×10^{-4} M solution of xanthopterin were deposited on an as-prepared EBE film. Eight SERS spectra, taken using a 633 nm excitation and a 20 s exposure time, are shown for each drop in (a)-(c) respectively. The average %RSD and SNR are also shown for each set of data.

The first observation of the data shown in Figure 4.14 is that there is quite a bit of variation from droplet to droplet. The 1320 cm^{-1} peak intensity is greatest for the first droplet and drops off markedly for droplets 2 and 3, a feature that is consistent in the SNR values. The %RSD values are all around the 10% mark for the three droplets, though the variation in signal intensity over the three areas of the film examined are higher than desired.

The SERS response of the other two EBE films was also investigated with xanthopterin, with a summary of the %RSD and SNR data shown in the table below in Figure 4.15. The full spectra for these measurements are provided in the appendix.

| | Film 1 | | | Film 2 | | | Film 3 | | |
	Drop 1	Drop 2	Drop 3	Drop 1	Drop 2	Drop 3	Drop 1	Drop 2	Drop 3
%RSD	8.9	10.8	10.2	12.2	27.5	17.3	25.4	5.8	8.8
SNR	78.6	49.4	45.9	26.6	9.3	31.6	142.3	25.1	55.1

Figure 4.15: A summary of the %RSD and SNR values for xanthopterin for each of the three drops on the first unannnealed EBE film. The spectra for the second and third films are shown in Figure F.1 and Figure F.2.

The %RSD values for the droplets on the subsequent two films show quite a variation between droplets, and in some cases quite a variation within a single droplet. The SNR figures show similar levels of variation to those observed for the first droplet, namely that high variations are present across each of the films, suggesting a variable surface profile of films produced by this method.

The same investigation was also carried out using a solution of 1.8×10^{-5} M Rhodamine 6G as the SERS probe, which was again measured using the 633 nm laser source, and this time an exposure time of 3 s. A summary of the %RSD and SNR data is shown in the table below in Figure 4.16 and the spectra for each of the droplets are shown in the Appendix.

	Film 1			Film 2			Film 3		
	Drop 1	Drop 2	Drop 3	Drop 1	Drop 2	Drop 3	Drop 1	Drop 2	Drop 3
%RSD	11.5	10.3	22.7	9.1	8.1	19.1	10.6	17.3	13.5
SNR	70.9	33.2	58.8	38.9	39.5	76.3	163.2	112.4	123.5

Figure 4.16: A summary of the %RSD and SNR values for Rhodamine 6G for each of the three drops on the unannnealed EBE films. A 633 nm excitation and 3 second exposure time was used for the acquisition of this data. The spectra for the three films are shown in Figure F.3, Figure F.4 and Figure F.5.

The figures for the examination using Rhodamine 6G show a similar trend to those using xanthopterin, with the SNR varying to an undesired degree between films and between droplets deposited onto different areas on the same film. The %RSD values obtained were also similar to the xanthopterin analysis, with some of the droplets showing good spectral reproducibility and others showing variations of abour 20%.

Annealed EBE films were also investigated but all three showed a very poor response to xanthopterin, with only barely-observable signals obtained. Two of the films showed a reasonable response to droplets of Rhodamine 6G, and the droplets deposited on these films are summarised in Figure 4.17.

	Film 1			Film 3		
	Drop 1	Drop 2	Drop 3	Drop 1	Drop 2	Drop 3
%RSD	20.4	40.2	17.6	29.2	20.5	32.4
SNR	23.1	18.5	11.7	8.3	29.6	24.1

Figure 4.17: A summary of the %RSD and SNR values for Rhodamine 6G for each of the three drops on two of the annnealed EBE films. A 633 nm excitation and 3 second exposure time was used for the acquisition of this data. The spectra for the two films are shown in Figure F.6 and Figure F.7.

For these films both the SNR and %RSD values are very poor, showing little promise for the annealing of evaporated films in SERS analysis.

4.4.2 SERS response of nsPLD films

A similar investigation was performed using three 10 nm nsPLD films, the absorption profiles of which are shown in Figure 4.18.
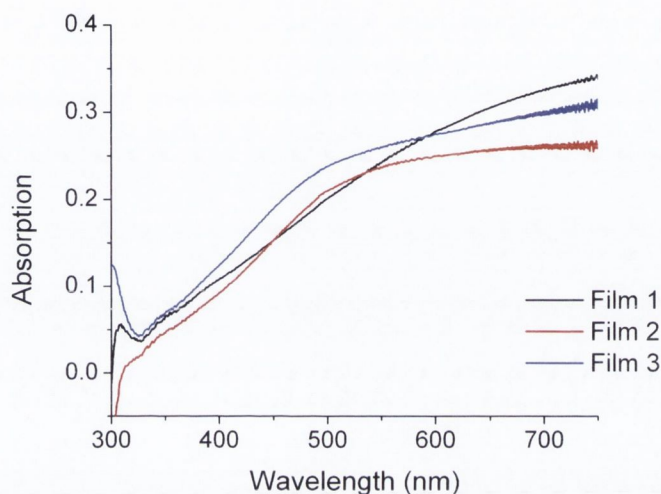

**Figure 4.18:** The UV/Vis spectra of the three nsPLD films.

From these absorption profiles, there is quite a bit of variation between the three films, with the first film showing a profile shifting towards the IR region of the spectrum. Regarding the SERS response of these films, three droplets of a 1×10^{-4} M solution of xanthopterin were again deposited onto each film. For the first film very little xanthopterin response was observed, though the second and third films each showed a response. The spectra in Figure 4.19 were taken from each of the three droplets deposited onto the second film, again obtained using a 20 s integration time and analysed according to their %RSD and SNR figures.
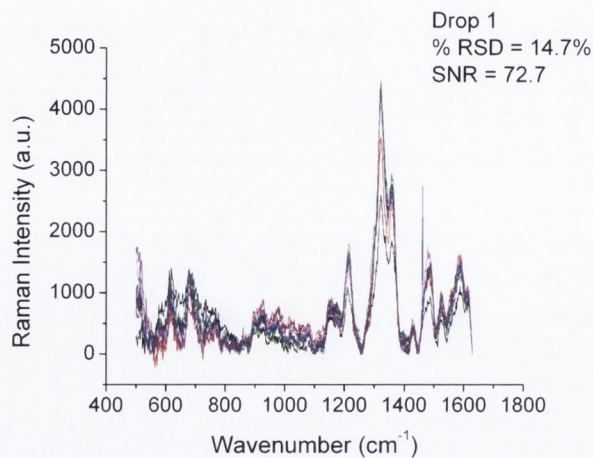
(a)
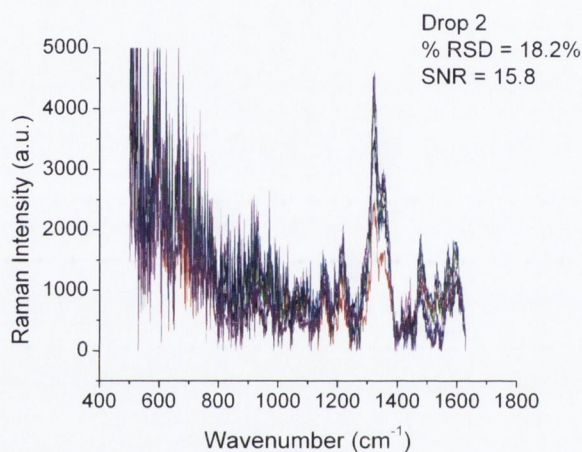
(b)
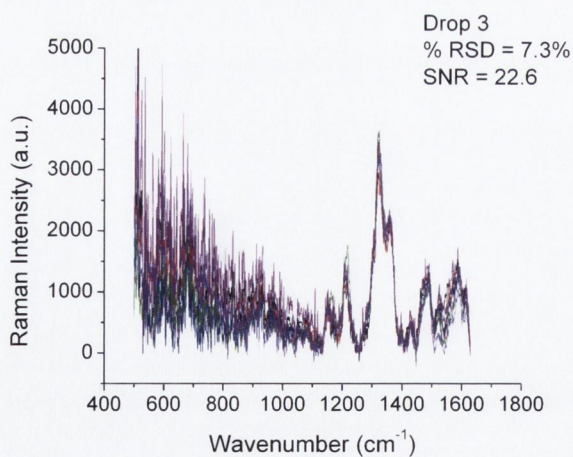
(c)

Figure 4.19: Three separate drops of a 1×10^{-4} M solution of xanthopterin were deposited onto a 10 nm nsPLD film. Eight SERS spectra, taken using a 633 nm excitation and a 20 s exposure time, are shown for each drop in (a)-(c) respectively. The average %RSD and SNR are also shown for each set of data.

114

From these spectra it is evident that the SNR varies from region to region on the PLD film; even though the majority of the absolute peak heights are observed at about 4000 a.u. for each droplet the SNR varies from 15.8 to 72.7. There is also much variability across the %RSD values obtained indicating that, like the EBE substrate, the PLD films are too unpredictable for quantitative SERS. The two films investigated using xanthopterin are summarised in the table below, and the spectra for the third PLD film are shown in Figure F.8.

	Film 2			Film 3		
	Drop 1	Drop 2	Drop 3	Drop 1	Drop 2	Drop 3
%RSD	14.7	18.2	7.3	13.0	14.9	19.8
SNR	72.7	15.8	22.6	14.7	27.7	48.5

Figure 4.20: A summary of the %RSD and SNR values for xanthopterin for each of the three drops on two of the nsPLD films. A 633 nm excitation and 20 second exposure time was used for the acquisition of this data. The spectra for the third film are shown in Figure F.8

From this summary it is also evident that there is variation between films, something that can also be observed from results using Rhodamine 6G as the probe. 633 nm laser excitation was again used for this investigation, with a 3 s exposure time, and a summary of the results can be seen in the table below with the spectra displayed in Figure F.9, Figure F.10 and Figure F.11.

|	Film 1			Film 2			Film 3		
	Drop 1	Drop 2	Drop 3	Drop 1	Drop 2	Drop 3	Drop 1	Drop 2	Drop 3
%RSD	4.5	6.4	5.3	9.8	8.5	7.2	6.0	6.8	10.4
SNR	55.6	48.3	80.9	112.9	74.0	70.6	53.0	55.5	56.3

Figure 4.21: A summary of the %RSD and SNR values for Rhodamine 6G for each of the three drops on the nsPLD films. A 633 nm excitation and 3 second exposure time was used for the acquisition of this data. The spectra for the three films are shown in Figure F.9, Figure F.10 and Figure F.11.

From the spectra and summary data presented in this section it can be observed from the SNR and %RSD figures that there is substantial variation within each individual droplet, and subsequently between different areas on individual films and between different films.

Quantitative analysis using the films would thus be unachievable without some form of standardisation. The ability to implement careful control over the homogeniety of the films surfaces could help to develop techniques for the preparation of SERS substrates of greater reproducibility using PLD and EBE.

### 4.4.3 Combined SERS response of PLD films with silver colloids

Solutions of 1.8×10^{-5} M Rhodamine 6G mixed with silver colloids were also prepared, in a 1-to-1 ratio of colloid-to-analyte solution. These solution were then deposited onto each of three nsPLD films, prepared separately from the films mentioned in the preceding section, and investigated for their SERS responses. A 0.1 s exposure time was used in this instance, instead of 3 s, to avoid saturation when using the colloids, and spectra were also taken of 1.8×10^{-5} M Rhodamine 6G without colloids for comparison. The spectra for the first three droplets of the Rhodamine 6G solution without colloids are shown in Figure 4.22 and those for the Rhodamine 6G solution with colloids in Figure 4.23.
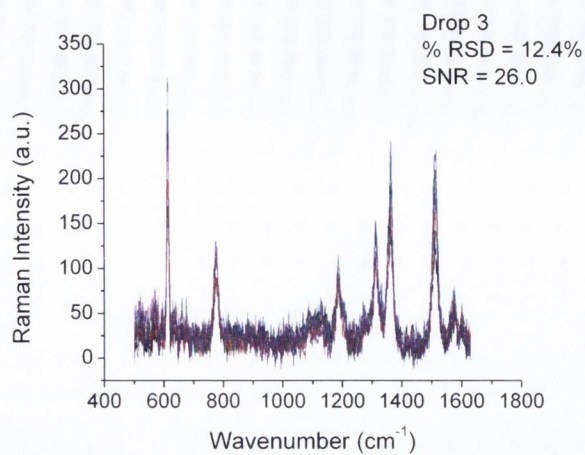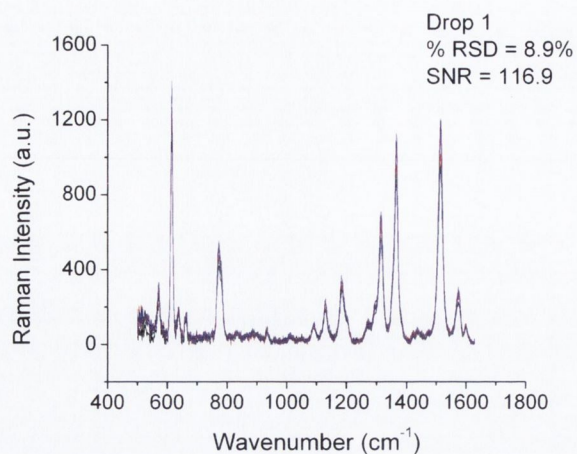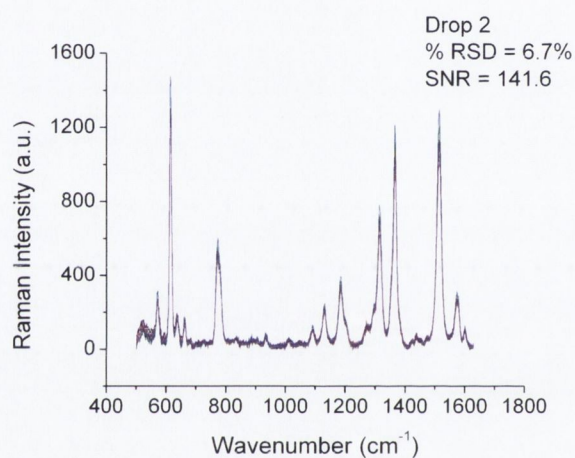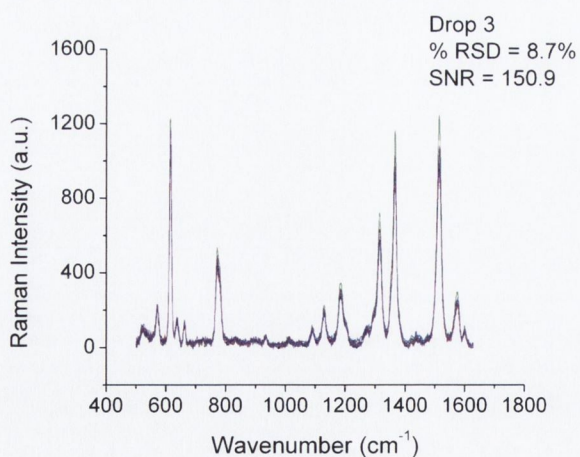
(a)
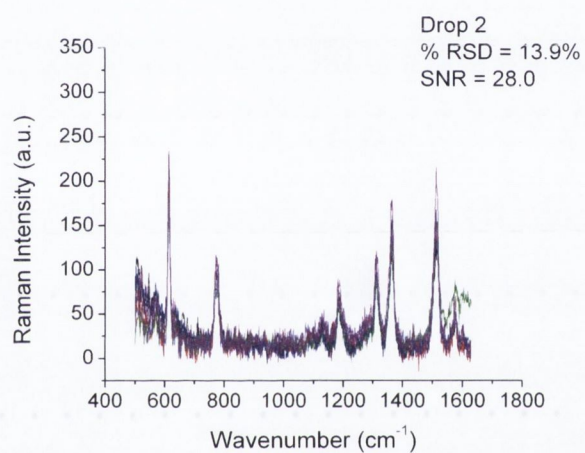
(b)
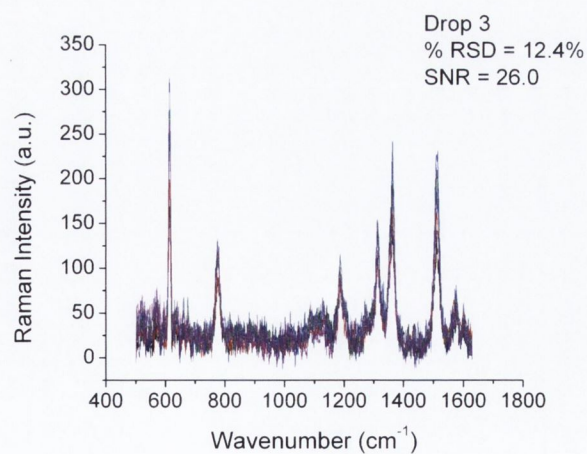
(c)

Figure 4.22: Three separate drops of a 1.8×10^{-5} M solution of Rhodamine 6G were deposited onto a 10 nm nsPLD film. The spectra, taken using a 633 nm excitation and a 0.1 s exposure time, are shown for each drop in (a)-(c) respectively. The average %RSD and SNR are also shown for each set of data.

117

(a)

(b)

(c)

Figure 4.23: Three separate drops of a 1.8×10^{-5} M solution of Rhodamine 6G, mixed with silver colloids, were deposited onto a 10 nm nsPLD film. The spectra, taken using a 633 nm excitation and a 0.1 s exposure time, are shown for each drop in (a)-(c) respectively. The average %RSD and SNR are also shown for each set of data.

118

From the spectra presented in these figure it is evident that the solutions incorporating the colloids are stronger both in terms of their absolute peak heights and also in their SNR values. The %RSD values are also superior for the colloid-based samples. Regarding the droplet to droplet measurements, and indeed the film to film measurements, summaries of each of these sets of data can be observed in Figure 4.24(a) and (b).

	Film 1			Film 2			Film 3		
	Drop 1	Drop 2	Drop 3	Drop 1	Drop 2	Drop 3	Drop 1	Drop 2	Drop 3
%RSD	21.9	13.9	12.4	14.4	6.7	18.8	15.5	16.0	15.5
SNR	31.1	28.0	26.0	34.0	33.3	28.1	20.2	17.1	18.9

(a)

	Film 1			Film 2			Film 3		
	Drop 1	Drop 2	Drop 3	Drop 1	Drop 2	Drop 3	Drop 1	Drop 2	Drop 3
%RSD	8.9	6.7	8.7	11.0	6.2	19.3	11.7	6.9	20.7
SNR	116.9	141.6	150.9	134.6	135.7	163.9	115.3	146.6	176.0

(b)

Figure 4.24: A summary of the %RSD and SNR values for the 1.8×10^{-5} Rhodamine 6G solutions (a) in the absence and (b) in the presence of silver colloids, for each of the three droplets deposited onto the nsPLD films. A 633 nm excitation and 0.1 second exposure time was used for the acquisition of this data. The additional spectra for the second and third films are shown in Figure F.12 and Figure F.13 for the non-colloid based samples and in Figure F.14 and Figure F.15 for the colloid based samples.

There are again variations between droplets on the same films and between the different films measured, though the colloid-based study does mostly show a reasonable performance in terms of the %RSD within droplets. The SNR is also good across the colloid-based samples, though there is more variance in the values than would be desired. The 1.8×10^{-5} Rhodamine 6G solution was also measured on a glass microslide, with a summary of these observations shown in Figure 4.25.

	Glass		
	Drop 1	Drop 2	Drop 3
%RSD	26.8	17.9	21.4
SNR	127.2	143.6	137.3

Figure 4.25: A summary of the %RSD and SNR values for Rhodamine 6G for each of the three drops on the glass microslide. A 633 nm excitation and 0.1 second exposure time was used for the acquisition of this data. The spectra are shown in Figure F.16.

The absolute peak height values for the Rhodamine 6G SERS spectra on the glass microslides showed a slightly lower response to those observed from the PLD films, though the SNR values don't really reflect this observation, possibly to a greater background noise generated from the PLD films. The observed increase in the absolute peak intensities could be due to reflection of SERS signals back off the silvered film surface.

4.5 Comparison of a PLD film with a commercial substrate

A comparative test of the SERS performance of the PLD films was undertaken by using a 7 nm nsPLD film and a commercial SERS substrate called Klarite® obtained from Renishaw Diagnostics.[189] The analysis used Rhodamine 6G and benzotriazole as the SERS probes for the comparison.[190] The Klarite® substrate consists of micron-sized gold pyramid structures, ordered periodically on the surface of the film. SEM images, taken on a Zeiss Ultra Plus SEM in the Advanced Microscopy Laboratory (AML) in the Centre for Research on Adaptive Nanostructures and Nanodevices (CRANN), of the features are shown in Figure 4.26, showing the structures to measure at about 1.2 μm along each edge.

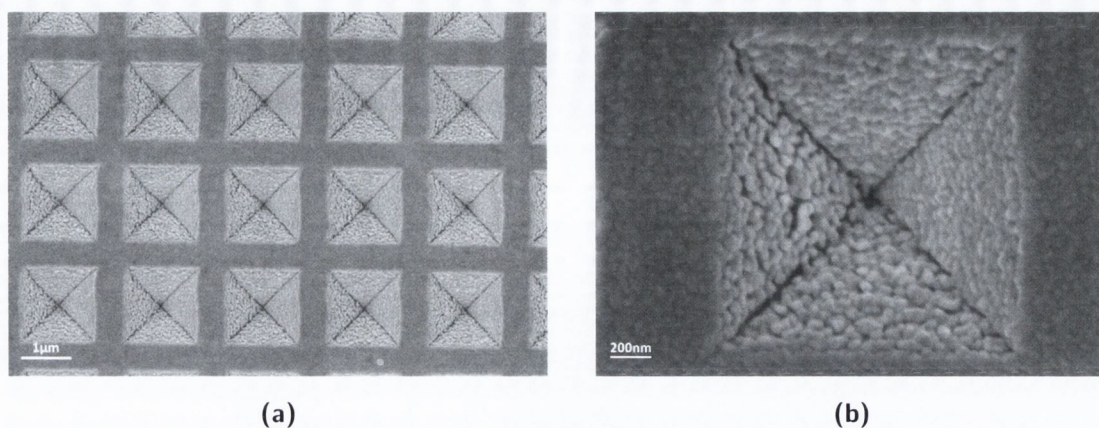**(a)**   **(b)**

Figure 4.26: (a) SEM image of the Klarite® films, showing a low-magnification view of an array of the surface features on the films. (b) shows a higher magnification on one of these features.

These Klarite® films provided a good opportunity to examine a uniform substrate in direct contrast to our substrate prepared by PLD, which is randomly ordered. The SERS response from each of these substrates was investigated, with a particular emphasis on the reproducibility of the obtained signals. The data shown in Figure 4.27 is of Rhodamine 6G and benzotriazole, with the average peak heights shown for the major peaks of each species, with error bars representing the variance in data over ten averaged spectra.

Evident from this is that the colloids and the 7 nm film outperform the Klarite® film in terms of signal obtained. Meanwhile the error bars in Figure 4.27 show the Klarite® film to be the most reproducible. The 7 nm film doesn't perform much worse than the colloids in the case of the Rhodamine 6G analysis, and the colloids show a very high variation. This figure diminishes somewhat in the analysis of the benzotriazole, though the performance of the PLD film also decreases. The Klarite® in both cases shows the lowest signal, but the highest reproducibility. The changes in reproducibility measurements in the colloids and the PLD film when moving from one probe to another serve to highlight the reproducibility issues in these media.
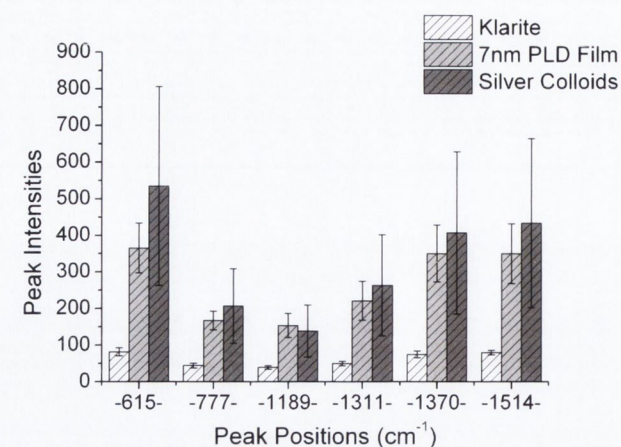
(a)
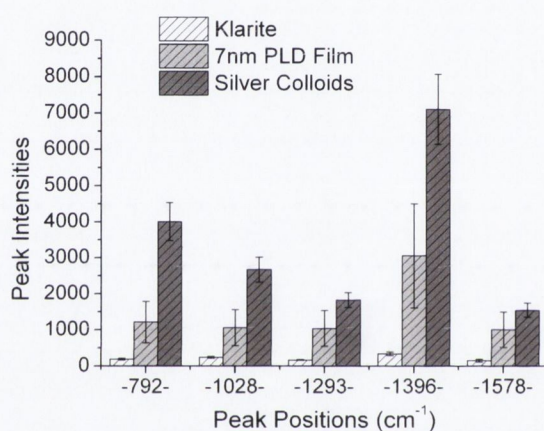
(b)

Figure 4.27: SERS response of three enhancing media using (a) Rhodamine 6G and (b) benzotriazole as the probes.

A further examination of the performance of the three media in terms of reproducibility was carried out using the normal distribution about the calculated mean.[138] This was performed by taking the 613 cm^{-1} peak of Rhodamine 6G, from which an average peak height was calculated from ten separate spectra, each taken at separate areas within the deposited Rhodamine 6G droplets. Using this information a plot was developed according to the following formula for normal distribution:

$$f(x) = \frac{1}{\sigma\sqrt{2\pi}}e^{\frac{-(\mu-x)^2}{2\sigma^2}}$$

(4.1)

where μ is the mean peak height, σ is the standard deviation and σ^2 is the data variance. The function is plotted against each of the obtained peak-height values, and can also

be further modelled by plotting incremental values of x to cover the range observed in the data. The resultant distribution plot is shown in Figure 4.28.
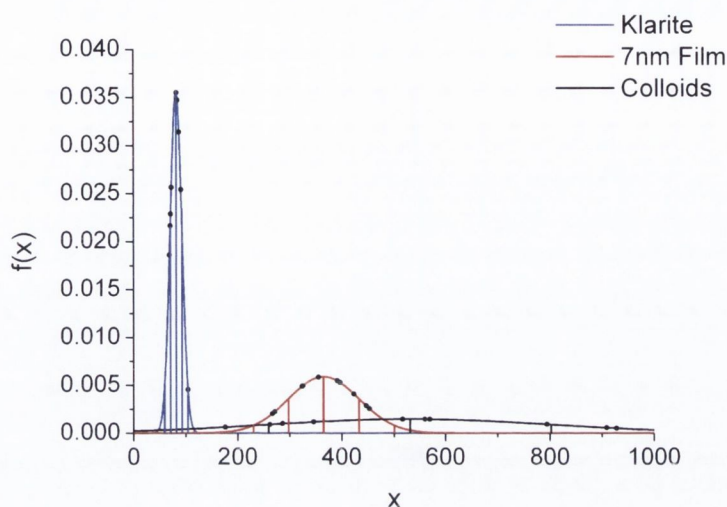
Figure 4.28: Normal distribution for the $613cm^{-1}$ peak for each of the three enhancing media.

The measured x−values are shown as the data points on the modelled graphs, corresponding to the intensity of each of the measured peak heights for the 613 cm^{-1} peak for each medium. The central vertical line within each curve represents the mean value based on the 10 data-points measured, while the lines to either side of this represent one standard deviation of data, both above and below this mean value. The $f(x)$ value on the vertical axis can be described as the probability of a scan resulting in the mean peak height. As can be seen from Figure 4.28, the Klarite® performs best in terms of the probability of a scan resulting in the mean value, but as has been shown in Figure 4.27 there is a large trade-off for this in terms of the signal intensity. A similar result was found for xanthopterin, although the data for that is not shown here. While the PLD film performs better in terms of its signal intensity, further study involving a larger number of films would be of benefit to fully validate the extent of this observation.

4.6 Conclusions

The SERS response of silver films produced by EBE and PLD was investigated. The 633 nm laser source was focused onto the interface between a droplet of the probe solution

and the film surface and both the EBE and PLD films were found to produce SERS activity. EBE films, both as-prepared and annealed at 400°C, were characterised using AFM, with the resultant images showing a greater concentration of nanoparticulate features on the surface of the annealed film. The RMS surface roughness measurement also showed a greater surface roughness for the annealed films, a relationship that was also observed for fsPLD films.

PLD films were fabricated using two laser systems, which result in slightly different nanoparticle film morphologies. Thickness investigations of these films suggested that films of at least 5 nm thickness were necessary for appreciable SERS activity, and increases in signal were observed up to 10 nm film thickness.

Reproducibility of the EBE films was investigated through the preparation of six 10 nm films, three of which were measured as-prepared and three of which were annealed. Three nsPLD films were also prepared for this study. On each film 3 droplets of the probe solution (xanthopterin and Rhodamine 6G) were deposited, with 10 spectra being taken from within each of these droplets. The spectra were then integrated, with the highest and lowest valued spectra being removed and the remaining eight being averaged. Signal-to-noise ratio (SNR) and relative standard deviation (%RSD) values were calculated for this data, and it was found that the annealed EBE films performed very poorly for both of these figures. The non-annealed EBE films and the nsPLD films showed better SNR and %RSD figures, though variations between droplets on different areas of the film surface and between the different films themselves were observed to be undesirably high. From this it can be ascertained that the films would be unsuitable for quantitative analysis in their current form and would require some form of standardisation mechanism introduced to the measurements, or optimisation of the film surface to reduce the variable SERS responses.

The SERS performance of a 7 nm nsPLD film was compared to that of a commercial substrate obtained from Renishaw Diagnostics called Klarite®. In terms of SERS response the PLD film was found to perform better than the commercial film, but the uniform nanostructures of the Klarite® film performed much better in terms of reproducibility.

Films produced by both EBE and PLD were found to produce SERS, though the response was not as strong as when using silver colloids. There is still potential for the future investigation of these films towards SERS of pterins, though a strong emphasis on their reproducibility would be essential.

5

Conclusions & Future Work

The motivation for this thesis was the investigation of spectroscopic techniques towards pterin detection. The optical properties of pterins were initially considered, with spectra taken of their absorption and fluorescence profiles, comparing to literature sources where available. The optical response of the pterins in different pH environments was found to vary, which is an important factor regarding detection in biological systems. The effects of molecular oxygen on the optical properties was investigated, with the presence of oxygen found to reduce the absorption and fluorescence properties of the pterins.

Silver nanoparticles were prepared according to a method developed by Leopold and Lendl.[113] These colloids were found to provide a good SERS response, though further investigations of the reproducibility between colloid batches found that the SERS signal varied from batch to batch, and sometimes significantly within a single batch. Droplet evaporation was not found to contribute to significant SERS variations as long as measurements are taken within a 5-minute timeframe.

As a means of tackling the irreproducibility issues, standardisation methods were investigated, initially with Rhodamine 6G acting as an internal standard for a range of Rhodamine B concentrations, with a more linear response obtained. A similar type of analysis was also applied to pterins with different mix ratios of xanthopterin to isoxanthopterin being prepared. While this experiment could benefit from a greater number of data points there was an initial observation that some form of linear relationship could be obtained.

Droplets deposited onto glass microslides were used for the majority of the SERS work

but an investigation into the use of stainless steel wells showed the latter to produce a better SERS response and better reproducibility. Aggregation was also found to provide a far greater signal

Finally, two methods for silver film production were investigated - pulsed laser deposition (PLD) and e-beam evaporation (EBE). The PLD films were found to perform better at thicknesses greater than 5 nm so three PLD films of 10 nm thickness and six EBE films of 10 nm thickness, three annealed and three non-annealed, were prepared and investigated for their SERS performance. The PLD films and non-annealed EBE films were found to perform best regarding signal intensity, with the former showing the best reproducibility. This preliminary work should provide an opportunity to investigate these films further, particularly involving the preparation variables, such as film thickness and deposition rate, that could lead to better film performance. The PLD technique was also compared to a commercial substrate from Renishaw called Klarite®, with the SERS response found to be superior, though with poorer reproducibility.[190]

Future work in this area would involve further investigations of the fluorescence and SERS responses of a more extensive range of the family of pterins. Future fluorescence investigations could include considerations of metal-enhanced fluorescence.[191,192] This could potentially be achieved through the use of polyelectrolyte layers as spacer layers between the fluorophore of interest and the enhancing metal substrate. The metal substrate itself could consist of a deposited colloidal layer or of nanoparticle films prepared by PLD or EBE.

As well as improvement of the silver colloid reproducibility, different nanomaterials for SERS would be another area of future interest, perhaps investigating the potential for improved SERS response from nanotriangles.[129] Further pterin quantification experiments could also be designed using some form of internal standardisation technique. The silver films prepared using PLD and EBE also showed some promise, and optimisation of their preparation and reproducibility could lead to their development as useful SERS platforms.

Pterin detection is a worthwhile objective, as they are species that occur in many

biologically relevant situations. Moreover information on their concentrations could be useful in cancer diagnosis. While separation techniques coupled with fluorometric detection provide good sensitivity on this front, surface-enhanced Raman spectroscopy, if reproducibility issues are able to be adequately controlled, could offer an alternative detection mechanism.

Appendices

A

Appendix A: Synthesis and analysis of gold nanoparticles

In this appendix a brief discussion of the experimental details will be provided for gold nanoparticles that were synthesised for an investigation into their plasmonic properties. Some characterisation and imaging data will also be presented with this discussion.

A.1   Gold Nanoparticle Synthesis

Synthesis of the gold nanoparticles (NPs) was conducted according to the work of Gittins and Caruso.[193] The first stage of the synthesis involved the transfer of the metal salt from an aqueous solution through to organic phase, in this case toluene.

The first stage of the synthesis procedure involved the addition of a 30 mM aqueous gold chloride ($HAuCl_4$) solution to a 25 mM tetraoctylammonium bromide (TOAB) solution in toluene. This is carried out in a separator funnel and shaking to mix the solutions initiates a phase transfer of the gold from the aqueous phase to the organic toluene phase. The aqueous phase was removed from the separator funnel once it had turned clear and the toluene solution was added to a round-bottomed flask.

With the gold solution in the toluene, the reduction of gold was initiated through addition of an aqueous 0.4 mM solution of sodium borohydrate ($NaBH_4$) dropwise until

the colour changed from yellow to a deep violet-blue. At this point the rest of the NaBH$_4$ was added to the flask and the mixture was covered and left to stir and react overnight.

Following reduction of the gold the aqueous phase was again separated out to leave the organic phase with the gold. A solution of aqueous 0.1 mM 4-dimethylaminopyridine (DMAP) was then added to the solution to instigate a phase transfer of the nanoparticles across from the organic to the aqueous phase.

A.2 UV/Vis Characterisation

UV/Vis analysis was carried out to calculate the extinction spectra of the gold colloids, as is shown in Figure B.2.
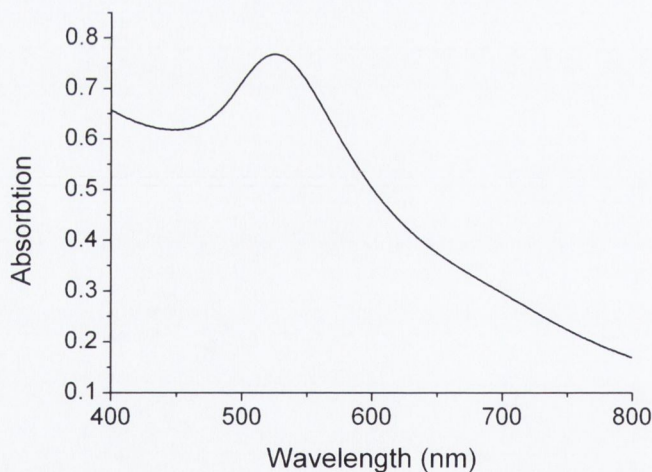
Figure A.1: The UV/Vis spectrum of the gold colloids.

The gold colloids showed a peak at about 530 nm, alongside quite a high background absorption.

134

A.3   Size Analysis of Gold Colloids

The Malvern Zeta Sizer Nano ZS was used for size and zeta potential analysis of the gold nanoparticle solution, which has a measurement range of 0.3 nm - 10.0 μm. The first scan of the original nanoparticle solution revealed an average nanoparticle diameter of 230 nm, which suggested that there was perhaps clustering involved in the solution. On a 1 in 5 dilution of the sample this diameter was reduced to 114.2 ± 8.8 nm, over an average of 6 samples.
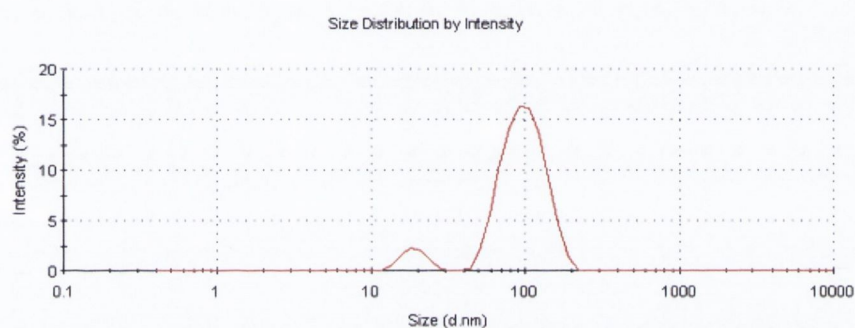
Figure A.2: Distribution of particle size with respect to the scattered laser intensity.

The plot in Figure A.2 displays on the y-axis the relative percentage of 633 nm laser light scattered by particles in various size classes. This is measured according to the random Brownian motion that particles undergo in solution. As this motion is partly due to the interaction of the particles with the solvent molecules, different sizes of particles will undergo differing degrees and velocities of movement as a result of these interactions. The analysis above uses a Dynamic Light Scattering (DLS) approach that involves a laser source being shone through the sample, with the intensity fluctuations that reach the detector being directly proportional to the sizes of the particles in solution. The larger, and hence slower, particles will result in more prolonged fluctuations, hence the greater relative percentage intensity reading at 100 nm in Figure A.2. The smaller and faster particles result in more frequent fluctuations at the detector, giving a far smaller relative intensity reading for the 18 nm peak.

The Zetasizer has a measurement range of 0.6 nm to 8.9 μm and uses the information gathered from the intensity fluctuations at the detector to generate a correlation func-

tion from which it generates a value for the diffusion coefficient. With this diffusion coefficient (D) the hydrodynamic diameter (D_H) of the nanoparticles can be calculated using the Stokes-Einstein equation,

$$D = \frac{k_b t}{3\pi \eta D_H} \tag{A.1}$$

where η is the viscosity (in this case water = 0.8872), k_B is Boltzmanns Constant and T is the temperature (in this case room temperature). The hydrodynamic diameter accounts for the particle core and also considers surface structures such as adsorbed molecules and also the concentration of ions in the medium. This results in the hydrodynamic diameter being slightly larger than those obtained through electron microscope images, where the nanoparticles are dried and out of solution, and these hydrodynamic diameter values can change with the suspension conditions.[194,195]

The Zetasizer is then able to take the intensity information and, using Mie Theory, convert the data to a volume-based format, which is of course proportional to mass and thus the proportional representation of particles within a suspension. Assumptions made for the conversion are that the particles are all spherical, they all have a homogeneous and equivalent density and that the refractive index and absorbance is known. The data for the volume plot is a better representation of the relative amounts of each peak in the distribution while the intensity plot is more accurate for representing the size of each peak in the distribution. The plot for the volume distribution is shown in Figure A.3.
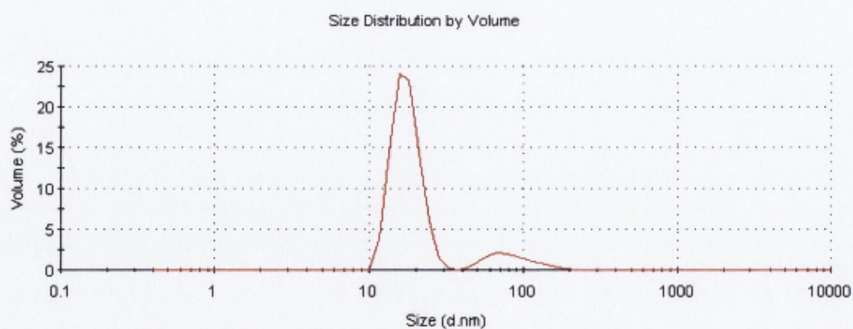
Figure A.3: Distribution of particle size with respect to the volume occupied.

This plot shows that the most abundant particle size in the solution is that of 15.7 nm hydrodynamic diameter. Comparisons to the nanoparticle sizes achieved by Gittins

et. al. shows a difference in that their particles registered at 5.2 nm in aqueous media through analytical ultracentrifugation measurements.[193]

A.3.1   AFM of Gold Colloids

Tapping-mode AFM was carried out on the gold colloids using a Digital Instruments multimode SPM with a Nanoscope IIIa controller with a nano scope 3A controller, with the resulting image in Figure A.4 showing clusters of the nanoparticles along with isolated particles and smaller aggregations.
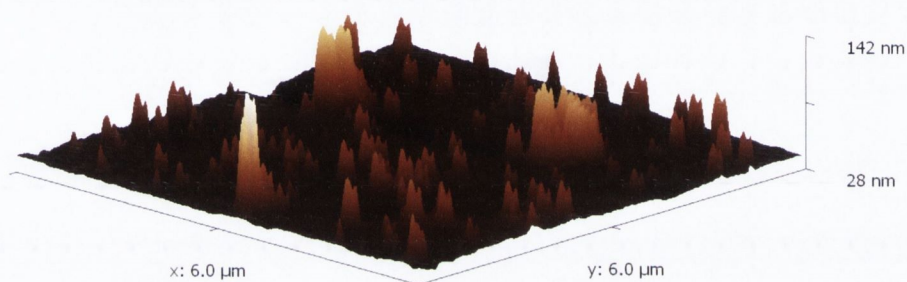
Figure A.4: A 3D representation of the AFM data for the gold colloids.

As can be seen from the image above, the colloid clusters rise to about 100 nm above the substrate, while the size of a single nanoparticle appears to vary over the area measured. In order to obtain some more lateral information on the sizes of the nanoparticles, profile data was extracted, which is shown below in Figure A.5.

As can be seen from the profiles in Figure A.5(b), the large colloid clusters protrude about 80 nm from the substrate surface, while the lateral dimensions of the two clusters are about 500 nm and 1 μm respectively. Line 2 was drawn to accommodate some of the smaller features on the graph, and from the representation of the profile in Figure A.5(b) these feature measure about 200 nm across.

(a)   (b)
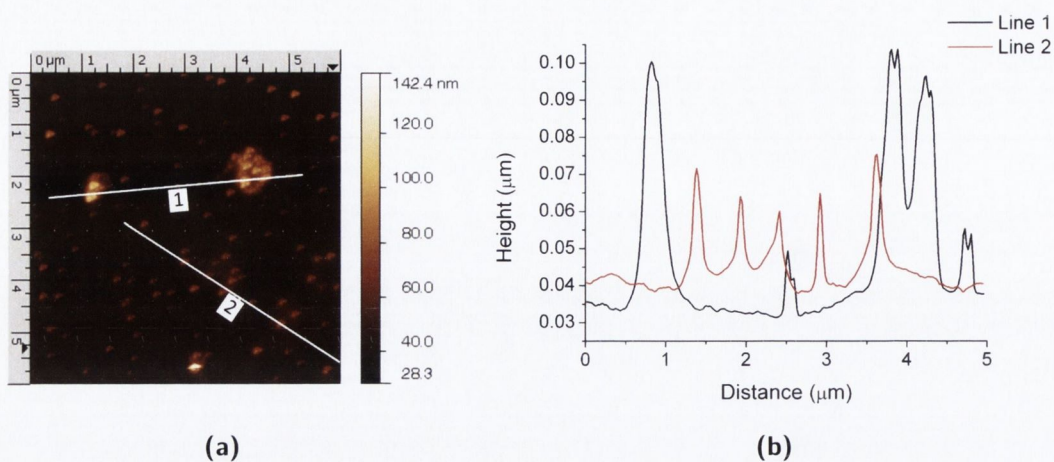
Figure A.5: (a) A 2D representation of the gold nanoparticles and (b) the surface profile along the two lines of measurement, shown in (a).

A.4 SEM Images of Gold Colloids

A Zeiss Supra 35 VP SEM was used in the Centre for Microscopy and Analysis in Trinity College in order to get a clearer picture of the size and appearance of the colloids. Shown below in Figure A.6 is a collection of three SEM images taken of the gold colloid clusters.

(a)

(b)

(c)
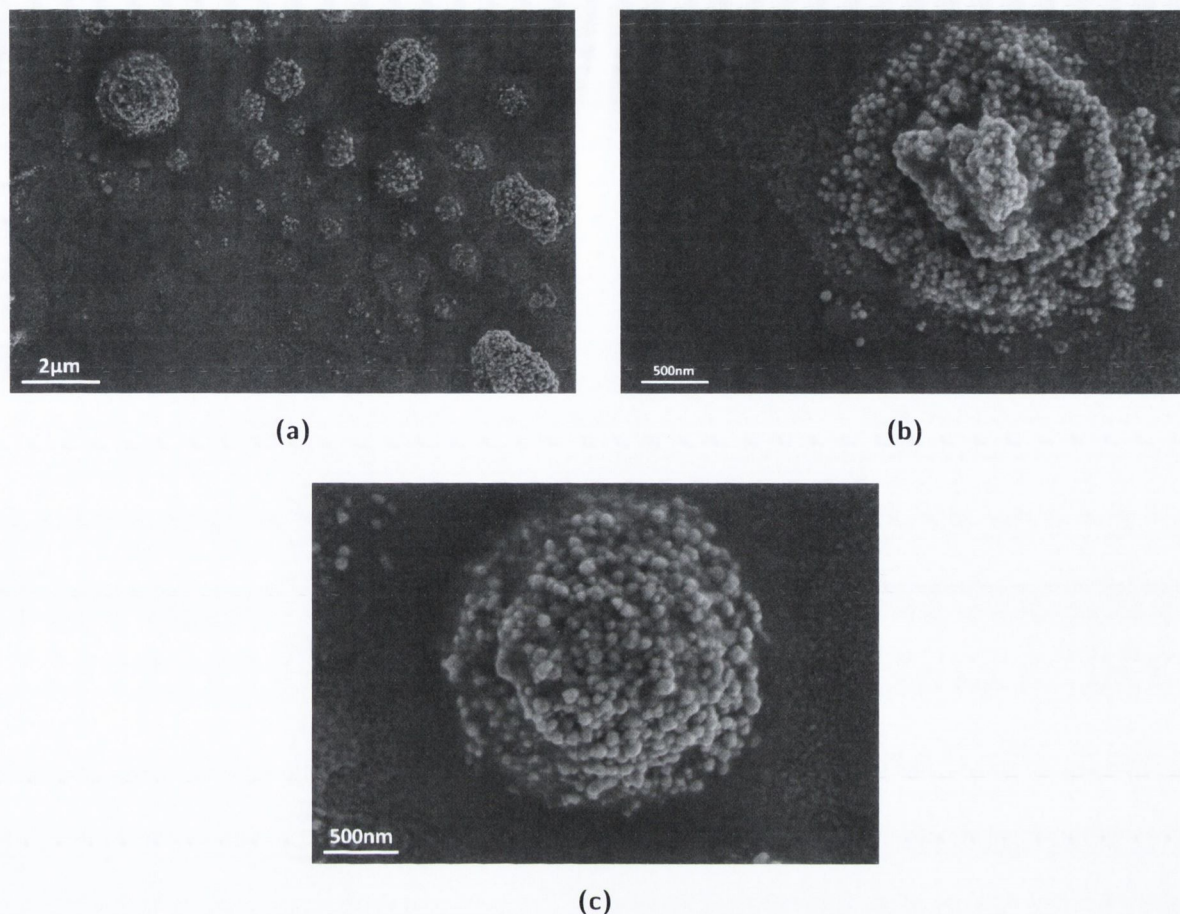
Figure A.6: (a) shows a low magnification image of a group of gold clusters, located towards the edge of the dried droplet. Figure (b) & (c) show a higher magnification images of two clusters.

Using this image the size of 30 colloidal particles was estimated, with an average size for the gold colloids subsequently found to be 66 ± 15nm.

A.5 Determination of Nanoparticle Concentration

SEM analysis of a dried droplet of the synthesised colloidal gold solution yielded an average particle size of 66 ± 15 nm. From the synthesis procedure a 30 mM solution of $HAuCl_4$ was used as the source for the gold. A 30 mM solution is composed of 0.03 moles of gold atoms per litre of the dissolved compound. In this synthesis only 30 mL of the $HAuCl_4$ was prepared, and so this results in 9×10^{-4} moles. Using Avogadro's number, the number of molecules in 1 mole of any substance is equal to 6.022×10^{23}

molecules. In the synthesis carried out it is possible to work out that the number of molecules of $HAuCl_4$ used is:

9×10^{-4} moles $\times$ 6.022×10^{23} molecules/mole $= 5.42 \times 10^{20}$ molecules

Because there is only one atom of gold per molecule of $HAuCl_4$ then there must also be 5.42×10^{20} atoms of gold involved in the initial reaction mixture.

Using the atomic radius of gold to be equal to 174 pm[196] the atomic volume occupied by a gold atom was derived to be 2.207×10^{-29} m^3 using the volume of a sphere, $\frac{4}{3}\pi r^3$. Using the average diameter of the gold nanoparticles observed in the SEM images, the average radius was used to calculate the average volume of the nanoparticles using the ideal assumption that the nanoparticles were all spherical in shape. This gave an average nanoparticle volume of 1.483×10^{-22} m^3.

The unit cell of gold structures is face-centred cubic (fcc),[197,198] as shown in Figure A.7 below, and consists of half of a centred atom on each face of the unit cell as well as one-eighth of an atom located at each of the unit cell vertices. An fcc unit cell has a packing factor (the ratio of the volume of atoms to the total volume of the cell) of 0.74 and each unit cell holds an equivalent volume of 4 atoms. This model was hence used in constructing a numerical approximation for the amount of gold atoms in an average gold nanoparticle of diameter 66 nm.
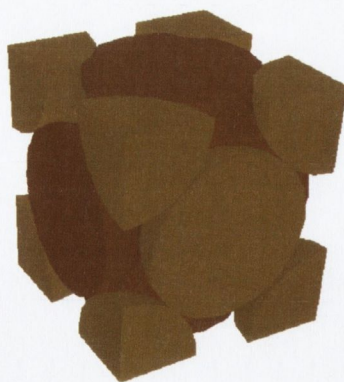
Figure A.7: fcc unit cell for gold.

Because the packing factor of the fcc unit cell is 0.74 the volume of the unit cell can be worked out from the ratio

$$\frac{\text{Volume of atoms in cell}}{\text{Total volume of cell}} = 0.74 \tag{A.2}$$

The volume of 4 atoms is 8.828×10^{-29} m^3 so the total volume of the unit cell is thus 1.193×10^{-28} m^3. That means that for every four atoms the volume of free space equates to this value minus the volume taken up by the four atoms, which is 3.102×10^{-29} m^3. Dividing this figure by 4 will give the amount of free space associated with each atom, which works out to be 7.755×10^{-30} m^3. The effective volume of each atom can now be calculated from the volume of the atom plus the volume of the associated free space, which works out to be 2.983×10^{-29} m^3.

The number of atoms per nanoparticle of diameter 66 nm can now be calculated by dividing the nanoparticle volume by the effective volume of one atom, to give a total of 4.972×10^6 atoms per nanoparticle.

The number of gold atoms in the prepared solution was 5.317×10^{20} so dividing this figure by the number of atoms per nanoparticle will give the total number of nanoparticles in the synthesised solution. This figure works out to be 1.069×10^{14} nanoparticles.

This can then be converted to a concentration using Avogadro's number and the amount of solution yielded. Dividing the number of nanoparticles by Avogadro's number gives the number of moles of nanoparticles, which in this case turns out to be 1.775×10^{-10} moles. 83 mL of solution was yielded so, assuming full transfer and capture of the gold nanoparticles, these two figures can be used to calculate an estimated colloid particle concentration of 2.14 nM.

A.5.1 SERS using Gold Nanoparticles

Both benzotriazole and xanthopterin were tested for SERS analysis, the resulting spectra of which are plotted in Figure A.8.

Both of these spectra were taken using gold colloids that had been centrifuged and
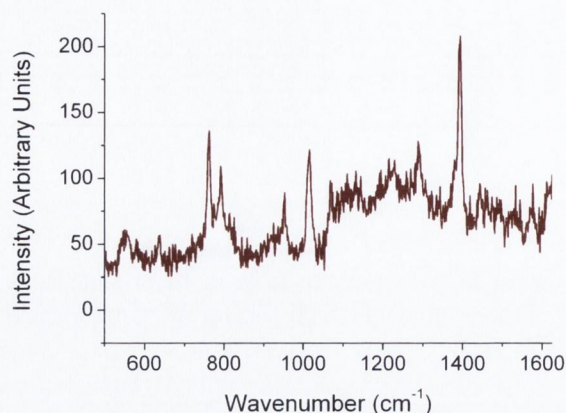
(a)
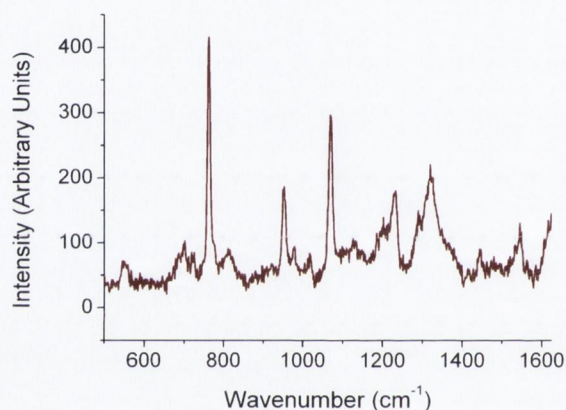
(b)

Figure A.8: Gold colloid SERS spectra of (a) 4.2×10^{-4} M benzotriazole using a 5-second exposure and (b) 2.5×10^{-4} M xanthopterin taken using a 10-second exposure. A 633 nm excitation source was used in both instances.

then redispersed in 10 mM NaCl. In the spectrum of the benzotriazole sample, there are features present of this compound, notably the peak at about 1400 cm^{-1} and the right-hand peak of the doublet just blow 800 cm^{-1}, but the other features don't fit into the benzotriazole spectrum. The case is similar for the xanthopterin spectrum shown in Figure A.8(b), which shows a typical xanthopterin characteristic at about 1320 cm^{-1} with the broad feature, but the remaining peaks are not what would be expected, and indeed correspond with the unknown features in the benzotriazole spectrum. A spectrum was taken of the gold colloids alone, which resulted in the subsequent discovery of a spectrum belonging to one of the synthesis reactants, DMAP, as shown in in Figure A.9. This spectrum was taken using silver colloids, to show the spectrum better.
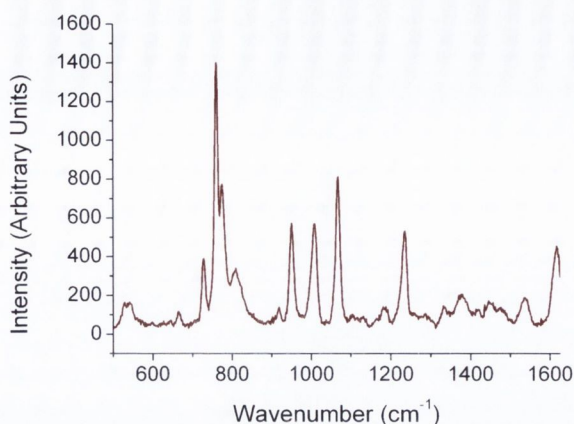
Figure A.9: SERS spectrum taken of DMAP using the silver colloids.

The gold colloids showed a markedly worse SERS response than the silver colloids and so they were discarded from further SERS analysis. However, only very preliminary investigations were carried out, and the use of centrifugation to eliminate the contaminant and the consideration of different aggregating agents may yield improved responses.

A.6   Investigation of Linear Arrangements of Gold Nanoparticles

Linear alignment of the gold colloids was investigated,[199] the aim being to produce linearly-arranged gold nanochains. The principal method examined here was with regard to the linear arrangement of the gold nanoparticles with respect to their affinity with one another. According to the work of Gittins et. al.[193] the surface stabiliser molecules (in this case DMAP) become desorbed from the molecule surface and aggregate in solutions of pH less than 3. The effect of pH was thus investigated, both in the acidic and the basic domain, to see whether linear aggregation could be achieved through dipole-dipole interactions. A second method was also investigated regarding the polarity of the solvent used. Liao and co-workers[200] have reported that re-dispersing nanoparticles in ethanol can weaken the affinity of the stabilisers for the nanoparticle surface, again with a view to template-free nanochain arrangement of the particles.

A series of dilutions was prepared at acidic and basic pH values using an Orion 420a pH

meter and dilute HCl and NaOH solutions to vary the pH values and the concentrations were diluted to half that of the original nanoparticle solution. The acidic pH values were measured to be 3.14 and 4.14 and those of basic pH to be 10.16 and 10.99. A neutral pH of 7.12 was also used to act as a reference. The solutions were also heated for 30 minutes at $60 - 70°C$ before being analysed using UV/Vis spectrometry and imaged under a light microscope.

Following the analysis in aqueous solution the respective nanoparticle solutions were centrifuged to remove the bulk of the nanoparticles, before being redispersed in ethanol. This further set of solutions was then again analysed using UV/Vis and light microscopy.

The solutions were also heated for 30 minutes at $60 - 70°C$ as UV/Vis spectra previously taken after heating had shown the development of a higher wavelength band, which would potentially signify a longitudinal surface plasmon band. On this occasion however, spectra of the nanoparticles showed no such band for any of the various nanoparticle samples in solution. When deposited and dried onto microslides, however, there is a clear absorption band at around 720 nm, indicating the longitudinal plasmon resonance, though this is likely due to aggregation upon drying. These observations are shown in Figure A.10(a) and (b).
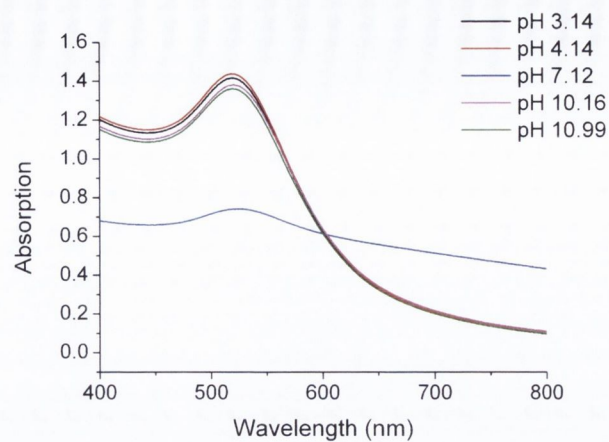
(a)
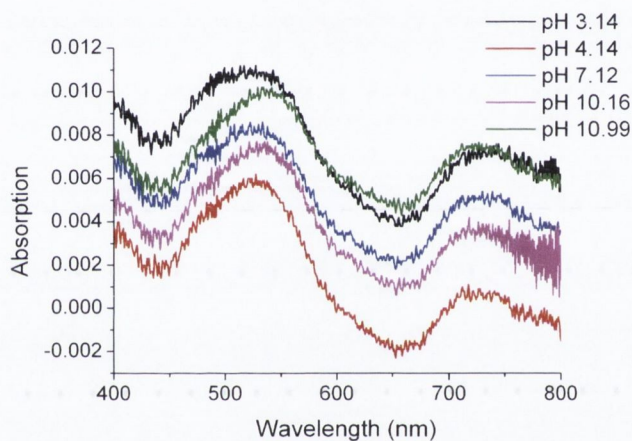
(b)
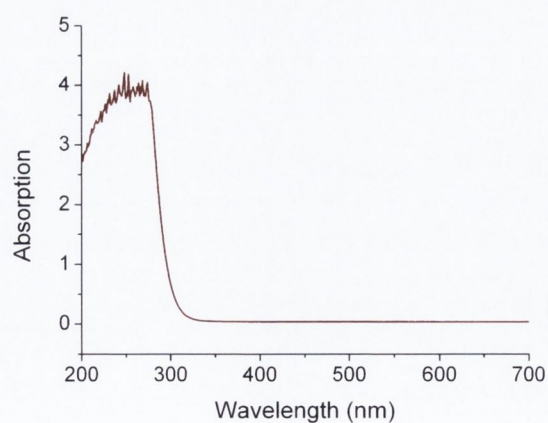
(c)

Figure A.10: Absorption spectra of (a) the gold colloids in different pH solutions, (b) the colloids deposited and dried onto a glass microslide and (c) a blank glass microslide.

In this procedure 3 μL of the solution was dropped onto a glass microslide and allowed

145

to dry at room temperature before being measured. The solution of pH 7.12 showed a peculiar trend; the colour was markedly different from the acidic and basic solutions, despite the dilution occurring only in de-ionised water. This had not been previously observed and may have been due to some form of contamination of the water source. On the microslide the spectrum is more consistent with the rest of the samples, though the presence of the higher wavelength band also suggests little change due to the introduction of acidic and basic pHs.

The second method aimed at the formation of nano-chain arrangements was explored via the re-dispersion of the nanoparticles in ethanol. As a less polar compound than water the affinity for the solvent towards the stabilisers coating the nanoparticles is far reduced. With the stabilisers less attracted to the nanoparticle surface, it was investigated as to the formation of nano-chains due to dipole-dipole interactions. A drop of 3 μL was again deposited onto a microslide and the absorption spectrum is shown below in Figure A.11, where it can be seen that there is an extended absorption band when compared to the solutions in aqueous form. The control in the figure refers to the originally synthesised nanoparticle solution, centrifuged and redispersed as with the rest of the samples but with no prior pH treatment or dilution.
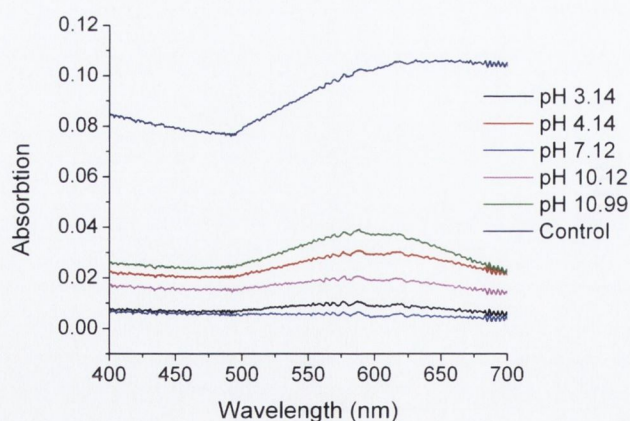
Figure A.11: Absorption spectra of gold nanoparticle solutions dispersed in ethanol and dried onto a glass microslide.

Light microscope images were taken of samples of 3 μL volume dried on microslides. Some of the images of the samples are shown in Figure A.12 and focus on the pH 10.16

and 10.99 samples at 1/2 dilution, as these offered the greatest suggestion of linear formations.

As can be seen in the images there appear to be some form of linear structures in aqueous solution. Figure A.12(b), taken with a $100\times$ magnification of the pH 10.99 sample, shows some suggestion of a linear arrangement in clusters of nanoparticles. This form of structure was also noticed in the pH 10.16 sample, Figure A.12(c), but was not evident in the lower pH samples. In the ethanol samples the control is shown in Figure A.12(d) where there was a large gold deposit due to the much higher concentration of nanoparticles in solution. On the surface of the gold layer there was no evidence of any linear formations. In the 10.16 and 10.99 pH samples, Figure A.12(e) and Figure A.12(f), there was evidence that the gold layers had some form of linear arrangement, but in more of a fractal arrangement than on the scale of nano-chains. A possible alternative is that the pH treatment of the aqueous samples prior to their redispersion in ethanol instigates a tendency to form a networked structure as opposed to a mass film-type deposition.

(a)   (b)   (c)

(d)   (e)   (f)
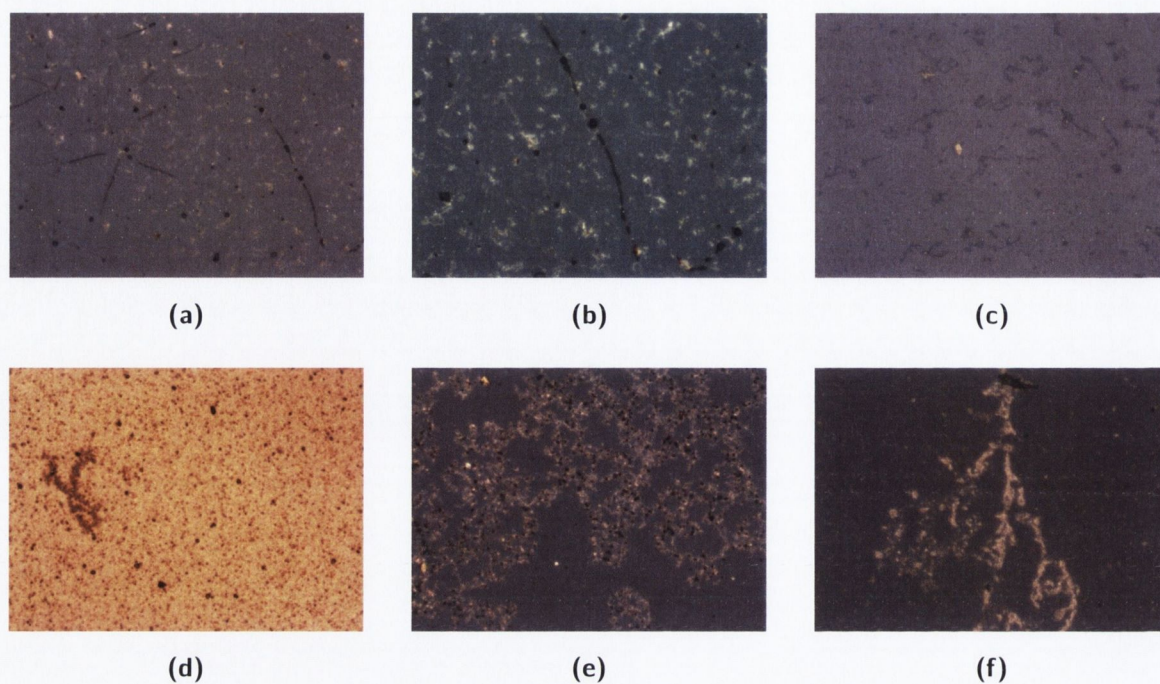
Figure A.12: (a) A 50× magnification of the pH 10.99 heated sample with a further magnification of 100× shown in (b). Image (c) shows the pH 10.16 sample at 50× magnification. (d) is an image of the control sample in ethanol, where a large gold deposit was observed. (e) shows a 50× image of the pH 10.16 sample in ethanol and (f) shows a 100× image of the pH 10.99 sample in ethanol.

SEM images were also taken of some of the above samples, though the colloids were already quite old at this stage. Images for colloids mixed with a pH 10 solution are shown below in Figure A.13.

2μm   400nm

(a)   (b)
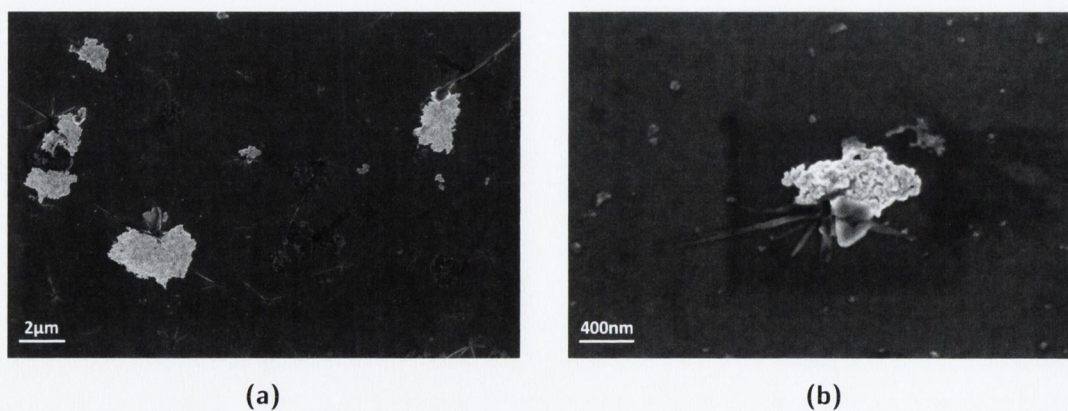
Figure A.13: SEM images of the gold colloids in a pH 10 solution. (b) is a magnified image of (a).

The linear features that were evident in Figure A.12 are still present here, though they do not appear to represent a linear arrangement of gold nanoparticles. Images were also taken for colloids in a pH 3 solution, and for colloids dispersed in ethanol.

(a) (b)
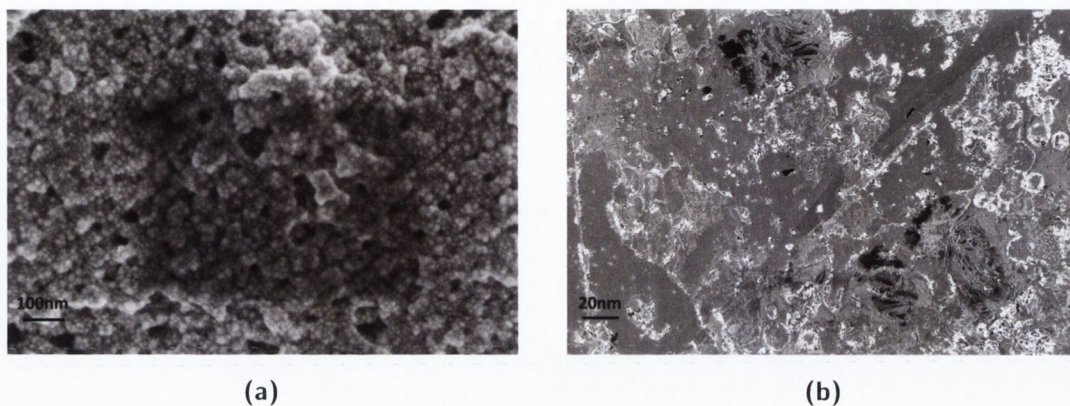
Figure A.14: SEM images of the gold colloids in (a) a pH 3 solution and (b) dispersed in ethanol.

The pH 3 colloids don't appear to show much change from the standard colloid solution, but the ethanol-based sample appears to create a more film-like effect. The absorption plots in Figure A.11 show quite a large change from the colloidal suspension, and this could perhaps explain that change.

150

Appendix B: Synthesis and analysis of silver nanowires

One-dimensional nanostructures have received a certain amount of attention due to their interesting properties.[201] In this appendix a brief discussion of the experimental details will be provided for silver nanowires that were synthesised for investigation into their plasmonic properties in the early stages of the project, before SERS was considered for investigation. Some characterisation and imaging data will also be presented with this discussion.

B.1 Synthesis of Silver Nanowires

The synthetic technique employed towards silver nanowire production was according to the work of Sun et al.[202] who quote nanowire lateral dimensions on the order of $30 - 40$ nm and lengths up to about $50 \ \mu$m. The use of a surfactant in the reactant solutions is important in its capacity to influence NW growth to these aspect ratios of 1000. Another important parameter in the technique is careful control of the reaction temperature as any alteration has been seen to affect the resultant NW length.

The experimental work was carried out using a standard reflux setup, with a 3-neck round-bottomed flask connected to a thermometer for temperature control, a Liebig

condenser for refluxing capabilities and the third neck being used for introduction of samples or removal of a sample after a desired period. The setup for the synthesis is shown in Figure B.1.
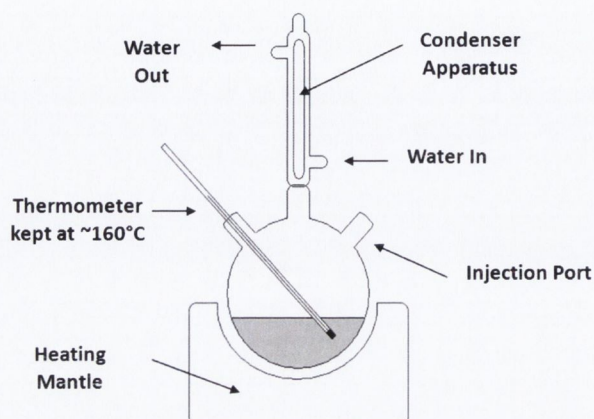
Figure B.1: Apparatus used in silver nanowire synthesis.

The synthesis was begun through the addition of 5mL of ethylene glycol ($HOCH_2CH_2OH$) to the round-bottomed flask. This was then heated to 160°C and stirred continuously with a magnetic stirring bar. A solution of platinum chloride ($PtCl_2$) was then prepared using 2×10^{-5} g in 0.5 mL of ethylene glycol. The solution was then added to the refluxing apparatus at 160°C where the ethylene glycol acts as both a solvent for the $PtCl_2$ powder and also as a reducing agent to induce the formation of platinum nanoparticles. This process is known as the polyol process, and was first described by Fievet et. al.[203] These platinum nanoparticles act as seeds for the subsequent growth of the silver NWs and the initial concentration of the $PtCl_2$ is important in that an increase in the number of seeds in solution decreases the diameter of the silver NWs. Analysis from the Sun et. al. source paper states that a 10-fold increase in $PtCl_2$ concentration at the beginning of the synthesis stage decreases the NW diameter from 40 nm to 30 nm.[202] The approach taken here was with the lower concentration of platinum seeds and so the resultant NWs were expected to have a 40 nm diameter.

Four minutes after the $PtCl_2$ solution was added to the reaction mixture, solutions of silver nitrate ($AgNO_3$) and poly(vinyl pyrrolidone) (PVP) were also added. The $AgNO_3$ solution was prepared as 0.05 g in 2.5 mL ethylene glycol and the PVP surfactant as 0.2 g in 5 mL of the same solvent. The $AgNO_3$ becomes reduced immediately by

the ethylene glycol, and in the presence of the PVP surfactant, a mixture of silver nanoparticles are formed in two size ranges. Smaller particles of < 5 nm in diameter are formed in a homogeneous nucleation process while larger particles of $20 - 30$ nm diameter are formed via heterogeneous nucleation on the platinum seeds. From the work of Zhang et. al. it is known that the PVP plays a role in preventing the agglomeration of the silver nanoparticles in solution.[204] The chemical and physical bonding of the surfactant to the surface of the silver prevents particle-particle contact and thus any aggregation of the colloidal dispersion. Refluxing the mixture continuously at $160°C$ causes an Ostwald ripening effect whereby the smaller particles dissolve into solution and grow upon the more energetically favourable larger particles. The PVP is then important in inducing a NW growth from the larger particles in solution. This process is not clearly understood but no nanowire growth was observed in the absence of the PVP, or indeed without the $PtCl_2$ that acts as the source of the platinum seeds.

After the addition of the $AgNO_3$ the solution turned a translucent brown colour but as the reaction proceeded the colour changed to an opaque milky texture. Samples were obtained from the reaction mixture, in accordance with the source paper for means of comparison,[202] after 10, 20, 40 and 60 minutes when the reaction was stopped and the solution was cooled to room temperature.

B.2 UV/Vis Characterisation

UV/Vis analysis was carried out for the silver nanowires at varying reaction times.
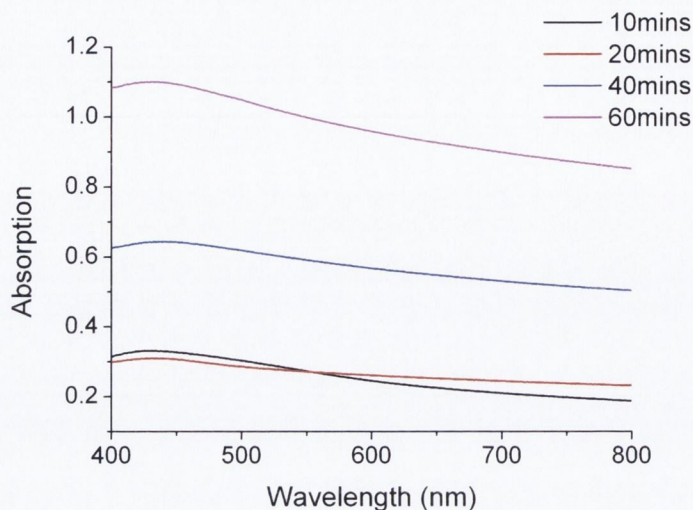
Figure B.2: The UV/Vis spectrum of the silver nanowires at different reaction times.

The silver nanowires showed a changing spectrum with regards to the reaction time, with the 10 minute sample showing absorption predominantly in the $400-450$ nm region before absorption in the higher wavelength region of the spectrum begins to occur after 20 minutes as the nanowires begin to form. As the reaction moves on through $40-60$ minutes the absorption across the region increases as the silver nanowires continue to be produced.

B.3   Transmission Electron Microscopy of Silver Nanowires

The silver nanowires were imaged using a Jeol 2100 Transmission Electron Microscope (TEM) in the Centre for Microscopy and Analysis, with the results shown for the solution after 10 minutes reaction and after the full 60 minute reaction.

From the images shown above in Figure B.3, no nanowires at all were found in the 10 minute sample, while in the 60 minute sample there were many. Nanoparticles that had not begun the transition to nanowires were still found in this sample though, as can be seen in Figure B.3(b). The nanowire shown above has dimensions of about 50 nm diameter and 3 μm length.

(a) (b)
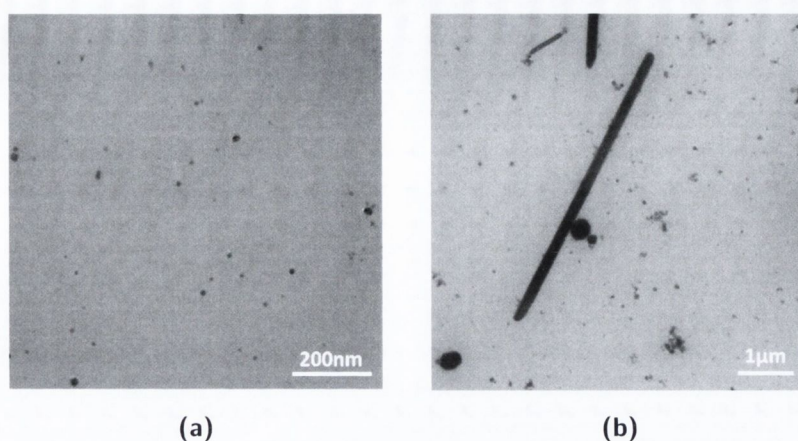
Figure B.3: Silver nanowires after (a) 10 minutes and (b) 60 minutes reaction.

B.4 Investigation into Silver Nanowire Alignment

The reaction solution of nanowires in ethylene glycol was diluted 1/30 in ethanol and then centrifuged at 1700 rpm for 20 minutes. The resulting liquid phase was removed and the product at the bottom of the tube was then re-dissolved in more ethanol and centrifuged again under the same conditions. This process was repeated 6 times.

Analysis of the drying of the solutions under the microscope showed that the ethanol evaporates very quickly, with the droplet retracting inwards towards its centre at an initially rapid rate. This rate slows down towards the centre, and the remaining liquid part takes an unusually long time to dry up fully. This could be because there is still a small fraction of the original ethylene glycol solvent left in the solution.

Light microscope images showed that the nanowires in the solution tend to orient themselves parallel to the direction of the droplet recession, that is to say in a radial fashion around the centre of the droplet, as shown in Figure B.4(a). The effects of scratching grooves into the surface of a glass slide were also examined, with the droplet being placed over the groove in an attempt to model a microchannel in order to induce capillary transport of the droplet. Initial results on this showed a single sample that suggested that this method could be useful in terms of nanowire alignment. This is shown in Figure B.4(b). The rest of the droplets analysed, however, did not show the same suggestion of alignment along the channels and little evidence of any capillary

flow being generate in the channels.

(a)   **(b)**
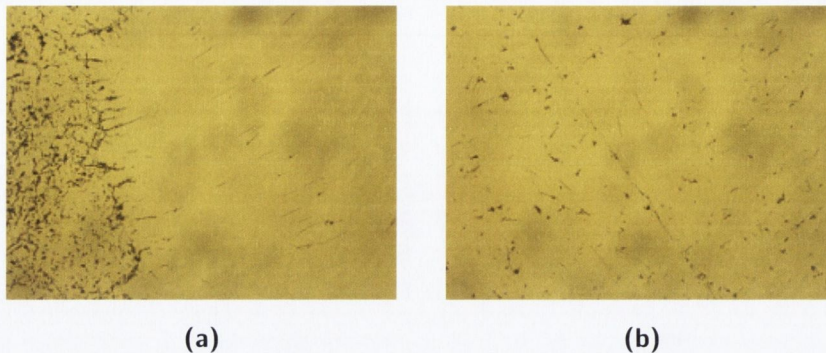
Figure B.4: (a) Evidence of radial alignment of the silver nanowires based on the rapid evaporation of the ethanol solvent. (b) Suggestion of the use of microchannels on the surface of a glass slide for nanowire alignment.

In order to pursue the method of using the microchannels etched into the glass surface, a few methods were investigated. One involved etching the channels at different angles radially around an injection point to see if the previous alignment might have been influenced by any anisotropy in the glass surface. A second method involved etching lines of different depths and widths based on the force applied to the diamond scribe. The third method used a second slide placed over the top of the channel to effectively produce a sealed and covered microchannel, in the hope of promoting capillary flow.

The methods investigated failed to show any further suggestions of nanowire alignment along the channels, although the method with the enclosed channels was hard to judge based on the method for the construction of the channels. Using the ethanol-based solvent solutions it was found that pressing the slides together as much as possible could not stop the solution from leaching out across the entire slide and not just along the desired channel. This method would need to be analysed in more detail.

A further technique that was examined was that of electric field alignment of the nanowires. The glass substrates were coated with two electrodes, composed of a conducting, metal epoxy at 4 mm apart. These were hooked up to a voltmeter and the solution was placed in between the interfaces of the two electrodes. As the voltage was increased through around 2.5 V it was found that the nanowires in the solution would begin moving across the channel. Reversing the electrical contacts would move the

wires in the opposite direction. This has potential in aligning the nanowires, although using the metal epoxies proved unsuitable as the epoxy would oxidise and particles of it would come out and into solution. One solution to this could be by evaporating silver contacts onto the glass slides, still leaving a gap of about 4 mm between them.

B.5 SERS using Silver Nanowires

The nanowires as prepared were not good SERS substrates due to contamination, as shown in Figure B.5. Because they were not prepared explicitly for SERS analysis no in-depth study was carried out; further investigation into centrifugation and aggregation of the mixture may provide improved SERS activity.
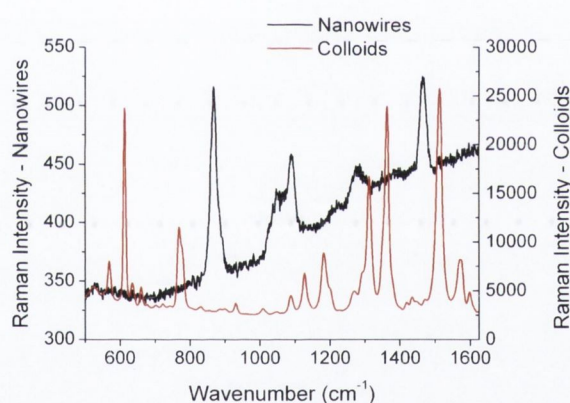
Figure B.5: SERS of Rhodamine 6G using silver nanowires (black spectrum) compared to using silver colloids (red spectrum).

Appendix C: SERS using silver triangular nanoplates

Triangular nanoplates were obtained from the labs of John Kelly in the Department of Chemistry.[129] The great advantage of using these materials is the ability to tune their absorption characteristics, based on the aspect ratio of the nanoplate dimensions. The absorption peak of one set of nanoplates was chosen to occur at 633 nm, the wavelength of the exciting Raman laser. The second set of nanoplates had an absorption band at 500 nm, about halfway between the conventional silver colloids ($\lambda_{max} = 410$ nm) and the first nanoplate solution. The colloidal solution was diluted down so as to compare all media at the same absorption value. The absorption spectra and the resulting SERS responses are shown in Figure C.1.

While the nanoplates produce an inferior SERS spectrum to that of the colloids it is nevertheless an elegant technique. The 633 nm absorbing nanoplates showed a better SERS response to the 500 nm absorbing one, likely due to resonance with the exciting wavelength. Xanthopterin was also investigated using the nanoplates but no efficient spectra were obtained. Proper aggregation procedures would probably improve this result, though this was not investigated at the time because the full importance of aggregation had not been realised.
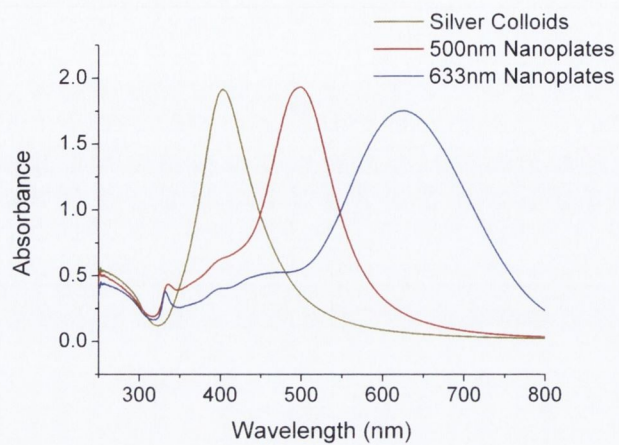
(a)
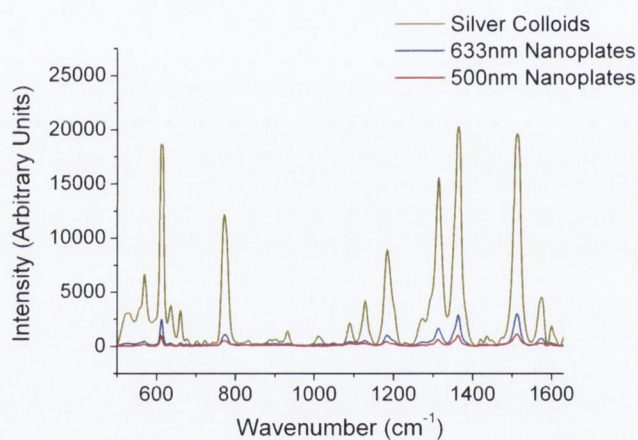
(b)
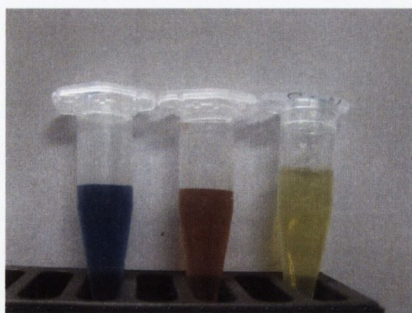
(c)

Figure C.1: (a) shows the absorption spectra for the triangular nanoplates and the silver colloids, (b) shows the SERS response of each of the materials using Rhodamine 6G and (c) shows a photograph of the nanoplates and the silver colloids in vials.

Appendix D: Investigation of droplet-on-film profiles

Shown below are CCD images using the 10× objective, which show the 7 nm PLD substrate both outside and inside one of the sample droplets. It is evident that at the same focus the area outside the drop is in focus while moving inside the droplet the substrate surface moves out-of-focus. This is important when working with PLD substrates as SERS is known to be a short-range effect, and the focus needs to be changed when moving to the droplet, although it is not as easy to focus through the solution as it is on the bare substrate.

(a)   (b)
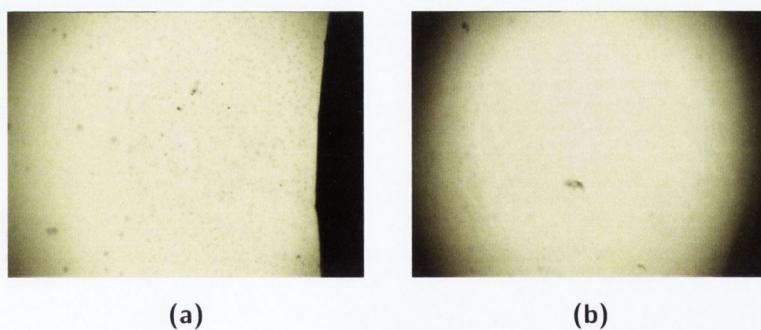
Figure D.1: White light image of (a) the bare 7 nm fsPLD substrate and (b) the substrate as seen through the sample droplet, both images taken at the same focus.

D.1 Droplet height profile

An experiment was set up to look at the SERS response as the focus of the objective lens was changed. Using a glass microslide and focusing on both the top and bottom surfaces allowed for an estimation of the distance moved for one turn of the focusing dial on the microscope. This distance was estimated at 0.2 μm, and was applied to droplets of benzotriazole placed onto the 7 nm fsPLD film. This was accomplished both using benzotriazole alone and also when mixed with the silver colloid solution, the results of which can be seen in Figure D.2.
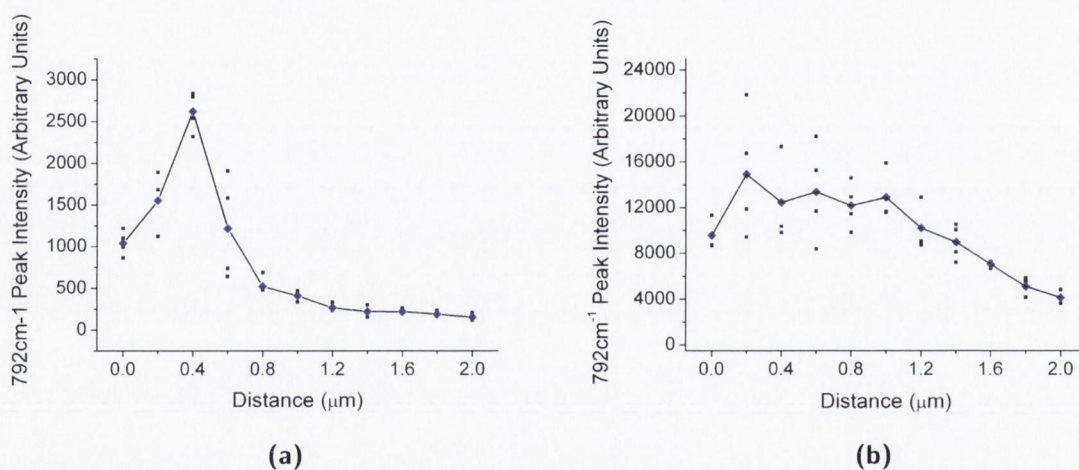
Figure D.2: (a) Rhodamine B deposited onto the fsPLD films and (b) Rhodamine B mxed with silver colloids before being deposited onto the substrates.

Figure D.2(a) and (b) shows an expected relationship between the focusing point of the laser and the signal obtained. Using the peak height for the 792 cm^{-1} benzotriazole peak, the average from four spectra was taken at each focal position, with point 0 referring to the laser focused onto the substrate outside of the droplet. The short-range effect of SERS manifests itself in Figure D.2(a) as a narrow peak, as the highest signals are found at the point when the film comes into focus at about 0.4 μm removed from the initial focus point outside the droplet. Signals are still evident outside of this peak region, though they are much smaller, and are probably due to out-of-focus or scattered light. In Figure D.2(b) the relationship between the signal and the focal position is not as critical, due to the presence of the colloids in solution providing a SERS response

regardless, which is a big advantage of using the colloid/substrate combination. The highest signals are still in the $0.2 - 0.6$ μm range though.

D.2   Droplet Contact Angle

Also investigated was the droplet profile on the different fsPLD film thicknesses. Droplets of water were deposited onto each film, and onto a bare glass microslide, before their profile was photographed using a Canon IXUS 80IS. The resulting images can be seen below in Figure D.3.

Visually, the change in the droplet from the glass microslide to the 7 nm nsPLD films is quite dramatic, with the droplets offering a much more rounded and hydrophobic profile than on the glass. This relationship was plotted by using the contact angle, which is defined in the schematic at the top-left of Figure D.3, for each of the droplets shown here. This data is plotted in Figure D.4, and also displayed is the change in the droplet height, which was measured through comparison with a metal ruler laid flat down on the table beside the droplet, with its thickness pre-determined through the use of a micrometer.
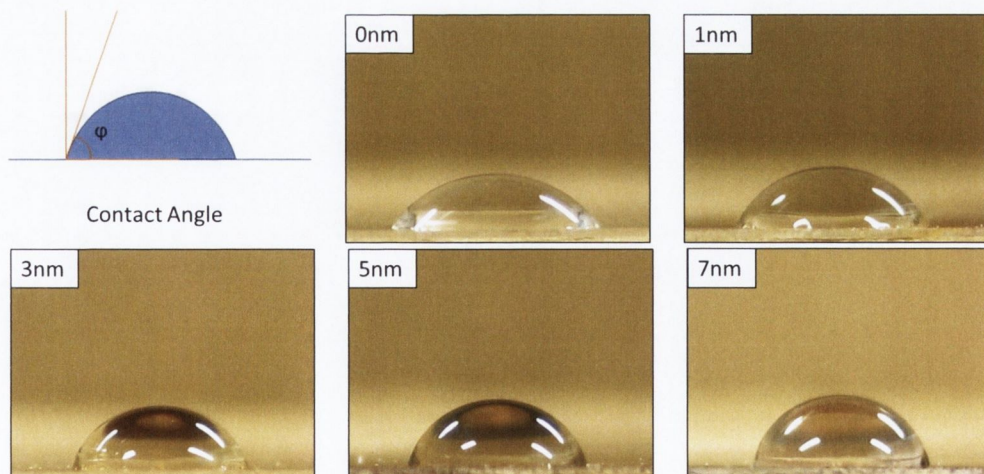
Figure D.3: Droplet profiles for water deposited onto a glass microslide (0 nm) and the 4 fsPLD thicknesses. Also shown is a schematic for the determination of the contact angle.

As can be seen from the data in Figure D.4, the contact angle generally increases with increasing thickness, although the 5 nm film doesn't quite hold true with this trend. The

droplet height shows a similar profile to the contact angle data. A more hydrophobic surface could be useful in SERS as repulsion of the solvent molecules could result in the target analytes adsorbing more readily.
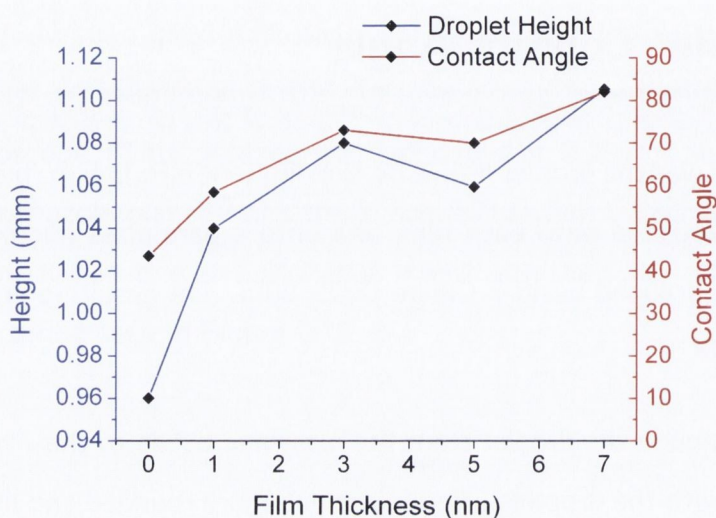
Figure D.4: Height and contact angle change with regards to fsPLD film thickness.

The changing droplet shape should also influence the focus position of the laser when moving the laser into the droplet. It is impossible to get the focus exactly correct using the CCD image as different wavelengths will refract at different wavelengths regardless, so more work would need to be done on this in order to gauge the full relationship.

Appendix E: Additional SERS Spectra - Chapter 3

This appendix contains the sets of spectra referred to in Chapter 3.
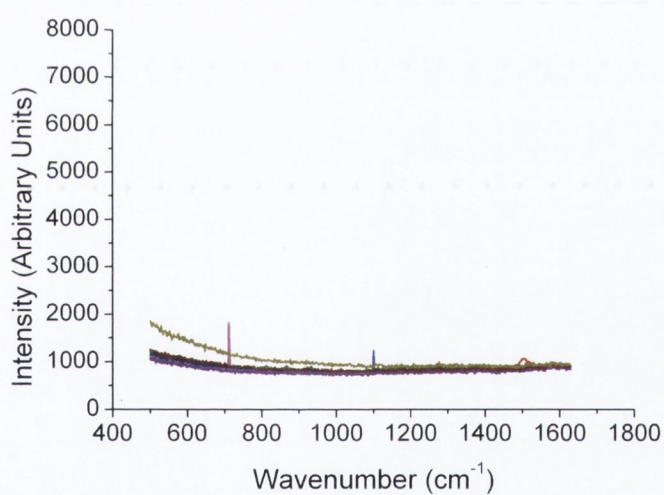
Figure E.1: Raman spectra of the Batch 1 colloids taken using a 633 nm excitation wavelength and 10 s exposure time.
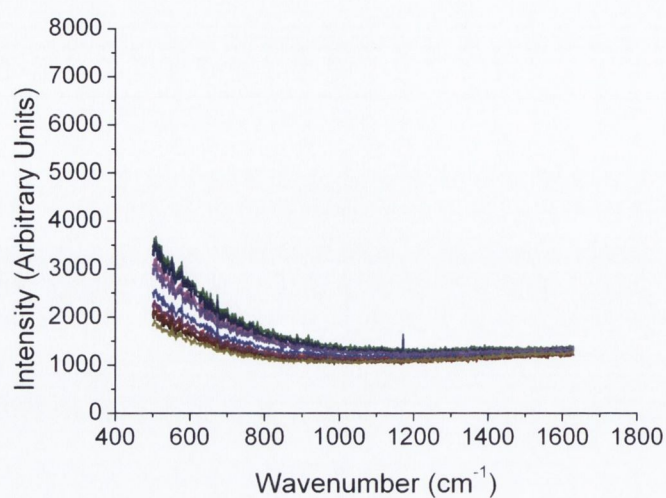
Figure E.2: Raman spectra of the Batch 2 colloids taken using a 633 nm excitation wavelength and 10 s exposure time.
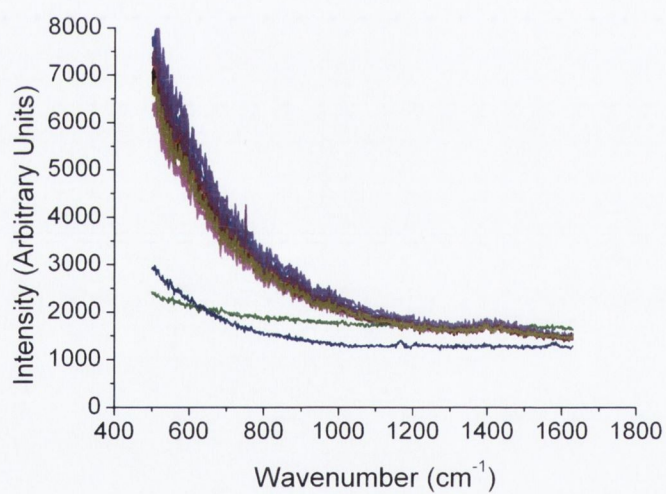
Figure E.3: Raman spectra of the Batch 4 colloids taken using a 633 nm excitation wavelength and 10 s exposure time.
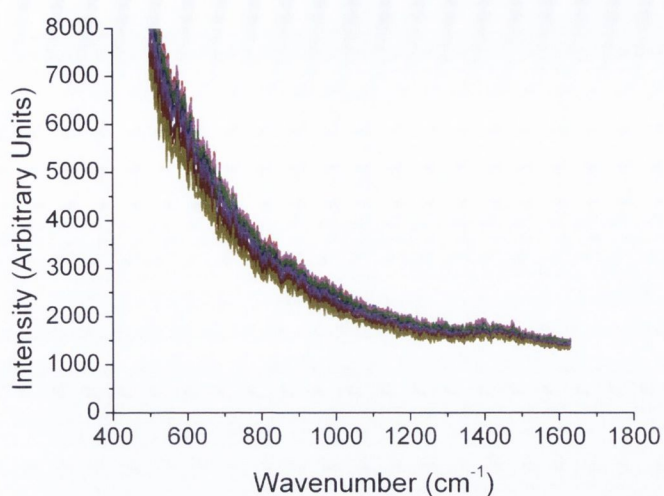
Figure E.4: Raman spectra of the Batch 5 colloids taken using a 633 nm excitation wavelength and 10 s exposure time.
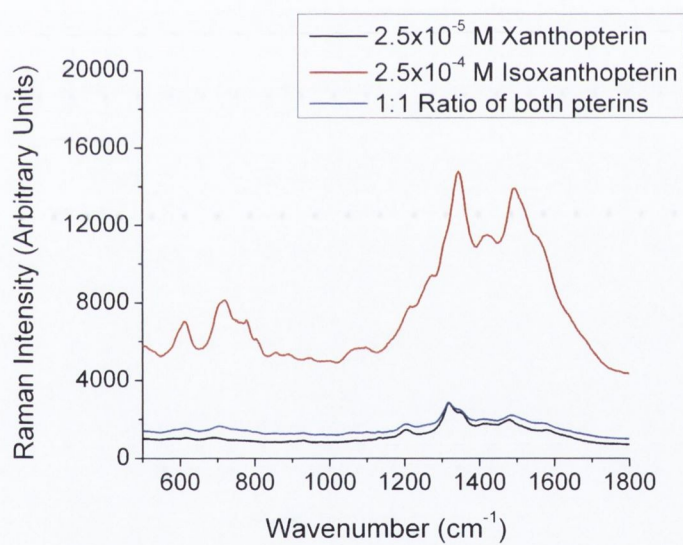
Figure E.5: SERS spectra of 5×10^{-5} M isoxanthopterin, xanthopterin and a mixture of the two at a 1 : 1 ratio. All spectra were taken at 532 nm and a 5 s exposure time.
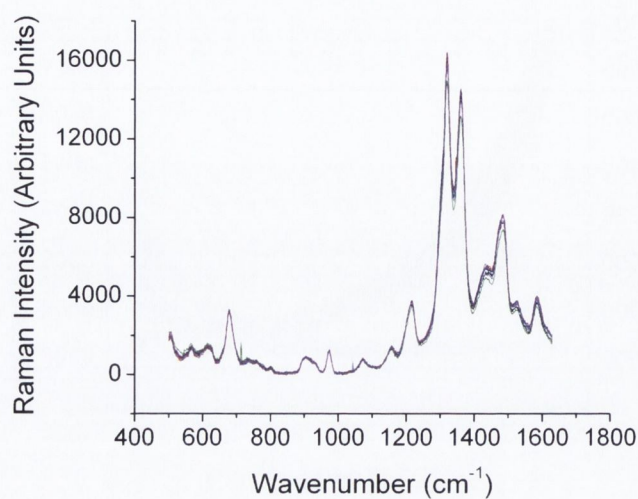
Figure E.6: The eight SERS spectra of the 10×10^{-5} M xanthopterin solution with colloids aggregated using 10 mM NaCl. The spectra were taken in the stainless steel wells at 633 nm using a 20 s exposure.
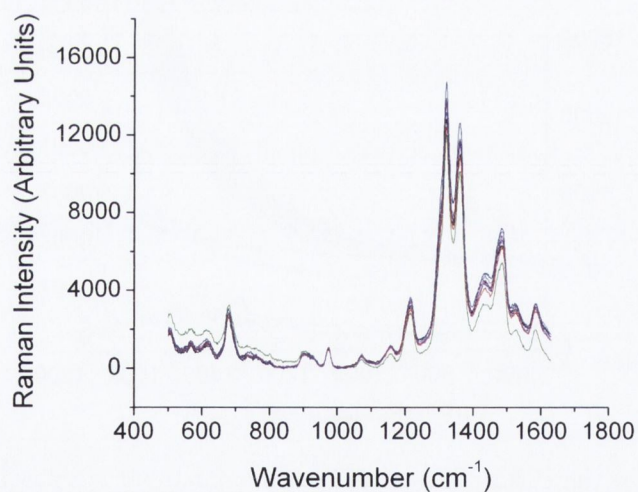
Figure E.7: The eight SERS spectra of the 8×10^{-5} M xanthopterin solution with colloids aggregated using 10 mM NaCl. The spectra were taken in the stainless steel wells at 633 nm using a 20 s exposure.
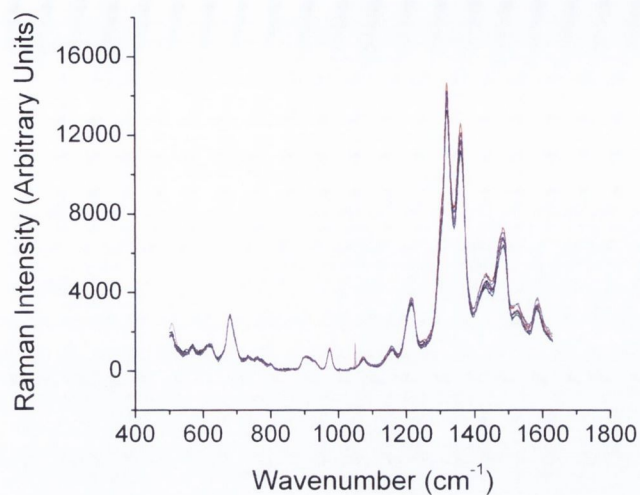
Figure E.8: The eight SERS spectra of the 6 ×10^{-5} M xanthopterin solution with colloids aggregated using 10 mM NaCl. The spectra were taken in the stainless steel wells at 633 nm using a 20 s exposure.
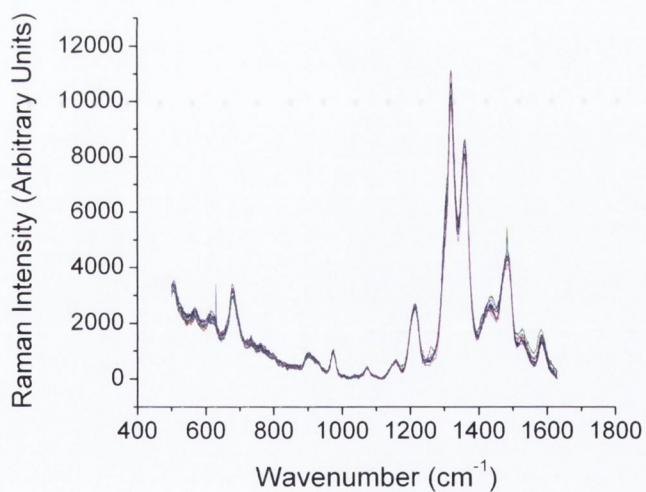
Figure E.9: The eight SERS spectra of the 4 ×10^{-5} M xanthopterin solution with colloids aggregated using 10 mM NaCl. The spectra were taken in the stainless steel wells at 633 nm using a 20 s exposure.
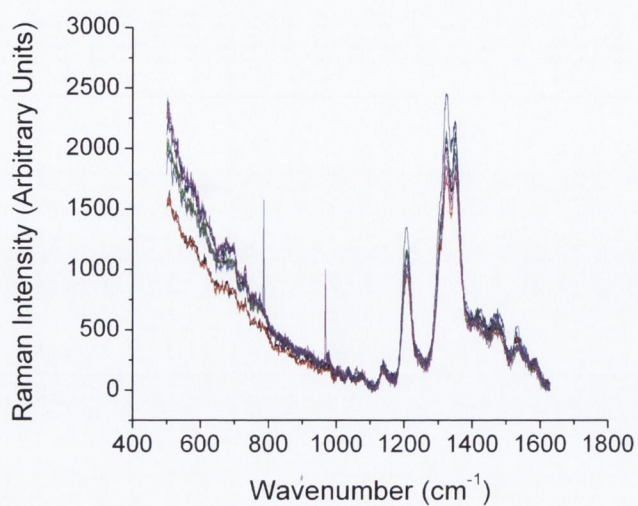
Figure E.10: The eight SERS spectra of the 2×10^{-5} M xanthopterin solution with colloids aggregated using 10 mM NaCl. The spectra were taken in the stainless steel wells at 633 nm using a 20 s exposure.
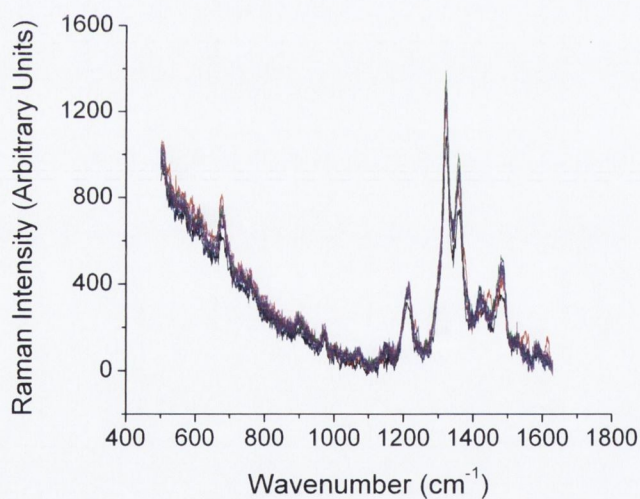
Figure E.11: The eight SERS spectra of the 10×10^{-5} M xanthopterin solution using no aggregating agent. The spectra were taken in the stainless steel wells at 633 nm using a 20 s exposure.
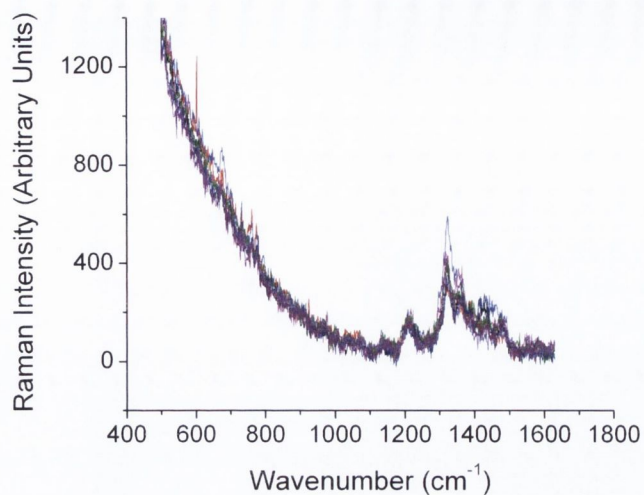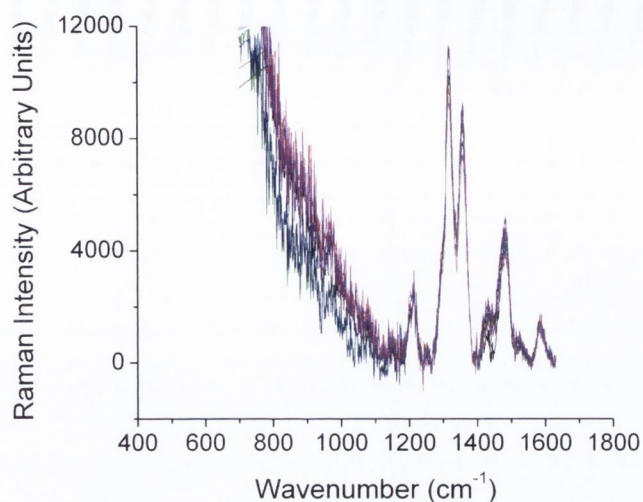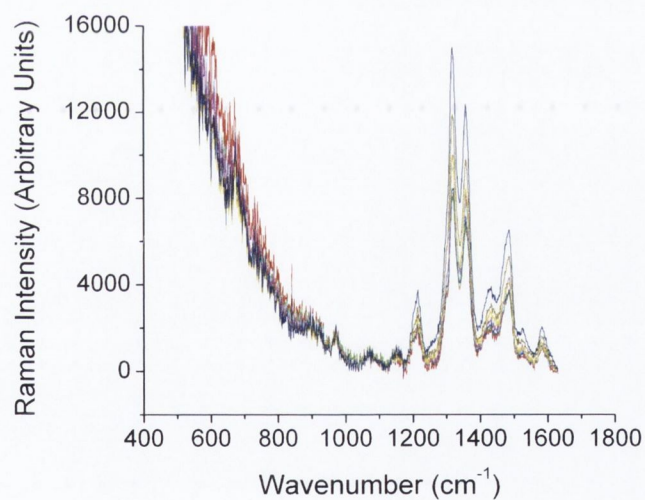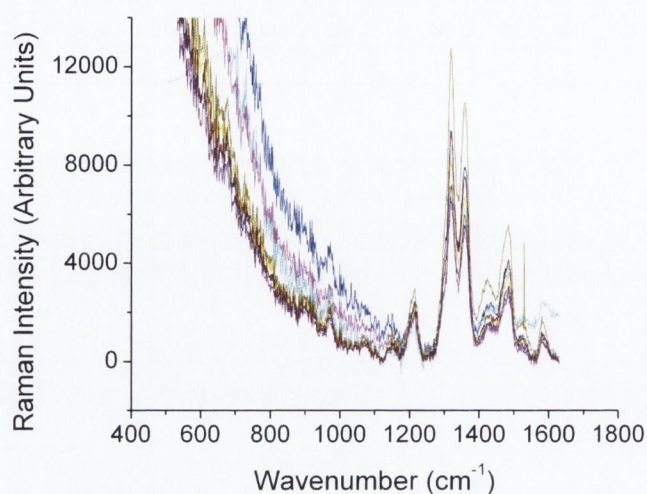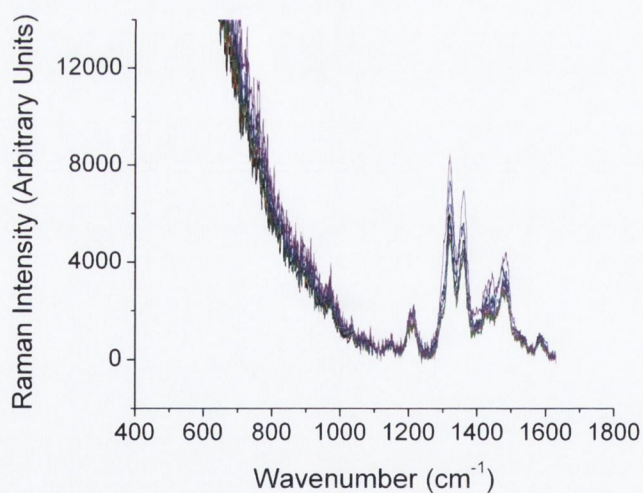
Figure E.12: The eight SERS spectra of the 8 $\times 10^{-5}$ M xanthopterin solution using no aggregating agent. The spectra were taken in the stainless steel wells at 633 nm using a 20 s exposure.
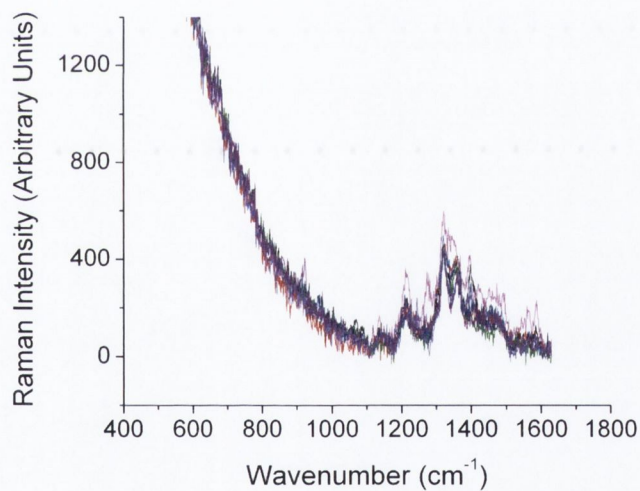
Figure E.13: The eight SERS spectra of the 6 $\times 10^{-5}$ M xanthopterin solution using no aggregating agent. The spectra were taken in the stainless steel wells at 633 nm using a 20 s exposure.
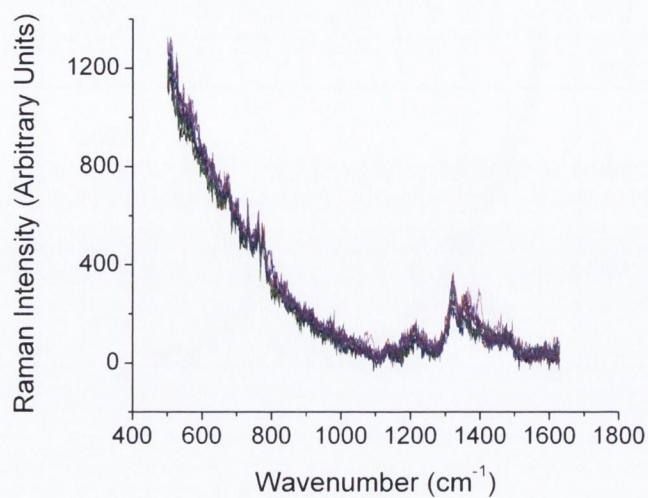
Figure E.14: The eight SERS spectra of the 4×10^{-5} M xanthopterin solution using no aggregating agent. The spectra were taken in the stainless steel wells at 633 nm using a 20 s exposure.
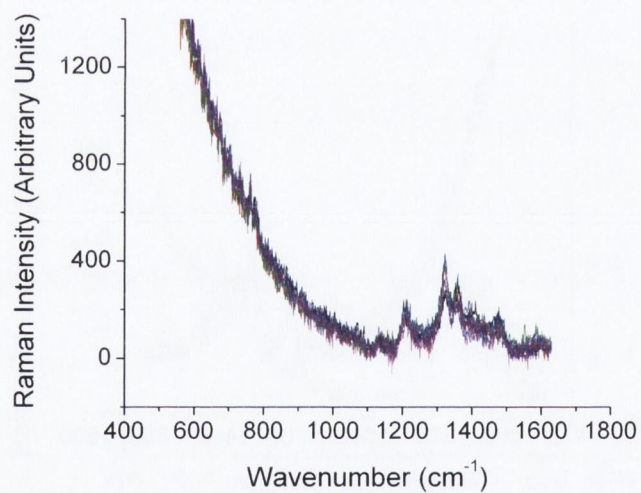
Figure E.15: The eight SERS spectra of the 2×10^{-5} M xanthopterin solution using no aggregating agent. The spectra were taken in the stainless steel wells at 633 nm using a 20 s exposure.

Figure E.16: The eight SERS spectra of the 10×10^{-5} M xanthopterin solution with colloids aggregated using 10 mM NaCl. The spectra were taken on glass microslides at 633 nm using a 20 s exposure.
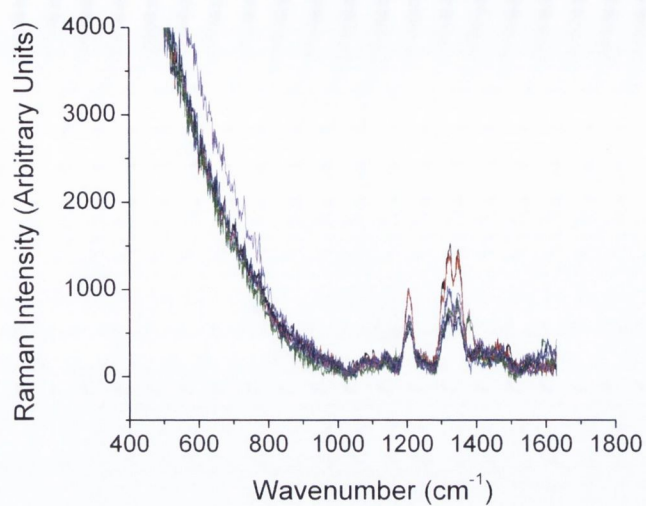

Figure E.17: The eight SERS spectra of the 8×10^{-5} M xanthopterin solution with colloids aggregated using 10 mM NaCl. The spectra were taken on glass microslides at 633 nm using a 20 s exposure.

Figure E.18: The eight SERS spectra of the 6×10^{-5} M xanthopterin solution with colloids aggregated using 10 mM NaCl. The spectra were taken on glass microslides at 633 nm using a 20 s exposure.

Figure E.19: The eight SERS spectra of the 4×10^{-5} M xanthopterin solution with colloids aggregated using 10 mM NaCl. The spectra were taken on glass microslides at 633 nm using a 20 s exposure.

Figure E.20: The eight SERS spectra of the 2×10^{-5} M xanthopterin solution with colloids aggregated using 10 mM NaCl. The spectra were taken on glass microslides at 633 nm using a 20 s exposure.

Appendix F: Additional SERS Spectra - Chapter 4

This appendix contains the sets of spectra referred to in Chapter 4. A list of the featured spectra is thus:

Figure F.1 & Figure F.2: Unannealed EBE films 2 and 3 with xanthopterin, 20 s exposure time.

Figure F.3 - Figure F.5: Unannealed EBE films 1-3 with Rhodamine 6G, 3 s exposure time.

Figure F.6 & Figure F.7: Annealed EBE films 1 and 3 with Rhodamine 6G, 3 s exposure time.

Figure F.8: nsPLD film 3 with Xanthopterin, 20 s exposure time.

Figure F.9 - Figure F.11: nsPLD films 1-3 with Rhodamine 6G, 3 s exposure time.

Figure F.12 & Figure F.13: nsPLD films 2 and 3 with Rhodamine 6G, 0.1 s exposure time.

Figure F.14 & Figure F.15: nsPLD films 2 and 3 with Rhodamine 6G mixed with silver colloids, 0.1 s exposure time.
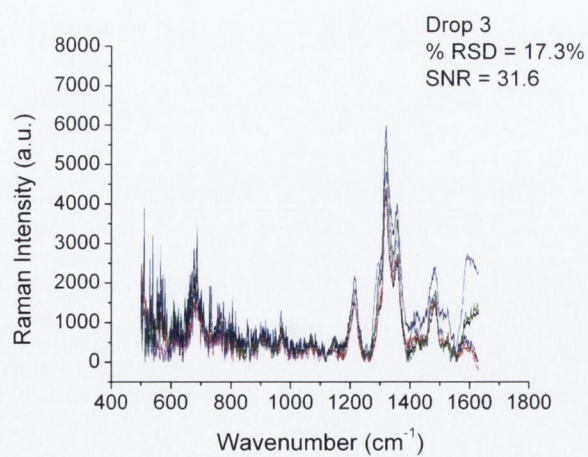
Figure F.16: Glass microslide with Rhodamine 6G mixed with silver colloids, 0.1 s exposure time.
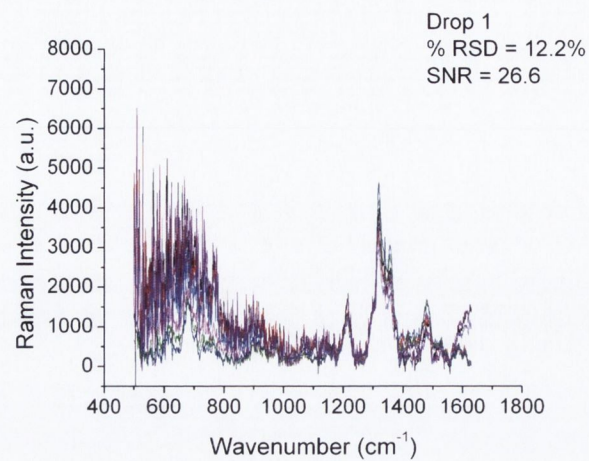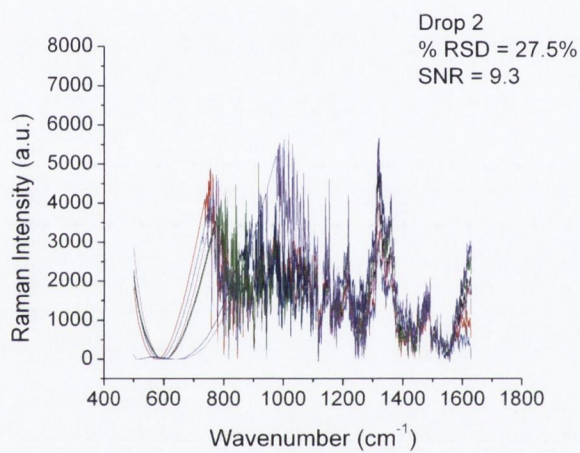
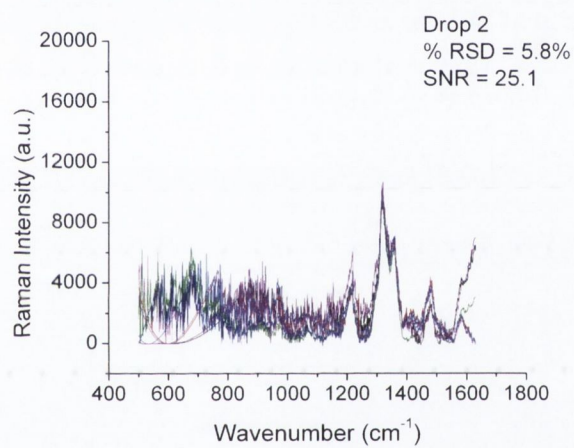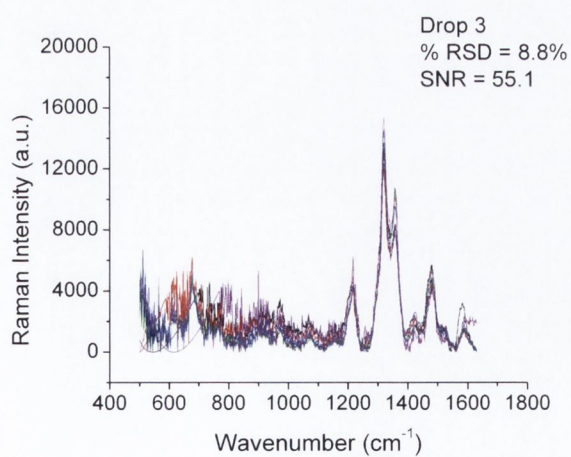**Figure F.1:** Three separate drops for a 1×10^{-4} M solution of xanthopterin deposited onto the second unannealed EBE film. The spectra were taken using a 633 nm excitation and a 20 s exposure time, and are shown for each drop in (a)-(c) respectively. The average %RSD and SNR are also shown for each set of data.
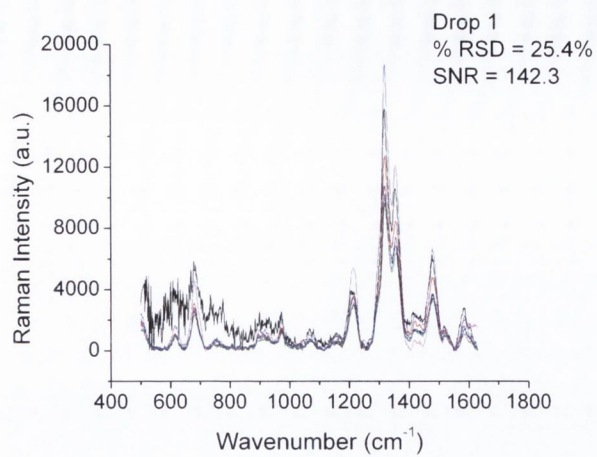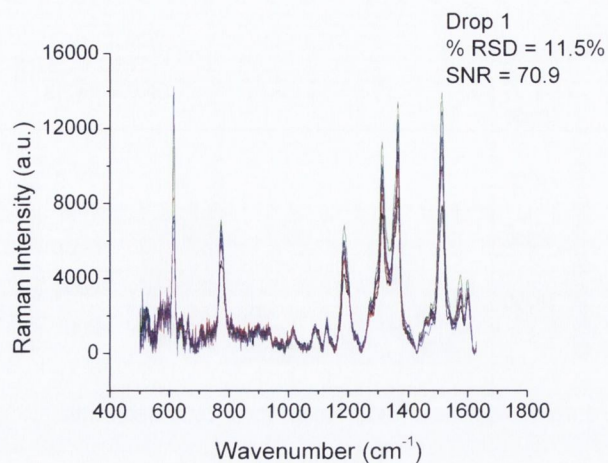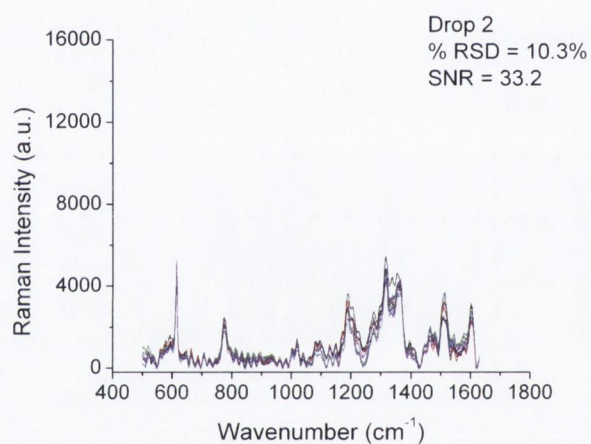
Figure F.2: Three separate drops for a 1×10^{-4} M solution of xanthopterin deposited onto the third unannealed EBE film. The spectra were taken using a 633 nm excitation and a 20 s exposure time, and are shown for each drop in (a)-(c) respectively. The average %RSD and SNR are also shown for each set of data.
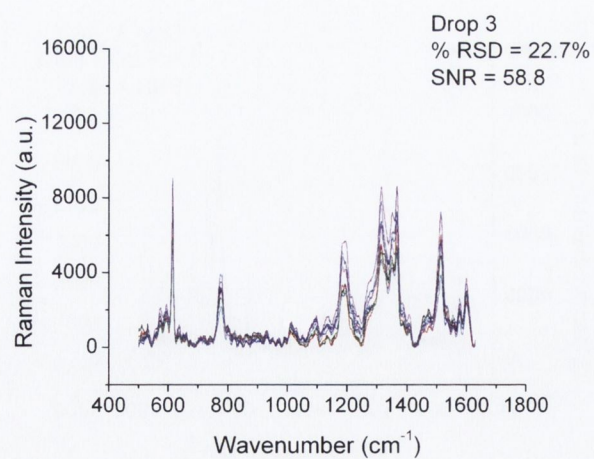
Figure F.3: Three separate drops for a 1.8×10^{-5} M solution of Rhodamine 6G deposited onto the first unannealed EBE film. The spectra were taken using a 633 nm excitation and a 3 s exposure time, and are shown for each drop in (a)-(c) respectively. The average %RSD and SNR are also shown for each set of data.
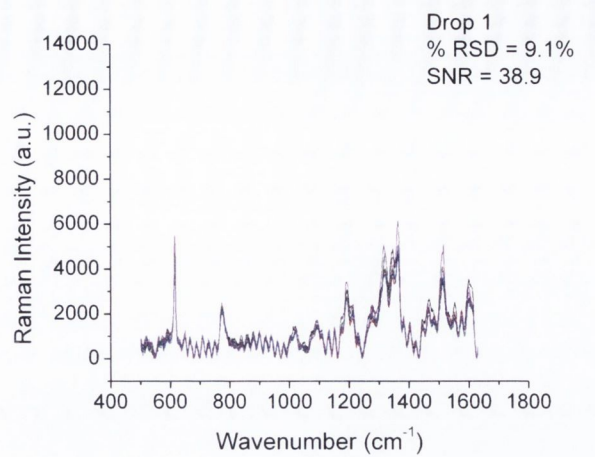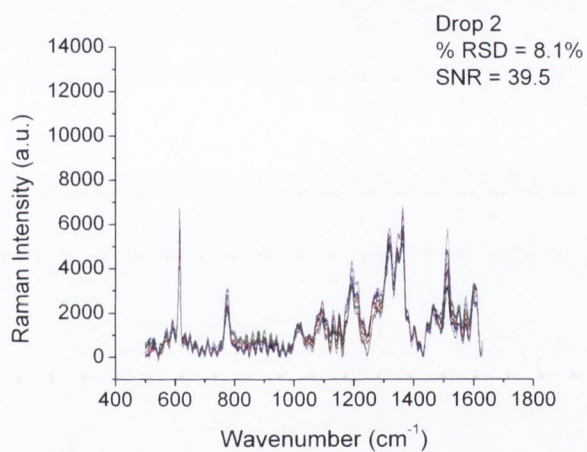
Drop 1
% RSD = 9.1%
SNR = 38.9

(a)

Drop 2
% RSD = 8.1%
SNR = 39.5

(b)

Drop 3
% RSD = 19.1%
SNR = 76.3

(c)

Figure F.4: Three separate drops for a 1.8×10^{-5} M solution of Rhodamine 6G deposited onto the second unannealed EBE film. The spectra were taken using a 633 nm excitation and a 3 s exposure time, and are shown for each drop in (a)-(c) respectively. The average %RSD and SNR are also shown for each set of data.

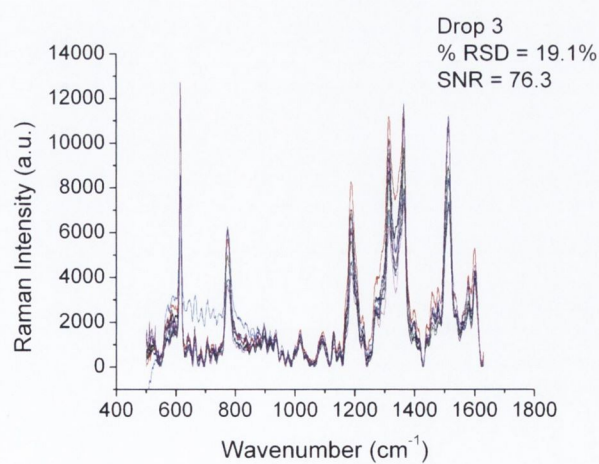**Figure F.5:** Three separate drops for a 1.8×10^{-5} M solution of Rhodamine 6G deposited onto the third unannealed EBE film. The spectra were taken using a 633 nm excitation and a 3 s exposure time, and are shown for each drop in (a)-(c) respectively. The average %RSD and SNR are also shown for each set of data.
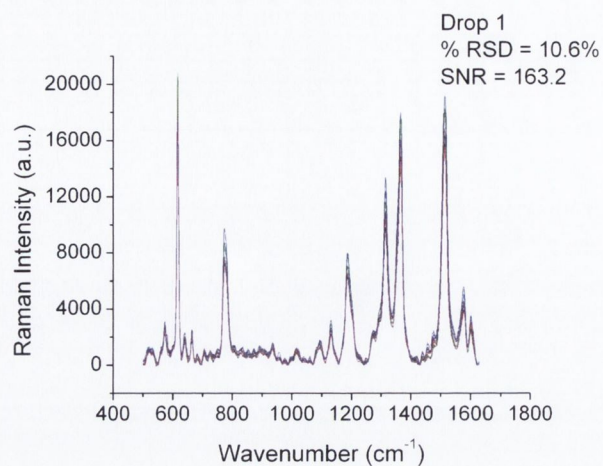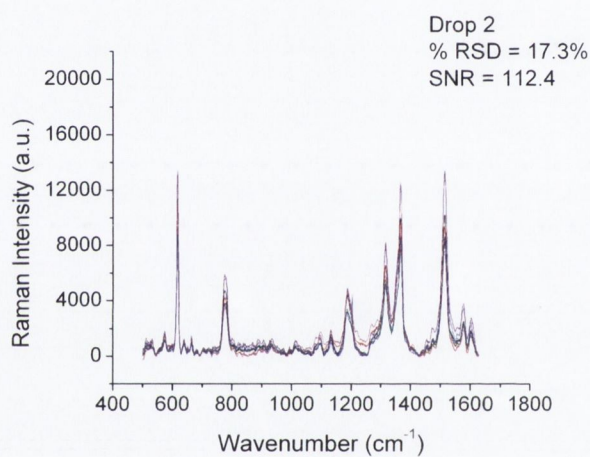
Figure F.6: Three separate drops for a 1.8×10^{-5} M solution of Rhodamine 6G deposited onto the first annealed EBE film. The spectra were taken using a 633 nm excitation and a 3 s exposure time, and are shown for each drop in (a)-(c) respectively. The average %RSD and SNR are also shown for each set of data.
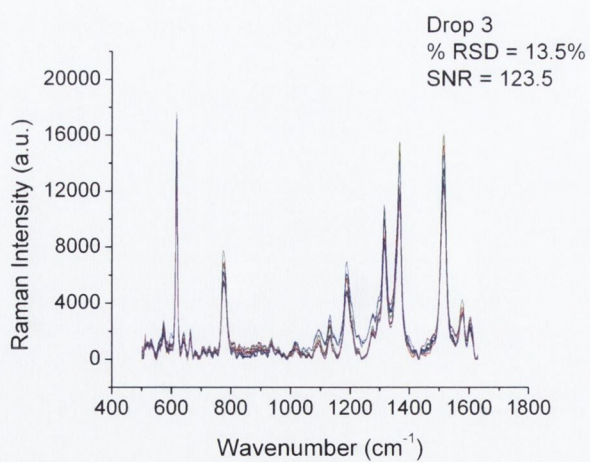
Figure F.7: Three separate drops for a 1.8×10^{-5} M solution of Rhodamine 6G deposited onto the third annealed EBE film. The spectra were taken using a 633 nm excitation and a 3 s exposure time, and are shown for each drop in (a)-(c) respectively. The average %RSD and SNR are also shown for each set of data.
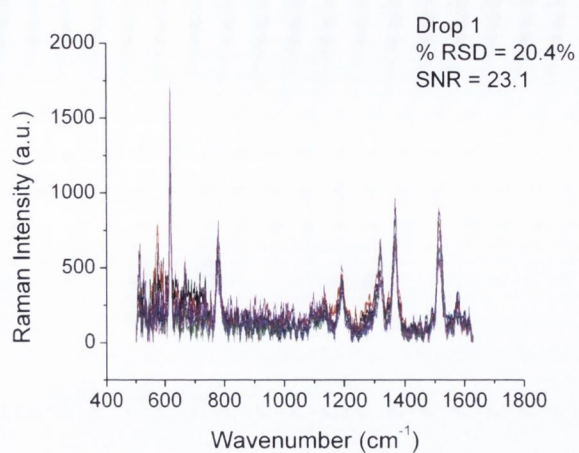
Figure F.8: Three separate drops for a 1×10^{-4} M solution of xanthopterin deposited onto the third nsPLD film. The spectra were taken using a 633 nm excitation and a 20 s exposure time, and are shown for each drop in (a)-(c) respectively. The average %RSD and SNR are also shown for each set of data.

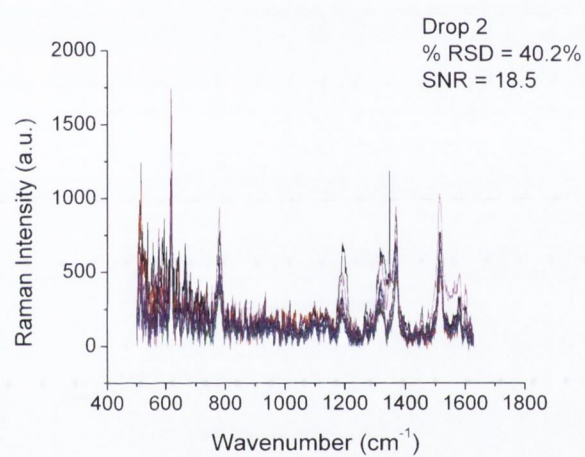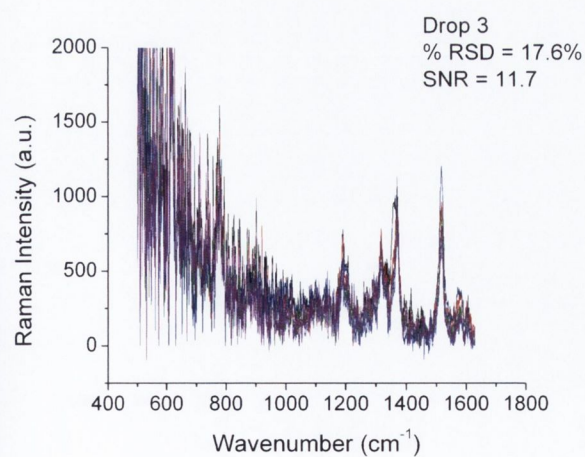**Figure F.9:** Three separate drops for a 1.8×10^{-5} M solution of Rhodamine 6G deposited onto the first nsPLD film. The spectra were taken using a 633 nm excitation and a 3 s exposure time, and are shown for each drop in (a)-(c) respectively. The average %RSD and SNR are also shown for each set of data.
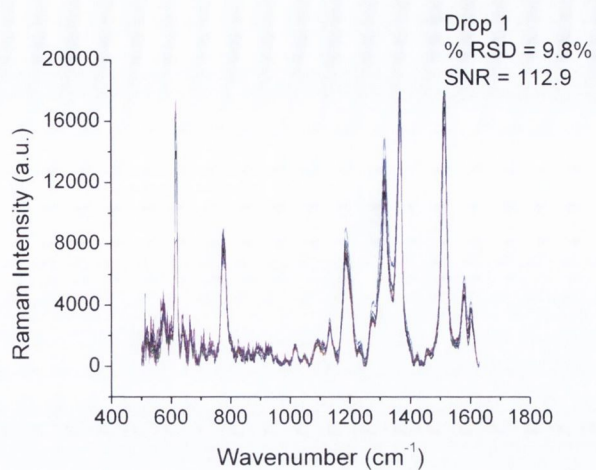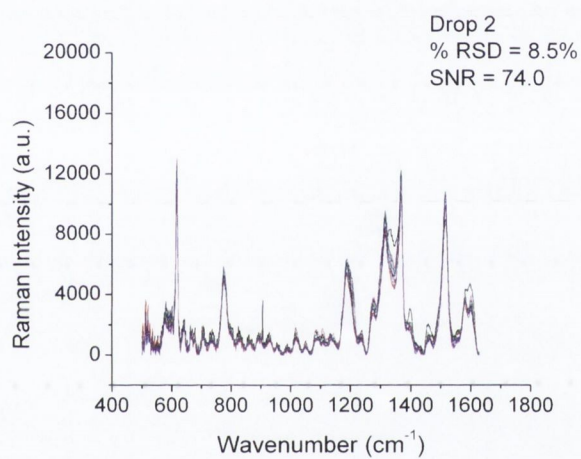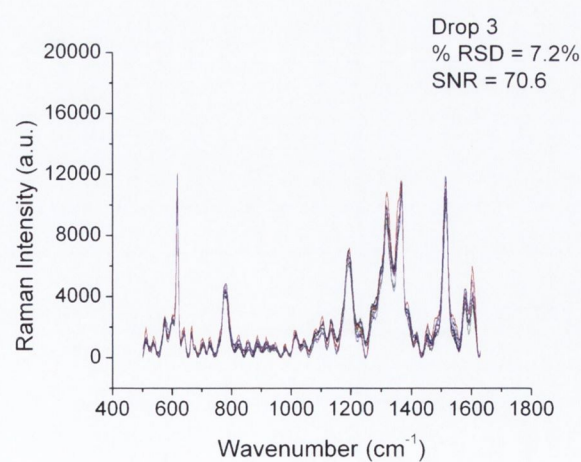
Figure F.10: Three separate drops for a 1.8×10^{-5} M solution of Rhodamine 6G deposited onto the second nsPLD film. The spectra were taken using a 633 nm excitation and a 3 s exposure time, and are shown for each drop in (a)-(c) respectively. The average %RSD and SNR are also shown for each set of data.
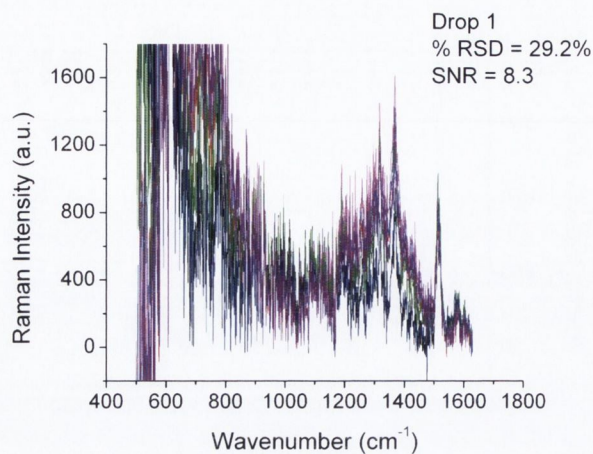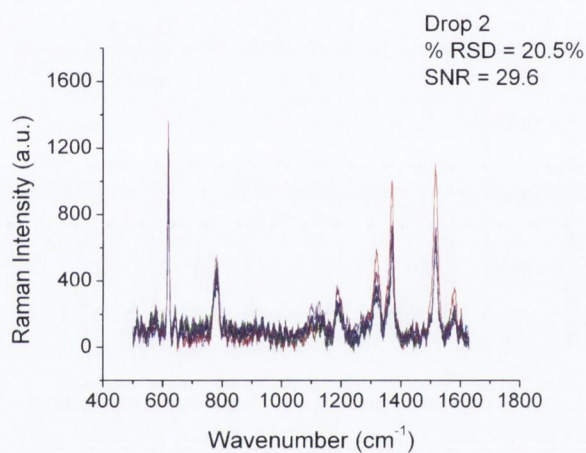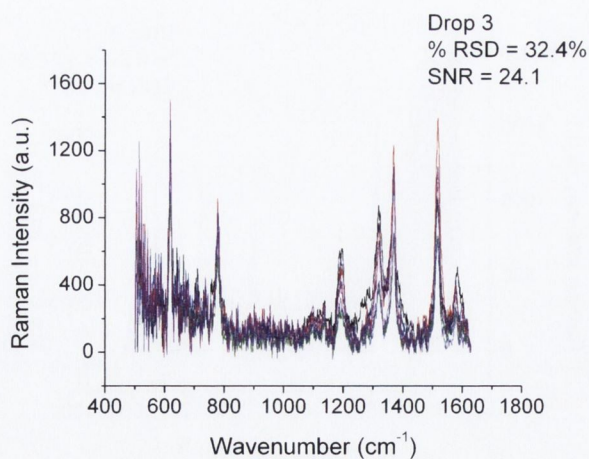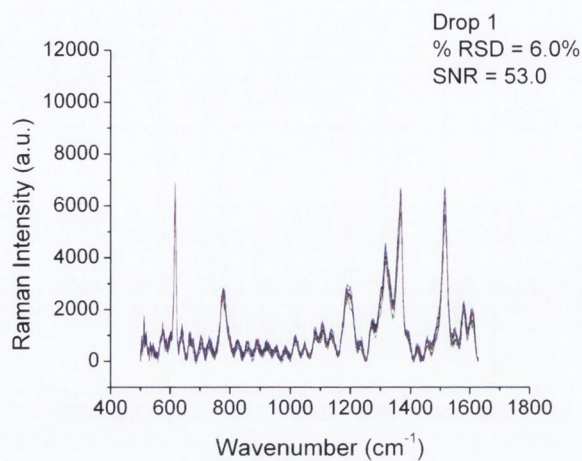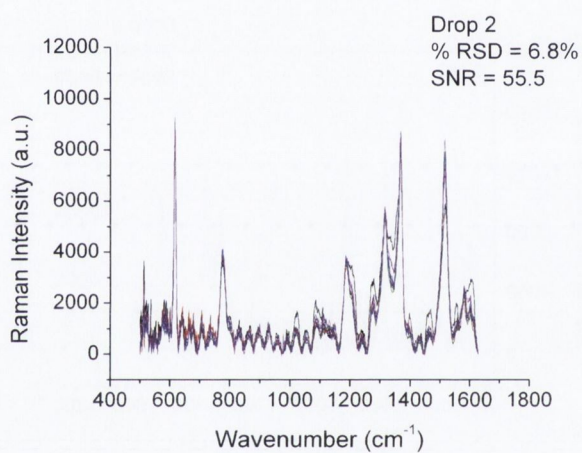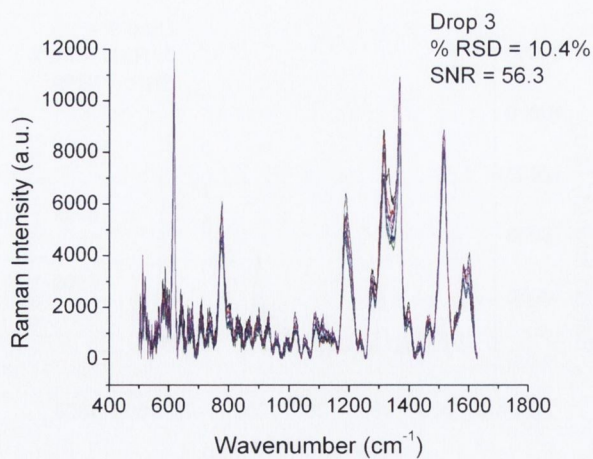
Figure F.11: Three separate drops for a 1.8×10^{-5} M solution of Rhodamine 6G deposited onto the third nsPLD film. The spectra were taken using a 633 nm excitation and a 3 s exposure time, and are shown for each drop in (a)-(c) respectively. The average %RSD and SNR are also shown for each set of data.

188
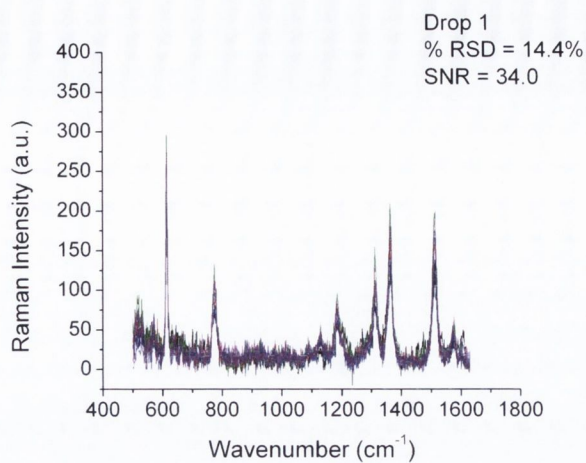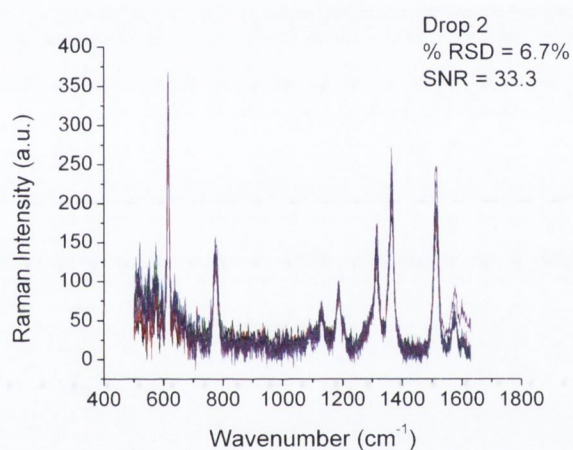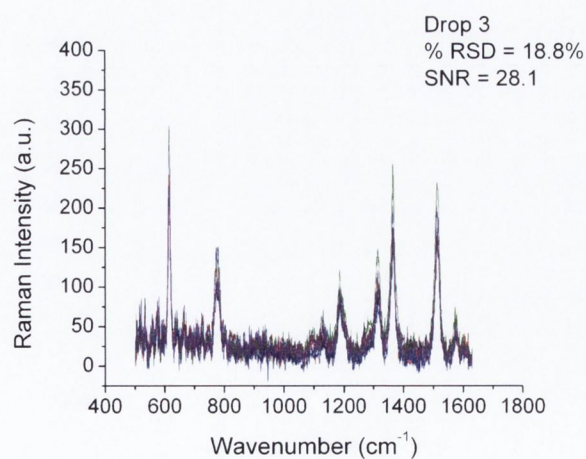
Figure F.12: Three separate drops of a 1.8×10^{-5} M solution of Rhodamine 6G deposited onto the second nsPLD film. The spectra were taken using a 633 nm excitation and a 0.1 s exposure time, and are shown for each drop in (a)-(c) respectively. The average %RSD and SNR are also shown for each set of data.
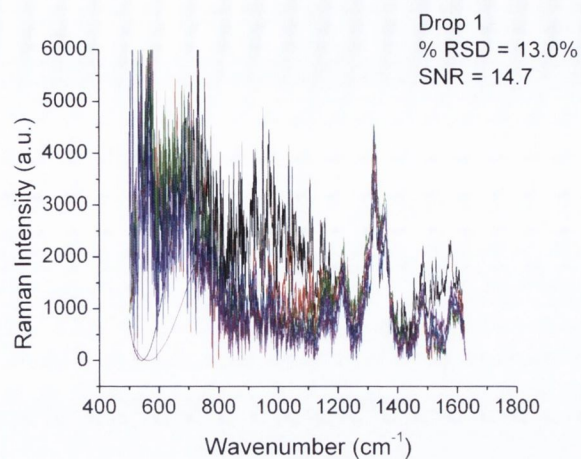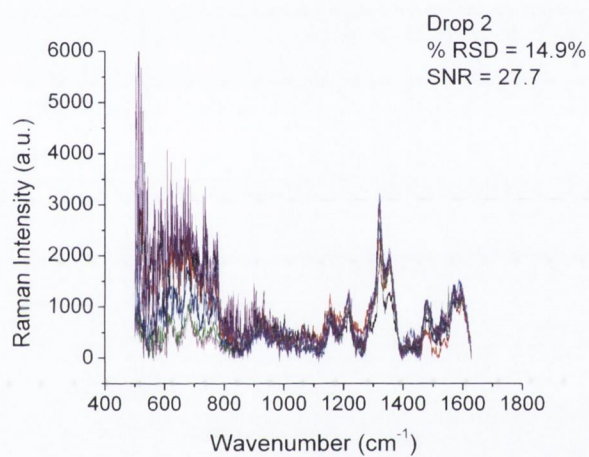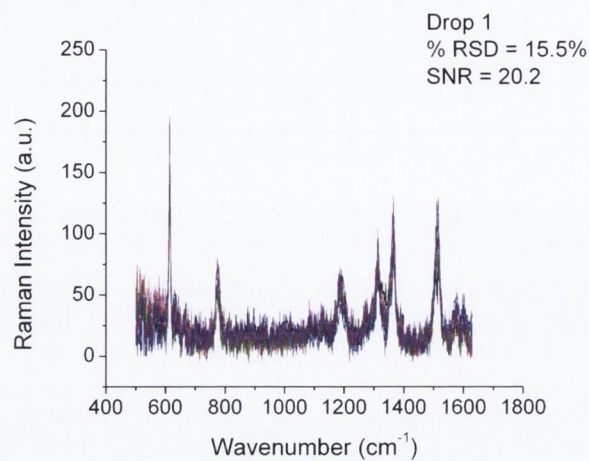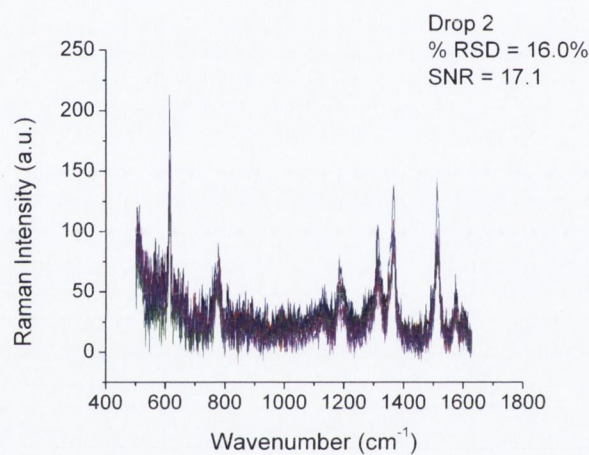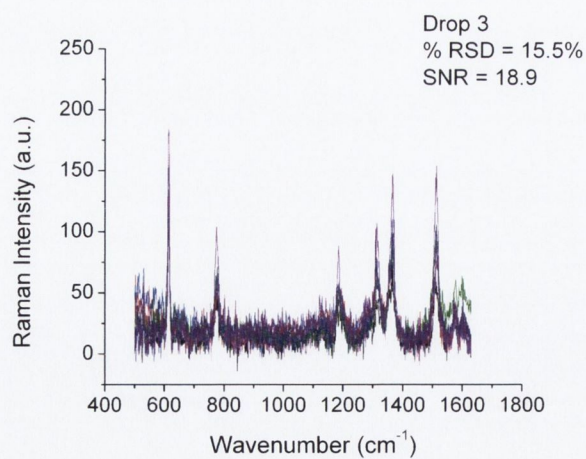
Figure F.13: Three separate drops of a 1.8×10^{-5} M solution of Rhodamine 6G deposited onto the third nsPLD film. The spectra were taken using a 633 nm excitation and a 0.1 s exposure time, and are shown for each drop in (a)-(c) respectively. The average %RSD and SNR are also shown for each set of data.
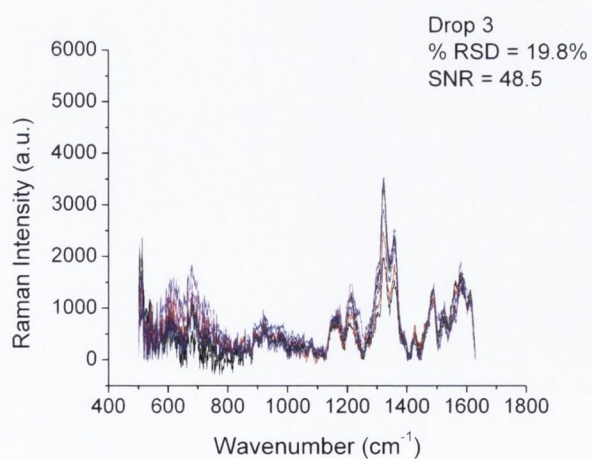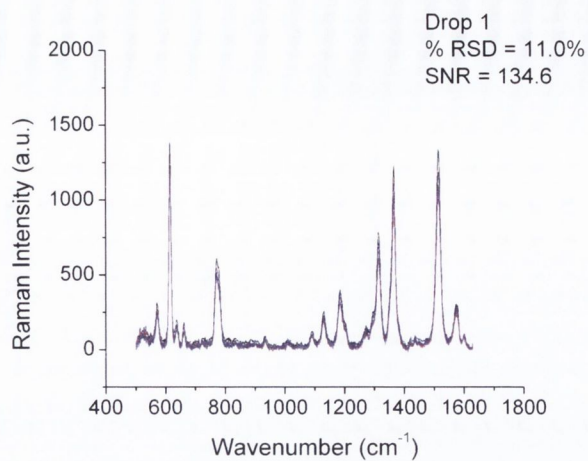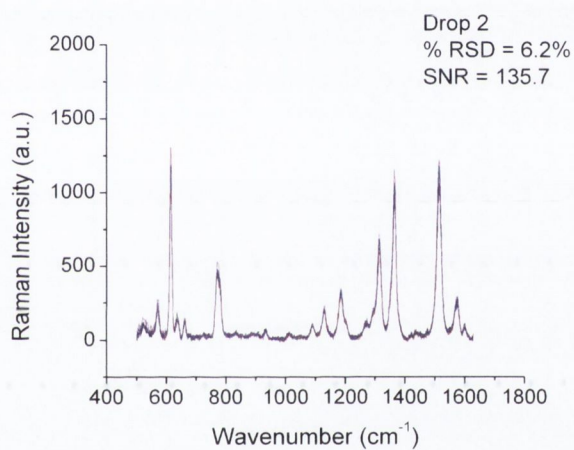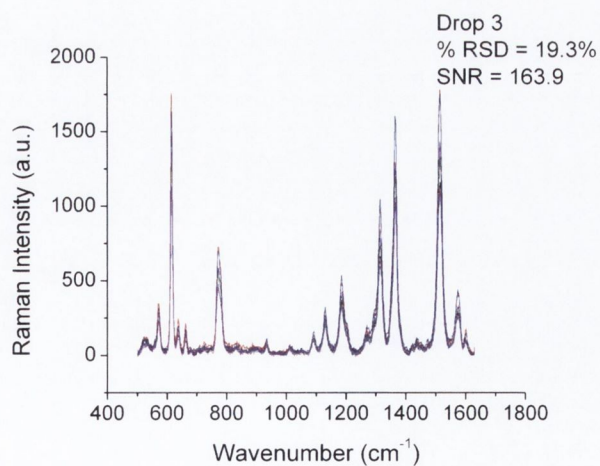
Figure F.14: Three separate drops of a 1.8×10^{-5} M solution of Rhodamine 6G, mixed with silver colloids and deposited onto the second nsPLD film. The spectra were taken using a 633 nm excitation and a 0.1 s exposure time, and are shown for each drop in (a)-(c) respectively. The average %RSD and SNR are also shown for each set of data.
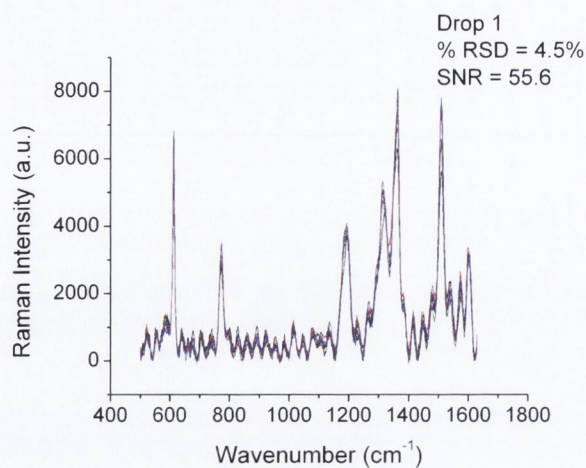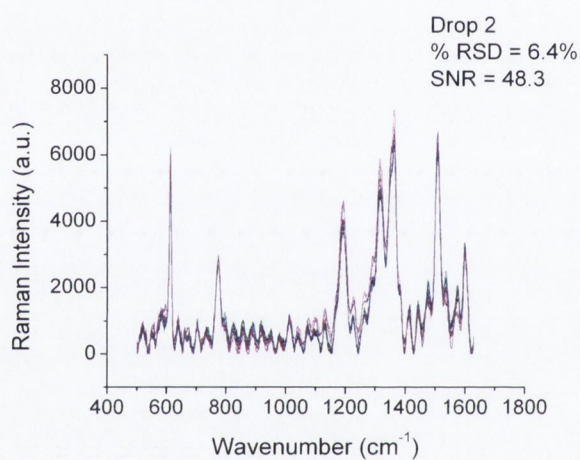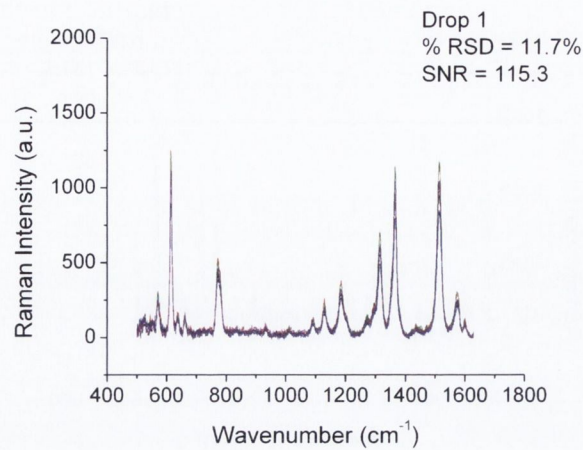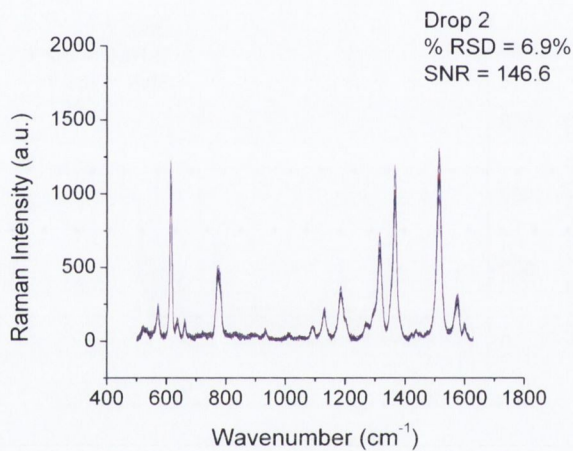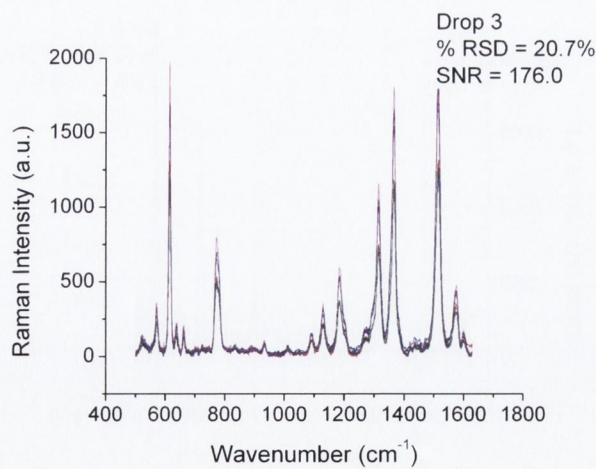
Figure F.15: Three separate drops of a 1.8×10^{-5} M solution of Rhodamine 6G, mixed with silver colloids and deposited onto the third nsPLD film. The spectra were taken using a 633 nm excitation and a 0.1 s exposure time, and are shown for each drop in (a)-(c) respectively. The average %RSD and SNR are also shown for each set of data.
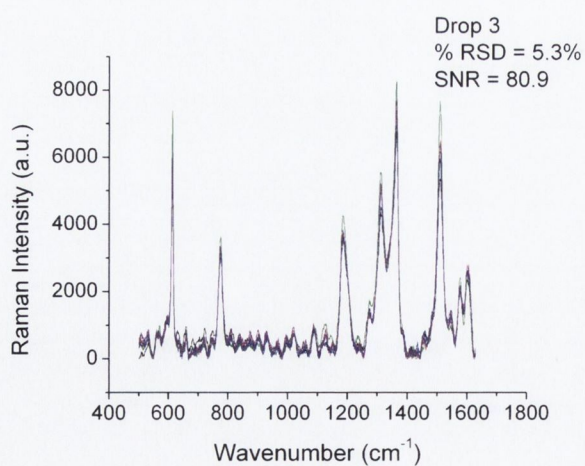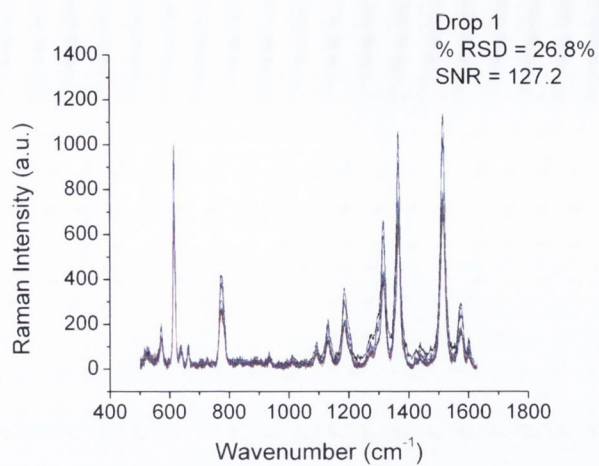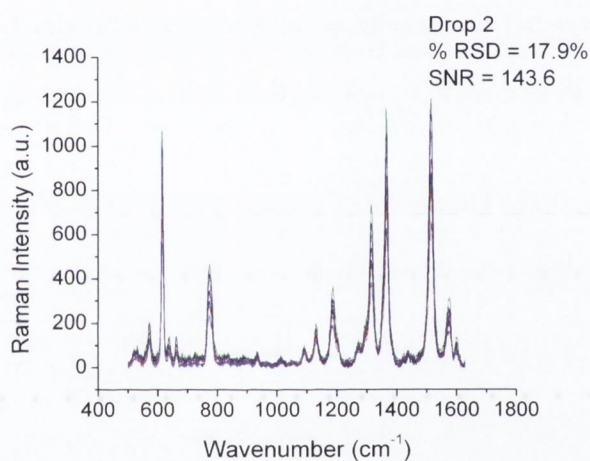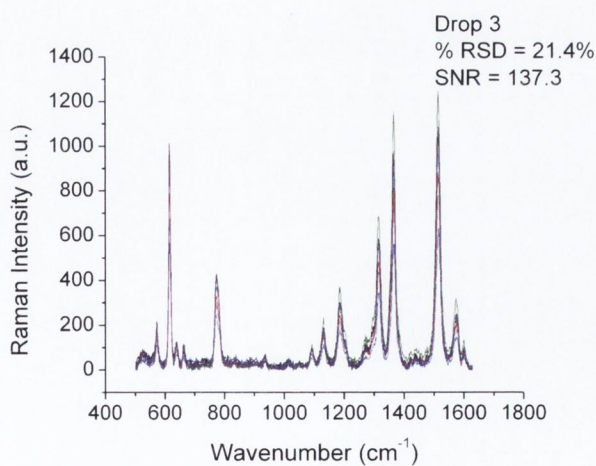
Figure F.16: Three separate drops of a 1.8×10^{-5} M solution of Rhodamine 6G, mixed with silver colloids and deposited onto a glass microslide. The spectra were taken using a 633 nm excitation and a 0.1 s exposure time, and are shown for each drop in (a)-(c) respectively. The average %RSD and SNR are also shown for each set of data.

# Bibliography

[1] I. Newton, "A letter of Mr. Isaac Newton, Professor of the Mathematicks in the University of Cambridge; containing his new theory about light and colors," *Philosophical Transactions of the Royal Society of London*, vol. 6, pp. 3075–3087, Jan. 1671.

[2] J. Maxwell, "On physical lines of force," *Philosophical Magazine*, pp. 11–23, Feb. 1861.

[3] M. Planck, "On the Law of Distribution of Energy in the Normal Spectrum On the Law of Distribution of Energy in the Normal Spectrum," *Annalen der Physik*, vol. 4, pp. 553–563, 1901.

[4] A. Einstein, "Concerning an heuristic point of view toward the emission and transformation of light," *Annalen der Physik*, vol. 17, pp. 132–148, 1905.

[5] F. G. Hopkins, "Note on a yellow pigment in butterflies," *Nature*, vol. 40, p. 335, 1889.

[6] F. G. Hopkins, "The Pigments of the Pieridae: A Contribution to the Study of Excretory Substances Which Function in Ornament," *Philosophical Transactions of the Royal Society B: Biological Sciences*, vol. 186, pp. 661–682, Jan. 1895.

[7] R. L. Blakey and S. J. Benkovic, eds., *Folates and Pterins, Volume 2 - Chemistry and Biochemistry of Pterins*. New York: John Wiley and Sons, Inc., 1985.

[8] A. F. Landymore and N. J. Antia, "White-light promoted degradation of leucopterin and related pteridines dissolved in seawater, with evidence for involvement of complexation from major divalent cations of seawater," *Marine Chemistry*, vol. 6, pp. 309–325, 1978.

[9] R. L. Rutowski, J. M. Macedonia, N. Morehouse, and L. Taylor-Taft, "Pterin pigments amplify iridescent ultraviolet signal in males of the orange sulphur butterfly, Colias eurytheme.," *Proceedings. Biological sciences / The Royal Society*, vol. 272, pp. 2329–35, Nov. 2005.

[10] W. C. Dunlap and M. Susic, "Photochemical decomposition rates of pteridines and flavins in seawater exposed to surface solar radiation," *Marine Chemistry*, vol. 19, pp. 99–107, 1986.

[11] A. Albert, D. J. Brown, and G. Cheeseman, "Pteridine studies. Part III. The solubility and the stability to hydrolysis of pteridines," *Journal of the Chemical Society*, pp. 4219–4232, 1952.

[12] "www.shircks.com."

[13] M. Vignoni, F. M. Cabrerizo, and C. Lorente, "New Results on the photochemistry of biopterin and neopterin in aqueous solution," *Photochemistry and Photobiology*, vol. 85, pp. 365–373, 2009.

[14] M. Vignoni, F. M. Cabrerizo, C. Lorente, C. Claparols, E. Oliveros, and A. H. Thomas, "Photochemistry of dihydrobiopterin in aqueous solution.," *Organic & Biomolecular Chemistry*, vol. 8, pp. 800–810, Feb. 2010.

[15] M. P. Serrano, M. Vignoni, M. L. Dántola, E. Oliveros, C. Lorente, and A. H. Thomas, "Emission properties of dihydropterins in aqueous solutions.," *Physical Chemistry Chemical Physics*, vol. 13, pp. 7419–25, Apr. 2011.

[16] M. Kritsky, T. Lyudnikova, E. Mironov, and I. Moskaleva, "The UV radiation-driven reduction of pterins in aqueous solution," *Journal of Photochemistry and Photobiology B: Biology*, vol. 39, pp. 43–48, May 1997.

[17] W. B. Watt and S. R. Bowden, "Chemical phenotypes of pteridine colour forms in Pieris butterflies," *Nature*, vol. 210, pp. 304–306, 1966.

[18] K. Ito and S. Kawanishi, "Photoinduced hydroxylation of deoxyguanosine in

DNA by pterins: sequence specificity and mechanism.," *Biochemistry*, vol. 36, pp. 1774–81, Feb. 1997.

[19] G. Petroselli, R. Erra-Balsells, F. M. Cabrerizo, C. Lorente, A. L. Capparelli, A. M. Braun, E. Oliveros, and A. H. Thomas, "Photosensitization of 2'-deoxyadenosine-5'-monophosphate by pterin.," *Organic & Biomolecular Chemistry*, vol. 5, pp. 2792–2729, Sept. 2007.

[20] G. Petroselli, M. L. Da, F. M. Cabrerizo, A. L. Capparelli, C. Lorente, E. Oliveros, and H. Thomas, "Oxidation of 2'-Deoxyguanosine 5'-Monophosphate photoinduced by pterin : Type I versus Type II mechanism," *Journal of the American Chemical Society*, no. 2, pp. 298–308, 2008.

[21] C. Lorente and A. H. Thomas, "Photophysics and photochemistry of pterins in aqueous solution.," *Accounts of chemical research*, vol. 39, pp. 395–402, June 2006.

[22] "http://www.chemicaldictionary.org/dic/X/Xanthopterin_846.html."

[23] "http://www.hmdb.ca/metabolites/HMDB00704."

[24] N. Saleh, J. Graham, A. Afaneh, Y. a. Al-Soud, G. Schreckenbach, and F. T. Esmadi, "Pteridine-based fluorescent pH sensors designed for physiological applications," *Journal of Photochemistry and Photobiology A: Chemistry*, vol. 247, pp. 63–73, Nov. 2012.

[25] M. Plotkin, S. Volynchik, N. Y. Ermakov, A. Benyamini, Y. Boiko, D. J. Bergman, and J. S. Ishay, "Xanthopterin in the Oriental hornet (Vespa orientalis): light absorbance is increased with maturation of yellow pigment granules.," *Photochemistry and photobiology*, vol. 85, no. 4, pp. 955–61, 2009.

[26] R. S. Hall, R. Agarwal, D. Hitchcock, J. M. Sauder, K. Stephen, S. Swaminathan, and F. M. Raushel, "Discovery and structure determination of the orphan enzyme isoxanthopterin deaminase," *Biochemistry*, vol. 49, no. 20, pp. 4374–4382, 2010.

[27] H. Ninnemann, "Some aspects of blue light research during the last decade," *Photochemistry and Photobiology*, vol. 61, no. 1, pp. 22–31, 1995.

[28] P. Galland and H. Senger, "The role of pterins in the photoreception and metabolism of plants," *Photochemistry and Photobiology*, vol. 48, pp. 811–820, 1988.

[29] W. Pfleiderer, "Nature pteridine pigments pigments found in butterflies wings and insect eyes," *Chimia*, vol. 48, pp. 488–489, 1994.

[30] M. Obika and J. Matsumoto, "Morphological and biochemical studies on amphibian bright-colored pigment cells and their pterinosomes," *Experimental Cell Research*, vol. 52, pp. 646–659, 1968.

[31] K. R. Royal, *Analysis of red and yellow pigments in two mutants of the Siamese Fighting Fish, Betta splendens.* PhD thesis, Drake University, 1970.

[32] K. J. McGraw, M. B. Toomey, P. M. Nolan, N. I. Morehouse, M. Massaro, and P. Jouventin, "A description of unique fluorescent yellow pigments in penguin feathers.," *Pigment cell research / sponsored by the European Society for Pigment Cell Research and the International Pigment Cell Society*, vol. 20, pp. 301–304, Aug. 2007.

[33] F. Gaill and M. Momzikoff, "The presence of riboflavin and two pterins in ascidians (Tunicata) and their excretion into sea water," *Marine Biology*, vol. 29, pp. 315–319, 1975.

[34] T. Fukushima and J. C. Nixon, "Analysis of reduced forms of biopterin in biological tissues and fluids," *Analytical Biochemistry*, vol. 102, pp. 176–188, 1980.

[35] N. Kokolis, "Evolution of DNA and tetrahydrobiopterin during rat liver regeneration," *International Journal of Biochemistry*, vol. 6, pp. 475–478, 1975.

[36] D. A. Häberle, H. Schiffl, G. Mayer, G. Hennings, and H. Rembold, "Renal balance of pterin cofactors in the rat. A clearance and micropuncture study," *Pflügers Archiv*, vol. 375, pp. 9–16, 1978.

[37] T. Fukushima and T. Shiota, "Pterins in human urine.," *Journal of Biological Chemistry*, vol. 247, pp. 4549–56, July 1972.

[38] M. T. Abou-Saleh, R. Ghubash, L. Karim, M. Krymski, and D. N. Anderson, "The role of pterins and related factors in the biology of early postpartum depression," *European Neuropsychopharmacology*, vol. 9, pp. 295–300, June 1999.

[39] J. L. Lord, A. de Peyster, P. J. E. Quintana, and R. P. Metzger, "Cytotoxicity of xanthopterin and isoxanthopterin in MCF-7 cells.," *Cancer Letters*, vol. 222, pp. 119–24, May 2005.

[40] S. Kar, S. Dey, and C. R. Bhattacharjee, "Effect of 2-amino-4-hydroxypteridine on induced tumor (Daltons Lymphoma) in animal model," *Assam University Journal of Science & Technology : Physical Sciences and Technology*, vol. 6, pp. 6–9, 2010.

[41] I. Smith, D. W. Howells, and K. Hyland, "Pteridines and mono-amines: relevance to neurological damage.," *Postgraduate Medical Journal*, vol. 62, pp. 113–123, Feb. 1986.

[42] D. Voet, J. G. Voet, and C. W. Pratt, *Fundamentals of Biochemistry*. New York ; Chichester: Wiley, Mar. 1999.

[43] S. Gamagedara, S. Gibbons, and Y. Ma, "Investigation of urinary pteridine levels as potential biomarkers for noninvasive diagnosis of cancer.," *Clinica Chimica Acta*, vol. 412, pp. 120–128, Jan. 2011.

[44] F. Cañada Cañada, A. Espinosa-Mansilla, A. Muñoz de la Peña, and A. Mancha de Llanos, "Determination of marker pteridins and biopterin reduced forms, tetrahydrobiopterin and dihydrobiopterin, in human urine, using a post-column photoinduced fluorescence liquid chromatographic derivatization method.," *Analytica Chimica Acta*, vol. 648, pp. 113–122, Aug. 2009.

[45] T. Yamamoto, Y. Moriwaki, S. Takahashi, Z. Tsutsumi, J. Yamakita, Y. Nasako, K. Hiroishi, and K. Higashino, "Determination of human plasma xanthine oxidase

activity by high-performance liquid chromatography.," *Journal of Chromatography B.*, vol. 681, pp. 395–400, June 1996.

[46] A. E. Mansilla, I. D. Merds, and F. Salinas, "Analysis of pteridines and creatinine in urine by HPLC with serial fluorimetric and photometric detectors," *Chromatographia*, vol. 53, pp. 510–514, 2001.

[47] I. Durán Merás, A. Espinosa Mansilla, and M. J. Rodríguez Gómez, "Determination of methotrexate, several pteridines, and creatinine in human urine, previous oxidation with potassium permanganate, using HPLC with photometric and fluorimetric serial detection.," *Analytical Biochemistry*, vol. 346, pp. 201–209, Nov. 2005.

[48] A. Ormazabal, A. García-Cazorla, Y. Fernández, E. Fernández-Alvarez, J. Campistol, and R. Artuch, "HPLC with electrochemical and fluorescence detection procedures for the diagnosis of inborn errors of biogenic amines and pterins.," *Journal of Neuroscience Methods*, vol. 142, pp. 153–158, Mar. 2005.

[49] A. Mancha de Llanos, M. M. De Zan, M. J. Culzoni, A. Espinosa-Mansilla, F. Cañada Cañada, A. Muñoz de la Peña, and H. C. Goicoechea, "Determination of marker pteridines in urine by HPLC with fluorimetric detection and second-order multivariate calibration using MCR-ALS.," *Analytical and Bioanalytical Chemistry*, vol. 399, pp. 2123–35, Feb. 2011.

[50] M. J. Culzoni, A. Mancha de Llanos, M. M. De Zan, A. Espinosa-Mansilla, F. Cañada Cañada, A. Muñoz de la Peña, and H. C. Goicoechea, "Enhanced MCR-ALS modeling of HPLC with fast scan fluorimetric detection second-order data for quantitation of metabolic disorder marker pteridines in urine.," *Talanta*, vol. 85, pp. 2368–2374, Oct. 2011.

[51] F. Han, B. H. Huynh, H. Shi, B. Lin, and Y. Ma, "Pteridine analysis in urine by capillary electrophoresis using laser-induced fluorescence detection.," *Analytical Chemistry*, vol. 71, pp. 1265–1269, Apr. 1999.

[52] S. E. Gibbons, I. Stayton, and Y. Ma, "Optimization of urinary pteridine analysis

conditions by CE-LIF for clinical use in early cancer detection.," *Electrophoresis*, vol. 30, pp. 3591–3597, Oct. 2009.

[53] A. Jiménez Girón, E. Martín-Tornero, M. Hurtado Sánchez, I. Durán Merás, and A. Espinosa Mansilla, "A simple HPLC-ESI-MS method for the direct determination of ten pteridinic biomarkers in human urine," *Talanta*, vol. In Press, p. http://dx.doi.org/10.1016/j.talanta.2012.09.061, Oct. 2012.

[54] S.-H. Cho, J.-U. Na, H. Youn, C.-S. Hwang, C.-H. Lee, and S.-O. Kang, "Tepidopterin, 1-O-(L-threo-biopterin-2-yl)-β-N-acetylglucosamine from Chlorobium tepidum," *Biochimica et Biophysica Acta*, vol. 1379, pp. 53–60, 1998.

[55] K. Teigen, N. A. Frø ystein, and A. Martínez, "The structural basis of the recognition of phenylalanine and pterin cofactors by phenylalanine hydroxylase: implications for the catalytic mechanism.," *Journal of Molecular Biology*, vol. 294, pp. 807–823, Dec. 1999.

[56] D. S. Wishart, M. J. Lewis, J. A. Morrissey, M. D. Flegel, K. Jeroncic, Y. Xiong, D. Cheng, R. Eisner, B. Gautam, D. Tzur, S. Sawhney, F. Bamforth, R. Greiner, and L. Li, "The human cerebrospinal fluid metabolome.," *Journal of Chromatography B.*, vol. 871, pp. 164–173, Aug. 2008.

[57] B. Brutovský, J. Uličný, P. Miškovský, V. Lisý, and L. Chinsky, "Resonance Raman Spectra of Selected Pterin Molecules . Genetic Algorithms Approach to Force Field Scaling," *Journal of Raman Spectroscopy*, vol. 29, pp. 833–839, 1998.

[58] Z. Feng, C. Liang, M. Li, J. Chen, and C. Li, "Surface-enhanced Raman scattering of xanthopterin adsorbed on colloidal silver," *Journal of Raman Spectroscopy*, vol. 32, pp. 1004–1007, Dec. 2001.

[59] R. J. Stokes, E. McBride, C. G. Wilson, J. M. Girkin, W. E. Smith, and D. Graham, "Surface-enhanced Raman scattering spectroscopy as a sensitive and selective technique for the detection of folic acid in water and human serum.," *Applied Spectroscopy*, vol. 62, pp. 371–376, Apr. 2008.

[60] R. Stevenson, R. J. Stokes, D. MacMillan, D. Armstrong, K. Faulds, R. Wadsworth, S. Kunuthur, C. J. Suckling, and D. Graham, "In situ detection of pterins by SERS.," *The Analyst*, vol. 134, pp. 1561–1564, Aug. 2009.

[61] C. E. Wayne and R. P. Wayne, *Photochemistry*. Oxford University Press, 1996.

[62] A. Sharma and S. Schulman, *Introduction to fluorescence spectroscopy*. New York ; Chichester: Wiley, Oct. 1999.

[63] E. Le Ru and P. G. Etchegoin, *Principles of surface-enhanced Raman spectroscopy and related plasmonic effects*. Amsterdam ; Boston: Elsevier, 2009.

[64] C. N. Banwell and E. M. McCash, *Fundamentals of Molecular Spectroscopy*. McGraw-Hill Publishing Company, 4th ed., 1994.

[65] N. Monardes, "Historia medicinal del las cosas que se traen de nuestra Indias Occidentales," 1574.

[66] A. Kircher, "Ars Magna Lucis et Umbrae," 1646.

[67] J. F. W. Herschel, "On a case of superficial colour presented by a homogeneous liquid internally colourless," *Philosophical Transactions of the Royal Society of London*, vol. 135, pp. 143–145, Jan. 1845.

[68] G. G. Stokes, "On the change of refrangibility of light," *Philosophical Transactions of the Royal Society of London*, vol. 142, pp. 463–562, 1852.

[69] B. Herman, *Fluorescence Microscopy*. BIOS Scientific Publishers Limited, 2nd ed., 1998.

[70] C. V. Raman and K. S. Krishnan, "A New Type of Secondary Radiation," *Nature*, vol. 121, pp. 501–502, Mar. 1928.

[71] R. A. Álvarez Puebla, "Effects of the excitation wavelength on the SERS spectrum," *Journal of Physical Chemistry Letters*, vol. 3, pp. 857–866, 2012.

[72] S. A. Meyer, E. C. Le Ru, and P. G. Etchegoin, "Quantifying resonant Raman

cross sections with SERS," *Journal of Physical Chemistry A*, vol. 114, pp. 5515–5519, May 2010.

[73] A. C. Benniston, P. Matousek, I. E. McCulloch, A. W. Parker, and M. Towrie, "Detailed picosecond Kerr-gated time-resolved resonance Raman spectroscopy and time-resolved emission studies of Merocyanine 540 in various solvents," *The Journal of Physical Chemistry A*, vol. 107, pp. 4347–4353, June 2003.

[74] J. K. Hurst, P. Wormell, G. B. Bacskay, and A. R. Lacey, "Molecular vibrations of pteridine and two symmetric tetraazanaphthalenes," *Journal of Physical Chemistry A*, vol. 104, pp. 7386–7397, 2000.

[75] Y. Xia and N. J. Halas, "Shape-controlled synthesis and surface plasmonic properties of metallic nanostructures," *MRS Bulletin*, vol. 30, no. May, pp. 338–348, 2005.

[76] S. A. Maier, *Plasmonics: Fundamentals and Applications.* Springer, 2007.

[77] P. L. Stiles, J. A. Dieringer, N. C. Shah, and R. P. Van Duyne, "Surface-enhanced Raman spectroscopy," *Annual Review of Analytical Chemistry*, vol. 1, pp. 601–626, Jan. 2008.

[78] D. L. Jeanmarie and R. P. Van Duyne, "Surface Raman Spectroelectrochemistry, Part 1: Heteroclic, aromatic and aliphatic amines adsorbed on the anodized silver electrode.," *Journal of Electroanalytical Chemistry and Interfacial Electrochemistry*, vol. 84, pp. 1–20, 1977.

[79] M. G. Albrecht and J. A. Creighton, "Anomalously intense Raman spectra of pyridine at a silver electrode," *Journal of the American Chemical Society*, vol. 99, pp. 5215–5217, 1977.

[80] S. Nie and S. R. Emory, "Probing single molecules and single nanoparticles by surface-enhanced Raman scattering," *Science*, vol. 275, pp. 1102–1106, Feb. 1997.

[81] K. Kneipp, Y. Wang, H. Kneipp, L. Perelman, I. Itzkan, R. Dasari, and M. Feld,

"Single molecule detection using surface-enhanced Raman scattering (SERS)," *Physical Review Letters*, vol. 78, pp. 1667–1670, Mar. 1997.

[82] M. V. Cañamares, J. V. Garcia-Ramos, S. Sanchez-Cortes, M. Castillejo, and M. Oujja, "Comparative SERS effectiveness of silver nanoparticles prepared by different methods: a study of the enhancement factor and the interfacial properties.," *Journal of colloid and interface science*, vol. 326, pp. 103–9, Oct. 2008.

[83] J. R. Lombardi and R. L. Birke, "A unified view of surface-enhanced Raman scattering," *Accounts of Chemical Research*, vol. 42, pp. 734–742, June 2009.

[84] J. R. Lombardi, R. L. Birke, T. Lu, and J. Xu, "Charge-transfer theory of surface enhanced Raman spectroscopy: Herzberg-Teller contributions," *Journal of Chemical Physics*, vol. 84, no. 8, pp. 4174–4180, 1986.

[85] S. Mahajan, J. J. Baumberg, A. E. Russell, and P. N. Bartlett, "Reproducible SERRS from structured gold surfaces.," *Physical chemistry chemical physics : PCCP*, vol. 9, pp. 6016–20, Dec. 2007.

[86] M. Moskovits, "Surface-enhanced Raman spectroscopy: a brief retrospective," *Journal of Raman Spectroscopy*, vol. 36, pp. 485–496, June 2005.

[87] Z. Q. Tian, "Surface-enhanced Raman spectroscopy: advancements and applications," *Journal of Raman Spectroscopy*, vol. 36, pp. 466–470, June 2005.

[88] K. Kneipp, Y. Wang, R. D. Ramachandra, and S. Feld, "Approach to Single Molecule Detection Using Surface-Enhanced Resonance Raman Scattering (SERRS): A Study Using Rhodamine 6G on Colloidal Silver," *Applied Spectroscopy*, vol. 49, no. 6, pp. 780–784, 1995.

[89] G. McNay, D. Eustace, W. E. Smith, K. Faulds, and D. Graham, "Surface-enhanced Raman scattering (SERS) and surface-enhanced resonance Raman scattering (SERRS): A review of applications.," *Applied spectroscopy*, vol. 65, pp. 825–37, Aug. 2011.

[90] G. Sciutto, L. Litti, C. Lofrumento, S. Prati, M. Ricci, M. Gobbo, A. Roda,

E. Castellucci, M. Meneghetti, and R. Mazzeo, "Alternative SERRS probes for the immunochemical localization of ovalbumin in paintings: an advanced mapping detection approach.," *Analyst*, vol. 138, pp. 4532–41, Aug. 2013.

[91] G. Kalaivani, N. S. V. Narayanan, A. Sivanesan, A. Kannan, A. Kaminska, and R. Sevvel, "Regenerative silver nanoparticles for SERRS investigation of met-myoglobin with conserved heme pocket," *RSC Advances*, vol. 3, pp. 6839–6846, 2013.

[92] K. S. McKeating, S. Sloan-Dennison, D. Graham, and K. Faulds, "An investigation into the simultaneous enzymatic and SERRS properties of silver nanoparticles," *Analyst*, 2013.

[93] W. Jacobson and D. M. Simpson, "The fluorescence spectra of pterins and their possible use in the elucidation of the antipernicious anaemia factor," *Biochemical Journal*, vol. 40, pp. 3–14, 1946.

[94] D. M. Simpson, "Applications of Fluorimetric Analysis to the Study of Pterins," *Analyst*, vol. 72, pp. 382–385, 1947.

[95] A. H. Thomas, C. Lorente, A. L. Capparelli, M. R. Pokhrel, A. M. Braun, and E. Oliveros, "Fluorescence of pterin, 6-formylpterin, 6-carboxypterin and folic acid in aqueous solution: pH effects," *Photochemical & Photobiological Sciences*, vol. 1, pp. 421–426, June 2002.

[96] F. M. Cabrerizo, G. Petroselli, C. Lorente, A. L. Capparelli, A. H. Thomas, A. M. Braun, and E. Oliveros, "Substituent effects on the photophysical properties of pterin derivatives in acidic and alkaline aqueous solutions.," *Photochemistry and photobiology*, vol. 81, no. 5, pp. 1234–40, 2005.

[97] J. R. Albani, *Principles and Application of Fluorescence Spectroscopy*. Oxford : Blackwell, 2007.

[98] C. A. Nichol, G. J. Smith, and D. S. Duch, "Biosynthesis and metabolism of

tetrahydrobiopterin and molybdopterin," *Annual Review of Biochemistry*, vol. 54, pp. 729–764, 1985.

[99] K. U. Schallreuter, J. M. Wood, M. R. Pittelkow, M. Gütlich, K. R. Lemke, W. Rödl, N. N. Swanson, K. Hitzemann, and I. Ziegler, "Regulation of melanin biosynthesis in the human epidermis by tetrahydrobiopterin," *Science*, vol. 263, pp. 1444–1446, 1994.

[100] J. R. Lakowicz, *Principles of Fluorescence Spectroscopy*. New York : Springer, 3rd ed., 2006.

[101] S. Kao, A. N. Asanov, and P. B. Oldham, "A Comparison of Fluorescence Inner-Filter Effects for Different Cell Configurations," *Instrumentation Science & Technology*, vol. 26, pp. 375–387, 1998.

[102] A. Albert, "Quantitative studies of the avidity of naturally occurring substances for trace metals," *Biochemical Journal*, vol. 54, pp. 646–654, 1953.

[103] A. Thomas, M. R. Feliz, and A. L. Cappareili, "Equilibrium and kinetic studies of cobalt(II) complexation by folic acid," *Transition Metal Chemistry*, vol. 21, pp. 317–321, 1996.

[104] A. H. Thomas, G. Suárez, F. M. Cabrerizo, R. Martino, and A. L. Capparelli, "Study of the photolysis of folic acid and 6-formylpterin in acid aqueous solutions," *Journal of Photochemistry and Photobiology A: Chemistry*, vol. 135, pp. 147–154, 2000.

[105] V. D. Monópoli, A. H. Thomas, and A. L. Capparelli, "Kinetics and equilibrium study of nickel (II) complexation by pterin," *International Journal of Chemical Kinetics*, vol. 32, pp. 231–237, 2000.

[106] A. Thomas, F. G. Einschlag, M. R. Féliz, and A. L. Capparelli, "First steps in the photochemistry of folate in alkaline medium," *Journal of Photochemistry and Photobiology A: Chemistry*, vol. 116, pp. 187–190, July 1998.

[107] G. Suárez, F. M. Cabrerizo, C. Lorente, A. H. Thomas, and A. L. Capparelli,

"Study of the photolysis of 6-carboxypterin in acid and alkaline aqueous solutions," *Journal of Photochemistry and Photobiology A: Chemistry*, vol. 132, pp. 53–57, Mar. 2000.

[108] A. Mancha de Llanos, M. M. De Zan, M. J. Culzoni, A. Espinosa-Mansilla, F. Cañada Cañada, A. Muñoz de la Peña, and H. C. Goicoechea, "Determination of marker pteridines in urine by HPLC with fluorimetric detection and second-order multivariate calibration using MCR-ALS.," *Analytical and bioanalytical chemistry*, vol. 399, pp. 2123–35, Feb. 2011.

[109] M. M. Müller, H. C. Curtius, M. Herold, and C. H. Huber, "Neopterin in clinical practice.," *Clinica Chimica Actacta*, vol. 201, pp. 1–16, Sept. 1991.

[110] Y.-Q. Wan, L.-J. Tang, and T. Tan, "Simultaneous determination of xanthopterin and isoxanthopterin in human urine by synchronous fluorescence spectroscopy," *Journal of Fluorescence*, vol. 20, pp. 1191–1198, Nov. 2010.

[111] F. M. Cabrerizo, M. L. Dántola, A. H. Thomas, C. Lorente, A. M. Braun, E. Oliveros, and A. L. Capparelli, "Photooxidation of pterin in aqueous solutions: biological and biomedical implications.," *Chemistry & biodiversity*, vol. 1, pp. 1800–11, Nov. 2004.

[112] D. E. Johnson, H.-W. Ai, P. Wong, J. D. Young, R. E. Campbell, and J. R. Casey, "Red fluorescent protein pH biosensor to detect concentrative nucleoside transport.," *The Journal of Biological Chemistry*, vol. 284, pp. 20499–20511, July 2009.

[113] N. Leopold and B. Lendl, "A New Method for Fast Preparation of Highly Surface-Enhanced Raman Scattering (SERS) Active Silver Colloids at Room Temperature by Reduction of Silver Nitrate with Hydroxylamine Hydrochloride," *J. Phys. Chem. B*, vol. 107, pp. 5723–5727, 2003.

[114] R. Tantra, R. J. C. Brown, and M. J. T. Milton, "Strategy to improve the reproducibility of colloidal," *J. Raman Spectroscopy*, vol. 38, no. July, pp. 1469–1479, 2007.

[115] D. Pristinski, S. Tan, M. Erol, H. Du, and S. Sukhishvili, "In situ SERS study of Rhodamine 6G adsorbed on individually immobilized Ag nanoparticles," *Journal of Raman Spectroscopy*, vol. 37, pp. 762–770, July 2006.

[116] G. P. Glaspell, C. Zuo, and P. W. Jagodzinski, "Surface Enhanced Raman Spectroscopy Using Silver Nanoparticles: The Effects of Particle Size and Halide Ions on Aggregation," *Journal of Cluster Science*, vol. 16, pp. 39–51, Mar. 2005.

[117] C. Rodger, V. Rutherford, P. C. White, and W. E. Smith, "Towards Quantitative Surface Enhanced Resonance Raman Scattering (SERRS) : a Study of Aggregation and Concentration for Two Rhodamine Dyes," *Journal of Raman Spectroscopy*, vol. 29, pp. 601–606, 1998.

[118] M. A. De Jesús, K. S. Giesfeldt, and M. J. Sepaniak, "Improving the analytical figures of merit of SERS for the analysis of model environmental pollutants," *Journal of Raman Spectroscopy*, vol. 35, pp. 895–904, Oct. 2004.

[119] R. J. C. Brown, J. Wang, R. Tantra, R. E. Yardley, and M. J. T. Milton, "Electromagnetic modelling of Raman enhancement from nanoscale substrates: a route to estimation of the magnitude of the chemical enhancement mechanism in SERS," *Faraday Discussions*, vol. 132, pp. 201–213, 2006.

[120] R. G. Freeman, R. M. Bright, M. B. Hommer, and M. J. Natan, "Size selection of colloidal gold aggregates by filtration: effect on surface-enhanced Raman scattering intensities," *Journal of Raman Spectroscopy*, vol. 30, pp. 733–738, Aug. 1999.

[121] J. C. Jones, C. McLaughlin, D. Littlejohn, D. A. Sadler, D. Graham, and W. E. Smith, "Quantitative assessment of surface-enhanced resonance Raman scattering for the analysis of dyes on colloidal silver.," *Analytical Chemistry*, vol. 71, pp. 596–601, Feb. 1999.

[122] Y. Sun and Y. Xia, "Shape-controlled synthesis of gold and silver nanoparticles," *Science*, vol. 298, pp. 2176–2179, Dec. 2002.

[123] B. Y. Xia, B. Gates, Y. Yin, and Y. Lu, "Monodispersed colloidal spheres: Old materials with new applications," *Advanced Materials*, vol. 12, no. 10, pp. 693–713, 2000.

[124] S. E. J. Bell and N. M. S. Sirimuthu, "Quantitative surface-enhanced Raman spectroscopy.," *Chemical Society Reviews*, vol. 37, pp. 1012–24, May 2008.

[125] X.-M. Lin, Y. Cui, Y.-H. Xu, B. Ren, and Z.-Q. Tian, "Surface-enhanced Raman spectroscopy: substrate-related issues.," *Analytical and Bioanalytical Chemistry*, vol. 394, pp. 1729–1745, Aug. 2009.

[126] R. Aroca, *Surface Enhanced Vibrational Spectroscopy*. No. 1, Hoboken, NJ: Wiley, Mar. 2006.

[127] P. C. Lee and D. Meisel, "Adsorption and surface-enhanced Raman of dyes on silver and gold sols," *Journal of Physical Chemistry*, vol. 86, pp. 3391–3395, 1982.

[128] R. Sanci and M. Volkan, "Surface-enhanced Raman scattering (SERS) studies on silver nanorod substrates," *Sensors and Actuators B: Chemical*, vol. 139, pp. 150–155, May 2009.

[129] D. E. Charles, D. Aherne, M. Gara, D. M. Ledwith, Y. K. Gun'ko, J. M. Kelly, W. J. Blau, and M. E. Brennan-Fournet, "Versatile solution phase triangular silver nanoplates for highly sensitive plasmon resonance sensing," *ACS Nano*, vol. 4, no. 1, pp. 55–64, 2010.

[130] C. L. Haynes, A. D. Mcfarland, and R. P. V. Duyne, "Surface-enhanced Raman Spectroscopy," *Analytical Chemistry*, vol. 77, pp. 338A–346A, 2005.

[131] T. M. Cotton, S. G. Schultz, and R. P. Van Duyne, "Surface-enhanced resonance Raman scattering from cytochrome c and myoglobin adsorbed on a silver electrode," *Journal of the American Chemical Society*, vol. 102, pp. 7960–7962, 1980.

[132] L. A. Dick, A. J. Haes, and R. P. V. Duyne, "Distance and orientation depen-

dence of heterogeneous electron transfer: A surface-enhanced resonance Raman scattering study of cytochrome c bound to carboxylic acid terminated alkanethiols adsorbed on silver electrodes," *Journal of Physical Chemistry B*, vol. 104, pp. 11752–11762, 2000.

[133] A. Stewart, S. Zheng, M. R. McCourt, and S. E. J. Bell, "Controlling assembly of mixed thiol monolayers on silver nanoparticles to tune their surface properties.," *ACS Nano*, vol. 6, pp. 3718–3726, May 2012.

[134] X. Zhang, J. Zhao, A. V. Whitney, J. W. Elam, and R. P. Van Duyne, "Ultrastable substrates for surface-enhanced Raman spectroscopy: Al2O3 overlayers fabricated by atomic layer deposition yield improved anthrax biomarker detection," *Journal of the American Chemical Society*, vol. 128, pp. 10304–10309, Aug. 2006.

[135] S. M. Mahurin, J. John, M. J. Sepaniak, and S. Dai, "A reusable surface-enhanced Raman scattering (SERS) substrate prepared by atomic layer deposition of alumina on a multi-layer gold and silver film.," *Applied Spectroscopy*, vol. 65, pp. 417–422, Apr. 2011.

[136] X. X. Han, Y. Ozaki, and B. Zhao, "Label-free detection in biological applications of surface-enhanced Raman scattering," *Trends in Analytical Chemistry*, vol. 38, pp. 67–78, Sept. 2012.

[137] L. G. Liu and W. Bassett, "Compression of silver and phase transformation of sodium chloride," *Journal of Applied Physics*, vol. 44, pp. 1475–1479, 1973.

[138] M. J. Adams, *Chemometrics in Analytical Spectroscopy*. Cambridge: The Royal Society of Chemistry, 2nd ed., 2004.

[139] P. Mouroulis and J. Macdonald, *Geometrical Optics & Optical Design*. New York ; Oxford: Oxford University Press, 1997.

[140] M. Cyrankiewicz, T. Wybranowski, and S. Kruszewski, "Study of SERS efficiency

of metallic colloidal systems," *Journal of Physics: Conference Series*, vol. 79, p. 012013, Aug. 2007.

[141] M. Meyer, E. C. Le Ru, and P. G. Etchegoin, "Self-limiting aggregation leads to long-lived metastable clusters in colloidal solutions.," *The Journal of Physical Chemistry B*, vol. 110, pp. 6040–6047, Mar. 2006.

[142] H. Bengter, C. Tengroth, and S. P. Jacobsson, "New light on Ag-colloid preparation for surface-enhanced FT-Raman spectroscopy: the role of aggregation," *Journal of Raman Spectroscopy*, vol. 36, pp. 1015–1022, Nov. 2005.

[143] A. Otto, A. Bruckbauer, and Y. Chen, "On the chloride activation in SERS and single molecule SERS," *Journal of Molecular Structure*, vol. 661-662, pp. 501–514, Dec. 2003.

[144] S. E. J. Bell and N. M. S. Sirimuthu, "Quantitative surface-enhanced Raman spectroscopy," *Chemical Society Reviews*, vol. 37, pp. 1012–1024, May 2008.

[145] R. Stevenson, R. J. Stokes, D. MacMillan, D. Armstrong, K. Faulds, R. Wadsworth, S. Kunuthur, C. J. Suckling, and D. Graham, "In situ detection of pterins by SERS.," *The Analyst*, vol. 134, pp. 1561–4, Aug. 2009.

[146] C. Smyth, S. Mehigan, Y. P. Rakovich, S. E. J. Bell, and E. M. McCabe, "Pterin detection using surface-enhanced Raman spectroscopy incorporating a straightforward silver colloid-based synthesis technique.," *Journal of Biomedical Optics*, vol. 16, p. 077007, July 2011.

[147] A. G. Ryder, J. D. Vincentis, B. Li, P. W. Ryan, N. M. S. Sirimuthu, and K. J. Leister, "A stainless steel multi-well plate (SS-MWP) for high-throughput Raman analysis of dilute solutions," *Journal of Raman Spectroscopy*, vol. 41, pp. 1266–1275, Oct. 2010.

[148] T. Donnelly, B. Doggett, and J. Lunney, "Pulsed laser deposition of nanostructured Ag films," *Applied Surface Science*, vol. 252, pp. 4445–4448, Apr. 2006.

[149] C. Account, "TCD Instructions for Matlab Installation TCD Instructions for Matlab Installation,"

[150] W. Eberhardt, "Clusters as new materials," *Surface Science*, vol. 500, pp. 242–270, Mar. 2002.

[151] M. J. Natan, "Concluding Remarks : Surface enhanced Raman scattering," *Faraday Discussions*, vol. 132, p. 321, 2006.

[152] T. R. Jensen, M. D. Malinsky, C. L. Haynes, and R. P. Van Duyne, "Nanosphere Lithography: Tunable Localized Surface Plasmon Resonance Spectra of Silver Nanoparticles," *The Journal of Physical Chemistry B*, vol. 104, pp. 10549–10556, Nov. 2000.

[153] C. L. Haynes and R. P. Van Duyne, "Plasmon-sampled surface-enhanced Raman excitation spectroscopy," *Journal of Physical Chemistry B*, vol. 107, pp. 7426–7433, July 2003.

[154] A. D. McFarland, M. A. Young, J. A. Dieringer, and R. P. Van Duyne, "Wavelength-scanned surface-enhanced Raman excitation spectroscopy.," *Journal of Physical Chemistry B*, vol. 109, pp. 11279–11285, June 2005.

[155] L. A. Dick, A. D. McFarland, C. L. Haynes, and R. P. Van Duyne, "Metal film over nanosphere (MFON) electrodes for surface-enhanced Raman spectroscopy (SERS): Improvements in surface nanostructure stability and suppression of irreversible loss," *Journal of Physical Chemistry B*, vol. 106, pp. 853–860, Jan. 2002.

[156] M. Litorja, C. L. Haynes, A. J. Haes, T. R. Jensen, and R. P. Van Duyne, "Surface-enhanced Raman scattering detected temperature programmed desorption : Optical properties , nanostructure , and stability of silver film over SiO2 nanosphere surfaces," *Journal of Physical Chemistry B*, vol. 105, pp. 6907–6915, 2001.

[157] X. Zhang, C. R. Yonzon, and R. Van Duyne, "Nanosphere lithography fabri-

cated plasmonic materials and their applications," *Journal of Materials Research*, vol. 21, pp. 1083–1092, 2006.

[158] H. Ko, S. Singamaneni, and V. V. Tsukruk, "Nanostructured surfaces and assemblies as SERS media," *Small*, vol. 4, pp. 1576–1599, Oct. 2008.

[159] M. J. Banholzer, J. E. Millstone, L. Qin, and C. A. Mirkin, "Rationally designed nanostructures for surface-enhanced Raman spectroscopy.," *Chemical Society Reviews*, vol. 37, pp. 885–897, May 2008.

[160] D. P. Fromm, A. Sundaramurthy, A. Kinkhabwala, P. J. Schuck, G. S. Kino, and W. E. Moerner, "Exploring the chemical enhancement for surface-enhanced Raman scattering with Au bowtie nanoantennas.," *Journal of Chemical Physics*, vol. 124, p. 61101, Feb. 2006.

[161] N. Felidj, J. Aubard, G. Levi, J. R. Krenn, A. Hohenau, G. Schider, A. Leitner, and F. R. Aussenegg, "Optimized surface-enhanced Raman scattering on gold nanoparticle arrays," *Applied Physics Letters*, vol. 82, no. 18, p. 3095, 2003.

[162] A. Tao, P. Sinsermsuksakul, and P. Yang, "Tunable plasmonic lattices of silver nanocrystals," *Nature Nanotechnology*, vol. 2, pp. 435–440, July 2007.

[163] Y. Lu, G. L. Liu, and L. P. Lee, "High-density silver nanoparticle film with temperature-controllable interparticle spacing for a tunable surface enhanced Raman scattering substrate.," *Nano Letters*, vol. 5, pp. 5–9, Jan. 2005.

[164] P. N. Bartlett, J. J. Baumberg, S. Coyle, and M. E. Abdelsalam, "Optical properties of nanostructured metal films," *Faraday Discussions*, vol. 125, p. 117, 2004.

[165] S. Mahajan, M. Abdelsalam, Y. Suguwara, S. Cintra, A. Russell, J. Baumberg, and P. Bartlett, "Tuning plasmons on nano-structured substrates for NIR-SERS.," *Physical Chemistry Chemical Physics*, vol. 9, pp. 104–109, Jan. 2007.

[166] C. Gellini, M. Muniz-Miranda, M. Innocenti, F. Carlà, F. Loglio, M. L. Foresti, and P. R. Salvi, "Nanopatterned Ag substrates for SERS spectroscopy," *Physical Chemistry Chemical Physics*, vol. 10, pp. 4555–4558, Aug. 2008.

[167] W. Lee, S. Y. Lee, R. M. Briber, and O. Rabin, "Self-assembled SERS substrates with tunable surface plasmon resonances," *Advanced Functional Materials*, vol. 21, pp. 3424–3429, Sept. 2011.

[168] B. Zhang, H. Wang, L. Lu, K. Ai, G. Zhang, and X. Cheng, "Large-area silver-coated silicon nanowire arrays for molecular sensing using surface-enhanced Raman spectroscopy," *Advanced Functional Materials*, vol. 18, pp. 2348–2355, Aug. 2008.

[169] C. Ruan, G. Eres, W. Wang, Z. Zhang, and B. Gu, "Controlled fabrication of nanopillar arrays as active substrates for surface-enhanced Raman spectroscopy," *Langmuir*, vol. 23, pp. 5757–5760, May 2007.

[170] E. Giorgetti, S. Trigari, A. Rindi, G. Margheri, S. Sottini, G. Dellepiane, G. Brusatin, L. Brigo, M. Muniz-Miranda, and I. Timtcheva, "Tunable gold nanostars for surface enhanced Raman spectroscopy," *Physica Status Solidi B*, vol. 249, pp. 1188–1192, June 2012.

[171] C. Cheng, B. Yan, S. M. Wong, X. Li, W. Zhou, T. Yu, Z. Shen, H. Yu, and H. J. Fan, "Fabrication and SERS performance of silver-nanoparticle-decorated Si/ZnO nanotrees in ordered arrays," *ACS Applied Materials & Interfaces*, vol. 2, pp. 1824–1828, July 2010.

[172] X. X. Han, B. Zhao, and Y. Ozaki, "Surface-enhanced Raman scattering for protein detection.," *Analytical and Bioanalytical Chemistry*, vol. 394, pp. 1719–1727, Aug. 2009.

[173] L. Chen, X. Han, J. Yang, J. Zhou, W. Song, B. Zhao, W. Xu, and Y. Ozaki, "Detection of proteins on silica-silver core-shell substrates by surface-enhanced Raman spectroscopy," *Journal of Colloid and Interface Science*, vol. 360, pp. 482–487, Aug. 2011.

[174] H. Cui, P. Liu, and G. W. Yang, "Noble metal nanoparticle patterning deposition using pulsed-laser deposition in liquid for surface-enhanced Raman scattering," *Applied Physics Letters*, vol. 89, p. 153124, 2006.

[175] C. D'Andrea, F. Neri, P. M. Ossi, N. Santo, and S. Trusso, "The controlled pulsed laser deposition of Ag nanoparticle arrays for surface enhanced Raman scattering.," *Nanotechnology*, vol. 20, p. 245606, June 2009.

[176] N. Agarwal, F. Neri, S. Trusso, A. Lucotti, and P. Ossi, "Au nanoparticle arrays produced by Pulsed Laser Deposition for Surface Enhanced Raman Spectroscopy," *Applied Surface Science*, vol. 258, pp. 9148–9152, Sept. 2012.

[177] E. Fazio, F. Neri, C. D'Andrea, P. M. Ossi, N. Santo, and S. Trusso, "SERS activity of pulsed laser ablated silver thin films with controlled nanostructure," *Journal of Raman Spectroscopy*, vol. 42, pp. 1298–1304, Feb. 2011.

[178] N. R. Agarwal, E. Fazio, F. Neri, S. Trusso, C. Castiglioni, A. Lucotti, N. Santo, and P. M. Ossi, "Ag and Au nanoparticles for SERS substrates produced by pulsed laser ablation," *Crystal Research and Technology*, vol. 46, pp. 836–840, Aug. 2011.

[179] R. Dolbec, E. Irissou, M. Chaker, D. Guay, F. Rosei, and M. A. El Khakani, "Growth dynamics of pulsed laser deposited Pt nanoparticles on highly oriented pyrolitic graphite substrates," *Physical Review B*, vol. 70, p. 201406, Nov. 2004.

[180] C. N. Afonso, J. Gonzalo, R. Serna, J. C. G. D. Sande, C. Ricolleau, C. Grigis, M. Gandais, D. E. Hole, and P. D. Townsend, "Vacuum versus gas environment for the synthesis of nanocomposite films by pulsed-laser deposition," *Applied Physics A: Materials Science & Processing*, vol. 69, pp. 201–207, 1999.

[181] S. Amoruso, R. Bruzzese, X. Wang, N. N. Nedialkov, and P. A. Atanasov, "Femtosecond laser ablation of nickel in vacuum," *Journal of Physics D: Applied Physics*, vol. 40, pp. 331–340, Jan. 2007.

[182] A. Merlen, F. Lagugné-Labarthet, and E. Harté, "Surface-enhanced Raman and fluorescence spectroscopy of dye molecules deposited on nanostructured gold surfaces," *Journal of Physical Chemistry C*, vol. 114, pp. 12878–12884, 2010.

[183] T. Wadayama, M. Oishi, and A. Hatta, "Surface enhanced Raman scattering of

organic sample powders spread over vacuum-evaporated silver thin film," *Applied Surface Science*, vol. 253, pp. 2713–2717, Dec. 2006.

[184] M. V. Chursanova, V. M. Dzhagan, V. O. Yukhymchuk, O. S. Lytvyn, M. Y. Valakh, I. A. Khodasevich, D. Lehmann, D. R. T. Zahn, C. Waurisch, and S. G. Hickey, "Nanostructured Silver Substrates With Stable and Universal SERS Properties: Application to Organic Molecules and Semiconductor Nanoparticles.," *Nanoscale Research Letters*, vol. 5, pp. 403–409, Jan. 2009.

[185] M. Fujimaki, K. Awazu, J. Tominaga, and Y. Iwanabe, "Surface-enhanced Raman scattering from Ag nanoparticles formed by visible laser irradiation of thermally annealed AgO[sub x] thin films," *Journal of Applied Physics*, vol. 100, no. 7, p. 074303, 2006.

[186] S. A. Maskevich, I. F. Sveklo, A. V. Feofanov, A. I. Yanul, V. A. Oleinikov, S. P. Gromov, O. A. Fedorova, M. V. Alfimov, I. R. Nabiev, and L. N. Kivach, "SERS-active substrates based on thin silver films annealed at high temperatures : A comparative study by techniques of atomic-force microscopy and surface-enhanced Raman scattering spectroscopy," *Optics and Spectroscopy*, vol. 81, no. 1, pp. 95–102, 1996.

[187] C. H. Kwon, D. W. Boo, H. J. Hwang, and M. S. Kim, "Temperature Dependence and Annealing Effects in Surface-Enhanced Raman Scattering on Chemically Prepared Silver Island Films," *Journal of Physical Chemistry B*, vol. 103, pp. 9610–9615, Nov. 1999.

[188] T. O'Haver, "An Introduction to Signal Processing with applications in Chemical Analysis," 2013.

[189] "A comparison of Klarite SERS Substrates with a rival," *Application Note from Renishaw Diagnostics*, pp. 1–2, 2011.

[190] C. Smyth, I. Mirza, J. Lunney, and E. McCabe, "Surface-enhanced Raman spectroscopy (SERS) using Ag nanoparticle films produced by pulsed laser deposition,"

Applied Surface Science, p. http://dx.doi.org/10.1016/j.apsusc.2012.09.078, Oct. 2012.

[191] C. D. Geddes and J. R. Lakowicz, "Metal-Enhanced Fluorescence," *Journal of Fluorescence*, vol. 12, no. 2, pp. 121–129, 2002.

[192] K. Aslan, Z. Leonenko, J. R. Lakowicz, and C. D. Geddes, "Annealed silver-island films for applications in metal-enhanced fluorescence: interpretation in terms of radiating plasmons.," *Journal of Fluorescence*, vol. 15, pp. 643–54, Sept. 2005.

[193] D. I. Gittins and F. Caruso, "Spontaneous phase transfer of nanoparticulate metals from organic to aqueous media," *Angewandte Chemie International Edition*, vol. 40, no. 16, pp. 3001–3004, 2001.

[194] J. H. Prescott, S.-j. Shiau, and R. L. Rowell, "Characterization of polystyrene latexes by hydrodynamic and electrophoretic fingerprinting," *Langmuir*, vol. 9, pp. 2071–2076, 1993.

[195] J. H. Prescott, R. L. Rowell, and D. R. Bassett, "Dependence of particle size on pH , electrolyte , and time for expandable copolymer latexes by hydrodynamic fingerprinting," *Langmuir*, vol. 13, pp. 1978–1986, 1997.

[196] E. Clementi, D. L. Raimondi, and W. L. Reinhardt, "Atomic Screening Constants from SCF Functions. II. Atoms with 37 to 86 Electrons," vol. 47, pp. 1300–1307, 1967.

[197] A. Maeland and T. B. Flanagan, "Lattice spacings of goldpalladium alloys," *Canadian Journal of Physics*, vol. 42, pp. 2364–2366, Nov. 1964.

[198] J. Reyes-Gasga, S. Tehuacanero-Nuñez, J. M. Montejano-Carrizales, X. Gao, and M. Jose-Yacaman, "Analysis of the contrast in icosahedral gold nanoparticles," *Topics in Catalysis*, vol. 46, pp. 23–30, Sept. 2007.

[199] C. Smyth, R. Reilly, Y. Rakovich, and E. McCabe, "Synthesis and formation of one-dimensional Au nanoparticle chains," *e-Journal of Surface Science and Nanotechnology*, vol. 7, pp. 327–329, 2009.

[200] J. Liao, Y. Zhang, W. Yu, L. Xu, C. Ge, J. Liu, and N. Gu, "Linear aggregation of gold nanoparticles in ethanol," *Colloids and Surfaces A: Physicochemical and Engineering Aspects*, vol. 223, pp. 177–183, Aug. 2003.

[201] B. Y. Xia, P. Yang, Y. Sun, Y. Wu, B. Mayers, B. Gates, Y. Yin, F. Kim, and H. Yan, "One-dimensional nanostructures: Synthesis , characterization, and applications," *Advanced Materials*, vol. 15, no. 5, pp. 353–389, 2003.

[202] Y. Sun, B. Gates, B. Mayers, and Y. Xia, "Crystalline Silver Nanowires by Soft Solution Processing," *Nano Letters*, vol. 2, pp. 165–168, Feb. 2002.

[203] F. Fievet, J. P. Lagier, and M. Figlartz, "Preparing monodisperse metal powers in micrometer and submicrometer sizes by the polyol process," *MRS Bulletin*, vol. 14, no. 12, pp. 29–34, 1989.

[204] Z. Zhang, B. Zhao, and L. Hu, "PVP protective mechanism of ultrafine silver powder synthesized by chemical reduction processes," *Journal of Solid State Chemistry*, vol. 121, pp. 105–110, 1996.